

**REPORT DOCUMENTATION PAGE**Form Approved  
OMB No. 0704-0188

Public reporting burden for this collection of information is estimated to average 1 hour per response, including the time for reviewing instructions, searching data sources, gathering and maintaining the data needed, and completing and reviewing the collection of information. Send comments regarding this burden estimate or any other aspect of this collection of information, including suggestions for reducing this burden to Washington Headquarters Service, Directorate for Information Operations and Reports, 1215 Jefferson Davis Highway, Suite 1204, Arlington, VA 22202-4302, and to the Office of Management and Budget, Paperwork Reduction Project (0704-0188) Washington, DC 20503.

**PLEASE DO NOT RETURN YOUR FORM TO THE ABOVE ADDRESS.****1. REPORT DATE (DD-MM-YYYY)**  
07-00-2003**2. REPORT DATE**  
Final Report**3. DATES COVERED (From - To)**  
Apr 1999 - Apr 2002**4. TITLE AND SUBTITLE**

Modeling of On-board Fuel Cell-Based Power Systems for Naval Ships

**5a. CONTRACT NUMBER****5b. GRANT NUMBER**  
N00014-99-1-0560**5c. PROGRAM ELEMENT NUMBER****5d. PROJECT NUMBER****5e. TASK NUMBER****5f. WORK UNIT NUMBER****6. AUTHOR(S)**White, Ralph E  
Dougal, Roger A.**7. PERFORMING ORGANIZATION NAME(S) AND ADDRESS(ES)**Departments of Chemical Engineering and Electrical Engineering  
University of South Carolina  
Swearingen Engineering Building 3A01  
Columbia, SC 29208**8. PERFORMING ORGANIZATION  
REPORT NUMBER****9. SPONSORING/MONITORING AGENCY NAME(S) AND ADDRESS(ES)**Office of Naval Research  
ONR 254, Ballston Centre Tower One  
800 North Quincy Street  
Arlington, VA 22217-5660**10. SPONSOR/MONITOR'S ACRONYM(S)**  
ONR**11. SPONSORING/MONITORING  
AGENCY REPORT NUMBER****12. DISTRIBUTION AVAILABILITY STATEMENT**

Approved for Public Release; distribution is Unlimited.

**BEST AVAILABLE COPY****20030929 026****13. SUPPLEMENTARY NOTES****14. ABSTRACT**

A ship service fuel cell power system has been explored in a multidisciplinary and multidimensional effort to improve understanding the dynamic behaviors of individual components and the performance of the system. Models of individual components of the system are developed in the Virtual Test Bed format, which then allows easy reconfiguration of the system and allows nearly unlimited studies of system tradeoffs. Developed models include those for the fuel cell stack, compressors and expanders, methanol re-former (as a precursor to strategic fuels reformer), hydride bed (as an alternative hydrogen storage technology) and control systems. These, together with other models developed under other research programs, have been combined into a system simulation that allows to study the first-order system response.

**15. SUBJECT TERMS**

fuel cell, modeling, ship service power, simulation, reformer, hydride

**16. SECURITY CLASSIFICATION OF:****a. REPORT**  
U**b. ABSTRACT**  
U**c. THIS PAGE**  
U**17. LIMITATION OF  
ABSTRACT**  
UU**18. NUMBER  
OF PAGES****19a. NAME OF RESPONSIBLE PERSON**  
Dr. Ralph E. White**19b. TELEPHONE NUMBER (Include area code)**  
803-777-3270

# **MODELING OF ON-BOARD FUEL CELL POWER PLANTS**

## **FINAL PROJECT REPORT**

**CONTRACT # N00014-99-1-0560**

**April 15, 1999 – April 14, 2002**

**Submitted to**

**Office of Naval Research**

**Submitted by**

**Ralph White<sup>#</sup>, Roger A. Dougal<sup>\*</sup>  
<sup>#</sup>Dept of Chemical Engineering  
<sup>\*</sup>Dept. of Electrical Engineering  
University of South Carolina  
Columbia, SC 29208**

**April 15, 2002**

## Table of Contents

<b>EXECUTIVE SUMMARY</b>	<b>1</b>
<b>INTRODUCTION</b>	<b>4</b>
<b>FUEL CELL TECHNOLOGIES</b>	<b>4</b>
<b>FUEL-CELL TEST STATION</b>	<b>4</b>
<b>CHARACTERIZE DYNAMIC PERFORMANCE</b>	<b>5</b>
Experimental Data	5
<b>Fuel Cell Models</b>	<b>5</b>
Performance Model	5
Generating Model Data	6
<b>SYSTEM-LEVEL MODEL</b>	<b>7</b>
<b>HYDROGEN STORAGE TECHNOLOGIES</b>	<b>8</b>
<b>CHARACTERIZATION OF HYDRIDE STORAGE</b>	<b>8</b>
<b>DETAILED MODEL</b>	<b>9</b>
<b>SYSTEM-LEVEL MODEL</b>	<b>10</b>
<b>CENTRIFIGUAL COMPRESSOR</b>	<b>12</b>
<b>METHANOL REFORMER</b>	<b>13</b>
<b>FEEDBACK CONTROL SYSTEM</b>	<b>14</b>
<b>SYSTEM MODEL</b>	<b>15</b>
<b>DELIVERABLES</b>	<b>19</b>
<b>MODELS</b>	<b>19</b>
VTB Models	19
<b>PUBLICATIONS AND PRESENTATIONS</b>	<b>21</b>
<b>PUBLICATIONS</b>	<b>21</b>
Journals	21
<b>PRESENTATIONS</b>	<b>21</b>
<b>CONCLUSIONS</b>	<b>21</b>
<b>APPENDICES</b>	<b>22</b>
<b>APPENDIX 1 – STUDENTS EDUCATION</b>	<b>22</b>
<b>APPENDIX 2 – FUEL CELL CO MODELING</b>	<b>22</b>
<b>APPENDIX 3 - MODEL HELP FILES</b>	<b>22</b>
<b>APPENDIX 4 - PUBLICATIONS</b>	<b>22</b>

## EXECUTIVE SUMMARY

A ship service fuel cell power system has been explored in a multidisciplinary and multidimensional effort to improve understanding the dynamic behaviors of individual

components and the performance of the system. Models of individual components of the system are developed in the Virtual Test Bed format, which then allows easy reconfiguration of the system and allows nearly unlimited studies of system tradeoffs. Developed models include those for the fuel cell stack, compressors and expanders, methanol reformer (as a precursor to strategic fuels reformer), hydride bed (as an alternative hydrogen storage technology) and control systems. These, together with other models developed under other research programs, have been combined into a system simulation that allows to study the first-order system response.

At the component level, research focused on

- characterizing and modeling the dynamics of proton exchange membrane (PEM) fuel cell stacks. The work was performed on both the standalone model and the VTB model.
- characterizing and modeling the dynamics of air compressor in VTB
- characterizing and modeling the methanol reformer in VTB
- characterizing and modeling metal hydride bed in both standalone model and VTB model
- Modeling a feedback control system using embedded MatLab object

At the system level, a representative shipboard fuel cell power system was assembled and simulated in VTB environment for study of the system transients.

Specific accomplishments of the studies included

- PEM Fuel Cells Standalone Model
  - A test stand was assembled for the purpose of characterising the transient response of PEM fuel cell systems
  - Half-cell data was gathered as input for formulation of a detailed fuel cell model.
  - A mathematical model for the effect of adding an air bleed to a reformat containing monodioxide in the anode feed was developed. The model can very well predict the oxidation rate of CO and the results are consistent with existing experimental data.
- PEM Fuel Cells VTB Model
  - The system level model was developed to account for the interactive reversible and irreversible potentials with dependencies of pressure, temperature, fuel and air consumptions, and heat production.
- Compressor

Several system level models of different level of details were developed for different research foci.

A general centrifugal compressor was developed.

- Hydrogen Storage
  - A large hydride bed was instrumented and experimentally characterised during charge and discharge processes.
  - A detailed model of the hydride bed was formulated.
  - A system-level model of the hydride bed was developed.
- Methanol Reformer
  - A CSTR model of the methanol reformer was developed.
- Feedback Control System
  - A MatLab/Simulink object for the feedback control system was developed based on the PID control algorithm.
- Shipboard Fuel Cell Power Plant System
  - The dynamic system is assembled in VTB computational environment. The system primarily consists of a PEM fuel cell stack that can be easily reconfigured in terms of voltage and power levels, a steam methanol reformer for fuel processing, or alternatively a hydride bed for fuel supply, a compressor driving air to the fuel cell. The compressor is driven by a motor, which uses the system output power once it starts.

## INTRODUCTION

This report summarizes progress in modeling of shipboard fuel cell power plant project conducted at the University of South Carolina as a collaborative effort between the Departments of Chemical Engineering and Electrical Engineering. The work had three significant foci. The first was enhancing our knowledge of the physical performance of individual electrochemical and mechanical power components through the development of detailed mathematical models. The second was integrating the knowledge obtained by standalone models into VTB simulation models of individual components. The third was to prototype a representative fuel cell power system in VTB environment for study of dynamic performance.

A significant focus of the work was on integrating the knowledge of chemical engineers into dynamic simulation models that could be used to study the electrical performance of fuel cell power systems. This report refers to the construction of various types of simulation models. First are stand-alone models that are generally used for detailed studies of the internal dynamics of a particular component, often including detailed representations of the physics, up to three-dimensional transport and reaction processes. Second are system-level models which generally have lower complexity since they are intended to represent mainly the characteristics observable at the terminals of the device. These models are useful for the study of systems that incorporate these devices. The process of model construction generally starts with physics-based models that attempt to fully describe experimental data, then progresses to simplification of those models into forms that run fast enough to be used effectively in system level studies. At this level, resolution of some of physical effects is generally lost.

This report is arranged as follows. In the next five sections, we summarize the model development of major components, such as PEM fuel cells, centrifugal compressor, methanol reformer, hydride bed and feedback control system. Then a representative fuel cell power system is described. Finally, we describe the project deliverables and the publications that resulted from this work. The appendices contain information related to developed models and copies of the publications, and the student education information.

## FUEL CELL TECHNOLOGIES

### FUEL-CELL TEST STATION

Experimental infrastructure and procedures were developed to measure the physical parameters and verify fuel-cell performance models. A "Dual Channel Fuel Cell Test Station" was purchased. Each channel consists of a single mass flow controller on the cathode channel to regulate air/O<sub>2</sub> flow and three mass flow controllers on the anode channel to regulate the flow of H<sub>2</sub>/reformat/N<sub>2</sub>, and to bleed in a calculated amount of carbon monoxide (CO) and air. A four-way valve allows connection of different gases to the anode and cathode main streams. Each channel also contains temperature controllers for the anode and cathode humidifier bottles, anode and cathode gas lines from the humidifier bottle to the cell, and the fuel cell itself. The fuel cell is connected to the anode and cathode gas inlets and outlets and to an electronic load bank. The load bank allows to electrically load the cells with constant current, constant voltage, sweeping voltage, or

pulse voltage. All the mass flow and temperature controllers, and the electronic load are computer controlled.

## CHARACTERIZE DYNAMIC PERFORMANCE

### Experimental Data

Figure 1 shows the performance of a typical fuel cell obtained at 70 °C at ambient pressure by scanning the voltage of the fuel cell from 1.0 V to 0.3v at 0.05 V increments and resting 30 s at each voltage. The initial drop of the curve (from 0.95 – 0.8 V) results from limitation by the reaction kinetics, predominantly the oxygen reduction reaction (ORR). The linear drop between 0.75 and 0.4 is controlled by ohmic drop in the catalyst layer and the membrane.

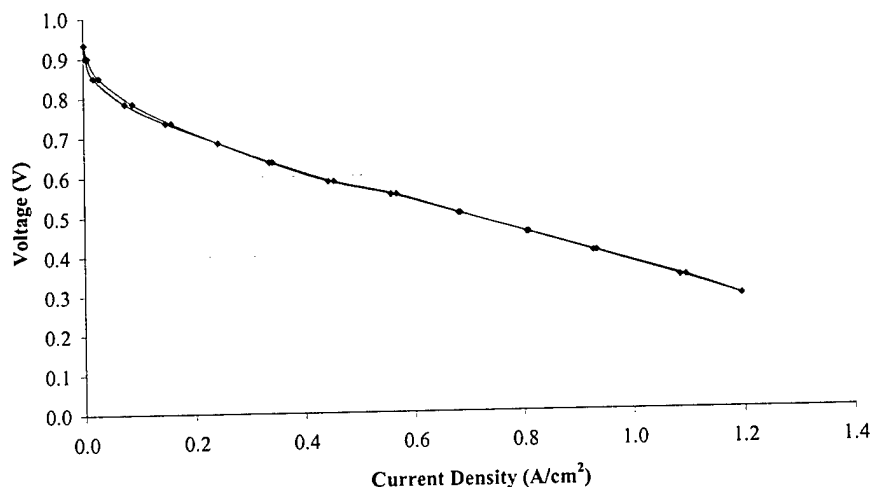


Figure 1. Performance of a 10 cm<sup>2</sup> fuel cell using H<sub>2</sub> and air at 70 °C at ambient pressure

This curve can also be used to qualitatively analyze the transient performance of the fuel cell. The fuel cell is typically operated at 0.6 V with a current density of 0.45 A/cm<sup>2</sup> with the humidity at equilibrium. If the cell voltage is increased to 0.8 V, the accompanying reduction in current to 0.1 A/cm<sup>2</sup> would produce less water at the cathode, which would dry the cathode and the membrane. Oppositely, decreasing the voltage to 0.4 V would cause the cathode to flood, but dry out the anode. The ohmic resistance at the anode would increase, as would the mass transfer resistance at the cathode. Characterising these transients will be the focus of Phase II work.

### Fuel Cell Models

A series of fundamental steady-state and transient models for fuel cells were developed. Some of the models are used to extract physical parameters from experimental data, and others are used to predict the performance of a fuel cell.

#### Performance Model

A typical cell model is divided into seven regions: flow channels, gas-diffusion layers, and catalyst layers on both the anode and cathode sides, and the separator. In the

flow channels, there are no reactions and the dominate transport mechanism is convection. In the gas-diffusion layer, the dominate transport mechanism is diffusion and therefore the Stefan-Maxwell equations apply. In the catalyst layer, both diffusion and reaction are involved. At steady state, the time derivatives are zero and diffusion is balanced by the reaction rate. To date, these equations have been incorporated into the numerical algorithm, but the performance curves have not yet been obtained.

### Generating Model Data

Model data is generated from measurements on a half-cell as shown in Figure 2. The left chamber is initially filled with nitrogen gas and then switched to oxygen gas. The oxygen diffuses through the Nafion<sup>®</sup> 117 membrane and is reduced at platinum sites. The right chamber is filled with an electrolyte solution of H<sub>2</sub>SO<sub>4</sub> and acts as a transport medium for ions moving from the Pt-working electrode to the Pt-counter electrode. An Ag-AgCl reference electrode is used as reference in all experimentation.

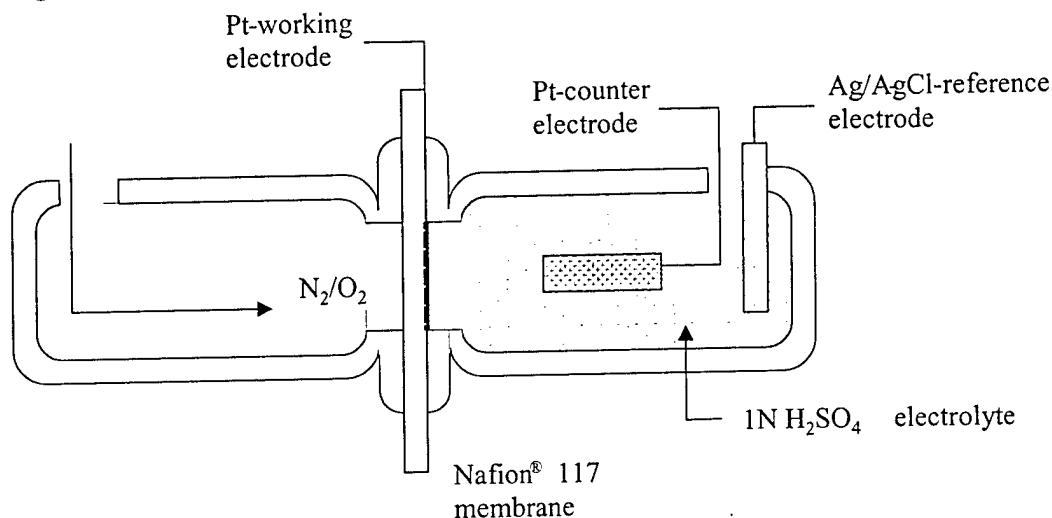


Figure 2. The half-cell experimental apparatus includes two chambers separated by a Nafion<sup>®</sup> 117 membrane platinized on one side. shows the measured current as a function of time.

Figure 3 shows the measured current as a function of time. A potential of +0.1V was applied between the platinized membrane and the Ag/AgCl electrode, the current was recorded until a steady-state was reached ( $\sim 0.070 \mu\text{Amps}$  for Nafion<sup>®</sup> 117 at 25 °C). The experiment was then begun by replaced the nitrogen with oxygen. The current was recorded until a new steady state (the limiting current,  $i_\infty$ ) was reached. For Nafion<sup>®</sup> 117, the experiment required six to ten minutes to reach  $i_\infty$  and data were taken every 0.50 seconds for all trials. After the background current was subtracted from the total measured current,  $i_\infty$  was found to vary from 80 to 275  $\mu\text{A}$  for temperatures of 10 °C to 80 °C, respectively.



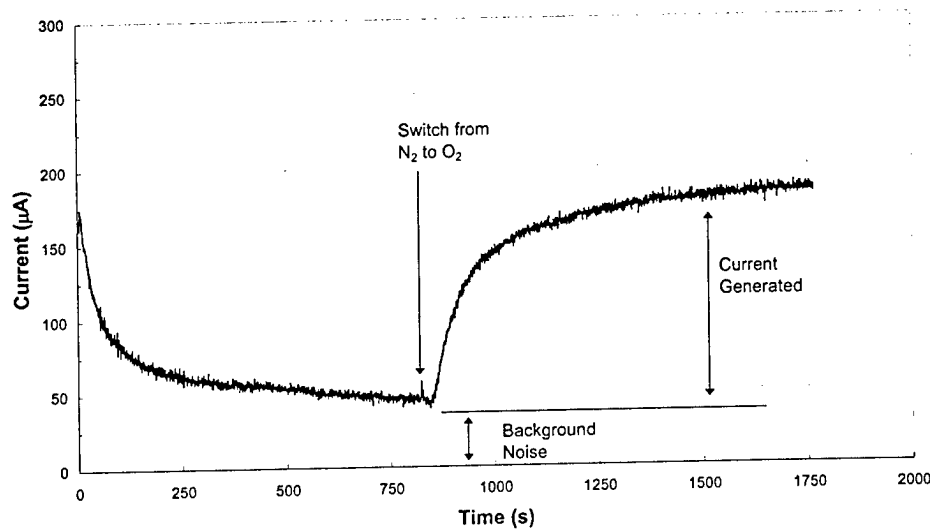


Figure 4 Oxygen reduction current vs. time for Nafion® 117 membrane at 40 °C. compares data for an individual test (40 °C) of oxygen diffusion across Nafion® 117 and the numerical fit using method of least squares. In all cases, the equation fit the data well, with the margin of error between the data set and the numerical fit being less than 2%. For higher temperatures, the current typically continues to increase slightly with time.

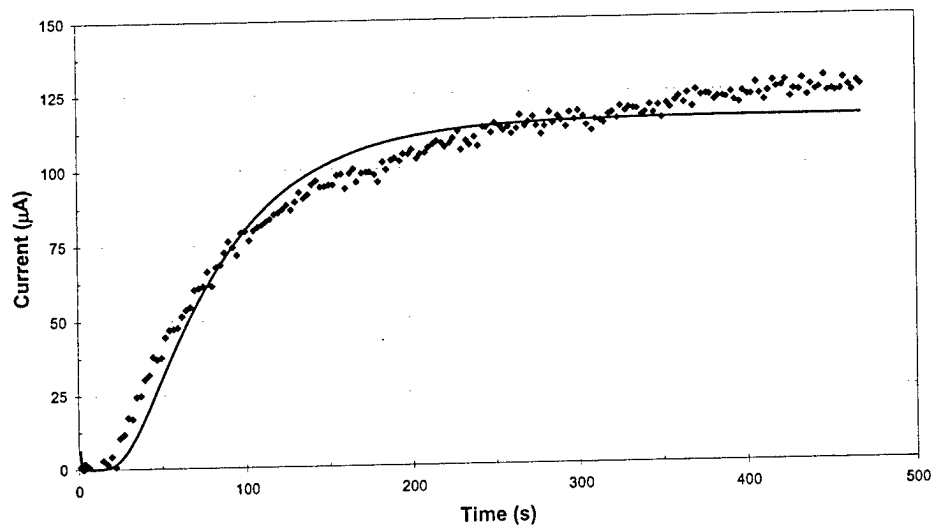


Figure 4. Comparison of the experimental data for oxygen diffusion in a Nafion® 117 membrane at 40 °C to least squares fit.

### SYSTEM-LEVEL MODEL

The VTB system level model of the PEM fuel cell was enhanced to include effects such as: 1) gas inlet pressure effect on voltage-current characteristics; 2) Thermal effect on voltage-current characteristics; and 3) natural thermal connection for heat removal. While the model contains the necessary complexity for system evaluation, it was designed with ease of use and high-speed simulation in mind. Examples of the model

output are shown in Figure 1, where the model is operated at several values of gas inlet pressure ranging from 150 Pa to 300 Pa and at several temperatures ranging from  $-10$  to  $+60$  C. The model was validated against manufacturer's data, as shown in Figure 2. Further details of the characteristic equations are available in the fuel cell model help file.

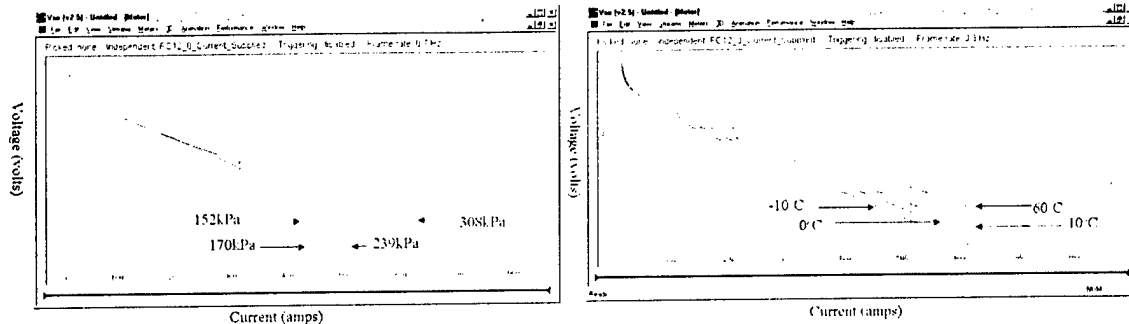


Figure 1. Pressure and temperature dependence of fuel cell voltage and current characteristics.

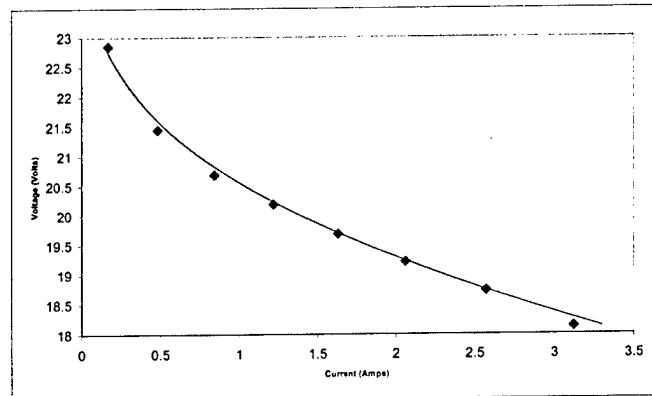


Figure 2. Comparison between V-I characteristics of model and manufacturer's data shows that the model is valid.

## HYDROGEN STORAGE TECHNOLOGIES

### CHARACTERIZATION OF HYDRIDE STORAGE

Development of a mathematical model for the discharge of hydrogen from a metal hydride bed requires definition of the thermodynamic relationship that describes the equilibrium loading of hydrogen in the metal hydride as a function of both pressure and temperature. Two adsorption isotherm relationships were developed in this project. The first one is based on a composite Langmuir model and the second one is based on a modified Virial model.

The prediction of the heat of adsorption/reaction from these models is critical to the accurate modeling of the discharge behavior of hydrogen from a metal hydride bed since it controls the temperatures in the bed. The models predict different values for the heat of adsorption/reaction since the composite Langmuir model has two values depending on whether the loading is above or below the switch point, and the modified Virial model has a loading and temperature dependent function. Experimental calorimetric data

are needed to verify the heat of adsorption/reaction predicted from these two different thermodynamic models. This issue will be addressed in HAPS II by constructing a dosing calorimeter that can be used to simultaneously measure the loading and heat of adsorption/reaction of hydrogen on metal hydrides of interest at different temperatures. Preliminary results of this kind of analysis are given below in the System Level Model section.

A Metal Hydride Hydrogen Storage Test Facility, shown in Figure 7, was designed and constructed for the purpose of parameterizing and validating the model. It consists of a Savannah River Technology Center metal hydride bed containing 26.0 kg of  $\text{La}_{1.06}\text{Ni}_{4.96}\text{Al}_{0.04}$  and flow control elements. Six runs were carried out at hydrogen flows varying from 5 to 40 SLPM.

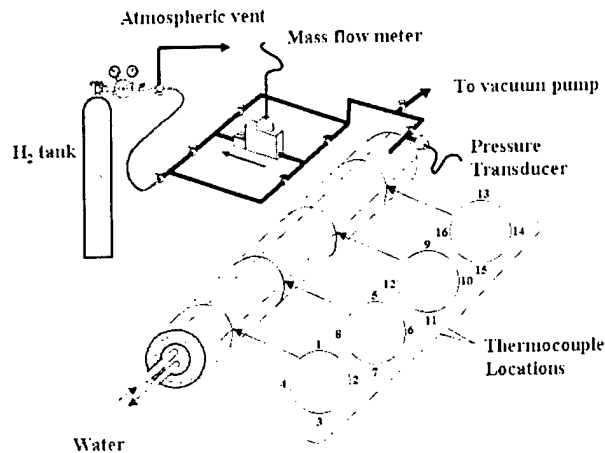


Figure 7. Schematic of the Metal Hydride Hydrogen Storage Test Facility.

The complexity of this experimental system represents a significant challenge to any modeling effort. Many more experiments need to be carried out under different initial and process conditions to properly validate the various assumptions used in the mathematical model, and to verify the thermodynamic and transport properties. This task will be carried out in HAPS II.

## DETAILED MODEL

The model that describes the dynamic discharge of hydrogen from a metal hydride bed has two components: 1) general equations that describe the dynamics inside the metal hydride bed, together with different assumptions that the user can utilize to simplify the general equations according to the mathematical capabilities of the simulator and 2) equations that describe the dynamics involved in a gas pressure regulator placed downstream from the metal hydride bed and a ready to use simplified model for initial use in the virtual test bed (VTB) has been created and will be implemented in HAPS II. Based on the above developments, a layout of the system described mathematically is presented in Figure 8. It consists of a cylindrical metal hydride bed connected in series with a gas pressure regulator downstream to provide hydrogen at a relatively constant pressure  $P_{FC}$  to, for example, a fuel cell.

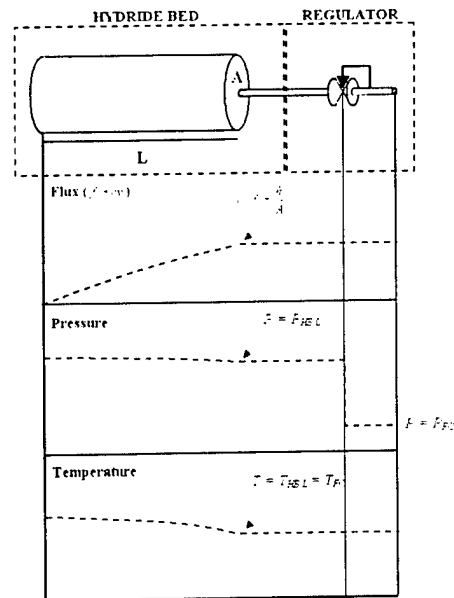


Figure 8. Schematic of the system described mathematically including the metal hydride bed and an inline gas regulator, and typical profiles of the main variables involved in the discharge of hydrogen from the bed.

The complexity of the complete model is user specified and depends on the capability of the simulator. The most rigorous model accounts for various mass and heat transfer resistances in both the axial and radial directions and accounts for internal heat exchange with a circulating fluid. The simplest model ignores resistances and isothermal local equilibrium conditions prevail. These bounding models represent extreme limits and can be used for actual process design and hypothetical process feasibility, respectively. They can also be used to judge complexity of a particular  $H_2$  discharge process by comparing with experimental data.

Results from various models utilizing various assumptions have not yet been compared to experimental data in a purely predictive mode. This requires obtaining the proper thermodynamic and transport relationships that are needed as input to the model and obtaining sufficient dynamic discharge data that can be used to validate the various models utilizing various simplifying assumptions. This will be another focus of the work to be carried out in HAPS II. It is anticipated that even this more rigorous model or one very similar to it can be used in the VTB simulator; hence, it will constitute a major component in the design and development of a hybrid advanced power source via the VTB.

### SYSTEM-LEVEL MODEL

A simplified dynamic model of the discharge of hydrogen from a cylindrical metal hydride bed has been developed for use in the Virtual Test Bed process simulator. The following simplifying assumptions were utilized in this model: no heat transfer resistance at the interface, plug flow, no internal cooling system, negligible heat loss by convection, negligible thermal conductivity, perfectly insulated system, and linear flux drop in the bed. This model still accounts for heat and mass transfer resistances through overall (or lumped) heat and mass transfer coefficients. At present, however, these two coef-

ficients must be obtained by fitting the model to experimental discharge data as discussed below. This dynamic model is currently being implemented in the VTB.

Preliminary experimental data obtained from the experimental metal hydride hydrogen storage test facility described above were used to calibrate this simple model by obtaining a set of heat and mass transfer coefficients from one run and applying them to predict the behavior of other runs. Note that the modified Virial model was used in these simulations. Only three-fourths of the cylinder is filled with the metal hydride to allow the material to expand when taking up hydrogen during charging. As a result, it was anticipated that this simplified first generation VTB model will not be able to accurately predict the dynamic behavior of this system, especially the heat effects. Nevertheless, preliminary modeling results of the dynamic discharge of hydrogen from this system under different molar discharge flow rates were quite encouraging (Figure 9). The model does very well at the low flow rate demand, but fails at higher flow rate demand (not shown).

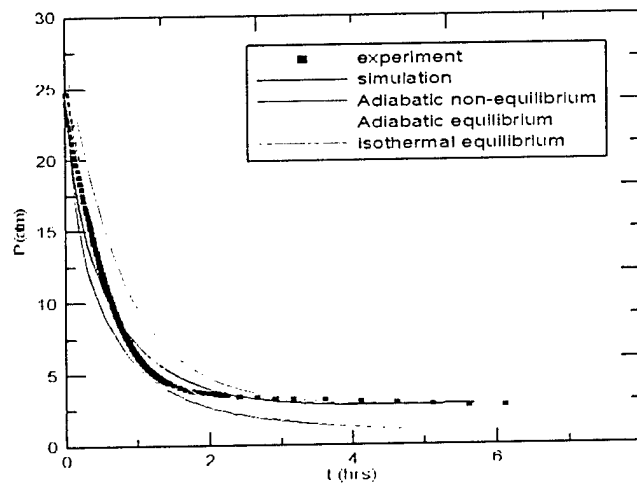


Figure 9. Comparison of the experimental pressure history with different model predictions during discharge at 5 SLPM  $H_2$  demand.

Figure 10 shows data obtained from VTB simulation of the simplified model that discharges hydrogen to a constant sink (fuel cell). The graphs show variation of the pressure, temperature and molar flow rate of the hydride bed,  $H_2$  concentration inside the hydride bed. From Fig 10, it is shown that the pressure declines rapidly initially from 15.0 atms and then decreases slowly after the pressure drops below 5.0 atms. It can also be seen that the temperature and  $H_2$  concentration decrease linearly with the time when the molar flow is constant.

Currently, the effort to refine the model is continued in conjunction with other projects. It will be further validated by comparing to the experimental data.

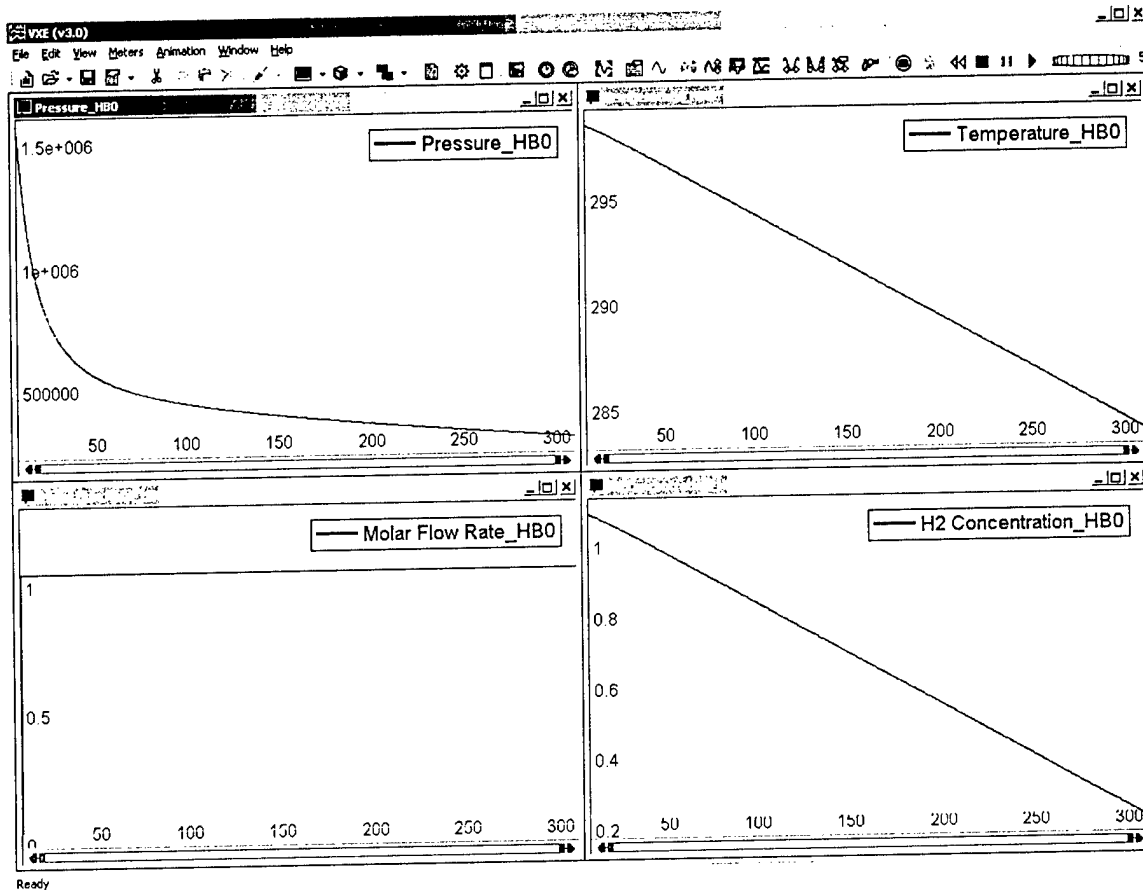


Figure 10. Simulation results of the hydride bed model under a constant hydrogen flow sink load.

## CENTRIFUGAL COMPRESSOR

We have developed several compressor models concerning different applications and different research foci. The simple and linear model is based on empirical data and valid near and within a limited range of the operating point. The output pressure is a linear function of mass flow and rotational speed. The compressor efficiency is a constant that users can input based on their field experience in steady state operation.

The latest development is a nonlinear centrifugal compressor model derived from the first principle, based on which energy transfer considerations are used to develop compressor characteristics. The centrifugal compressor model is presented jointly by the states of mass flow, pressure rise and rotational speed of the spool. Pressure rise is derived from the temperature changes in the compression process. Accordingly, pressure rise is further related to energy transfer by considering the temperature change. The actual energy transfer in the compressor is equivalent to ideal energy transfer minus energy losses. There are two major losses: incidence losses and friction losses. Incidence Losses are the losses due to incidence onto the rotor and vane diffuser. Frictional Losses are the losses due to friction in the impeller and diffuser. The variable speed compressor characteristic is developed based on these losses consideration.

The new model valid in a wide range. Rotational speed should be over 300 rpm to guarantee convergence. The isentropic efficiency of the compressor varies at different operating points. It is defined as:

$$\text{Efficiency} = (\text{ideal energy transfer} - \text{energy losses}) / \text{ideal energy transfer}$$

Furthermore, the efficiency will be corrected with losses in the volute and additional losses arising from clearance and backflow.

Figure 11 shows the simulation results of the compressor transient and steady state operation, under the condition of a constant load. The model is under validation now.

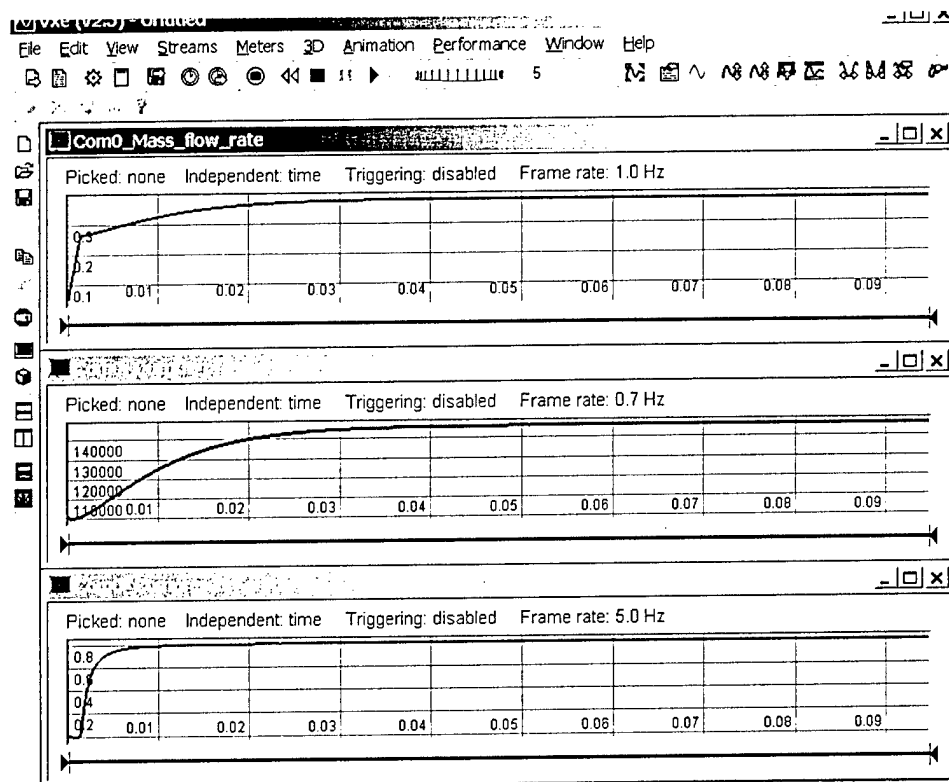


Figure 11. Transient and steady state of the VTB compressor model.

## METHANOL REFORMER

The reformer is assumed to be a CSTR model i.e. the temperature, concentrations variations inside the bed are neglected. The heat input to the reformer is assumed to be provided by a proportional controller that is within the reformer and is not shown explicitly. The reformer is designed to operate for steam to methanol ratio of 0.5 to 2.0, 150<sup>0</sup> C to 266<sup>0</sup> C temperature and 2 to 3 bar pressure.

The model allows one to specify the nominal power rating of the fuel cell stack that the reformer will feed (in order to estimate the hydrogen production rate and hence internal component sizes), the target operating temperature and pressure, and the design conversion ratio. The reformer model does not yet incorporate explicit closed-loop con-

control functions to control its operation, but instead it is forced to operate at near nominal operating conditions. Hence the hydrogen gas production often varies from the consumption rate of the fuel cell, depending on system load. Excess production is stored in a hydrogen tank, and insufficient production is made up for by drawing from the tank.

Figure 12 shows the simulation results of the reformer fed by a constant methanol source and loaded with a hydrogen storage tank. The fractional conversion (upper left) of methanol in the reformer bed changes as a function of temperature. Final value is 0.95. The temperature rise (the upper right) of the reformer bed from room temperature, 30 °C to the operating temperature, 266 °C with time.  $H_2$  (the lower left) obtained from the reformer exit in moles/s. Steady state value is 0.187 moles/s. The heat input in watts is shown by the lower right graph. The steady state value is 13700 watts (corresponding to a value of 81.69 W/°C).

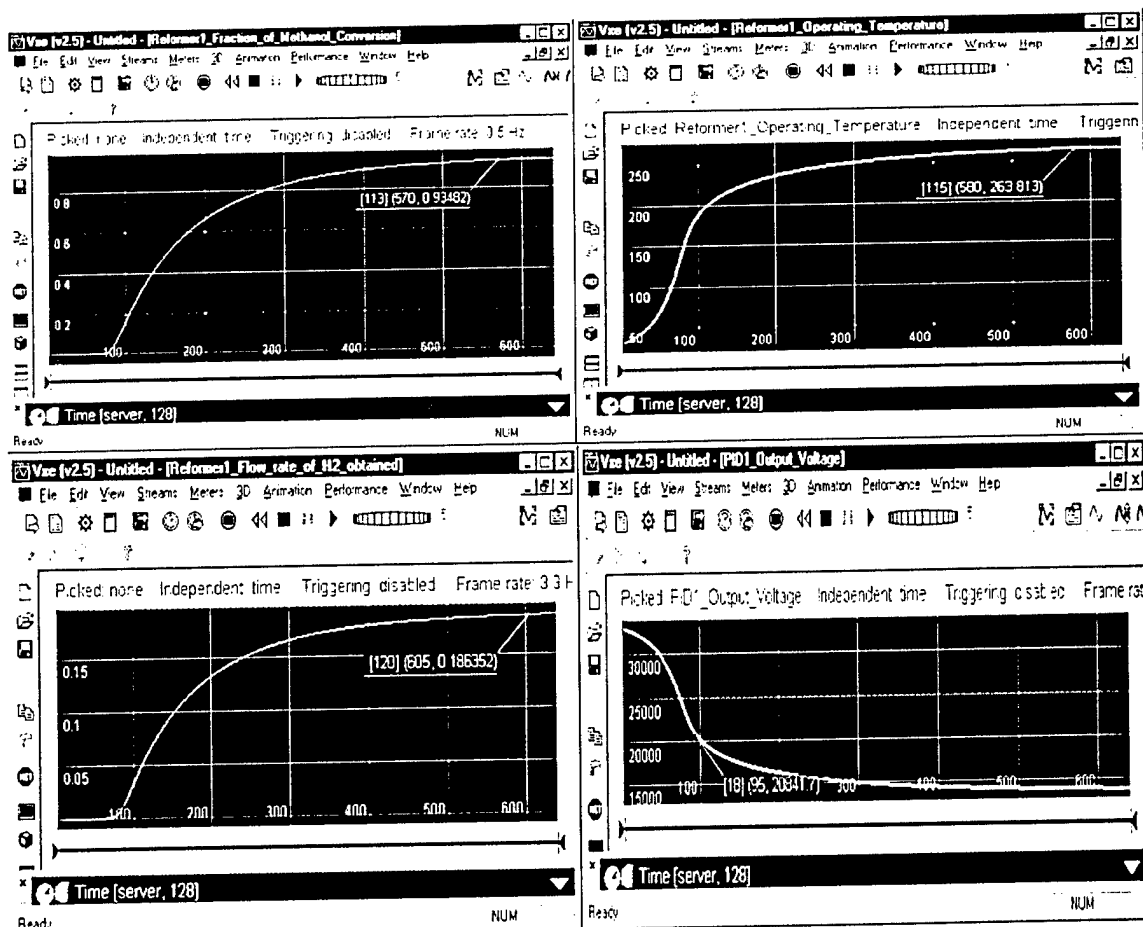


Figure 12. VTB simulation results of the reformer that connects to a constant methanol source and discharges to a hydrogen storage tank.

## FEEDBACK CONTROL SYSTEM

The feedback control system is designed using MatLab/Simulink, as shown in Figure 13. It represents a simple PID controller with a steady-state offset. This controller measures the current that is produced by the fuel cell, and calculates the necessary air-



flow for that operating condition. The “Current Scale” is the product of  $357 \times 10^9$  kg/amp-cell, the number of cells (1600), and the current that is measured. Normally, a fuel cell is feed anywhere between 50% and 200% excess airflow for cooling and humidity control. For this simulation, 100% airflow is chosen. Thus, the difference between the excess airflow and the necessary airflow is the error of the set point. This value is then passed to a proportional-integral-derivative controller, which is tuned intuitively. There is also a steady state offset (“Rest Duty Cycle”) summed to this value to ensure the compressor motor is idling, and needs not start from a dead stop. The “Saturation” block is simply to limit the duty cycle to a reasonable range (0-1). The input and output block numbers correspond to the input and output pins of the “Simulink Controller” object in VTB.

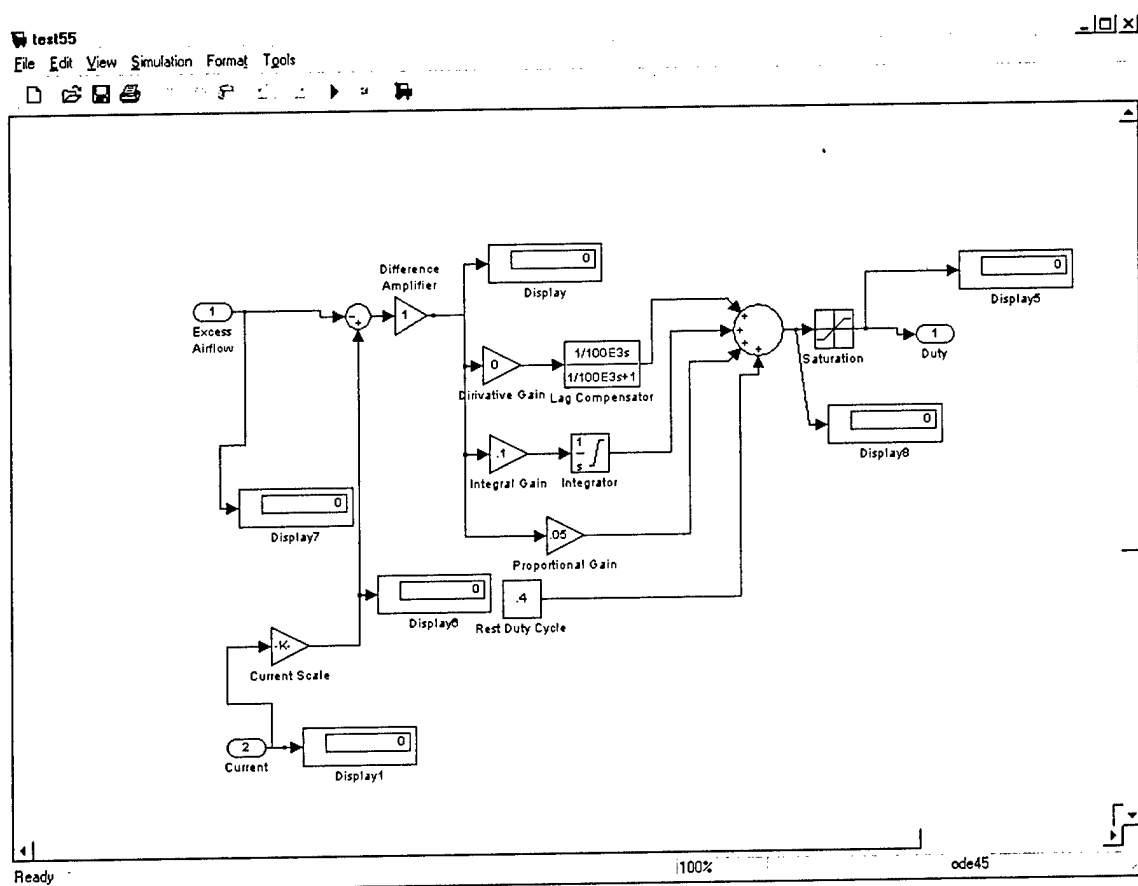


Figure 13. The PID controller design using Simulink.

## SYSTEM MODEL

Figure 14 illustrates the system configuration as represented in the Virtual Test Bed environment. Salient components of the system model include the fuel cell stack, the fuel reformer, a motor-driven compressor, motor drive electronics, and a controller that senses load current and stack exhaust gas flow. The other auxiliaries include the thermal environmental elements and the air bypass valve. The system currently is not rated yet since relative little information on the practical power plant is available.

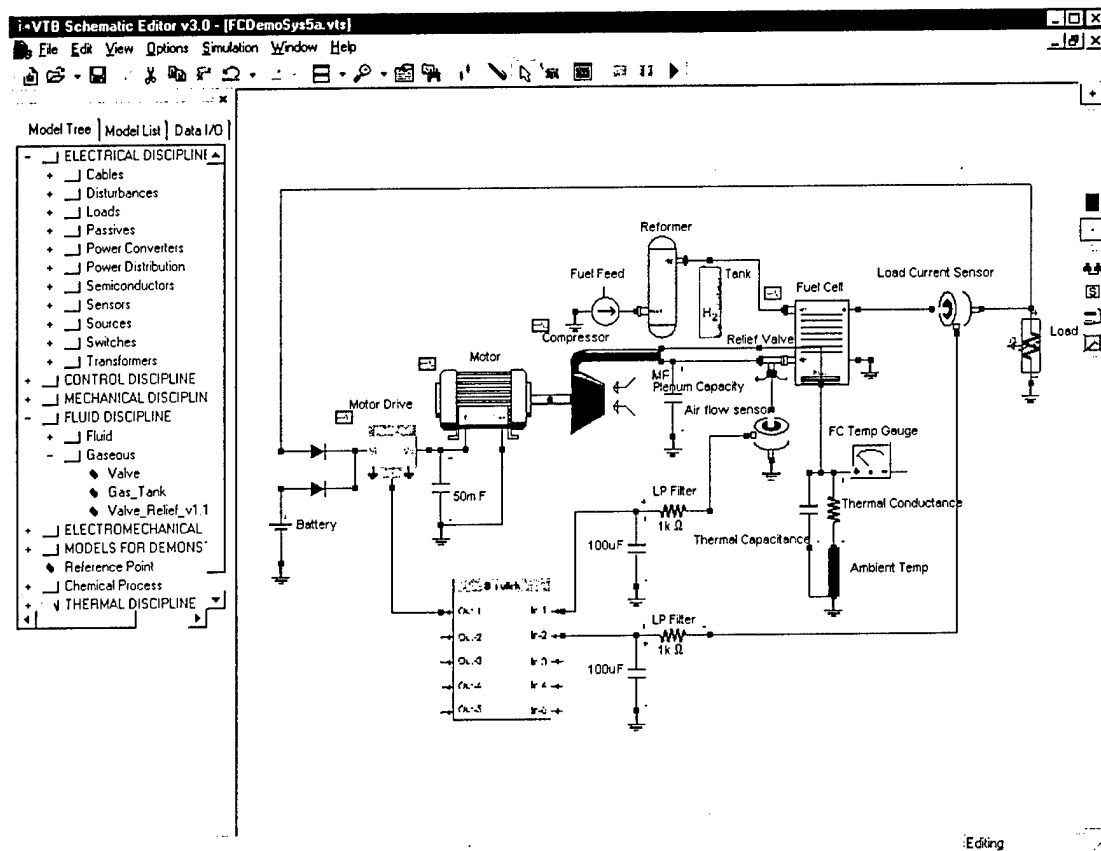


Figure 14. Schematic diagram of the fuel cell power plant in the VTB environment.

The fuel cell stack can be specified for its number of series and parallel cells, and the cell area. The heat generated inside the stack is stored in an external thermal capacitance that represents the lumped heat capacity of the fuel cell stack. Thermal energy is dissipated to the ambient through an external thermal conductance. The aerodynamics of air flow fields are not represented.

The compressor model accounts for the inlet and outlet gas temperatures, heating of the gas, efficiency, and speed-dependent pressure rise. It can be used in either direction, either as a pump or as an expander. The latter allows exhaust gases from the fuel cell to be recuperated and, with reheat, to run the air feed pump. That energy saving feature is not yet incorporated in the system model, but the component models will now support that activity.

The reformer model represents steam reformation of methanol into hydrogen. The model allows one to specify the nominal power rating of the fuel cell stack that the reformer will feed (in order to estimate the hydrogen production rate and hence internal component sizes), the target operating temperature and pressure, and the design conversion ratio. The reformer model does not yet incorporate explicit closed-loop control functions to control its operation, but instead it is forced to operate at near nominal operating conditions. Hence the hydrogen gas production often varies from the consumption rate of the fuel cell, depending on system load. Excess production is stored in a hydrogen tank, and insufficient production is made up for by drawing from the tank.

The Simulink control object that controls the power converter that operates the compressor drive motor. The VTB environment now includes sophisticated links to foreign simulation objects (such as Simulink), allowing the use of either compiled or interactive co-simulation models in the system definition.

Figures 15 and 16 show results from a typical system study. Here, we show the response of the system to a recurring 3-step change of the load from 20 kW for 20 seconds, increasing to 600 kW for 40 seconds, then reducing to 300 kW for the next 20 seconds, and repeating.

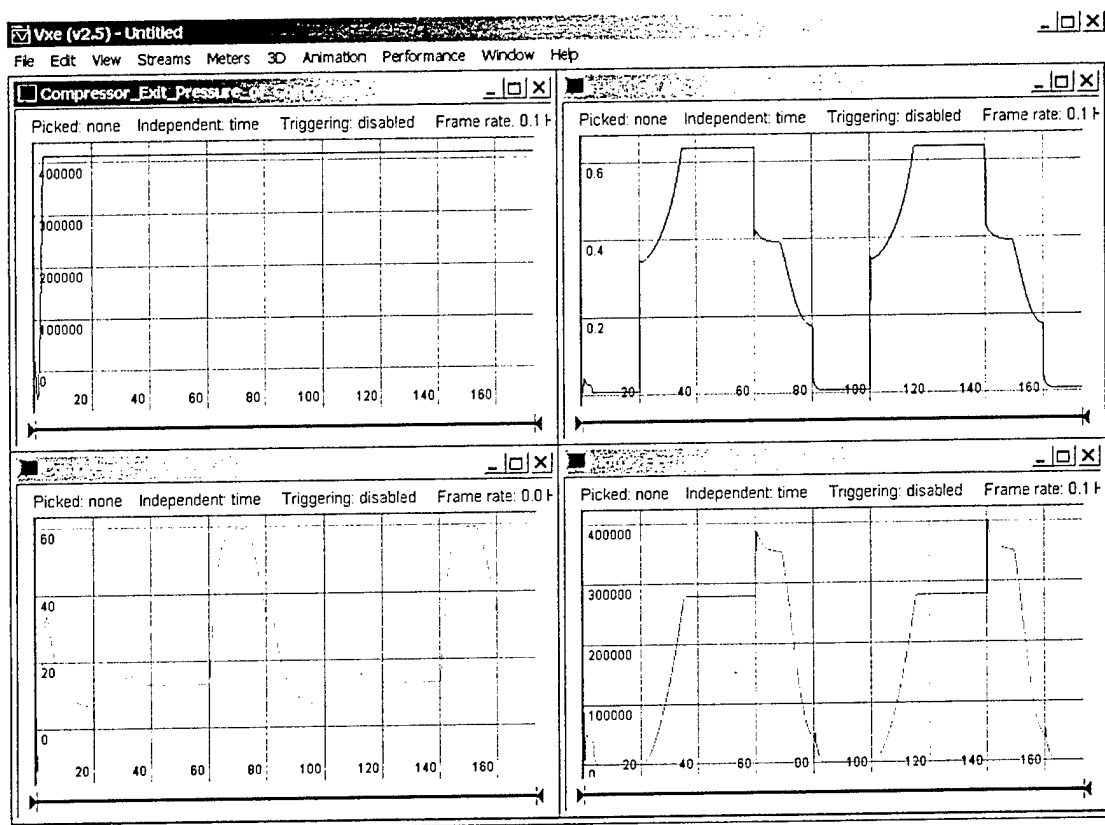


Figure 15. From top left to bottom right, exit pressure of the air pump in Pa, air consumption rate in kg/sec, compressor speed in rad/s, and electric power consumed by the motor in W.

One can observe several interesting phenomena in these graphs. When the load demands full power (600 kW), the stack voltage drops from approximately 1500 V open circuit to 850 volts. This suggests a need for extensive power conditioning between the stack and the load bus. This power conditioning has not yet been incorporated into the system model. The stack temperature increases by approximately 40 degrees C. The rate of heating is not constant, but follows somewhat the air mass flow. The air pump motor consumes a significant fraction of the system power, approximately 300 kW when the load draws 600 kW, but even more when the load draws only 300 kW (though in the example, it never reaches steady-state at the 300 kW power level.) The lag time of the motor speed in responding to the fuel cell stack air demands accounts for a significant part of the system dynamics. Heating of the fuel cell stack has a noticeable effect on system per-

formance. The cooling effect of excess air blowby is evident following each reduction in power demand, and the compressor motor can be seen to overspeed in those conditions.

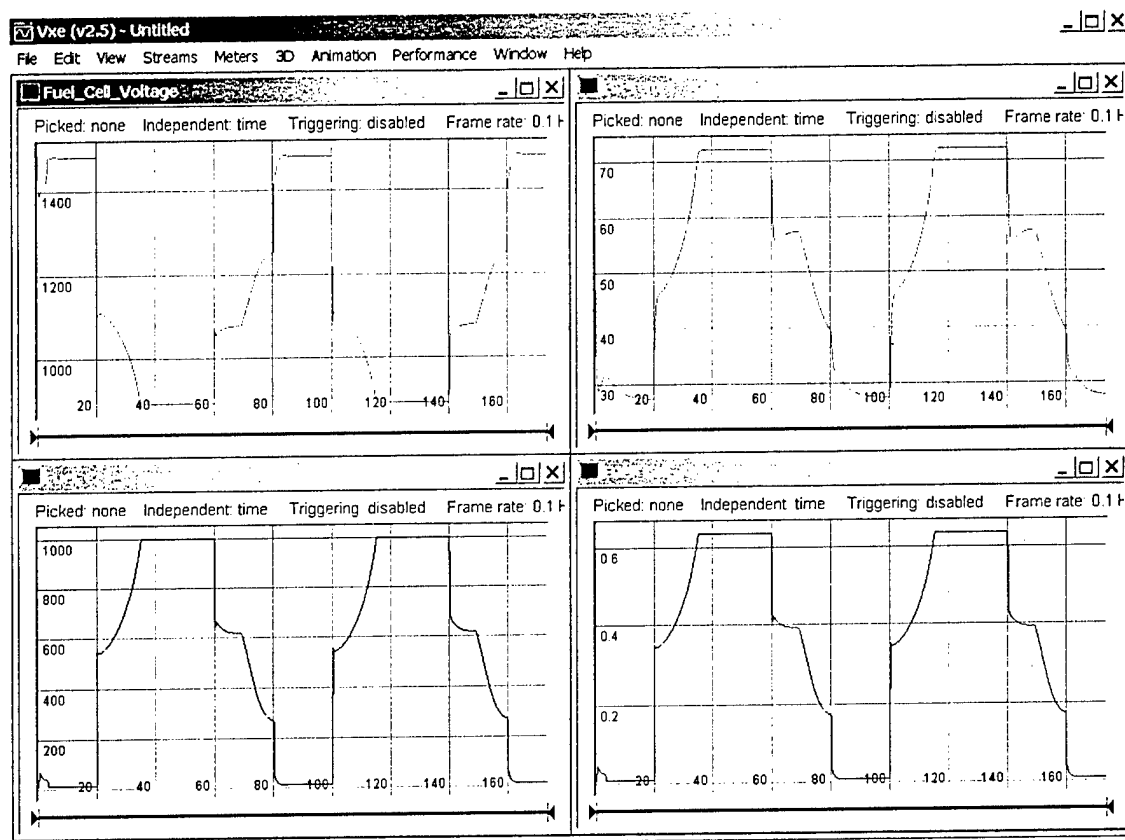


Figure 16. From top left to bottom right, terminal voltage of the fuel cell stack, temperature of the fuel cell stack (C), output current from the fuel cell (amps), and air consumption in kg/sec.

The system is not yet optimally designed, nor that the control algorithms are fully developed, so all of these results should be taken simply as examples, rather than as definitive predictions of the performance of a whole class of power plants. We have not yet taken pains to size all of the components correctly in relation to each other nor to size them carefully with respect to the total load power demand.

In the future research, we expect to more fully explore and understand methods for handling mixed streams of compressible gases within the VTB environment, to further improve the fuel cell stack and compressor models, to augment the system with power conversion equipment capable of regulating the bus voltage, and to incorporate additional features of the thermal systems. We will also study designs that use exhaust gas recuperators and expanders to power the inlet air pump. In addition, we will attempt to validate all models against real test data, where such data are available for comparable systems. Note that there are no PEM fuel cell plants operating at the MW level, so there is a dearth of test data to use for model validation. However, comparisons can be made to systems operating at lower power levels.

## DELIVERABLES

### MODELS

#### *VTB Models*

The following models were developed. Full descriptions of each appear in Appendix I in the form of the model help files.

Model ID	Description	Features
Fuel Cell 12.15_010716	Fuel cell	Temperature dependence, heat power generation, pressure dependence, Nernst equation based voltage and current characteristics, fuel and air consumption
Compressor1	General centrifigual compressor	The model presents states of mass flow, pressure rise and rotational speed of the spool based on the energy transfer considerations. Temperature change and efficiency of the isentropic compression are considered. Incidence loss and frictional loss are included.
Creformer	Steam methanol reformer	This is a CSTR model of the reformer. The temperature of the catalyst bed, methanol conversion and the pressure inside the reactor change with time but do not vary within the reformer. External heat input to the reformer is also included to control the reformer bed temperature at the desired value.
Hydride Bed	Cylindrical metal hydride bed	Mass and heat transfer resistances ignored. Isothermal local equilibrium assumed. Heat exchange of bed with the external heating/cooling system included. It can be connected in series with a gas pressure regulator downstream to provide hydrogen at a relatively

		constant pressure.
5in_5out_Matlab	PID controller (Mat-Lab/Simulink object)	Simple PID controller designed in MatLab/Simulink. The Simulink PID object embedded in VTB allows co-simulation of the Simulink with VTB time domain solver

## PUBLICATIONS AND PRESENTATIONS

### PUBLICATIONS

#### *Journals*

In print

1. A. T. Haug, J.W. Weidner, R.E. White, and W. Huang "**Development of a Novel CO Tolerant Anode**," accepted, *J. Electrochem. Soc.*, December, 2001.
2. A. T. Haug, J.W. Weidner, R.E. White, W. Huang, Steven Shi, Timothy Stoner, and Narendra Rana, "**Using Sputter Deposition to Increase CO Tolerance in a PEM Fuel Cell**," accepted, *J. Electrochem. Soc.*, December, 2001.
3. D. Tianping, J.W. Weidner, and R.E. White, "**Extension of Newman's Method to Electrochemical Reaction-Diffusion in a Fuel-Cell Catalyst Layer**," in press, *J. Power Sources*, September, 2001.
4. A. T. Haug, R.E. White, J.W. Weidner, W. Huang, Steven Shi, Timothy Stoner, and Narendra Rana, "**Increasing PEM Fuel Cell Catalyst Effectiveness Through Sputter Deposition**," *J. Electrochem. Soc.*, **149**, A280-A287 (2002).

### PRESENTATIONS

Presentations are listed here only if there was not a corresponding publication in conference proceedings. Otherwise, see above list of "Proceedings".

1. Haug, A., J. W. Weidner, R. E. White, and W. Huang "**Development of a Novel CO Tolerant Anode**," The Electrochemical Society, San Francisco, CA, September, 2001.
2. Haug, A., R.E. White, J.W. Weidner, W. Huang, Steven Shi, Timothy Stoner, and Narendra Rana, "**Increasing PEM Fuel Cell Catalyst Effectiveness Through Sputter Deposition**," The Electrochemical Society, Philadelphia, PA, May, 2002.
3. Blackwelder, M. "**Fuel Cell Model Implementation and System Evaluation**", Gordon Research Conference on Fuel Cells , Poster Session, Roger Williams University, Bristol RI, July/August, 2001.
4. Blackwelder, M. "**Fuel Cell Power Plant**", VTB Annual Review, Charleston, SC, July 2001.

## CONCLUSIONS

Major component models of the shipboard fuel cell power plant were developed. A example system for the power system was assembled and it can be used for study of system first order transient and steady state operation. The future work will focus on the validation of all component models against experimental data, and prototype the system in VTB environment with a feasible parameters, so that the system design optimization and operation performance can be obtained.

## APPENDICES

### APPENDIX 1 – STUDENTS EDUCATION

Following table lists the graduate students who were or have been supported by the fuel cell shipboard power plant project.

Name	Pursuing Degree	Major Field	Advisor	Enrolling Status
Mark Blackwelder	Ph. D.	Electrical	R. A. Dougal	Current
Ramasrishna Gundala	Ph. D.	Chemical	J. Weidner	Current
Andrew Haug	Ph. D.	Chemical	R. E. White	Current
Ananda Mondal	Ph. D.			Graduated
Venka Subraminian	Ph. D.	Chemical	R. E. White	Graduated
Wei Jiang	Ph. D.	Mechanical	J. Khan / R. A. Dougal	Current
Zhenhua Jiang	Ph. D.	Electrical	R. A. Dougal	Current
Ramaraja Ramasamy	Ph. D.	Chemical	J. Weidner	Current
Vijay Sethuraman	Ph. D.	Chemical	J. Weidner	Current

### APPENDIX 2 – FUEL CELL CO MODELING

See attached paper entitled “A Mathematical Model Predicting the Effects of Reformate and Air Bleed on a PEM Fuel Cell” by Andrew T. Haug, John W. Weidner, and Ralph E. White.

### APPENDIX 3 - MODEL HELP FILES

Description of model help files

### APPENDIX 4 – PUBLICATIONS (COPIES ATTACHED)

1. A. T. Haug, J.W. Weidner, R.E. White, and W. Huang “**Development of a Novel CO Tolerant Anode,**” *J. Electrochem. Soc.*, **149** (7) A862-A867 (2002).
2. A. T. Haug, J.W. Weidner, R.E. White, W. Huang, Steven Shi, Timothy Stoner, and Narendra Rana, “**Using Sputter Deposition to Increase CO Tolerance in a PEM Fuel Cell,**” *J. Electrochem. Soc.*, **149** (7) A868-A872 (2002).
3. D. Tianping, J.W. Weidner, and R.E. White, “**Extension of Newman’s Method to Electrochemical Reaction-Diffusion in a Fuel-Cell Catalyst Layer,**” *J. Power Sources*, 107 (1), 24-33, 2002.
4. A. T. Haug, R.E. White, J.W. Weidner, W. Huang, Steven Shi, Timothy Stoner, and Narendra Rana, “**Increasing PEM Fuel Cell Catalyst Effectiveness Through Sputter Deposition,**” *J. Electrochem. Soc.*, **149**, A280-A287 (2002).



## **APPENDIX 2 – FUEL CELL CO MODELING**

See attached paper entitled “A Mathematical Model Predicting the Effects of Reformate and Air Bleed on a PEM Fuel Cell” by Andrew T. Haug, John W. Weidner, and Ralph E. White.

A Mathematical Model Predicting the Effects of Reformate and Air Bleed on a  
PEM Fuel Cell

Andrew T. Haug, John W. Weidner, Ralph E. White  
Center for Electrochemical Engineering  
Department of Chemical Engineering  
University of South Carolina  
Columbia, South Carolina

Submitted to Dr. Paul Kohl

Editor

The Electrochemical Society, Inc.  
65 South Main Street  
Pennington, NJ 08534-2839, USA

ABSTRACT.....	3
INTRODUCTION.....	3
MODEL DEVELOPMENT.....	5
<i>Assumptions</i> .....	5
<i>H<sub>2</sub> + CO in the Anode Feed</i> .....	5
RESULTS AND DISCUSSION.....	15
PT ANODE: H <sub>2</sub> +CO (REFORMATE) FEED.....	16
PT ANODE: H <sub>2</sub> +CO+O <sub>2</sub> (REFORMATE) FEED.....	17
CONCLUSIONS.....	20
LIST OF SYMBOLS.....	40
REFERENCES.....	42
APPENDIX A: DERIVATION OF VOGEL'S ANODE CURRENT DENSITY EXPRESSION...	45
APPENDIX B: ALTERNATIVE H <sub>2</sub> /CO/O <sub>2</sub> MECHANISM INCORPORATING $\theta_{OH}$ .....	47
APPENDIX C: SPRINGER'S MODEL.....	49
APPENDIX D: MODEL SOURCE CODE.....	54

## Abstract

A model has been developed to explain the effects of introducing an air bleed to a PEMFC anode feed containing hydrogen and carbon monoxide. The basis for this model was the work by Springer et al (32) for a PEMFC anode stream containing hydrogen and CO. The appropriate coverage and flux equations have been modified to take into account the electrochemical oxidation of CO that has been proven in earlier work to be the primary means by which oxygen oxidizes CO. This model shows that the CO electrooxidation rate is greatly improved through the addition of oxygen to an anode feedstream. The model shows a good quantitative fit to performance data taken under various air-bleed concentrations for a PEMFC containing a Pt anode. The model then further explores the selectivity of the electrochemical reaction of oxygen with CO versus the catalytic oxidation with  $H_2$ . Finally, qualitative projections are made on the required increases in certain parameters that would result in improving the selectivity of  $O_2$  usage in the anode feedstream.

## Introduction

Proton-exchange membrane fuel cells (PEMFCs) are gaining popularity due to their benefits such as environmental friendliness and increased fuel efficiency. Because of the difficulties inherent to storing hydrogen, liquid fuels such as propane, natural gas and gasoline are used to produce reformat gas. Dry reformat is typically composed of 35 - 45 % hydrogen, 15 - 25 % carbon dioxide, 50 - 10000 ppm carbon monoxide and a balance of nitrogen. It has been shown extensively that CO poisons the platinum catalyst used in PEMFC systems (1,2,3). Fuel clean-up units including high and low temperature water-gas shift (WGS) reactors and a preferential oxidation (PROX) unit typically reduce CO levels to 10-100 ppm in the fuel stream. However, at concentrations as low as 10 ppm, CO lowers power output of the PEMFC containing Pt electrodes by 50% (4,5).

Springer et al (32) have developed a model that rigorously investigates the effects of CO on the PEMFC anode for reformat feedstreams. This includes the effects of  $H_2$  dilution and starvation and the effects of CO on the Pt anode performance.

Alloying Pt with various metals (8,9,10,11,12), increasing the fuel cell operating temperature, and adding oxygen to the anode feedstream (6,7) are all being investigated as means of increasing CO tolerance (13,14,15,16,17,18). The injection of oxygen into the fuel stream has also been shown to increase catalyst tolerance to CO (6,7,19,20). Injected as an 'air bleed', this method provides a greater concentration of oxygen on the catalyst surface that then reacts with CO to form CO<sub>2</sub>. It has been proven that the primary means by which oxygen oxidizes CO on the catalyst surface is by reacting with adsorbed hydrogen to form a hydroxyl species that then reacts electrochemically with adsorbed CO to form CO<sub>2</sub> (19,20). It is these kinetics occurring within a reformat feed containing oxygen that are modeled here.

To develop a model predicting the steady-state performance of a PEMFC in the cases where CO + H<sub>2</sub> and CO+H<sub>2</sub>+O<sub>2</sub> are present in the anode feed stream, two basic components are required: the necessary kinetic expressions to accurately describe the effects of CO on the PEMFC anode and the necessary governing equations for the various regions of the PEMFC (anode GDL, anode catalyst region, membrane, cathode catalyst region and cathode GDL).

Those necessary equations are presented here. Three separate derivations of expressions for CO interactions with Pt are given based on work by Vogel, Dhar and Springer (21,22,23,32). The 1-D version of Springer's model is then described and used to explain the Plug Power steady state data in the case of a reformat stream containing CO interacting with a Pt anode. Springer's work is then modified to describe the effects of an airbleed as shown in previous chapters.

## Model Development

### ASSUMPTIONS

Below are the assumptions for the 1-D (through the cell) model predicting the steady-state performance of a PEMFC membrane-electrode assembly. These are valid for both Springer's model and the modified version that accounts for the addition of oxygen to the anode feedstream.

- One dimensional flow of the of the species through the anode (24,25).
- The anode operates under isothermal conditions with uniform temperature distribution (24,26). This assumption is based on the high thermal conductivities and of the carbon portion of the electrode and even mixing that occurs in flow through porous media (24,27).
- Species are distributed evenly throughout the cross-sectional area of the anode.
- H<sub>2</sub>, CO, and water vapor will be treated as ideal gases that are well mixed (24,26).
- The porosity of the GDL and in the ACR is considered uniform.
- The catalyst in the ACR is assumed to be spread uniformly throughout the region.
- Pressure is considered uniform throughout the cell.
- The inlet gas is considered fully hydrated (24,25,27,28), however any liquid water entering the PEMFC anode is neglected.
- Reactions only occur in the active catalyst regions (ACRs) of the PEMFC. This reaction is considered homogeneous.
- It is assumed that the entire Pt particle area is active.
- The CO<sub>2</sub> and N<sub>2</sub> present in the anode ACR are considered inert.
- The rate of reaction in the ACR is mass transfer limiting (29,30).

### H<sub>2</sub> +CO IN THE ANODE FEED

In order to generate an expression relating anodic performance to the amount of CO in the feed stream, the derivation must first be made of the current generated by the dissociation of H<sub>2</sub> in terms of surface coverage of the Pt catalyst (23,31):

$$j = j_0 \left[ \frac{1}{\theta_H + (1 - \theta_H) e^{F\eta/RT}} \right]^2 \left( \frac{c_{H_2}}{c_{H_2}^0} e^{F\eta/RT} - 1 \right) \quad (0.1)$$

where  $\theta_H$  is the steady state hydrogen coverage,  $j_0$  is the exchange current density in  $A\ cm^{-3}$ ,  $c_{H_2}$  and  $c_{H_2}^0$  are the initial and local hydrogen concentrations in  $mol\ cm^{-3}$ ,  $\eta$  is the anode overpotential. A more detailed derivation is presented in Appendix A.

Vogel et al (23) deduced the empirical relationship shown in equation (0.3) and (0.2) for relating the reaction rates and current density of pure  $H_2$  to that of gas containing CO and  $H_2$  in phosphoric acid fuel cells.

$$k_s^{CO} = k_s (1 - \theta_{CO})^2 \quad (0.3)$$

$$\frac{j_{H_2\ w/CO}}{j_{H_2}} = (1 - \theta_{CO})^2 \quad (0.4)$$

where  $k_s$  and  $k_s^{CO}$  are the rate constants for  $H_2$  adsorption onto Pt for feedstreams containing pure  $H_2$  and  $H_2+CO$ , respectively. The performance loss by CO arises due to its ability to block reaction sites which otherwise would have been accessible to  $H_2$ . This is distinct from the Nernst loss, which arises because of reactant dilution, and is the basis for the relationship with  $\theta_{CO}$  (21). Thus, a final expression for the current density can be found, expressed in terms of the steady-state hydrogen concentration,  $c_{H_2}$ , equilibrium hydrogen coverage,  $\theta_{CO}$ , and CO coverage,  $\theta_{CO}$ .

$$j_{H_2\ w/CO} = j_0 \left[ \frac{1}{\theta_H + (1 - \theta_H) e^{F\eta/RT}} \right]^2 \left( \frac{c_{H_2}}{c_{H_2}^0} e^{F\eta/RT} - 1 \right) (1 - \theta_{CO})^2 \quad (0.5)$$

where  $j_{H_2\ w/CO}$  is the current generated when CO is present in the feed stream.

Dhar, Christner, et al (6) developed an expression for the coverage of CO on PAFCs at over the range of 130 to 190°C:

$$\theta_{\text{CO}} = \frac{-\Delta G_o^\circ}{r} - \frac{RT}{r} \ln(H) + \frac{RT}{r} \ln\left(\frac{c_{\text{CO}}}{c_{\text{H}_2}}\right) \quad (0.6)$$

$$\ln H = A + \frac{\Delta C_p}{R} \ln T - \frac{\Delta H^\circ}{RT} \quad (0.7)$$

where  $\Delta G_o^\circ$  is the standard free energy of adsorption for CO (kcal mol<sup>-1</sup>),  $r$  is an interaction parameter (kcal mol<sup>-1</sup>) and  $H$  is Henry's constant (atm mol<sup>-1</sup> L<sup>-1</sup>) for CO absorption in water,  $\Delta C_p$  and  $\Delta H^\circ$  are the change in heat capacity and standard change in enthalpy, respectively of CO oxidation and  $A$  is a constant.

The effects of CO on fuel cell performance increase dramatically as temperature decreases from PAFC conditions to typical PEMFC conditions (33). While Dhar and Vogel's work might be adaptable for typical PEMFC operating temperatures (40 - 100 °C), the effects of CO on fuel cell performance increase dramatically as the temperature is decreased from PAFC conditions to PEMFC conditions (33). Springer et al (32) have developed solutions specifically to explain the effects of CO poisoning on the PEMFC anode. A detailed description of this model is described in Appendix C. This model is both rigorous in the description of the PEMFC anode catalyst region and allows for the simulation of V-I curves that may be compared to existing data. The model takes into account cell temperature, pressure, hydrogen concentration and CO concentration. The original model is two dimensional, considering effects both through the cell and along the channel. However, the 1-D (through the cell) version is modified to account for the effects of an air bleed. This includes the addition of O<sub>2</sub> to the coverage and flux equations.



The model considers the PEM fuel cell as three separate regions as shown in Figure 20.

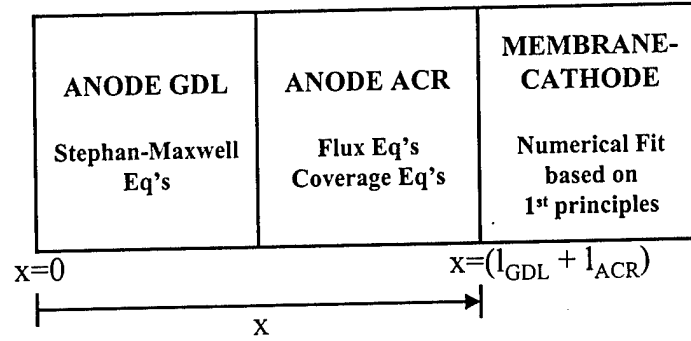


Figure 1 The Springer model sees the PEMFC as an anode GDL, active catalyst region (ACR) and a membrane-cathode region.

The basic features of the PEMFC membrane-electrode assembly (MEA) are all present. Because the focus of the model is on the anode, each of the anode regions by an individual set of equations while the membrane and cathode portions of the cell are grouped together and represented by a single equation.

The governing equations within the anode GDL region are given by the standard Stephan-Maxwell equations for multi-component diffusion as shown in equation (0.8).

$$\frac{\partial x_i}{\partial z} = \frac{T\tau R}{\varepsilon} \sum_{j \neq i} \frac{x_i \Phi_j - x_j \Phi_i}{P_s D_{Sij}} \quad (0.8)$$

where  $i$  and  $j$  represent the various anode species,  $x_i$  is the mole fraction of each species, and  $V_s$ ,  $P_s$  and  $T_s$  are standard molar volume, temperature and pressure. The addition of oxygen to the anode feedstream increases the number of species in the model from five to six and they are defined as follows: 1 =  $H_2$ , 2 =  $CO$ , 3 =  $N_2$ , 4 =  $CO_2$ , 5 =  $O_2$

and 6 = H<sub>2</sub>O. In the case where H<sub>2</sub>=1 and CO=2,  $\Phi_1 = J_h / 2F$ ,  $\Phi_2 = J_{CO} / 2F$  and  $\Phi_3 = \Phi_4 = \Phi_6 = 0$ . The flux of oxygen across the GDL is represented by (0.9):

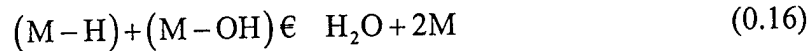
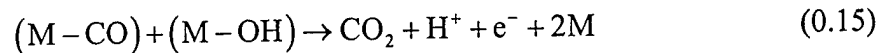
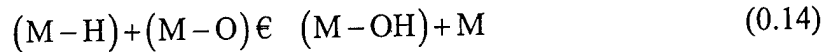
$$\Phi_5 = \left[ (J_{CO,O_2}^{tot} - J_{CO}^{tot}) + k_{eff} x_{O_2} P_a \theta_h \right] / 2F \quad (0.9)$$

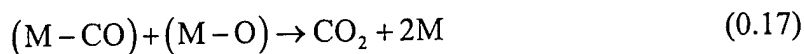
The multicomponent pressure-diffusion coefficients,  $P_S D_{Sij}$ , are calculated by the following expression (26):

$$P_S D_{Sij} = a \left( \frac{T_{CELL}}{\sqrt{T_{c,i} T_{c,j}}} \right)^b (p_{c,i} p_{c,j})^{\frac{1}{3}} (T_{c,i} T_{c,j})^{\frac{5}{12}} \left( \frac{1}{M_{c,i} M_{c,j}} \right)^{\frac{1}{2}} \epsilon^{\frac{3}{2}} \quad (0.10)$$

where  $T_{c,i}$  and  $p_{c,i}$  are the critical temperatures and pressures of the various components,  $M_{c,i}$  is the molecular weight of each component,  $a$  and  $b$  are fitting parameters and  $\epsilon$  is the Bruggeman coefficient.

The reaction mechanism becomes significantly more complex when oxygen is present anode feedstream (36,37,38,39,40,41,42,43,44,45,46,47,48,49,50):





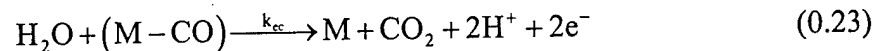
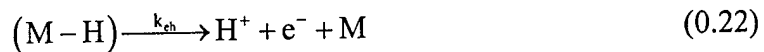
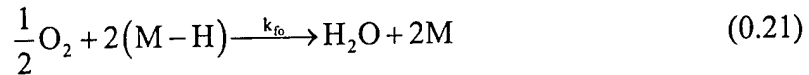
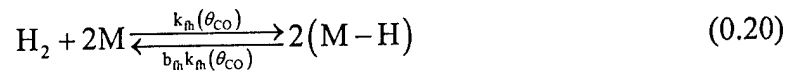
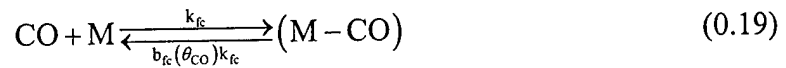
In the case of the Ruthenium filter,  $M = Ru$ . As described in the previous chapters, the addition of oxygen to the anode feedstream in the form of an air bleed results in the formation of addition hydroxyl ( $M-OH$ ) groups. It is the extent to which these groups are used for the electro-oxidation of CO that determines the effectiveness of the air bleed. For purposes of modeling the filter region, the rigorous incorporation of the entire reaction mechanism described in equations (0.11) - (0.18) is both too complex and unnecessary. This would result in four site coverage expressions ( $\theta_h, \theta_{CO}, \theta_O, \theta_{OH}$ ), three flux equations (for  $x_h, x_{CO}, x_{O_2}$ ), along with the appropriate inert species equations and voltage relationships. Like Springer et al have done with the  $H_2+CO$  reaction mechanism, the  $H_2+CO+O_2$  mechanism may be simplified for purposes of developing a solvable set of coverage expressions without sacrificing the effects of the air bleed. Simplifications of the mechanism have been proposed based on the following criteria:

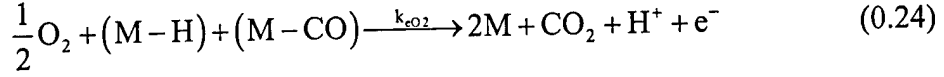
1. The rate of CO oxidation through equation (0.17) is negligible. It has been shown in the previous chapters that  $O_2$  oxidizes very little CO catalytically.
2. The model must take into account that  $O_2$  increases the CO electrooxidation rate above the level found when only CO is present in the feedstream.
3. The model must take into account that oxygen oxidizes both  $H_{ads}$  and  $CO_{ads}$ , and it is the selectivity of this oxidation between these two competing reactions ((0.15) and (0.16)) that determine the effectiveness of the airbleed.
4. All oxygen is consumed before it penetrates any significant distance into the ACR. As shown earlier in this work, a sputtered Ru filter of less than 100 nm was shown to oxidize 200 ppm CO when 2 vol. %  $O_2$  was present in the feedstream.
5. The model must simplify to the Springer model when no oxygen is present. Thus a single set of equation will represent all feeds (pure  $H_2$ , dilute  $H_2$ ,  $H_2+CO$ ,  $H_2+CO+O_2$ ) entering the PEMFC anode.

In accordance with #1, reaction (0.17) can be neglected in building the mechanism. Following #2 and #5 lead to the assumption that there is an exponential relationship between the addition of  $O_2$  and the rate of CO electrooxidation. Thus, when the amount of oxygen present reduces to zero ( $x_{O_2} \rightarrow 0$ ), the CO electrooxidation rate reduces to that described in the Springer model ( $j_{CO\ w/O_2} \rightarrow j_{CO}$ ). The  $O_2$  selectivity described in #3 is one of the key features of the model. Thus, the developed expressions for  $x_{O_2}$ ,  $\theta_O$  or  $\theta_{OH}$  must describe the competitive consumption of  $O_2$ .

Simplifying the reaction mechanism while taking into account the effects of  $\theta_{OH}$  is the most desirable as it is the amount of  $OH_{ads}$  present that most directly affects the rate of CO oxidation. However, the proposed simplified reaction mechanism (described in Appendix B) is still too complex to solve. Similar difficulties arise when  $\theta_O$  is used to account for increased CO oxidation and selective  $O_2$  consumption incorporated into the reaction mechanism.

Thus, the following simplified model was proposed:





This gives rise to the following coverage expressions:

$$\begin{aligned} \rho \dot{\theta}_{CO} = & k_{fc} x_{CO} P_A (1 - \theta_{CO} - \theta_h) - b_{fc} k_{fc} \theta_{CO} \\ & - k_{eO_2} x_{O_2} P_A \theta_{CO} \theta_h^m e^{\left(\frac{V_a + V_N}{b_{O_2}}\right)} - k_{ec} \theta_{CO} e^{\left(\frac{V_a + V_N}{b_c}\right)} = 0 \end{aligned} \quad (0.25)$$

$$\begin{aligned} \rho \dot{\theta}_h = & k_{fh} x_h P_A (1 - \theta_{CO} - \theta_h)^n - b_{fh} k_{fh} \theta_h^n - x_{O_2} P_a \theta_h^m k_{fO_2} \\ & - 2k_{eh} \theta_h \sinh\left(\frac{V_a + V_N}{b_h}\right) - k_{eO_2} x_{O_2} P_A \theta_{CO} \theta_h^m e^{\left(\frac{V_a + V_N}{b_{O_2}}\right)} = 0 \end{aligned} \quad (0.26)$$

$$b_{fc} = b_{fc}^0 \exp\left(\theta_{CO} \frac{\delta(\Delta G_{CO})}{RT}\right) \quad (0.27)$$

$$k_{fO_2} = k_{fO_2}^0 \exp\left(\frac{E_{O_2}}{RT}\right) \quad (0.28)$$

This version satisfies all the criteria set out for this model, while maintaining the simplicity needed achieve stable solutions. Instead of using  $\theta_{OH}$ , the competitive consumption of  $O_2$  is now directly related to oxygen concentration by using  $x_{O_2}$  as shown in (0.21) and (0.24). The model then maintains the simplicity that comes from having only two coverage expressions (for  $\theta_h$  and  $\theta_{CO}$ ) provides. As required by the mechanism, oxygen is consumed in the formation of water and the consumption of M-CO in (0.21) and (0.24). However, the adsorption and reaction of  $O_2$  with adsorbed hydrogen described in (0.13), (0.14) and (0.16) is now represented solely by (0.21).

$$\frac{\partial^2 x_h}{\partial z^2} = \left( \frac{j_h}{I_{Dh}} + k_{fO_2} x_{O_2} P_a \theta_h^m \right) \phi_{ACR} \quad (0.29)$$

$$I_{Dh} = \frac{2FP_a T_s D_h}{P_s V_s T}; \quad x_h|_{\text{filt}} = x_h|_{\text{GDL}}; \quad \left. \frac{\partial x_h}{\partial z} \right|_{\text{filt/ACR}} = 0 \quad (0.30)$$

$$\frac{\partial^2 x_{CO}}{\partial z^2} = \frac{(j_{CO \text{ w/O}_2}) \phi_{ACR}}{I_{DCO}} \quad (0.31)$$

$$I_{DCO} = \frac{2FP_a T_s D_{CO}}{P_s V_s T}; \quad x_{CO}|_{\text{filt}} = x_{CO}|_{\text{GDL}}; \quad \left. \frac{\partial x_{CO}}{\partial z} \right|_{\text{filt/ACR}} = 0 \quad (0.32)$$

$$\frac{\partial^2 x_{O_2}}{\partial z^2} = \left( \frac{(j_{CO \text{ w/O}_2} - j_{CO})}{I_{DO_2}} + k_{fO_2} x_{O_2} P_a \theta_h^m \right) \phi_{ACR} \quad (0.33)$$

$$I_{DO_2} = \frac{2FP_a T_s D_{O_2}}{P_s V_s T}; \quad x_{O_2}|_{\text{filt}} = x_{O_2}|_{\text{GDL}}; \quad \left. \frac{\partial x_{O_2}}{\partial z} \right|_{\text{filt/ACR}} = 0 \quad (0.34)$$

$$\frac{\partial^2 V_a}{\partial z^2} = \frac{(j_h + j_{CO \text{ w/O}_2})}{\sigma l_{\text{filt}}} \quad (0.35)$$

$$\left. \frac{\partial V_a}{\partial z} \right|_{\text{GDL/filt}} = 0; \quad V_a|_{\text{filt/ACR}} = V_{\text{filter}} \quad (0.36)$$

where the local and overall current densities for  $H_2$  and  $CO$  are given by equations (0.37) - (0.41):

$$j_{O_2} = k_{eO_2} x_{O_2} P_a \theta_{CO} \theta_h^m e^{\left( \frac{V_a + V_N}{b_{O_2}} \right)} \quad (0.37)$$

$$j_{CO} = k_{ec} \theta_{CO} e^{\left( \frac{V_a + V_N}{b_c} \right)} \quad (0.38)$$

$$j_h = 2k_{eh} \theta_h \sinh \left( \frac{V_a + V_N}{b_h} \right) \quad (0.39)$$

$$J_h^{\text{tot}} = 2F\Phi_1 = -I_{Dh} \frac{\partial x_h}{\partial z} \quad (0.40)$$

$$J_{CO}^{tot} = 2F\Phi_2 = -I_{DCO} \frac{\partial x_{CO}}{\partial z} \quad (0.41)$$

where  $j_{O_2}$  is the CO electrooxidation current resulting from  $O_2$  breaking down into  $OH_{ads}$  and then reacting electrochemically with  $CO_{ads}$ . Note that because this CO electrooxidation pathway is distinct from the pathway involving  $H_2O$ , it is represented by a different rate equation. The surface-area-to-volume ratio,  $\alpha_{Pt}$ , is set at  $1.0 \times 10^6 \text{ cm}^{-1}$ . The CO that is oxidized by hydroxyl group formation from water is represented by the traditional  $j_{CO}$  described in Springer's model. The bulk of the oxygen is consumed catalytically with adsorbed hydrogen and is represented by second term ( $k_{O_2} x_{O_2} P_a \theta_h^m$ ) in the  $O_2$  and  $H_2$  flux equations. However, in order to accurately determine the amount of  $O_2$  consumed along the ACR path via electrooxidation and hence determine the total rate of  $O_2$  consumption,  $j_{CO}$  must be subtracted from  $j_{CO \text{ w/O}_2}$ .

The membrane-cathode portion of the model is represented by the experimental relationship developed by Kim et al (35), shown in equation (0.42). This is used with equation (0.43) to complete the model in 1-D form by relating the anode cell potential,  $V_{ANODE}$ , to the cell voltage,  $V_{cell}$ .

$$V_{std} = K_1 - K_2 J_{tot} - K_3 \ln(J_{tot}) - K_4 \exp(K_5 J_{tot}) \quad (0.42)$$

$$V_{ANODE} = V_{std}(J_{tot}) - V_{cell} \quad (0.43)$$

where the constants  $K_1 - K_5$  account for the open circuit potential, tafel effects, IR (current-resistance) losses and gas diffusion limitations occurring in the membrane and cathode portions of the fuel cell. Equations (0.42) and (0.43) reduce the entire

membrane-cathode region to a boundary condition which is used in conjunction with the ACR flux equations.

The model equations were solved using MBAND(J). Due to the high non-linearity associated with the effects of an airbleed addition, 4001 nodepoints were required for the ACR region.

## Results and Discussion

The membrane-electrode assemblies tested had a cross-sectional area of 50 cm<sup>2</sup>. The cell was assembled and incubated for 4-to-8 hours at ambient pressure, cell temperature of 70°C, an anode feed of hydrogen, a cathode feed of air, a stoichiometric ratio ([actual flow]/[stoichiometric flow] required for a 1.0 A/cm<sup>2</sup> current) of 1.5 at the anode and 2.0 at the cathode. Single-cell performance curves were obtained under the conditions set in Table 1.

Table 1 Fuel Cell Test Conditions.

Pressure	1 atm (Anode and Cathode)
Cell Temperature	70°C
Stiocheometric Ratio (at 1 A/cm <sup>2</sup> )	1.5 Anode (Hydrogen) 2.0 Cathode (Air)
Feedstreams	Anode: Hydrogen, Reformate, Reformate + Air Bleed, H <sub>2</sub> + CO + Air Bleed Cathode: Air
Dry Reformate Composition	40% H <sub>2</sub> 20% CO <sub>2</sub> 50 ppm CO balance N <sub>2</sub>



### ***Pt Anode: H<sub>2</sub>+CO (Reformate) Feed***

Figure 2 compares the model's predictions to data obtained at Plug Power for a PEMFC containing 0.4 mg Pt/cm<sup>2</sup> in the anode for pure H<sub>2</sub> and reformate feeds. First order kinetics are used here to describe hydrogen adsorption and oxidation.

Several parameters were modified from the Springer model in order to attain the performance curves shown in Figure 2. Differences in materials used (Nafion type, catalyst loading, wt % catalyst on carbon, wt % Nafion in the catalyst regions) give rise to different membrane-cathode performance characteristics that require different constants to result in an accurate representation of the cells tested. Of more importance is that the values for  $k_{ec}$ ,  $b_{fc}^0$  and  $\delta(\Delta G_{CO})$  ( $1 \times 10^{-13}$  A cm<sup>-2</sup>,  $1 \times 10^{-10}$  atm and 15.0 kJ mol<sup>-1</sup> respectively) used in this work are significantly lower than in Springer's model ( $1 \times 10^{-8}$  A cm<sup>-2</sup>,  $1.51 \times 10^{-8}$  atm and 20.0 kJ mol<sup>-1</sup> for the same parameters). PEMFCs tested in this work demonstrated a lower CO tolerance than those examined at LANL.  $k_{ec}$ ,  $b_{fc}^0$  and  $\delta(\Delta G_{CO})$  all relate to rates of removal of CO and lowering any one of these three parameters results in the lowering of the CO removal rate. Therefore these values were adjusted to reflect the less CO tolerant PEMFC Pt anode catalyst used here.

Figure 3 shows the increase in anode potential with increasing current density. The cell potential required to oxidize pure H<sub>2</sub> ranges from 0 to 0.05 V as the current density increases from 0 to 1.3 A/cm<sup>2</sup>. As the amount of CO in the anode increases from 0 to 100 ppm, the anode potential required to achieve similar current densities increases (from 0.05 to 0.60 V for 0.1 A/cm<sup>2</sup>). Figure 3 and

Figure 4 show the correlation between the CO coverage and current density. As the anode potential is reached at which the CO coverage begins to decrease (roughly 0.5 V for 50 ppm CO) the cell current density increases significantly. The anode potential at which this occurs shows a steady increase as the amount of CO in the feed increases. These results are consistent with Springer's model for a similar system, showing that the model effectively reduces to Springer's version when no oxygen is present.

### ***Pt Anode: $H_2+CO+O_2$ (Reformate) Feed***

Figure 5 compares the cell performance predicted by the model for an anode feed containing  $H_2 + CO + O_2$  to actual performance data of a PEMFC MEA containing a Pt anode. Comparing Figure 5 to Figure 2 of  $H_2 + CO$  only in the anode feed (no oxygen is present), the model becomes a 1-D version of Springer's model. This is as it should be. Figure 5 also shows that the model also successfully demonstrates the effect of adding an airbleed to the reformate stream. The addition of 0.5 vol. %  $O_2$  (relative to the hydrogen concentration) results in a significant increase in the oxidation of all CO in the front portion of the Pt anode (as shown in Figure 6). As the amount of oxygen in the anode feed is increased to 2.0%, even more CO is oxidized. Increasing amounts of oxygen in the feedstream results in increasing local CO current densities,  $j_{CO}$ , as shown in Figure 7. All CO oxidized through an electrochemical reaction with  $O_2$  occurs in the front portion of the anode. This is consistent with experimental data where extremely thin Ru filters ( $< 1.0 \times 10^{-5}$  cm) were able to oxidize up to 200 ppm CO when a 2% air bleed is added to the filter. Figure 8 shows the effect of adding  $O_2$  on hydrogen electrooxidation rates. In the region of the anode where oxygen is present (shown in Figure 10),  $H_2$  is oxidized at a

higher rate due to the reduction of CO coverage. For higher concentrations of O<sub>2</sub>, more CO is oxidized, leaving the hydrogen oxidation rate higher even after all O<sub>2</sub> is consumed. This is because lower CO concentrations reduce CO coverage, allowing more free sites for H<sub>2</sub> to be oxidized. In all cases the bulk of the O<sub>2</sub> in the anode feed is consumed through catalytic reaction with H<sub>2</sub> resulting in the oxygen concentration reducing to zero well before the end of the ACR. When 0.5 and 2.0 % O<sub>2</sub> is added to the anode feedstream, initial CO electrooxidation rates increase by a factor of 500 and 1000 respectively. However, O<sub>2</sub> concentration quickly reduces to zero along the length of the ACR, returning CO oxidation rates to the same order of magnitude as a normal reformat stream. In all cases where Pt anodes were used, O<sub>2</sub> was unable to oxidize all CO present in the anode feed and the ACR effectively remained poisoned.

Figure 11 and Figure 12 show the effects of voltage on the amount of H<sub>2</sub> and CO consumed along the ACR. As cell voltage increases (and anode voltage,  $V_{\text{ANODE}}$ , decreases), the amount of CO consumed by electrooxidation with O<sub>2</sub> and H<sub>2</sub>O decreases. As the cell voltage increases from 0.25 to 0.80 V (and  $V_{\text{ANODE}}$  decreases from 0.37 to 0.029 V), the amount of CO oxidized along the ACR is roughly cut in half. Both means of CO electrooxidation are reduced as both reactions are voltage dependent. H<sub>2</sub> consumption behaves differently from that of CO because the H<sub>2</sub> is oxidized catalytically by O<sub>2</sub>. Figure 11 shows that the amount of H<sub>2</sub> consumed in the first 0.5  $\mu\text{m}$  of the ACR changes very little. However, the amount of H<sub>2</sub> consumed by O<sub>2</sub> is roughly 1% in all cases, and thus, the amount of H<sub>2</sub> consumed overall is still largely dependent upon the operating voltage and amount of CO present.

The catalytic and electrochemical consumption of oxygen is represented by  $k_{fO_2}x_{O_2}P_a\theta_h^m$  and  $k_{eO_2}x_{O_2}P_A\theta_{CO}\theta_h^m e^{\left(\frac{V_a+V_N}{b_{O_2}}\right)}$  respectively, where  $k_{fO_2}$  and  $k_{eO_2}$  are the preexponential factors for those expressions given in  $A\text{ cm}^{-2}\text{ atm}^{-1}$ . Decreasing  $k_{fO_2}$  results in an increase in the effect of oxygen on PEMFC performance to the point where  $O_2$  is able oxidize all CO present in the feedstream as shown Figure 13. As the CO is removed near the front of the ACR, the anode operates mostly “CO free” resulting PEMFC performance nearly equivalent to that of pure  $H_2$  operation as shown in Figure 14. Figure 15 shows that the  $H_2$  electrooxidation rate increases dramatically in the case where CO has been eliminated from the feedstream. As the  $H_2$  is then depleted along the length of the electrode, the electrooxidation rate appropriately reaches a maximum and begins to decrease to the Nernstian effects arising from hydrogen dilution.

Increasing the rate of  $O_2$  electrochemically consumed,  $k_{eO_2}$ , effects PEMFC performance similarly to decreasing  $k_{fO_2}$ . Figure 16 shows that as  $k_{eO_2}$  is increased, PEMFC performance increases.

The natural Tafel slope of the electrochemical oxidation of CO by  $O_2$ ,  $b_{O_2}$ , affects the dependence of the oxidation rate of CO on anode voltage,  $V_a$ . The Tafel slope for the electrochemical oxidation of CO by  $O_2$  is high relative to  $b_h$  and  $b_c$ . This makes sense, as the electrooxidation of  $H_2$  and CO electrooxidation by  $H_2O$  are far more voltage dependent. Literature has shown that water breaks down into  $OH_{ads}$  at a significant rate only at high anode voltages ( $\sim 0.7\text{ V}$ ).  $H_2$  kinetics are well documented as being sensitive to applied voltage. When  $O_2$  is added to the feedstream, the performance curves presented in Figure 5 show that significant performance increase even at high voltages at

both low and high voltages cell voltages. This corresponds to significant CO electrooxidation occurring at both high and low anode potentials. As shown in Figure 18, for lower values of  $b_{O_2}$ , CO oxidation primarily occurs at higher anode voltages (corresponding to lower cell voltages).

It is believed that catalytic oxidation rate between hydrogen and oxygen is slower on Ru than on Pt. This gives rise to the increased amount of CO desorbed and resultant increase in PEMFC performance relative to pure Pt and Pt:Ru alloys.

In comparing the model for the case when  $b_{O_2} = 0.48$  V,  $k_{fO_2} = 7 \times 10^{-4}$  A cm<sup>-2</sup> atm<sup>-1</sup> and  $k_{eO_2} = 3 \times 10^{-3}$  A cm<sup>-2</sup> atm<sup>-1</sup> to the data for the Ru Filter (shown in Figure 19), one can see that when all CO is oxidized in the filter region, performance does not match that of a pure H<sub>2</sub> feed. This is because CO is present as part of a reformat feed that contains only 40 vol. % hydrogen before humidification. The model successfully incorporates the effects of hydrogen dilution into the resulting performance curves. Increased voltage losses through the dilution effects of hydrogen are consistent with literature (32,51). Some performance loss can also be contributed to hydrogen consumption by oxygen. However, this amounts to a maximum of 4% (when 2 vol % oxygen relative to hydrogen is present in the feedstream). This performance reduction is far less than that resulting from CO poisoning.

## Conclusions

A model demonstrating the effects of adding an air bleed to a reformat feed containing CO has been presented here. The model compares well with data gathered for PEMFC containing a Pt anode when 0.5 and 2.0 vol % oxygen with respect to hydrogen is present in the anode feed. All oxygen is consumed before it has a chance to diffuse

very far into the anode filter, which is also consistent with existing data. When no oxygen is present in the anode feed, the model successfully reverts to the 1-D form of Springer's model for an anode reformat feed.

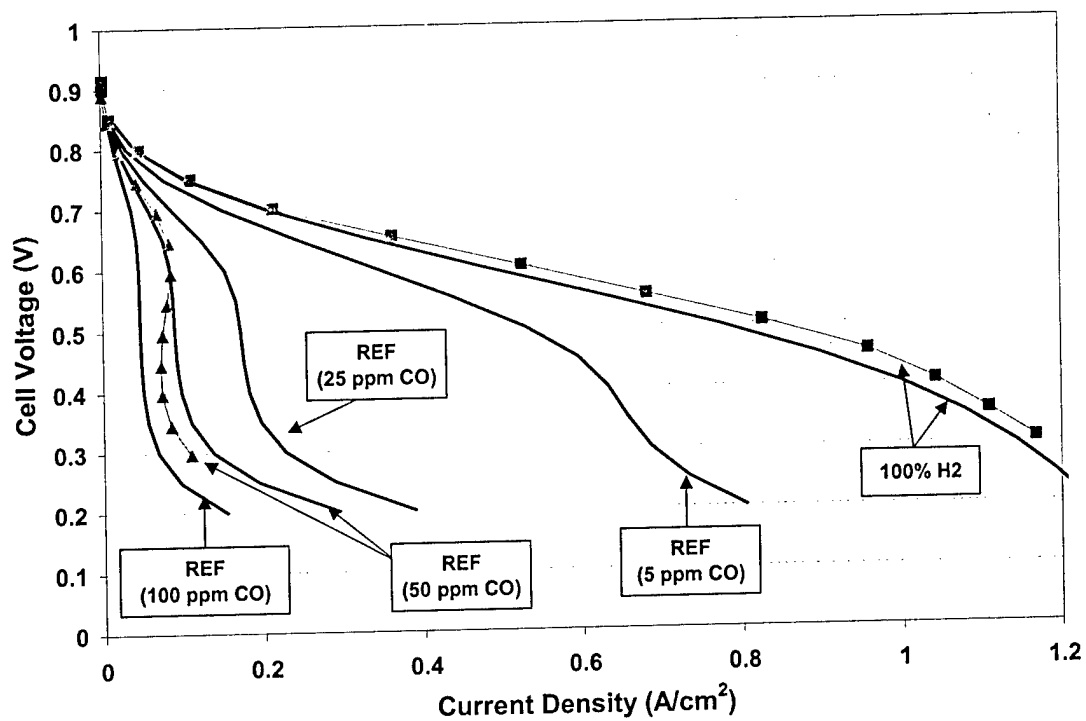


Figure 2 Comparison of the model to actual PEM fuel cell data taken at Plug Power.  $P = 1 \text{ atm}$ ,  $T = 70^\circ\text{C}$ .

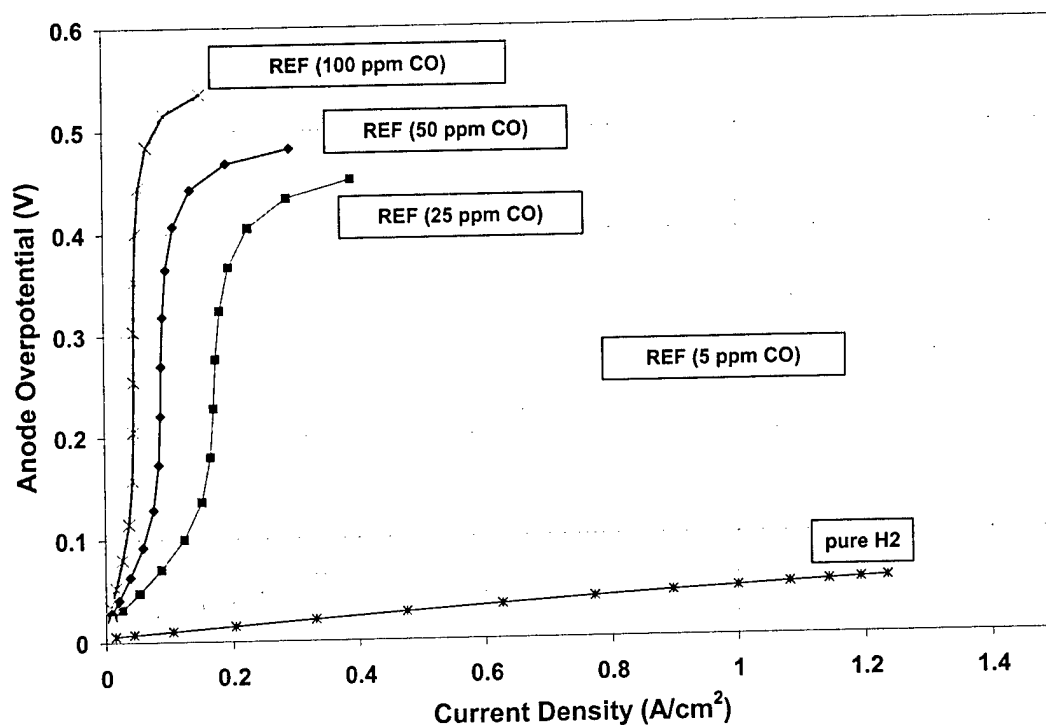


Figure 3 Anode overpotential versus current density for a variety of CO concentrations.  $P = 1\text{ atm}$ ,  $T = 70^\circ\text{C}$ .



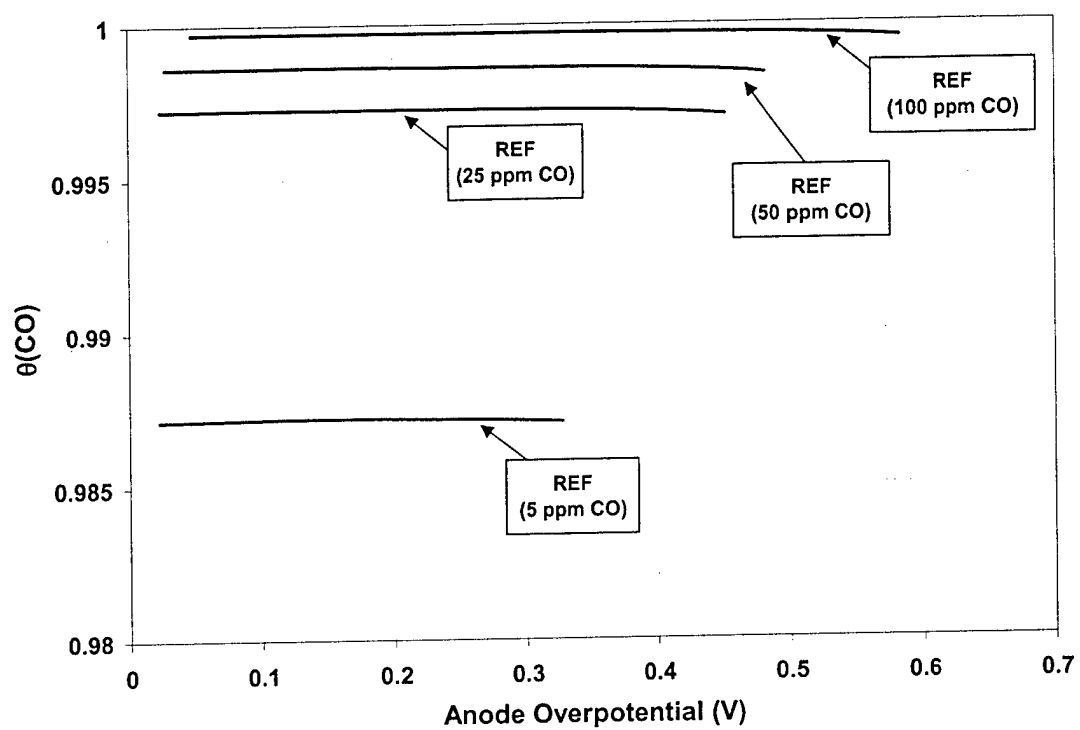


Figure 4 CO coverage at the ACR – membrane interface versus anode overpotential for a variety of CO concentrations.  $P = 1\text{ atm}$ ,  $T = 70^\circ\text{C}$ .

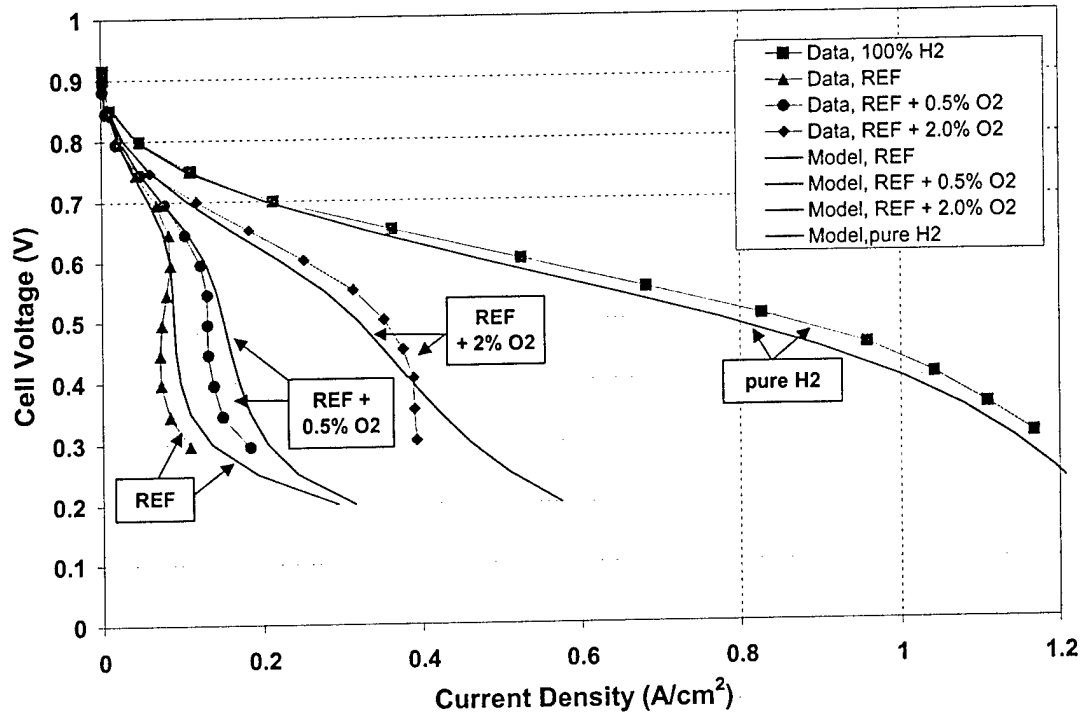


Figure 5 Comparison of single cell performance data to the developed model for the Pt + Ru filter for anode feeds of pure H<sub>2</sub> (before humidification), 40 % H<sub>2</sub> + 50 ppm CO (before humidification), and H<sub>2</sub> + 50 ppm CO + 1% O<sub>2</sub> (before humidification). P = 1atm, T = 70°C.

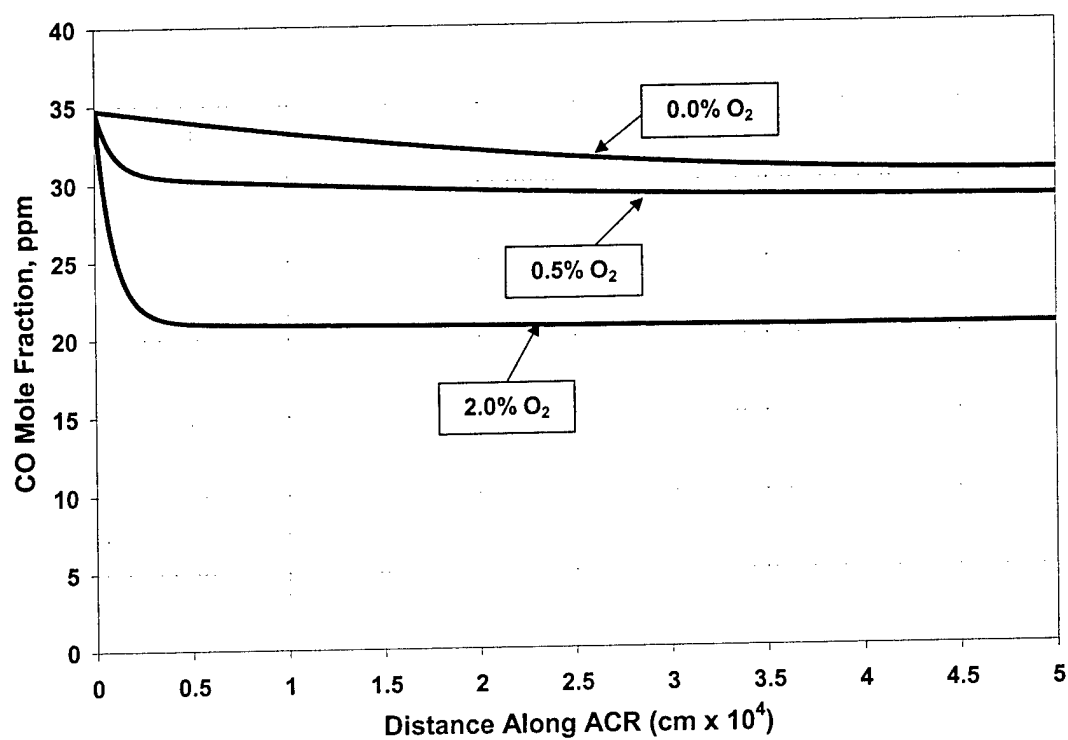


Figure 6 The calculation of CO concentration along the length of the anode catalyst region for various  $\text{O}_2$  concentrations.  $P = 1\text{ atm}$ ,  $T = 70^\circ\text{C}$ ,  $V_{\text{CELL}} = 0.4\text{ V}$ .

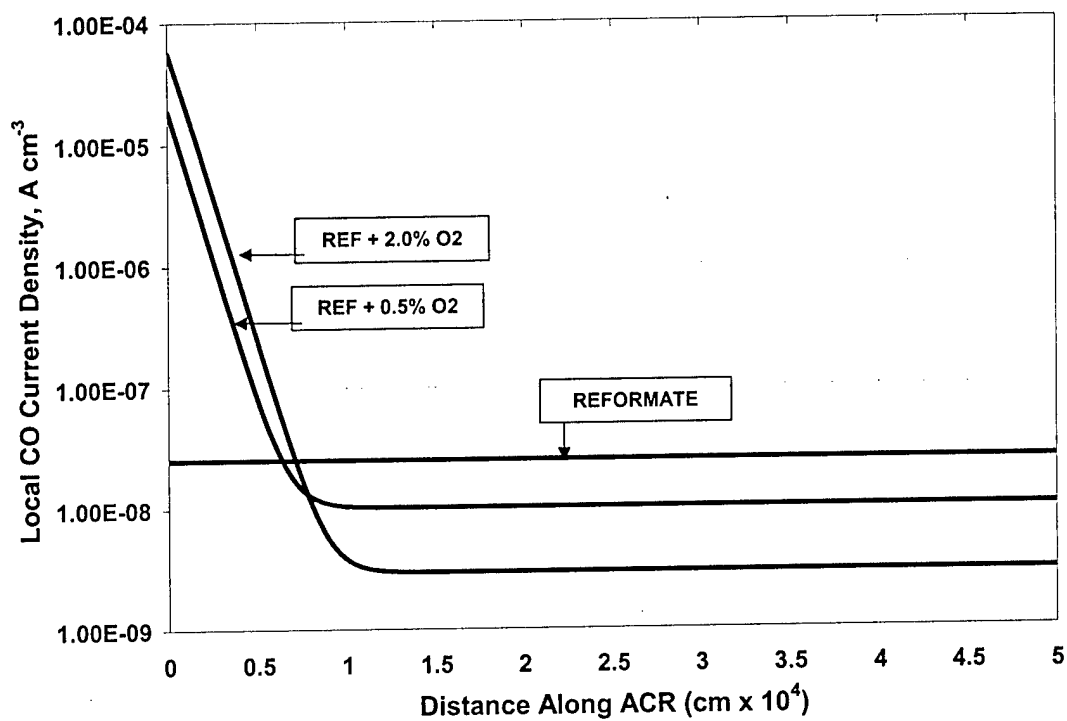


Figure 7 The calculation of local CO current densities along the length of the anode catalyst region for an anode feeds containing CO and CO + O<sub>2</sub>. P = 1atm, T = 70°C, V<sub>CELL</sub> = 0.4 V.

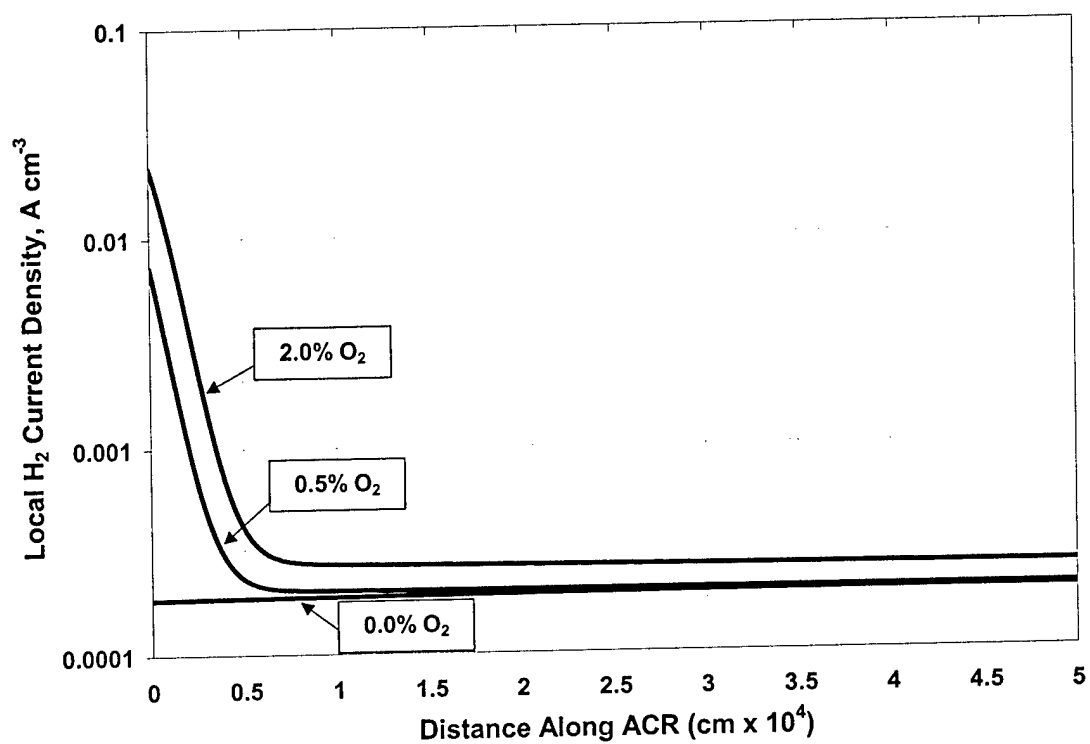


Figure 8 The calculation of local hydrogen current densities along the length of the anode catalyst region for an anode feeds containing CO and CO + O<sub>2</sub>. P = 1 atm, T = 70°C, V<sub>CELL</sub> = 0.4 V.

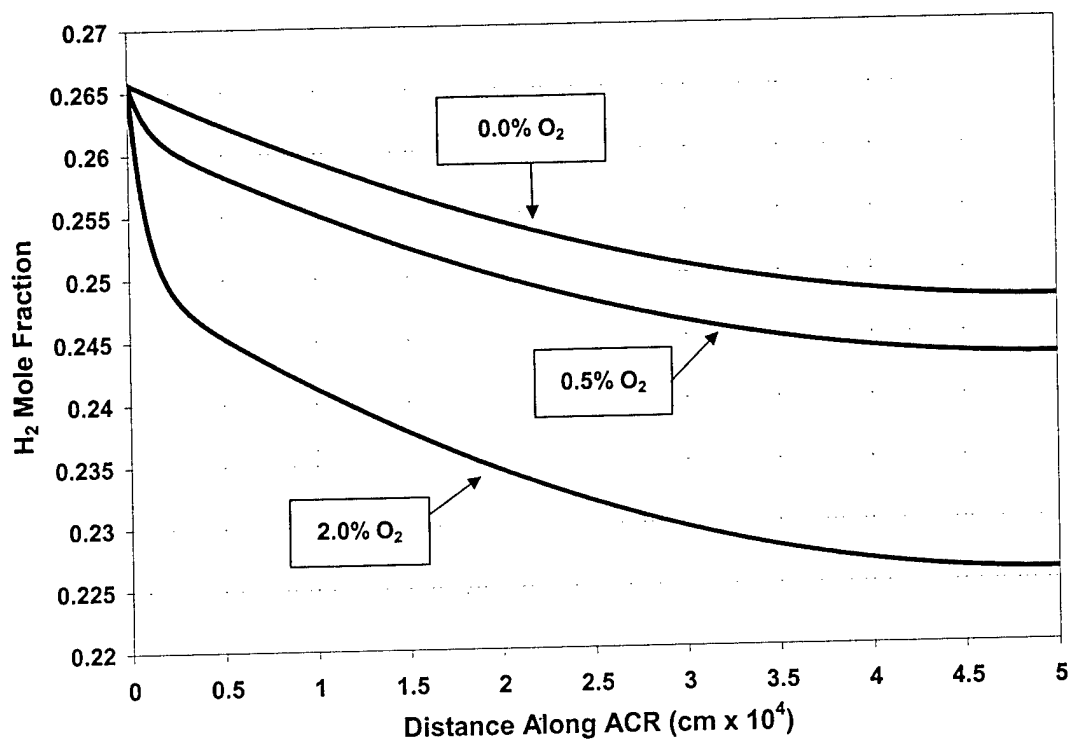


Figure 9 The calculation of H<sub>2</sub> concentration along the length of the anode catalyst region when CO and O<sub>2</sub> are added to the feedstream.  $P = 1 \text{ atm}$ ,  $T = 70^\circ\text{C}$ ,  $V_{\text{CELL}} = 0.4 \text{ V}$ .

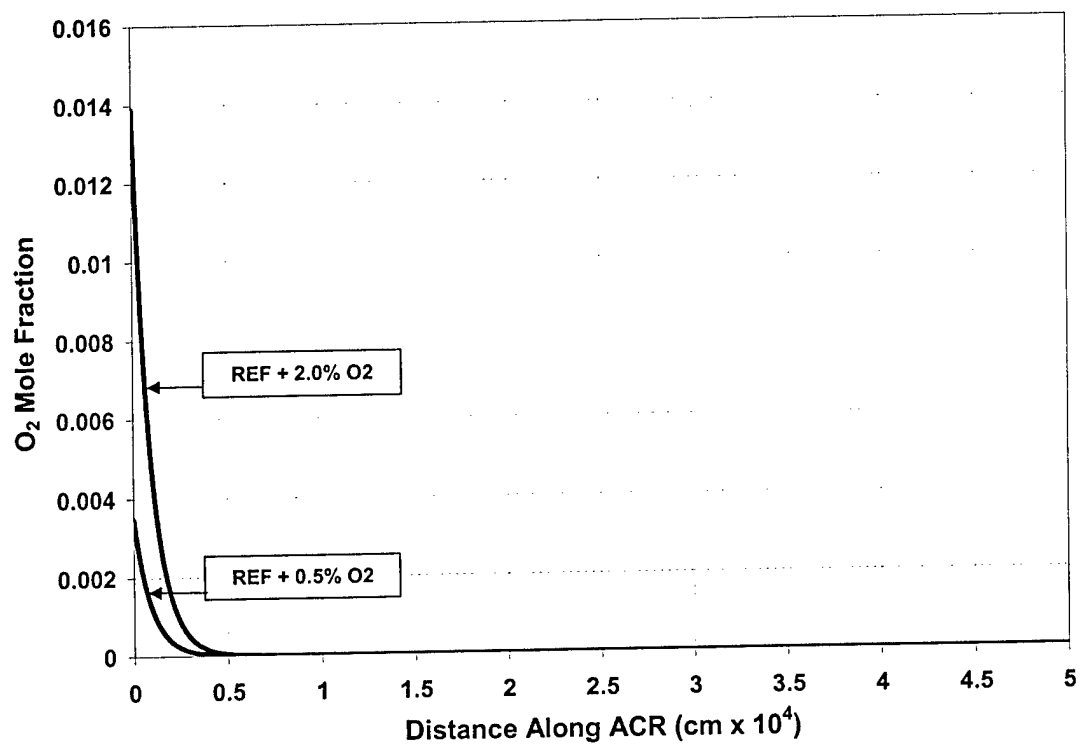


Figure 10 The calculation of O<sub>2</sub> concentration along the length of the anode catalyst region for an anode feed.  $P = 1\text{ atm}$ ,  $T = 70^\circ\text{C}$ ,  $V_{\text{CELL}} = 0.4\text{ V}$ .

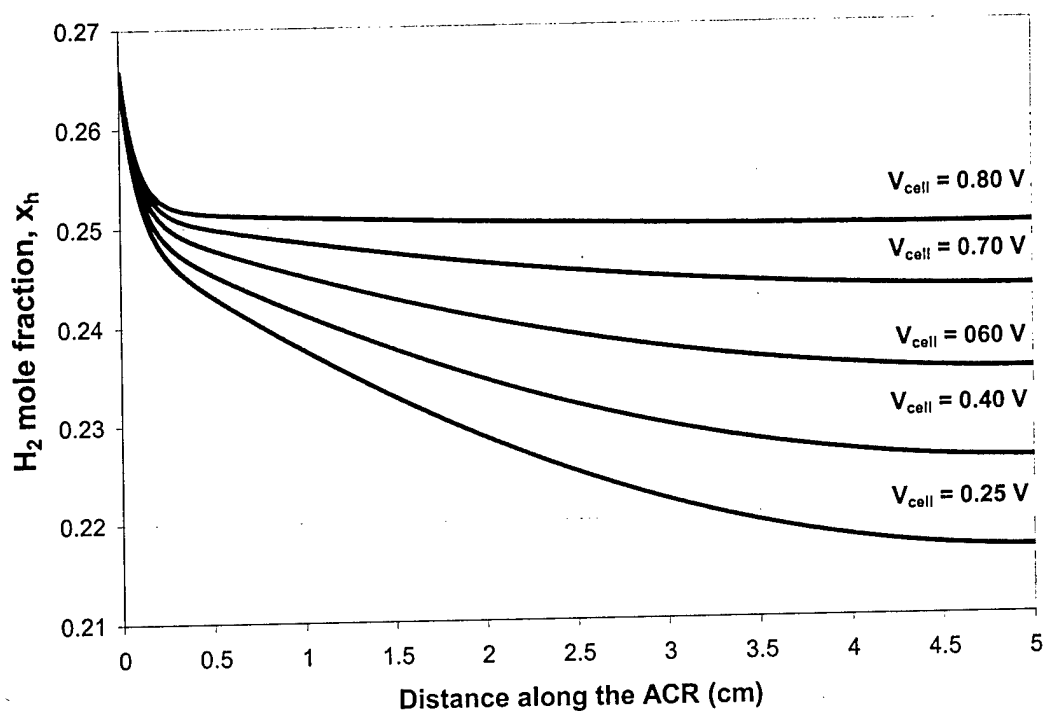


Figure 11

The calculation of CO concentration along the length of the anode catalyst region for a fully humidified anode stream.  $P = 1 \text{ atm}$ ,  $T = 70^\circ\text{C}$ . Initial feedstream composition (dry):  $x_{H_2} = 0.40$ ,  $x_{CO} = 50 \text{ ppm}$ , and 1%  $O_2$  (relative to  $H_2$ ).  $b_{O_2} = 0.48 \text{ V}$ ,  $k_{fO_2} = 7 \times 10^{-4} \text{ A cm}^{-2} \text{ atm}^{-1}$  and  $k_{eO_2} = 3 \times 10^{-3} \text{ A cm}^{-2} \text{ atm}^{-1}$ .



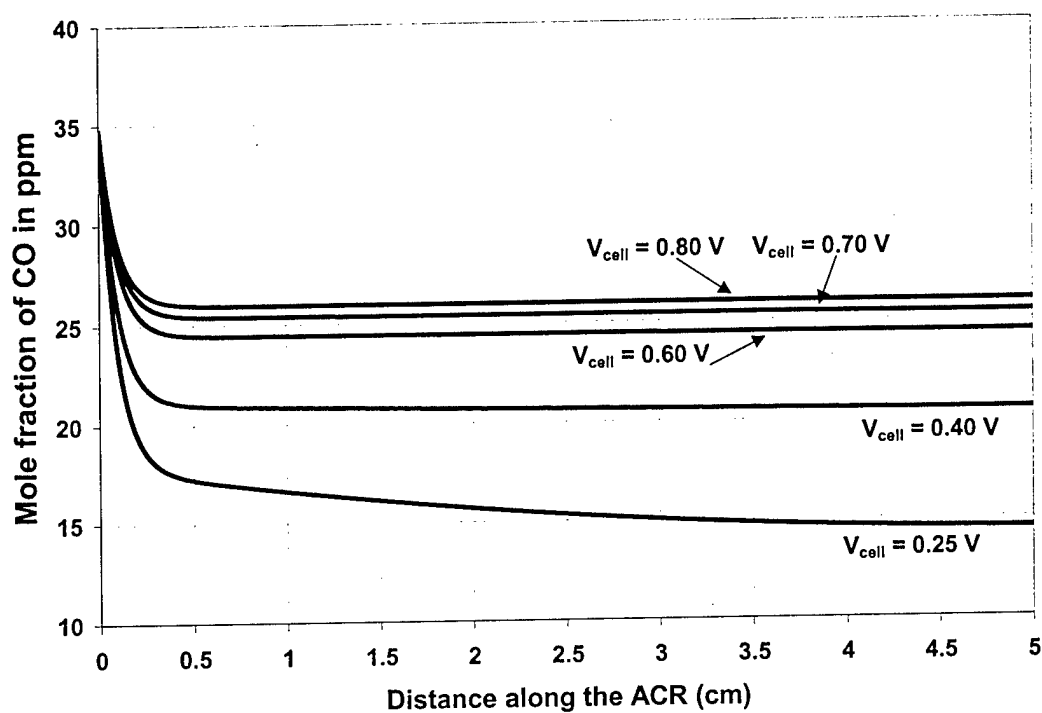


Figure 12

The calculation of CO concentration along the length of the anode catalyst region for a fully humidified anode stream.  $P = 1 \text{ atm}$ ,  $T = 70^\circ\text{C}$ . Initial feedstream composition (dry):  $x_{\text{H}_2} = 0.40$ ,  $x_{\text{CO}} = 50 \text{ ppm}$ , and 1%  $\text{O}_2$  (relative to  $\text{H}_2$ ).  $b_{\text{O}_2} = 0.48 \text{ V}$ ,  $k_{f\text{O}_2} = 7 \times 10^{-4} \text{ A cm}^{-2} \text{ atm}^{-1}$  and  $k_{e\text{O}_2} = 3 \times 10^{-3} \text{ A cm}^{-2} \text{ atm}^{-1}$ .

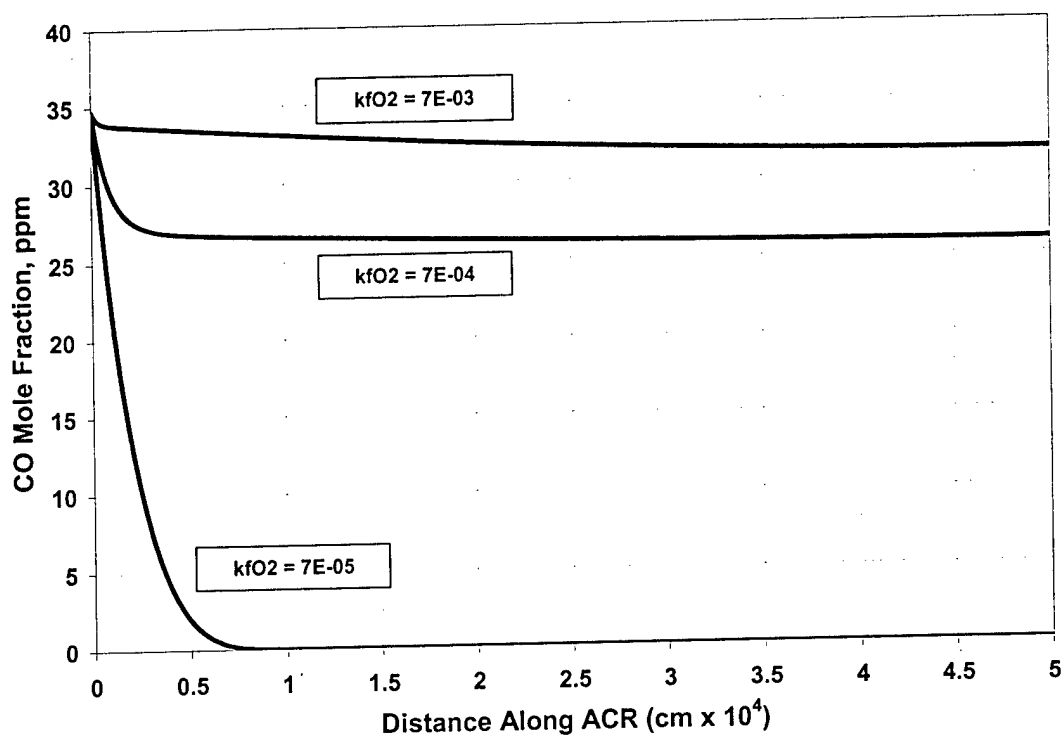


Figure 13 The effect of varying the rate constant,  $k_{fO_2}$ , for the catalytic reaction between  $H_2$  and  $O_2$  on the amount of CO oxidized along the ACR.  $P = 1 \text{ atm}$ ,  $T = 70^\circ\text{C}$ . Initial feedstream composition (dry):  $x_{H_2} = 0.40$ ,  $x_{CO} = 50 \text{ ppm}$ , and 1%  $O_2$  (relative to  $H_2$ ).  $b_{O_2} = 0.48 \text{ V}$ ,  $k_{eO_2} = 3 \times 10^{-3} \text{ A cm}^{-2} \text{ atm}^{-1}$ .

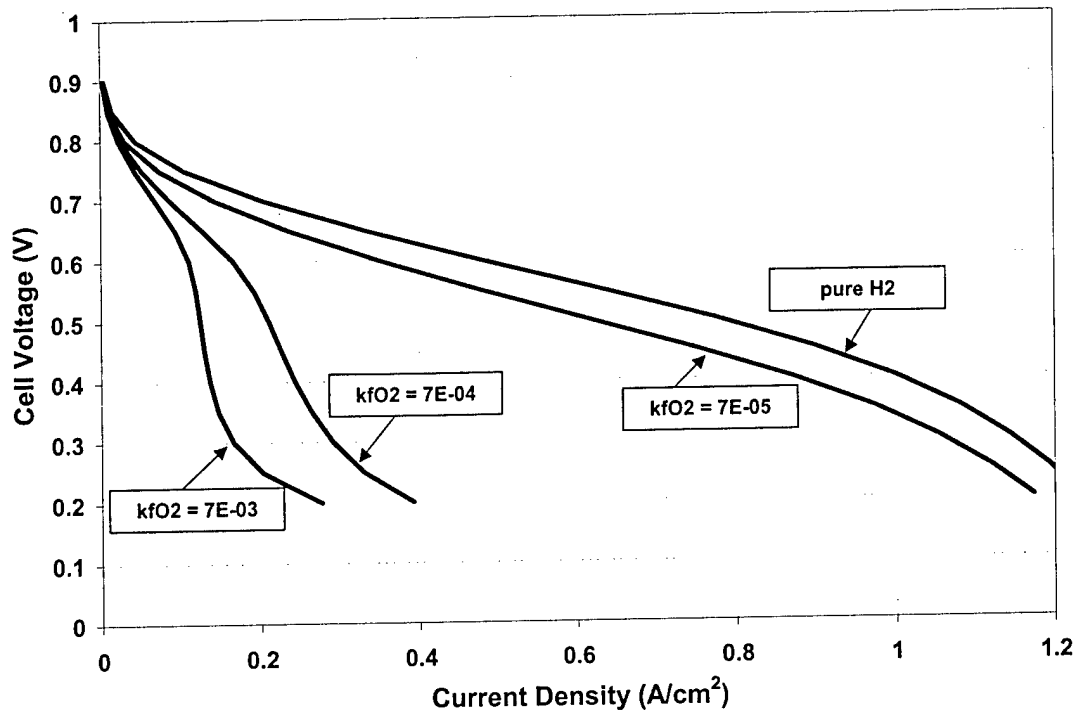


Figure 14 The effect of varying the rate constant,  $k_{fO_2}$ , for the catalytic reaction between  $H_2$  and  $O_2$  on PEMFC performance.  $P = 1 \text{ atm}$ ,  $T = 70^\circ\text{C}$ . Initial feedstream composition (dry):  $x_{H_2} = 0.40$ ,  $x_{CO} = 50 \text{ ppm}$ , and 1%  $O_2$  (relative to  $H_2$ ).  $b_{O_2} = 0.48 \text{ V}$ ,  $k_{eO_2} = 3 \times 10^{-3} \text{ A cm}^{-2} \text{ atm}^{-1}$ .

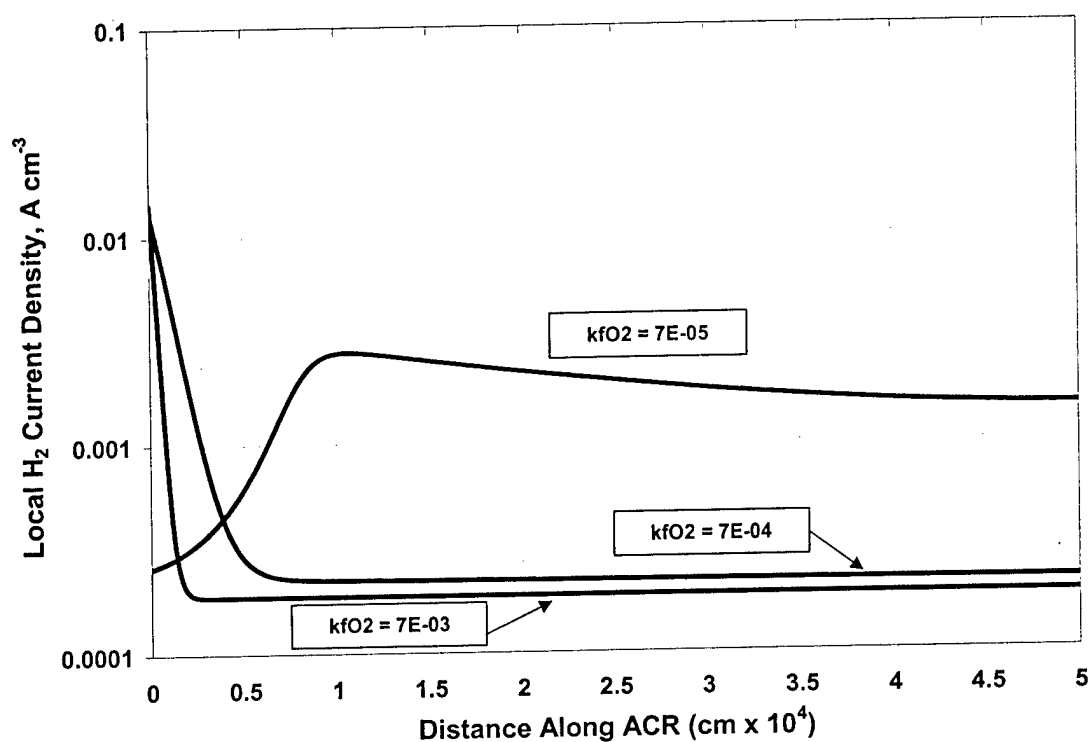


Figure 15

The effect of varying the rate constant,  $k_{fO_2}$ , for the catalytic reaction between  $H_2$  and  $O_2$  on local hydrogen current density,  $j_h$ , along the length of the ACR.  $P = 1\text{ atm}$ ,  $T = 70^\circ\text{C}$ . Initial feedstream composition (dry):  $x_{H_2} = 0.40$ ,  $x_{CO} = 50\text{ ppm}$ , and  $1\%$   $O_2$  (relative to  $H_2$ ).  $b_{O_2} = 0.48\text{ V}$ ,  $k_{eO_2} = 3 \times 10^{-3}\text{ A cm}^{-2}\text{ atm}^{-1}$ .

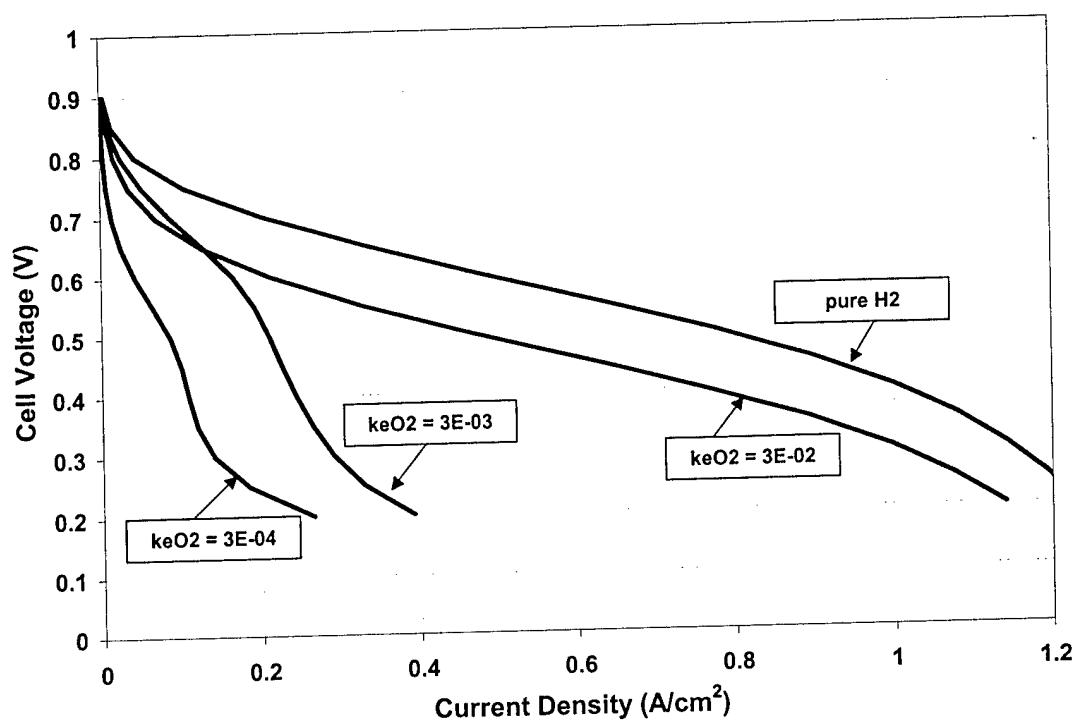


Figure 16 The effect of varying the rate constant,  $k_{eO_2}$ , for the electrochemical oxidation of CO by  $O_2$  on PEMFC performance.  $P = 1 \text{ atm}$ ,  $T = 70^\circ\text{C}$ . Initial feedstream composition (dry):  $x_{H_2} = 0.40$ ,  $x_{CO} = 50 \text{ ppm}$ , and 1%  $O_2$  (relative to  $H_2$ ).  $b_{O_2} = 0.48 \text{ V}$ ,  $k_{fO_2} = 7 \times 10^{-4} \text{ A cm}^{-2} \text{ atm}^{-1}$ .

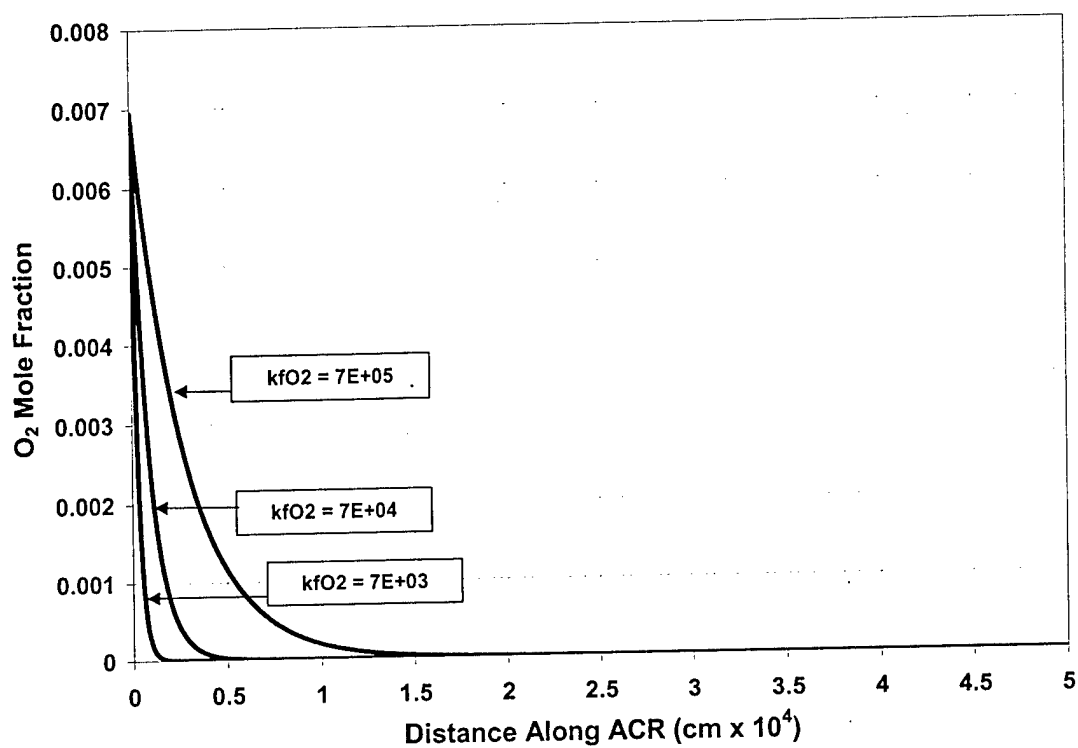


Figure 17 The effect of varying the rate constant,  $k_{fO_2}$ , for the catalytic reaction between  $H_2$  and  $O_2$  on oxygen concentration,  $x_{O_2}$ , along the length of the ACR.  $P = 1\text{ atm}$ ,  $T = 70^\circ\text{C}$ . Initial feedstream composition (dry):  $x_{H_2} = 0.40$ ,  $x_{CO} = 50\text{ ppm}$ , and 1%  $O_2$  (relative to  $H_2$ ).  $b_{O_2} = 0.48\text{ V}$ ,  $k_{eO_2} = 3 \times 10^3\text{ A cm}^{-2}\text{ atm}^{-1}$ .

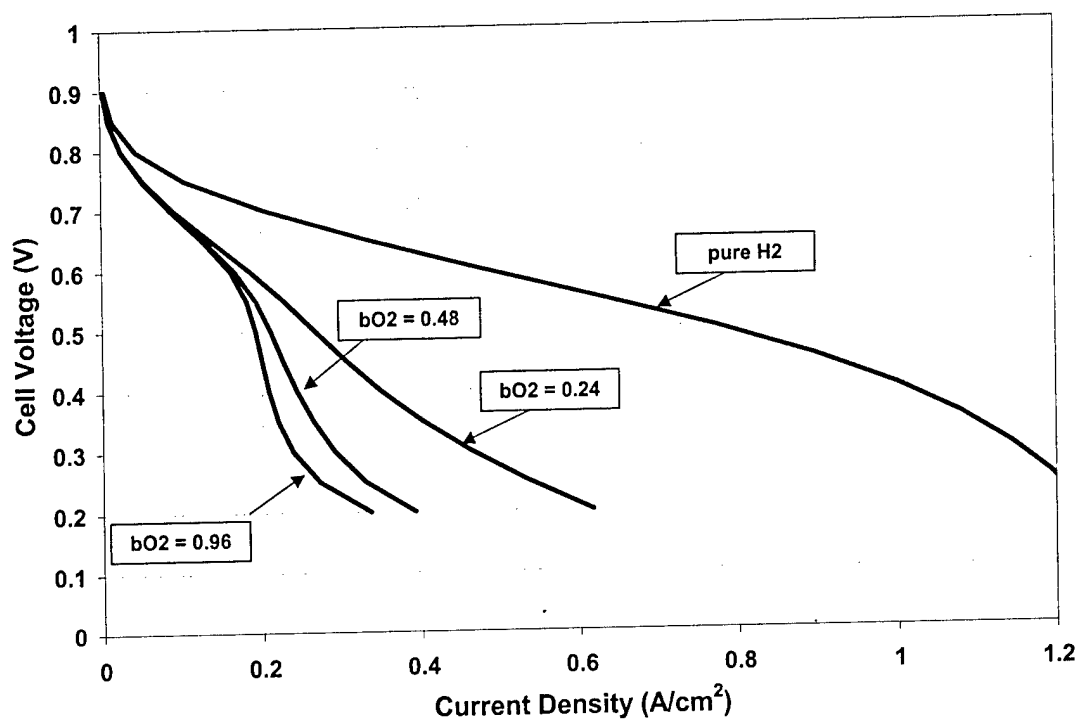


Figure 18 The effect of varying the rate constant,  $b_{O_2}$ , for the electrochemical oxidation of CO by  $O_2$  on PEMFC performance.  $P = 1\text{ atm}$ ,  $T = 70^\circ\text{C}$ . Initial feedstream composition (dry):  $x_{H_2} = 0.40$ ,  $x_{CO} = 50\text{ ppm}$ , and 1%  $O_2$  (relative to  $H_2$ ).  $k_{fO_2} = 7 \times 10^{-4}\text{ A cm}^{-2}\text{ atm}^{-1}$ ,  $k_{eO_2} = 3 \times 10^{-3}\text{ A cm}^{-2}\text{ atm}^{-1}$ .

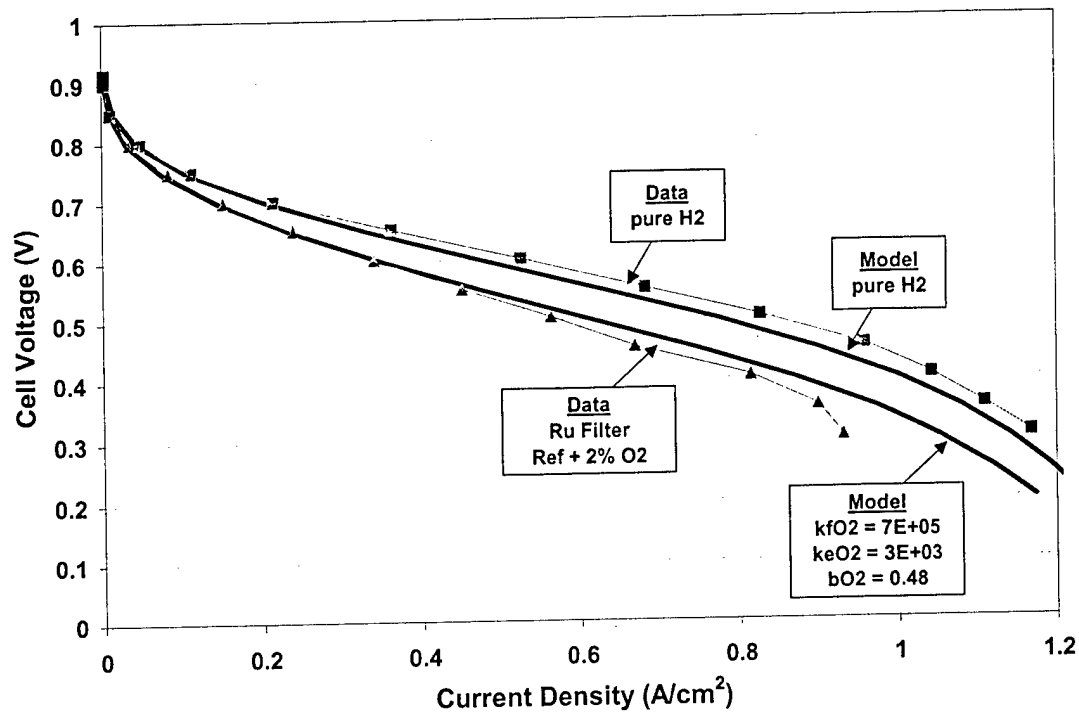


Figure 19 Comparison of the performance of the Pt + Ru filter to the model for a case where all CO is electrooxidized within the ACR.  $P = 1\text{ atm}$ ,  $T = 70^\circ\text{C}$ . Initial feedstream composition (dry):  $x_{\text{H}_2} = 0.40$ ,  $x_{\text{CO}} = 50\text{ ppm}$ , and  $1\% \text{ O}_2$  (relative to  $\text{H}_2$ ).  $b_{\text{O}_2} = 0.48\text{ V}$ ,  $k_{\text{fO}_2} = 7 \times 10^{-4}\text{ A cm}^{-2}\text{ atm}^{-1}$  and  $k_{\text{eO}_2} = 3 \times 10^{-3}\text{ A cm}^{-2}\text{ atm}^{-1}$ .



## List of Symbols

Table below lists the parameters, their definitions, values and units. (32,36,52)

Symbol	Definition	Units	Value (Pt ACR)
$l_{ACR}$	ACR thickness	cm	$5 \times 10^{-4}$
$l_{GDL}$	GDL thickness	cm	0.03
$k_{eh}$	pre-exponential hydrogen Tafel electro-oxidation rate	$A\ cm^{-2}$	4.0
$k_{ec}$	pre-exponential CO Tafel electro-oxidation rate times 2F	$A\ cm^{-2}$	$3 \times 10^{-11}$
$k_{eO_2}$	pre-exponential O <sub>2</sub> Tafel electro-oxidation rate times 2F	$A\ cm^{-2}\ atm^{-1}$	$3 \times 10^3$
$k_{fh}$	forward hydrogen adsorption rate times 2F	$A\ cm^{-2}\ atm^{-1}$	4000
$b_{fh}$	back-to-forward hydrogen adsorption ratio ( $1/K_{eq}$ )	atm	0.5
$k_{fc}$	forward CO adsorption rate times 2F	$A\ cm^{-2}\ atm^{-1}$	10
$b_{fc}$	back-to-forward CO adsorption ratio ( $1/K_{eq}$ )	atm	
$b_{fc}^0$	$b_{fc}$ at $\theta_{CO} = 0$	atm	$2.5 \times 10^{-10}$
$k_{fO_2}$	forward oxygen adsorption rate (convert to $mol\ cm^{-3}\ atm^{-1}$ by dividing by RT)	$s^{-1}$	
$k_{fO_2}^0$	forward oxygen adsorption rate pre-exponential factor	$s^{-1}$	$7 \times 10^4$
$b_c$	Natural Tafel slope for CO electro-oxidation via H <sub>2</sub> O	V	0.06
$b_h$	Natural Tafel slope for hydrogen electro-oxidation	V	0.032
$b_{O_2}$	Natural Tafel slope for CO electro-oxidation via H <sub>2</sub> O	V	0.48
$D_H$	Hydrogen diffusion coefficient in catalyst layer	$cm^2\ s^{-1}$	$2 \times 10^{-4}$
$D_{CO}$	CO diffusion coefficient in catalyst layer	$cm^2\ s^{-1}$	$5.34 \times 10^{-5}$
$D_{O_2}$	O <sub>2</sub> diffusion coefficient in catalyst layer	$cm^2\ s^{-1}$	$D_{O_2} = D_{O_2}^0 \exp\left(\frac{E_D}{RT}\right)$  $D_0 = 3.38 \times 10^{-4}$ $E_D = 16040\ J\ mol^{-1}\ K^{-1}$
$P_s D_{Sij}$	pressure-diffusion coefficient of species i in species j in the GDL	$atm\ cm^2\ s^{-1}$	
$\alpha_{SVR}$	surface to volume ratio of Pt in the ACR	$cm^{-1}$	$1 \times 10^6$
$\theta_h$	hydrogen surface coverage		
$\theta_{CO}$	CO surface coverage		
$\theta_O$	oxygen surface coverage		
$\theta_{OH}$	OH surface coverage		
$x_i$	mole fraction of species i		
$\Phi_i$	molar flux of species i	$mol\ cm^{-3}\ s^{-1}$	
$T_{c,i}$	Critical temperature of species i	K	
$p_{c,i}$	Critical pressure of species i	atm	

$M_i$	Molecular weight of species i	$\text{g mol}^{-1}$	
$V_a$	Local anode overpotential	V	
$V_{\text{anode}}$	Anode overpotential at the ACR-membrane interface	V	
$V_N$	Nernstian potential: $V_N = \frac{RT}{nF} \ln(x_h P_a)$	V	
$V_S$	Standard molar volume	$\text{cm}^3 \text{mol}^{-1}$	22414
$P_S$	Standard pressure	atm	1.0
$T_S$	Standard temperature	K	273.15
$I_{\text{Dh}}$	Hydrogen diffusion current density	$\text{A cm}^{-2}$	
$I_{\text{DCO}}$	CO diffusion current density	$\text{A cm}^{-2}$	
$I_{\text{DO2}}$	Oxygen diffusion current density	$\text{A cm}^{-2}$	
$j_h$	local hydrogen current density	$\text{A cm}^{-2}$	
$j_{\text{co}}$	local CO current density	$\text{A cm}^{-2}$	
$J_H^{\text{tot}}$	total hydrogen current density	$\text{A cm}^{-2}$	
$J_{\text{CO}}^{\text{tot}}$	total hydrogen current density	$\text{A cm}^{-2}$	
$J_{\text{tot}}$	total current density	$\text{A cm}^{-2}$	
F	Faradays constant	$\text{C mol}^{-1}$	96487
R	Universal gas constant	$\text{J mol}^{-1} \text{K}^{-1}$	8.315
		$\text{cm}^3 \text{atm mol}^{-1} \text{K}^{-1}$	82.06
$\delta(\Delta G_{\text{CO}})$	Variation of free energy of adsorption of CO between zero and full coverage of CO	$\text{J mol}^{-1}$	20,000
$E_{\text{O2}}$	The activation energy for the reaction of oxygen with adsorbed hydrogen	$\text{cal mol}^{-1}$	11,400
$j_0$	exchange current density	$\text{A cm}^{-3}$	
z	distance through the anode	cm	
$x_i$	mole fraction of species i		
$s_i$	stoichiometric coefficient of species i		
$\theta_i$	surface coverages of species I (CO, H <sub>2</sub> )		
$\theta_h$	equilibrium surface coverage		
$\eta$	electrochemical overpotential	V	
$\sigma$	conductivity of the electrically conductive phase	$\text{mho cm}^{-1}$	
$c_{\text{H}^+}^{\text{ref}}$	H <sub>2</sub> reference concentration	$\text{mol/cm}^3$	
T	Temperature	C	
eff	effective (accounting for a porous medium)		
ACR	Active Catalyst Region		
GDL	Gas Diffusion Layer		
MEM	membrane		

## References

1. H.P. Dhar, L.G. Christner, A.K. Kush, H.C. Maru. *J. Electrochem. Soc.*, **133**, 1574 (1986).
2. H.F. Oetjen, V.M. Schmidt, U. Stimming, and F. Trila. *J. Electrochem. Soc.*, **143**, 3838 (1996).
3. H.P. Dhar, L.G. Christner, A.K. Kush. *J. Electrochem. Soc.*, **134**, 3021 (1987).
4. B.N. Grgur, N.M. Markovic, P.N. Ross. *J. Electrochem. Soc.*, **146**, 1613 (1999).
5. R.J. Bellows, E.P. Marucchi-Soos, D.T. Buckley. *Ind. Eng. Chem. Res.*, **35**, 1235 (1996).
6. R.J. Bellows, E. Marucchi-Soos, R.P. Reynolds. *Electrochemical and Solid State Letters*, **1**, 69 (1998).
7. V.M. Schmidt, H.-F. Oetjen and J. Divisek. *J. Electrochem. Soc.* Vol. **144**, L237, (1997).
8. M. Iwase, S. Kawatsu. *Electrochemical Society Proceedings*. Vol. 95-23., p. 12-23, 1995.
9. M. Watanabe, H. Igarashi, T. Fujino. *Electroanalytical Chem.*, **67**, 1194 (1999).
10. B.N. Grgur, N.M. Markovic, P.N. Ross, Jr. *Electrochemical Soc. Proc.* Vol. 98-27, 176 (1998).
11. A.B. Anderson, E. Grantscharova, P. Schiller. *J. Electrochemical Soc.*, **142**, 1880 (1995).
12. M. Gotz, H. Wendt. *United States Fuel Cell Council's Grove Fuel Cell Seminar Abstracts*, Oct. 30 – Nov. 2, 1998, Palm Springs, CA., p. 616.
13. J.-T. Wang, R. F. Savinell, J. Wainright, M. Litt, H. Yu, *Electrochim. Acta*, **41**, 193 (1996)
14. R.W. Kopitzke; C.A. Linkous, H.R. Anderson, G.L. Nelson, *J Electrochem. Soc.*, **147**, 1677 (2000).
15. A. Küver, K. Potje-Kamloth, *Electrochem. Acta*, **43**, 2527 (1998).
16. J.-T. Weng, J.S. Wainright, U. Landau, R. F. Savinell, *J Electrochem. Soc.*, **142**, L121-123 (1995).
17. P.L. Antonucci, *Solid State Ionics*, **125**, 431 (1999).
18. P. Costamagna, C. Yang, A.B. Bocarsly, S. Srinivasan, *Electrochimica Acta* , **47**, 1023 (2002)
19. A. T. Haug, J. W. Weidner, R. E. White, W. Huang, T. Stoner. "Using Sputter Deposition to Increase CO Tolerance in a PEM Fuel Cell." *Accepted to J. Electrochem. Soc.*
20. A. T. Haug, J. W. Weidner, R. E. White, W. Huang. "The Development of a Novel CO Tolerant PEMFC Anode." *Accepted to J. Electrochem. Soc.*

21. H.P. Dhar, L.G. Christner, A.K. Kush, H.C. Maru, *J. Electrochem. Soc.*, **133**, 1574 (1986)
22. H.P. Dhar, L.G. Christner, A.K. Kush. *J. Electrochem. Soc.*, **134**, 3021 (1987)
23. W. Vogel, J. Lundquist, P. Ross, P. Stonehart, *Electrochimica Acta*, **20**, 79 (1975)
24. D.M. Bernardi and M.W. Verbrugge, *Electrochemical Society Proceedings*, **91-10**, (1991)
25. K.R. Weisbrod, S.A. Grot, N.E. Vanderborgh, *Electrochemical Society Proceedings*, **95-23**, 152 (1995)
26. D.M. Bernardi and M.W. Verbrugge, *AIChE Journal*, **37**, (1991)
27. K. Scott, W. Taama, J. Cruickshank, *J. of Power Sources*, **65**, 159 (1997)
28. T.V. Nguyen and R.E. White, *J. Electrochem. Soc.*, **140**, 2178 (1993)
29. T.E. Springer, T.A. Zawodski, S. Gottesfeld, *J. Electrochem. Soc.*, **138**, 2334 (1991)
30. W-K. Paik, T.E. Springer, S. Srinivasan, *J. Electrochem. Soc.*, **136**, 2334 (1989)
31. J.O'M. Bockris and A.K.N. Reddy, "Modern Electrochemistry." **2<sup>nd</sup> ed**, 910 (1974)
32. T. E. Springer, T. Rockward, T. A. Zawodzinski, S. Gottesfeld, *J. Electrochem. Soc.*, **148**, A11 (2001)
33. S.J. Lee, S. Mukerjee, E.A. Ticianelli, J. McBreen, *Electrochimica Acta*. **44**, 3283 (1999)
34. G. Zheng, B.N. Popov, and R.E. White, *J. Electrochem. Soc.* **143**, 435 (1996)
35. J. Kim, S. Lee, S. Srinivasan, *J. Electrochem. Soc.*, **142**, 2670 (1995)
36. L. K. Verheij, M. B. Hugenschmidt, *Surf. Sci.*, **412**, 37 (1998)
37. P.-A. Bui, D. G. Vlachos, P. R. Westmoreland, *Ind. Eng. Chem. Res.*, **36**, 2558 (1997)
38. S.H. Oh, R.M. Sinkevitch. *J. Catalysis*, **142**, 254 (1993).
39. N.M. Markovic, T.J. Schmidt, B.N. Grgur, H.A. Gasteiger, R.J. Behm, P.N. Ross. *J. Phys. Chem.*, **103**, 8568 (1999).
40. N.M. Markovic, B.N. Grgur, C.A. Lucas, P.N. Ross. *J. Phys. Chem. B*, **103**, 487 (1999).
41. K. Bleakley, P. Hu. *J. Am. Chem. Soc.*, **121**, 7644 (1999).
42. C. Zhang, P. Hu, A. Alavi. *J. Am. Chem. Soc.*, **121**, 7931 (1999).
43. E. Yeager, *J. Molecular Catalysis*. **38**, 5 (1986).
44. E. Yeager, *Electrochimica Acta*, **29**, 1527 (1984).
45. A. Alavi, P.J. Hu, T. Deutsch, P.L. Silvestrelli, J. Hutter, *Phys. Rev. Lett.*, **80**, 3650 (1998).
46. H.-I. Lee, G. Praline, J.M. White, *Surf. Sci.*, **91**, 581 (1980).

47. H.A. Gasteiger, N. Markovic, P.N. Ross, E.J. Cairns. *J. Phys. Chem.*, **98**, 617 (1994).
48. P. Ferreira-Aparicio, A. Guerrero-Ruiz, I. Rodriguez-Ramos. *Appl. Catalysis A*, **170**, 177 (1998).
49. P. Ferreira-Aparicio, I. Rodriguez-Ramos, J.A. Anderson, A. Guerrero-Ruiz. *Appl. Catalysis A*, **202**, 183 (2000).
50. P. Freni, G. Calogero, S. Cavallaro. *J. Power Sources*, **87**, 28 (2000).
51. T.A. Zawodzinski, T. Springer, J.W. Bauman, T. Rockward, F. Uribe, S. Gottesfeld, *Electrochemical Society Proceedings*, **98-27**, 127 (1998)
52. J. Jur, A. Haug, J. W. Weidner, R. E. White, "The Effects of Temperature, Pressure and Humidity on the Oxygen Diffusion Coefficient and Solubility of a Proton Exchange Membrane," *under revision*.

## Appendix A: Derivation of Vogel's anode current density expression

The derivation of the current generated by the dissociation of  $H_2$  in terms of surface coverage of the Pt catalyst done by Vogel is presented here. The surface coverage of the adsorbed  $H_2$  is governed by the electrode potential given by the Nernst equation (23,31):

$$\varepsilon = E_v^0 + \frac{RT}{F} \ln \frac{\theta_M}{\theta_{MH}} \quad (0.44)$$

$E_v^0$  is the open circuit electrode potential,  $\varepsilon$  is the actual electrode potential and  $\theta_M$ ,  $\theta_{MH}$  are the empty sites and sites covered by adsorbed hydrogen, respectively. At equilibrium, this expression becomes:

$$E = E_v^0 + \frac{RT}{F} \ln \frac{1 - \theta_H}{\theta_H} \quad (0.45)$$

Where  $\theta_H$  is the number of sites occupied by adsorbed hydrogen at steady state. Using the relationships shown in (0.46) and (0.47)

$$\eta \equiv \varepsilon - E \quad (0.46)$$

$$\theta_{MH} + \theta_M = 1 \quad (0.47)$$

$\theta_{MH}$  can be solved for using equations (0.44) and (0.45) to give (0.48):

$$\theta_{MH} = \frac{\theta_H}{\theta_H + (1 - \theta_H) e^{F\eta/RT}} \quad (0.48)$$

This expression can then be substituted into the rate expression for  $\text{H}_2 \rightarrow 2\text{H}^+ + 2\text{e}^-$ . The current density generated is related to the rate of reaction (23) which is derived from the Tafel-Volmer reaction in equation (0.49):

$$j_{\text{H}_2} = r_{\text{MH}} nF = nF(k_{\text{at}} c_{\text{H}_2} \theta_{\text{M}}^2 - k_{\text{ct}} \theta_{\text{MH}}^2) \quad (0.49)$$

$k_{\text{at}}$  is the rate of adsorption of  $\text{H}_2$  onto the catalyst and  $k_{\text{ct}}$  is that constant for hydrogen desorption. The number of electrons generated,  $n$ , is 2 and  $c_{\text{H}_2}$  is the concentration of  $\text{H}_2$  along the ACR. At equilibrium no current is generated ( $j=0$ ) and the equation (0.50) is obtained for the exchange current density (23):

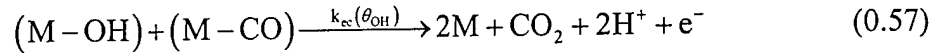
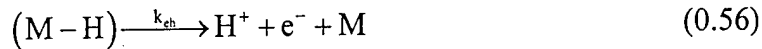
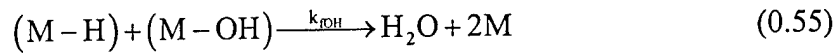
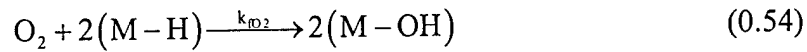
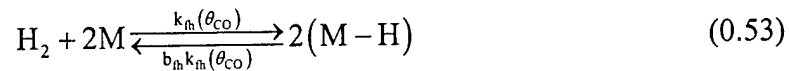
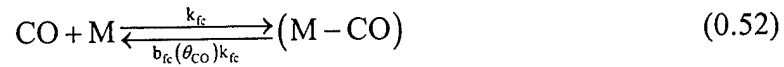
$$j_0 = 2Fk_{\text{at}} c_{\text{H}_2} \theta_{\text{M}}^2 = 2Fk_{\text{ct}} \theta_{\text{MH}}^2 \quad (0.50)$$

Noting that  $\theta_{\text{M}} = 1 - \theta_{\text{MH}}$ , the current density,  $j$ , can be solved for using (0.49) and (0.50), resulting in equation (0.51):

$$j = j_0 \left[ \frac{1}{\theta_{\text{H}} + (1 - \theta_{\text{H}}) e^{F\eta/RT}} \right]^2 \left( \frac{c_{\text{H}_2}}{c_{\text{H}_2}^0} e^{F\eta/RT} - 1 \right) \quad (0.51)$$

## Appendix B: Alternative H<sub>2</sub>/CO/O<sub>2</sub> Mechanism Incorporating $\theta_{OH}$

The following is the simplified mechanism that uses  $\theta_{OH}$  to determine the selectivity and effectiveness of O<sub>2</sub> usage.



$$\rho \dot{\theta}_{CO} = k_{fc} x_{CO} P_A (1 - \theta_{CO} - \theta_h - \theta_{OH}) - b_{fc} k_{fc} \theta_{CO} - k_{ec} e^{(\alpha_1 \theta_{OH})} e^{\left(\frac{V_a + V_N}{b_c}\right)} = 0 \quad (0.58)$$

$$\begin{aligned} \rho \dot{\theta}_h &= k_{fh} x_h P_A (1 - \theta_{CO} - \theta_h - \theta_{OH})^n - b_{fh} k_{fh} \theta_h^n - k_{fOH} \theta_{OH} \theta_h \\ &\quad - 2k_{eh} \theta_h \sinh\left(\frac{V_a + V_N}{b_h}\right) = 0 \end{aligned} \quad (0.59)$$

$$\begin{aligned} \rho \dot{\theta}_{OH} &= k_{fO_2} x_{O_2} P_A (1 - \theta_{CO} - \theta_h - \theta_{OH}) \theta_h - k_{fOH} \theta_h \theta_{OH} - k_{fOH} \theta_{OH} \theta_h \\ &\quad - 2k_{ec} \theta_{CO} e^{(\alpha_1 \theta_{OH})} e^{\left(\frac{V_a + V_N}{b_h}\right)} = 0 \end{aligned} \quad (0.60)$$

$$b_{fc} = b_{fc}^0 \exp\left(\theta_{CO} \frac{\delta(\Delta G_{CO})}{RT}\right) \quad (0.61)$$



$$k_{\text{fO}_2} = k_{\text{fO}_2}^0 \exp\left(\frac{E_{\text{O}_2}}{RT}\right) \quad (0.62)$$

$$b_{\text{fOH}} = b_{\text{fOH}}^0 \exp(\alpha_1 \theta_{\text{OH}}) \quad (0.63)$$

Like in the case where only CO and H<sub>2</sub> are present in the feedstream, first order hydrogen adsorption kinetics is used ( $n = 1$ ) for simplification of the model.

The critical element of this reaction mechanism is the usage of the hydroxyl group, M-OH. The production of M-OH beyond what occurs in a feedstream where only H<sub>2</sub> and CO are present is the result of the reaction shown in (0.53) – which is a simplification of O<sub>2</sub> adsorption and reaction with M-H. As O<sub>2</sub> adsorption is the rate-limiting step, that reaction coefficient is used for  $k_{\text{fO}_2}$  as shown in (0.62). Equations (0.13) and (0.14) have been combined, and since (0.14) occurs very quickly, the reaction rate is that of (0.13). In order for the model to simplify to the Springer model, the reverse reaction through which water dissociates in (0.16) is neglected. This is acceptable, because this phenomenon is taken into account by the base Springer model. CO oxidation through equation (0.17) has also been neglected in this reaction mechanism.

As it is the additional M-OH that gives rise to the added electrooxidation of CO, this has been incorporated into  $j_{\text{CO w/O}_2}$  as shown in (0.64).

$$j_{\text{CO w/O}_2} = 2k_{\text{ec}} \theta_{\text{CO}} e^{(\alpha_1 \theta_{\text{OH}})} e^{\left(\frac{V_a + V_N}{b_h}\right)} \quad (0.64)$$

This exponential term,  $e^{(\alpha_1 \theta_{\text{OH}})} \rightarrow 1$  as  $\theta_{\text{OH}} \rightarrow 1$ . This model assumes that  $\theta_{\text{OH}} \sim 0.0$  when no oxygen is present in the feedstream.

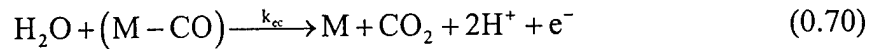
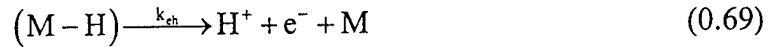
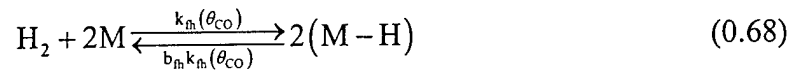
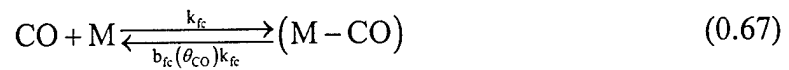
## Appendix C: Springer's Model

They have developed separate expressions for hydrogen and CO electrooxidation occurring on from the surface of the Pt anode:

$$j_h = 2k_{eh}\theta_h \sinh\left(\frac{V_a + V_N}{b_h}\right) \quad (0.65)$$

$$j_{CO} = 2k_{ec}\theta_{CO}e^{\left(\frac{V_a + V_N}{b_c}\right)} \quad (0.66)$$

where  $j_h$  and  $j_{CO}$  are the local electro-oxidation current densities for  $H_2$  and CO,  $\theta_h$  and  $\theta_{CO}$  are the surface coverages of  $H_2$  and CO, respectively,  $V_a$  and  $V_N$  are the anode and Nernst potentials,  $k_{eh}$  and  $k_{ec}$  are the electrooxidation rate constants for  $H_2$  and CO, and  $b_c$  and  $b_h$  are the Tafel slopes for  $H_2$  and CO electro-oxidation, respectively. While the expression for  $j_h$  doesn't directly contain  $\theta_{CO}$ , they are related through the coverage expressions and are based on the simplified reaction mechanism developed by Springer for an anode feed containing  $H_2$  and CO as shown below (32):



$$\rho \dot{\theta}_{CO} = k_{fc}x_{CO}P_A(1 - \theta_{CO} - \theta_h) - b_{fc}k_{fc}\theta_{CO} - k_{ec}e^{\left(\frac{V_a + V_N}{b_c}\right)} = 0 \quad (0.71)$$

$$\rho \dot{\theta}_h = k_{fh} x_h P_A (1 - \theta_{CO} - \theta_h)^n - b_{fh} k_{fh} \theta_h^n - 2k_{eh} \theta_h \sinh\left(\frac{V_a + V_N}{b_h}\right) = 0 \quad (0.72)$$

$$b_{fc} = b_{fc0} \exp\left(\theta_{CO} \frac{\delta(\Delta G_{CO})}{RT}\right) \quad (0.73)$$

$$k_{fc} = k_{fc}^0 \exp\left[-\frac{\delta(\Delta E_h)}{RT} \left(1 - e^{\left[\frac{p\theta_{CO}}{1-\theta_{CO}}\right]}\right)\right] \quad (0.74)$$

where  $n = 1$  or  $2$  ( $1^{st}$  or  $2^{nd}$  order),  $k_{fc}$ ,  $k_{fh}$ ,  $b_{fc}k_{fc}$ , and  $b_{fh}k_{fh}$  are the forward and reverse rate constants and are functions of  $\theta_{CO}$  and  $\theta_h$  as shown in equations (0.73) and (0.74). In this work  $k_{fc}$  is kept constant.  $P_A$  is cell pressure,  $x_{CO}$  and  $x_h$  are mole fraction of  $H_2$  and  $CO$  respectively,  $b_h$  and  $b_c$  are the natural Tafel slopes for  $H_2$  and  $CO$  electro-oxidation respectively.

This model is both rigorous in the description of the PEMFC anode catalyst region and allows for the simulation of V-I curves that may be compared to existing data. The model takes into account cell temperature, pressure, hydrogen concentration and  $CO$  concentration. The original model is two dimensional, considering effects both through the cell and along the channel. However, only the 1-D (through the cell) version is used described here. Thus, the Springer model chosen as a basis to develop a model for describing the Ru Filter.

These kinetic expressions are integrated into the overall model. The model considers the PEM fuel cell as three separate regions as shown in Figure 20.

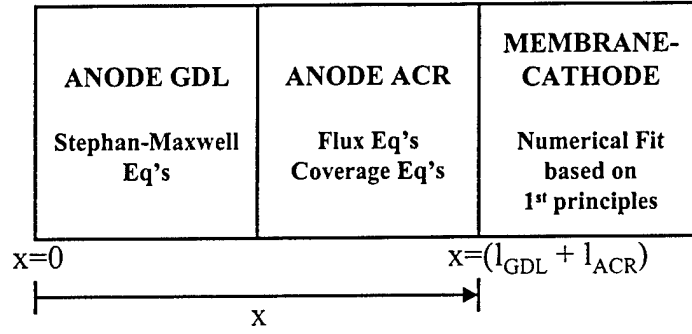


Figure 20 The Springer model sees the PEMFC as an anode GDL, active catalyst region (ACR) and a membrane-cathode region.

The flux equations for the anode active catalyst region (ACR) are given in equations (0.75) - (0.80):

$$\frac{\partial^2 x_h}{\partial z^2} = \frac{j_h}{I_{Dh}} \quad (0.75)$$

$$I_{Dh} = \frac{2FP_a T_s D_h}{P_s V_s T}; \quad x_h|_{ACR} = x_h|_{GDL}; \quad \left. \frac{\partial x_h}{\partial z} \right|_{ACR/MEM} = 0 \quad (0.76)$$

$$\frac{\partial^2 x_{CO}}{\partial z^2} = \frac{j_{CO}}{I_{DCO}} \quad (0.77)$$

$$I_{DCO} = \frac{2FP_a T_s D_{CO}}{P_s V_s T}; \quad x_{CO}|_{ACR} = x_{CO}|_{GDL}; \quad \left. \frac{\partial x_{CO}}{\partial z} \right|_{ACR/MEM} = 0 \quad (0.78)$$

$$\frac{\partial^2 V_a}{\partial z^2} = \frac{(j_h + j_{CO})}{\sigma l_{ACR}} \quad (0.79)$$

$$\left. \frac{\partial V_a}{\partial z} \right|_{GDL/ACR} = 0; \quad V_a|_{ACR/MEM} = V_{ANODE} \quad (0.80)$$

The membrane-cathode portion of the model is represented by the experimental relationship developed by Kim et al (35) as shown in equation (0.81). The membrane-

cathode potential,  $V_{std}$ , is calculated based on overall current density,  $J_{tot}$ , and then used to relate the anode potential,  $V_{ANODE}$ , to the cell potential,  $V_{cell}$ , in (0.82).

$$V_{std} = K_1 - K_2 J_{tot} - K_3 \ln(J_{tot}) - K_4 \exp(K_5 J_{tot}) \quad (0.81)$$

$$V_{ANODE} = V_{std}(J_{tot}) - V_{cell} \quad (0.82)$$

The constants used in this work to calculate  $V_{std}$  are given in Table 2 below:

Table 2: Values for the Membrane-Cathode Relationship

Symbol	Value	units
K1	0.795	V
K2	0.1895	V cm <sup>2</sup> A <sup>-1</sup>
K3	0.0176	V
K4	4.54 x 10 <sup>-4</sup>	V
K5	4.59	cm <sup>2</sup> A <sup>-1</sup>

Thus, cell performance curves can then be calculated that take into account the losses from the various regions as shown in Figure 21.

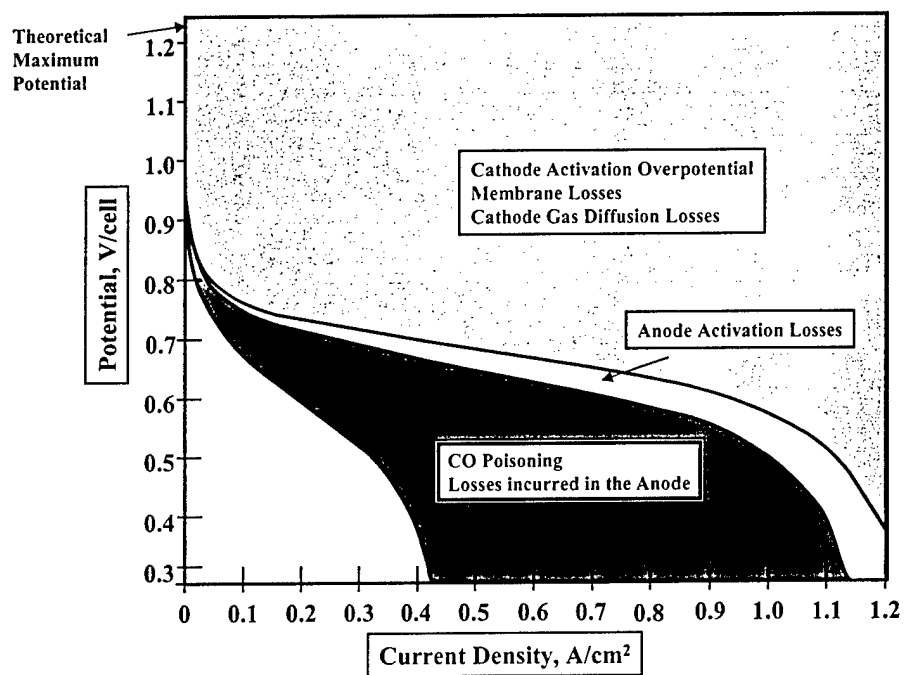


Figure 21 The various PEMFC performance losses taken into consideration by the Springer model are represented above. This model focuses primarily on the anode activation losses and losses due to the addition of CO to the anode feed stream.

## **Appendix D: Model Source Code**

**APPENDIX 3 - MODEL HELP FILES**

A Methanol Reformer VTB Model dated 11/15/00

“Simulink” Interface VTB Models dated 6/23/01

“Fuel Cell 12.15\_010716” VTB model dated 7/16/01

Metal Hydride Bed VTB Model dated 3/18/02

i VanePumpli VTB Model dated 6/10/02



## A Methanol Reformer VTB Model

Author: Ramakrishna Gundala

Date: 11/15/00

Model name: Reformer

DLL name: CReformer

Version number: 1.0

Report errors or changes to: [vtb@engr.sc.edu](mailto:vtb@engr.sc.edu)

### Pictorial Representation

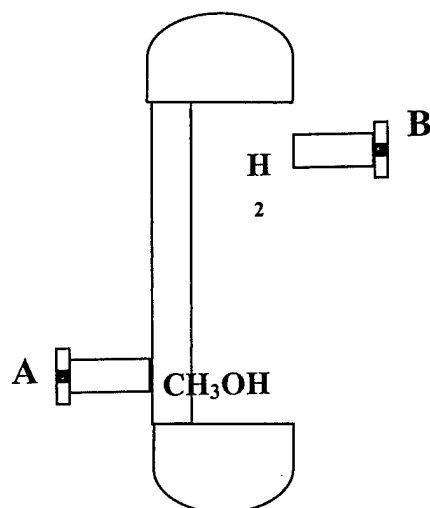


*Figure 1*

### Brief Description of Model

This is a CSTR model of the reformer. The temperature of the catalyst bed, methanol conversion and the pressure inside the reactor change with time but do not vary within the reformer. External heat input to the reformer is also included to control the reformer bed temperature at the desired value.

### Validity Range and Limitations

The reformer is designed to operate for steam to methanol ratio of 0.5 to 2.0, 150<sup>0</sup> C to 266<sup>0</sup> C temperature and 2 to 3 bar pressure.

## Terminals and Connectivity Information

This model has the following terminals.

Terminal Designation	Description
A	Input for steam and methanol mixture
B	Output for hydrogen, CO and CO <sub>2</sub> and unused methanol

## Parameters and Output Variables

This is a complete list of user accessible parameters. SI units are used throughout.

Parameter	Description	Default Value	Units
$Pow_d$	Required Power	1000	KW
$T_d$	Operating Temperature	266	<sup>0</sup> C
$P_d$	Operating Pressure	3	atm.
$S / M$	Steam to Methanol Ratio	1.1	-
$x_d$	Design Conversion of methanol	0.95	-
$T_0$	Initial temperature of reformer bed	266	<sup>0</sup> C
$UA_s$	Heat transfer conductance	3.99	Watts/ <sup>0</sup> C
$F_0$	Methanol feed rate for a 1MW system	3.30	moles/s

The following variables are computed within the model and are user accessible.

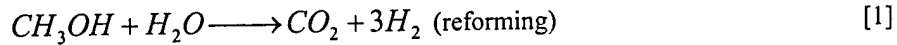
Variable Name	Units
Operating Temperature	<sup>0</sup> C
H <sub>2</sub> produced	moles
Weight of the bed	Kg
Fraction of CO in the reformer exit stream	-
Fraction of methanol converted	-
Power delivered	Watts
Heat requirement of the reformer	KJ/s
Pressure at the reformer outlet	atm.
Total methanol into the reformer	moles/s

## Assumptions in Model Derivation

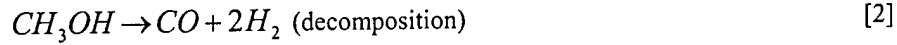
The reformer is assumed to be a CSTR model i.e. the temperature, concentrations variations inside the bed are neglected. The heat input to the reformer is assumed to be provided by a proportional controller that is within the reformer and is not shown explicitly.

## Mathematical Description of Model

Methanol (methyl alcohol) is catalytically steam reformed via the overall reaction:



Some portion of methanol also decomposes directly to CO via the reaction:



The rates  $r_1$  and  $r_2$  of the above reactions can be described adequately as

$$r_1 = -k_1 C_M \quad [3]$$

$$r_2 = -k_2 \quad [4]$$

where  $C_M$  stands for the methanol concentration and  $k_1$  and  $k_2$  are the rate constants which are functions of temperature and pressure as given below.

$$k_1 = \frac{(A_1 + B_1 \log(\frac{S}{M}))}{P_d C_1} \exp(-\frac{E_1}{R(T_d + 273)}) \quad [5]$$

$$k_2 = \frac{A_2 \exp(-\frac{E_2}{R(T_d + 273)})}{P_d C_2} \quad [6]$$

At constant temperature and pressure, the concentration of methanol as a function of the conversion ratio  $x$  can be expressed as

$$C_M(x) = (1-x) \frac{1 + \frac{S}{M}}{1 + \frac{S}{M} + 2x} C_M(0) \quad [7]$$

Combining equations (3) and (7) reaction rate  $r_1$  can be written as

$$r_1(x) = (1-x) \frac{1 + \frac{S}{M}}{1 + \frac{S}{M} + 2x} r_1(0) \quad [8]$$

The weight of the reformer can be easily obtained as a function of the methanol conversion ( $x$ ) after doing some simple algebra and is given as

$$W(x) = F[(\frac{U}{Z} + \frac{2Y}{Z^2}) \ln \frac{Y}{Y - xZ} - \frac{2x}{Z}] \quad [9]$$

Where, for simplicity, we use  $U = 1 + S/M$ ,  $r_1^0 = r_1(0)$  and  $r_2^0 = r_2(0)$ .  $Y = U(r_1^0 + r_2^0)$  and  $Z = Ur_1^0 - 2r_2^0$ .

The total output flow equals  $(1 + S/M + 2x)F$  and the  $H_2$  flow  $3xF - r_2^0 W(x)$

Rate of heat generation within the reformer due to the reaction is given by

$$\dot{Q}_{gen} = -(xF - k_2 W(x))\Delta H_{rxn1} - k_2 W(x)\Delta H_{rxn2} \quad [10]$$

Where  $\Delta H_{rxn1}$  is the enthalpy change of the reaction 1 and  $\Delta H_{rxn2}$  is the enthalpy change of reaction 2.

The heat balance gives

$$\dot{Q}_{ext} = \sum_{i=1}^5 F_{out\_i} C_{p_{out\_i}} (T - T_r) - \sum_{i=1}^2 F_{in\_i} C_{p_{in\_i}} (T - T_r) - \dot{Q}_{gen} \quad [11]$$

Where  $out\_i = (CH_3OH, H_2O, H_2, CO_2, CO)$ ,  $in\_i = (CH_3OH, H_2O)$ ,  $C_{p_i}$  is the heat capacity of component  $i$  and  $T_r$  is the reference temperature.

A proportional controller is used to regulate the reformer temperature according to the law,

$$\dot{Q}_{ext} = UA_s(T_s - T) \quad [12]$$

## Example of Model Use

In figure 2, the reformer is connected to a constant methanol source at the input and a  $H_2$  tank at the output.

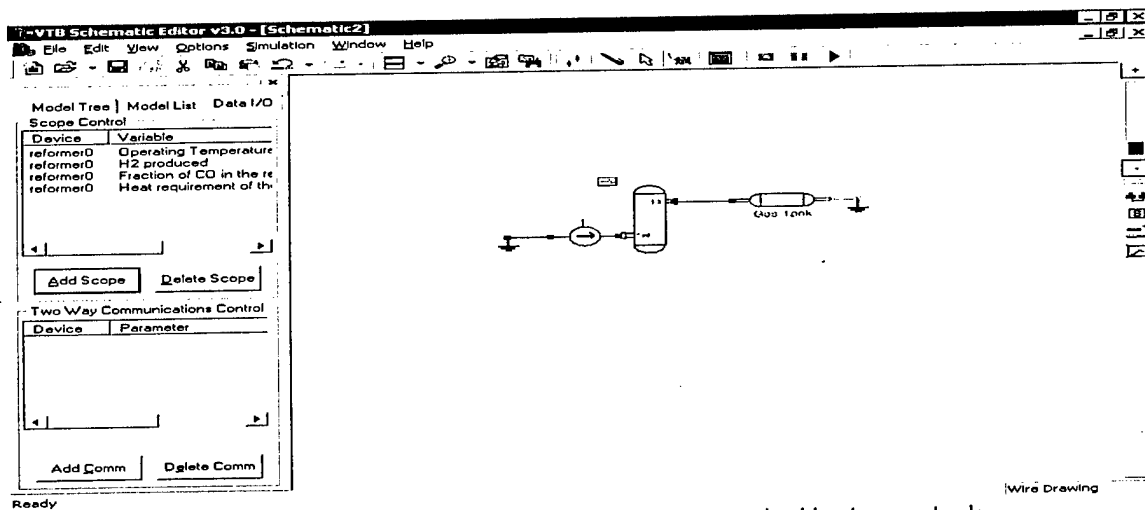


Figure 2: The reformer model connected to methanol source and a  $H_2$  storage tank.

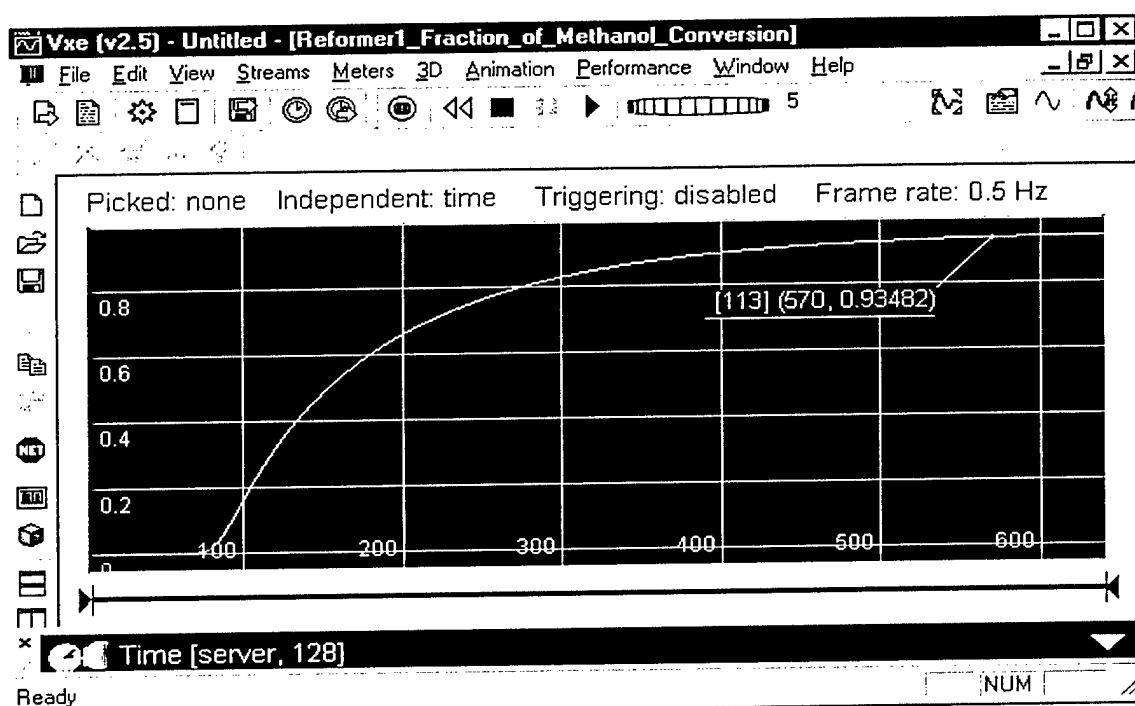


Figure 3. The fractional conversion of methanol in the reformer bed changes as a function of temperature. Final value is 0.95

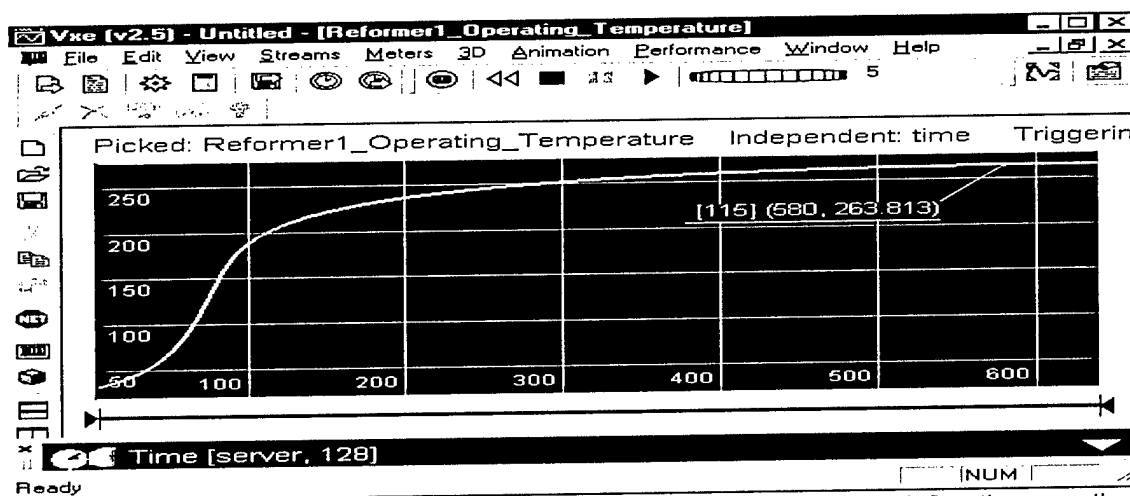


Figure 4. The temperature rise of the reformer bed from room temperature, 30 C to the operating temperature, 266 C with time.

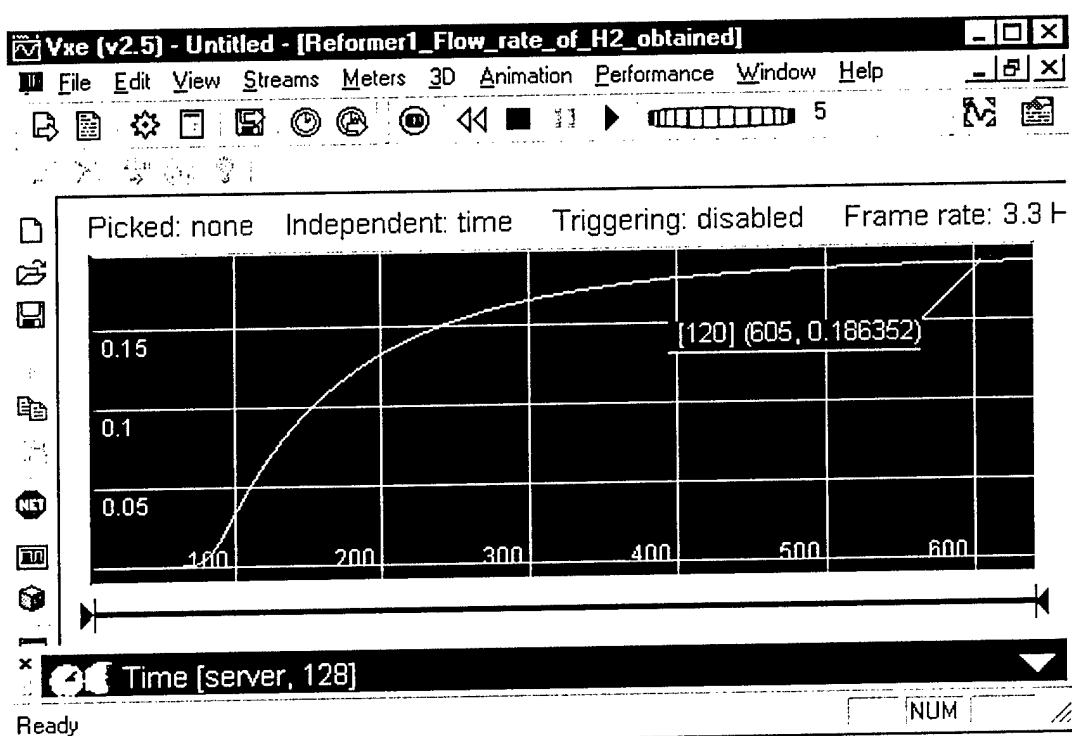


Figure 5.  $H_2$  obtained from the reformer exit in moles/s. Steady state value is 0.187 moles / s

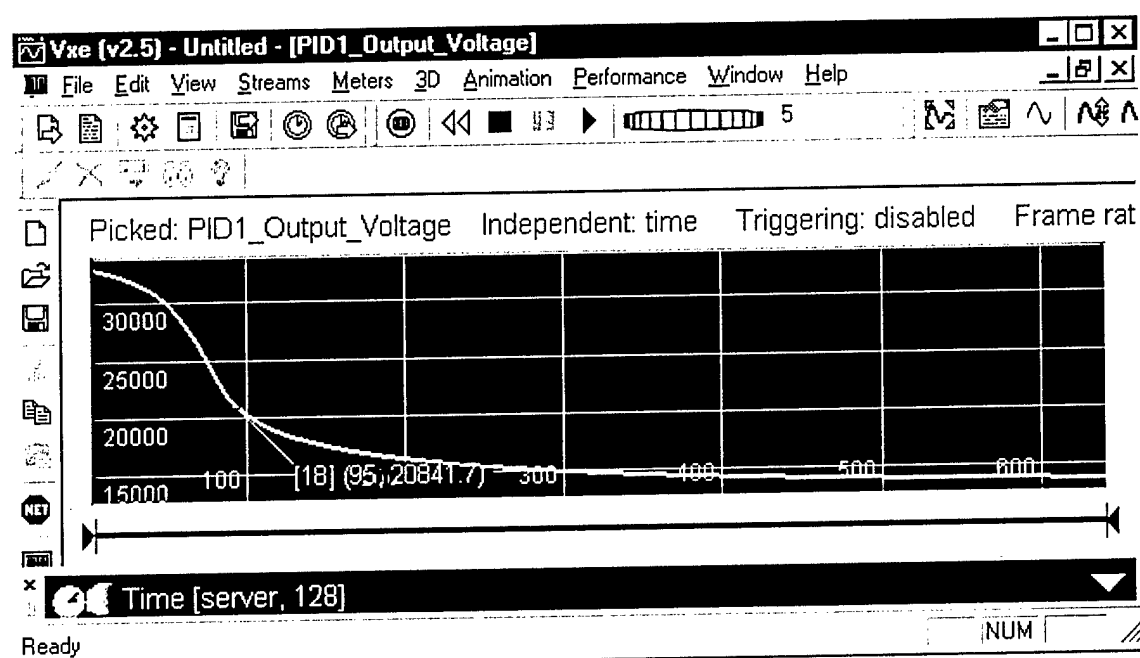


Figure 6. The heat input into the reformer. The steady state value is 81.69

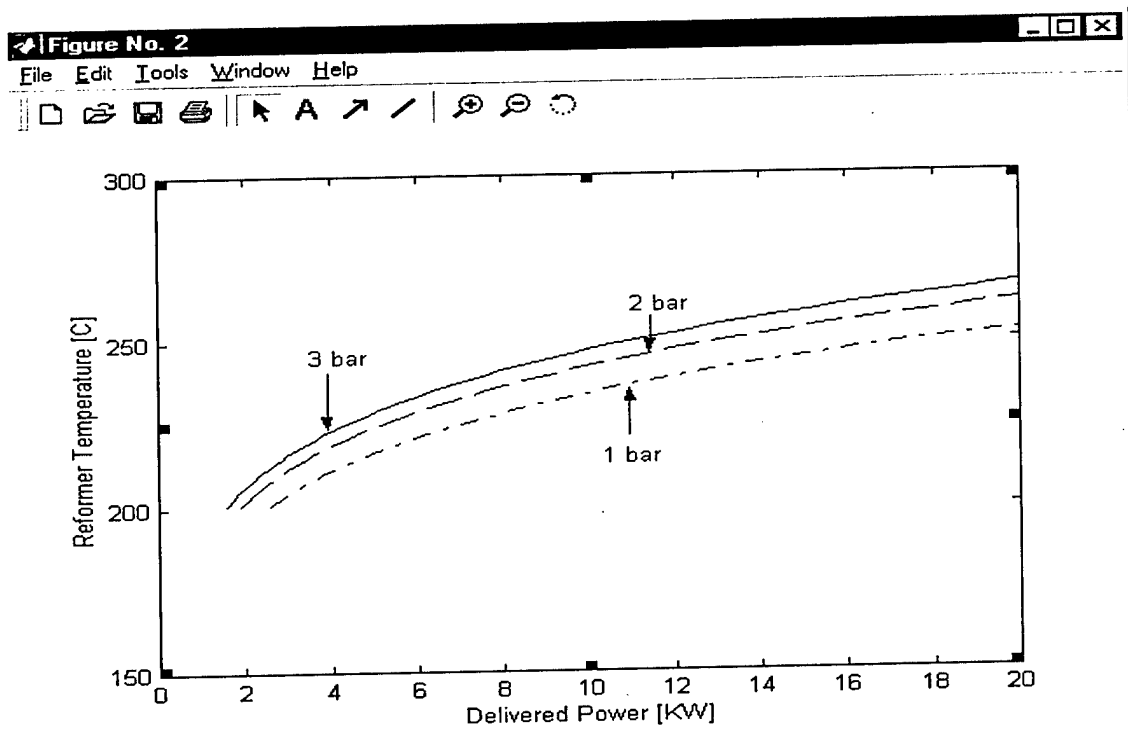


Figure 7: Operating temperature of methanol reformer below 20 KW design power at fixed reforming efficiency of 95 %. Operating pressure (- . - . -) 1 bar, (- - - -) 2 bar and (-----) 3 bar.

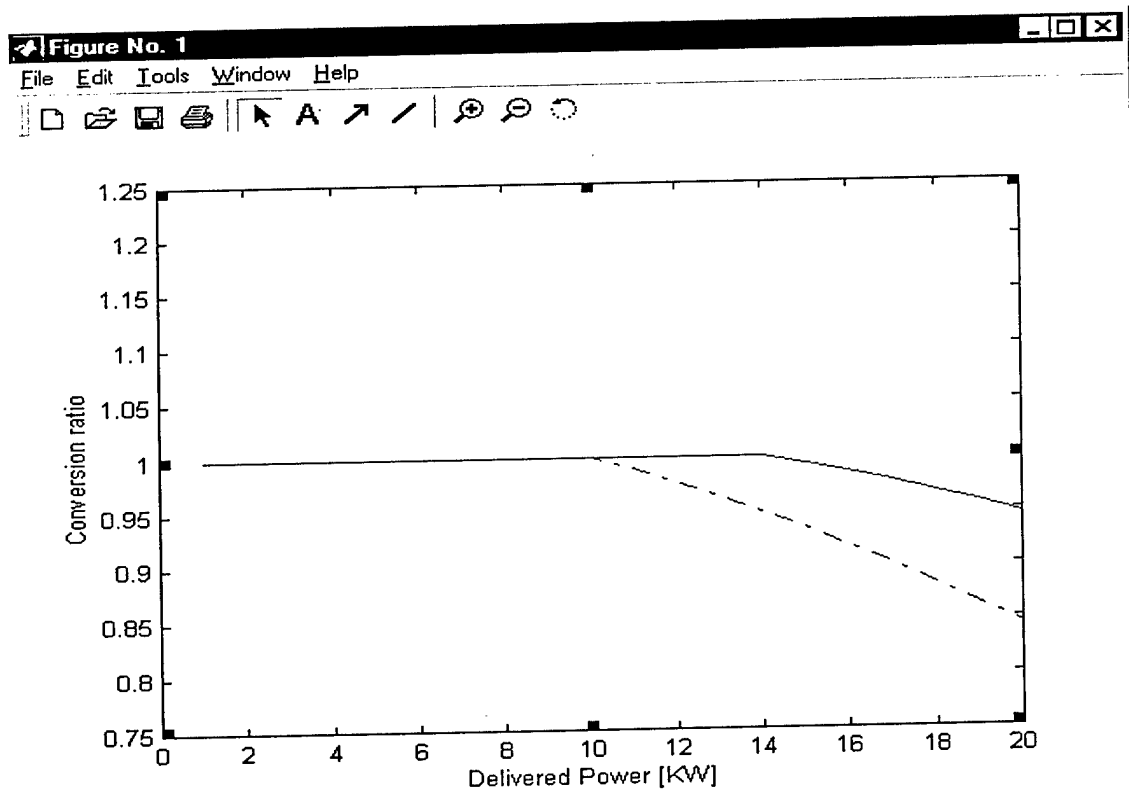


Figure 8. Conversion ratio of methanol in a reformer designed for 20 KW power at (- . - . -)  $x = 0.85$  or at (-----)  $x = 0.95$ .

## Model Validation

To validate the model, simulations were performed under different conditions and the results obtained conformed to the behavior of the reformer model along the expected lines. For example, the starting temperature is assumed to be 300 C and the reformer takes about 10 minutes to reach the steady state value. The simulations gave good results for a range of design temperatures, power requirements, and pressures.

## References

- [1] George Cokkinides and Ben Becker, "RC and AC Models in the VTB Domain Solver", Ver. 1.00, 1998, <http://vtb.engr.sc.edu/intranet/>
- [2] RABOU LPLM, "Modeling of a Variable-Flow Methanol Reformer For A Polymer Electrolyte Fuel-Cell", *Int J Hydrogen Energ.* 20 (10): 845-848 Oct 1995



## "Simulink" Interface VTB Models

Author: Teems Lovett, Antonello Monti

Date: June 23, 2001

Model name: 5in\_5out Simulink

DLL name: simulink55.dll

Version number: 2.0

Report errors or changes to: [lovett@engr.sc.edu](mailto:lovett@engr.sc.edu) or [monti@engr.sc.edu](mailto:monti@engr.sc.edu)

### Installation of Simulink Models

In order to install and use the Matlab-Simulink interface models there is a set of instructions that must be followed. These instructions include the setup to use Matlab remotely from VTB. Once these steps are accomplished then adding more Matlab-based interface models is simple and does not require repeating these steps.

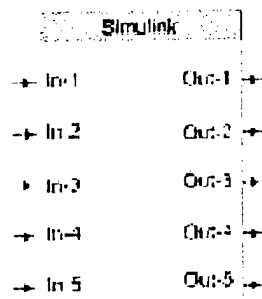
- Step 1. Copy the following DLL's from the Matlab installation folder on the host computer into the installation folder of the Virtual Test Bed. The DLL's must be copied into the directory with the VTB and Model Manager executables. The DLL's will be located in the bin folder of the Matlab installation path.

libeng.dll  
libmat.dll  
libmi.dll  
libmx.dll  
libut.dll  
libmatlbmx.dll

- Step 2. Download the calcsim.p from the model library web page and place this file into the same directory as step #1.

- Step 3. Start Matlab and set the same directory as used in steps #1 and #2 as a permanent path for Matlab.

### Pictorial Representation of Model



### Brief Description of Model

VTB-Simulink interface uses and requires a registered copy of Matlab to be loaded onto the host computer. The input ports are modeled as infinite impedance loads. The output ports are modeled as ideal voltage sources connected to ground. The VTB-Simulink interface requires a Simulink .mdl file to be located in an active or permanent path of Matlab. For this specific model the file is Test55.mdl. The voltages at the inputs of the VTB model are sent into the input ports of the Simulink file. The magnitude of the ideal output voltage sources is with respect to the outputs received from the Simulink file. Every time-step the

Simulink file is executed from Matlab and solved for the time difference between the previous time value and the present time value.

## Model Validity Range and Limitations

The VTB-Simulink models are restricted to the necessity of certain Matlab DLLs being located in the executable directory of the schematic editor. Also the loading of the VTB-Simulink models requires the Matlab DLLs being either in the working directory of Model Manager or the location of the DLL to be added to the database. A Simulink .mdl with the correct name and number of inputs and output is required to be in a working directory of Matlab.

The validity range of the VTB-Simulink models depends on the meeting of requirements and the validity of the Simulink file being interfaced into.

## List of Model Pins with Connectivity Information

Pin Designation	Description
N-input	Infinite impedance input nodes
N-output	Ideal voltage sources

## List of Parameters and Output Variables

This is a complete list of all parameters of the model. All models use SI units.

Parameter Name	Description	Default Value	Units
Iterations-skipped	Number of VTB iterations to be preformed before executing one step of the Simulink model.	1	NA

This is a list of output variables.

Variable Name	Description	Units
None	None	NA

## Assumptions in Model Derivation

Infinite impedance inputs and ideal voltage source outputs connected to ground.

## Mathematical Description of Model

The heart of the communication protocol with the Simulink solver is the Matlab engine. The Matlab engine allows data exchange between Matlab and C/C++ custom software. The interface is realized by a dedicated class inside the VTB architecture. This class manages the following procedure:

- At simulation start the VTB-class calls the Matlab engine
- The VTB calls a null-time execution of the target Simulink model. The result of this step is the calculation of the Simulink model size in terms of state variables, input and output number.
- At every step the VTB calls a step execution of the Simulink model giving as input the required data and receiving back the data for the next step
- The output is inserted in the input vector of the RCM

This data exchange is implemented by the authors via a dynamically linked library object and new Matlab commands that run through the Matlab engine a simulation step of the target Simulink model. A great advantage of this solution from the user viewpoint is the possibility to interact directly during the simulation both with the VTB Schematic Editor and the Simulink user interface. Parameters can be changed on the fly in both the environments thereby speeding up any testing activity.

## Example of Model Use

### A Vector Control of permanent magnet linear motor

This example is a vector control for a permanent magnet linear motor. As per the theory described previously, the power plant is described using VTB native models while the control is described by means of a Simulink model. In Figure 1 the VTB model is introduced.

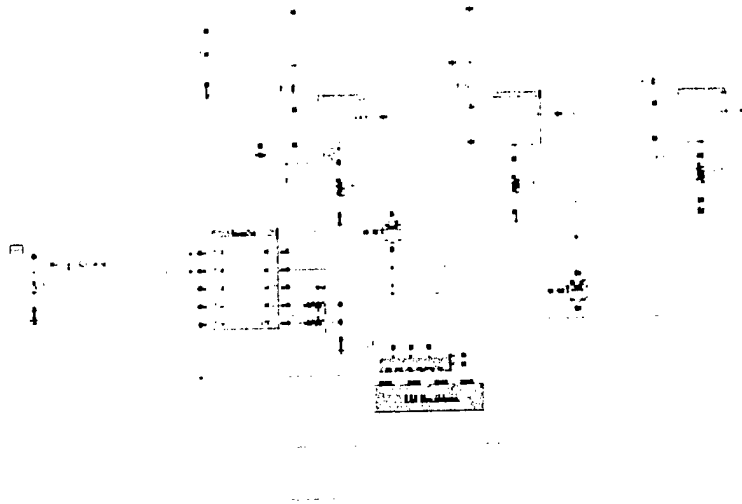


Figure 1: The VTB model used as example

The "Matlab Model" block represents the n-port (5-port) interconnection previously introduced.

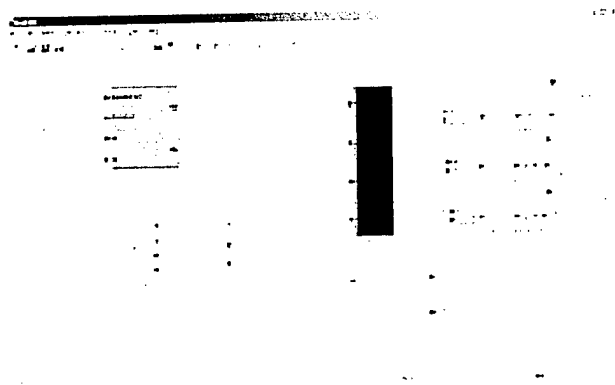


Figure 2: The correspondent Simulink file (test55.mdl)

Note that if you are not using all the 5 inputs or outputs as real variables for the Simulink program, you still have to declare 5 input and 5 output ports in the Simulink schema.

### Model Validation

Figure 3 shows a 3D visualization obtained at simulation time. In this case the speed is controlled to follow reference signal that is determined by means of the programmable source. The transient dynamics are apparent.

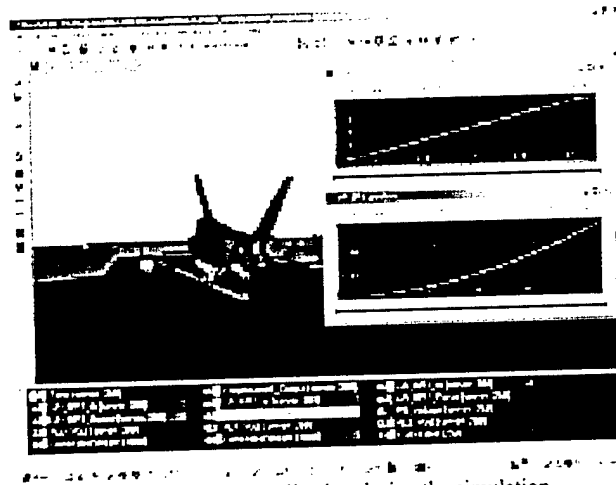


Figure 3: A 3D visualization during the simulation

## References

MATLAB online help documents

## "Fuel Cell 12.15\_010716" VTB Model

Author: Mark J. Blackwelder

Date:07/16/01

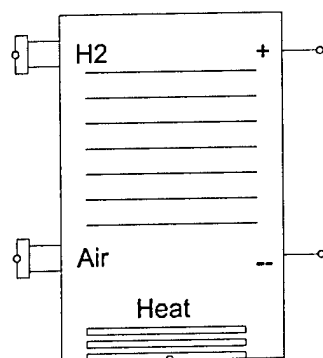
Model name: FC\_12

DLL name: Fuel\_Cell\_12\_010716.dll

Version number: 12.15

Report errors or changes to: [blackwel@enr.sc.edu](mailto:blackwel@enr.sc.edu)

### Pictorial Representation



### Brief Description

The fuel cell model imitates the operation of a polymer electrolyte membrane fuel cell. This includes the electrochemical voltage-current relationship, heat production, fuel and air consumption, and temperature and pressure dependence.

### Validity Range and Limitations

The model is valid only for current sourced. If current is forced against the electrochemical potential, then the results are invalid. For example, this model does not electrolyze water. The results are also invalid for pressure and temperature ranges outside of the experimental data used to fit the empirical parameters. For the default case, pressure outside the 7.4-30PSIG range, and temperature outside of the -10 to 60 degree Celsius range, are invalid. Also, note that air is consumed, not just oxygen. When mixed material streams are integrated into VTB, this will be modified such that oxygen is consumed, and the characteristics are dependent on the partial pressure of oxygen. The thermal transfer by mass streams is considered negligible.

### Terminals and Connectivity Information

This model has the following terminals.

Terminal Designation	Description
+	Positive electrochemical potential terminal
--	Negative electrochemical potential terminal
H2	Hydrogen fuel connection
Through Variable	Moles/Second
Across Variable	Pascals
Air	Air mass stream connection
Through Variable	Kilograms/Second

Heat	Thermal generation and transfer terminal
Through Variable	Watts
Across Variable	Degrees Celsius

## Parameters and Output Variables

This is a complete list of user accessible parameters. SI units are used throughout.

Parameter Name	Description	Default Value	Units
Open circuit potential per cell ( $E_o$ )	Depends on fuel and oxidant used	1000	millivolts
Exponential Squared pressure dependent term ( $n_o$ )	The portion of the exponent that is dependent on the square of the pressure	-2.843678952E-13	cm <sup>2</sup> /milliamp/pascal <sup>2</sup>
Exponential Linear pressure dependent term ( $n_1$ )	The portion of the exponent that is linearly dependent on the pressure	1.162035969E-7	cm <sup>2</sup> /milliamp/pascal
Exponential constant term ( $n_2$ )	The constant portion of the exponent	-6.390737001E-3	cm <sup>2</sup> /milliamp
Logarithmic Squared temperature dependent coefficient ( $b_o$ )	The portion of the logarithm that is dependent on the square of the pressure	3.091E-3	millivolts/cell/degree Kelvin <sup>2</sup>
Logarithmic Linear temperature dependent coefficient ( $b_1$ )	The portion of the logarithm that is linearly dependent on the pressure	-2.0524	millivolts/cell/degree Kelvin
Logarithmic Constant coefficient ( $b_2$ )	The constant portion of the logarithm	398.57	millivolts/cell
Resistive Squared temperature dependent coefficient ( $r_o$ )	The portion of the resistance that is dependent on the square of the temperature	1.5168E-5	Ohms/degree Kelvin <sup>2</sup> *cm <sup>2</sup> /cell
Resistive Linear temperature dependent coefficient ( $r_1$ )	The portion of the resistance that is linearly dependent on the temperature	-1.0024E-2	Ohms/degree Kelvin*cm <sup>2</sup> /cell
Resistive Constant coefficient ( $r_2$ )	The constant portion of the resistance	1.9202	Ohms*cm <sup>2</sup> /cell
Exponential Squared pressure dependent coefficient ( $m_o$ )	The portion of the exponential coefficient that is dependent on the square of the temperature	1.314167823E-11	millivolts/cell/Pascals <sup>2</sup>
Exponential linear pressure dependent coefficient ( $m_1$ )	The portion of the exponential coefficient that is linearly dependent on the temperature	-7.331599169E-6	millivolts/cell/Pascals
Exponential constant coefficient ( $m_2$ )	The constant portion of the exponential coefficient	1.046788384	millivolts/cell

BEST AVAILABLE COPY

Cell Area ( $A_{\text{cell}}$ )	The active area of the membrane electrode assembly	292	$\text{cm}^2$
Number of cells ( $N_{\text{cell}}$ )	The number of cells stacked in series	60	No Units
Heat Creation ( $U_o$ )	Higher Heating value of the $\text{H}_2\text{-O}_2$ chemical reaction, 1.23 if water vapor is the end product, 1.482 if liquid water	1.482	Joule-second/mole
Newton Steps	Maximum number of iterations to attempt to find a voltage-current operating point	25	No Units

The following variables are computed within the model and are user accessible.

Variable Name	Description	Units
Current Supplied	Amount of current sourced from fuel cell	Amps
Voltage	Fuel cell electrochemical potential of positive terminal with respect to negative terminal	Volts
Air Consumed	Amount of "air" consumed by chemical reaction	Kg/second
H2 Consumed	Amount of $\text{H}_2$ consumed by chemical reaction	Moles/second
Electrical Power out	Power supplied by fuel cell electrical terminals	Watts
Heat Power out	Power expelled by thermal terminal	Watts
Electrical Conductance	Nonlinear electrical conductance of fuel cell	Mhos

## Assumptions in Model Derivation

The thermal transfer by material streams is negligible. Water management effects on performance are negligible. This is not always the case. Air is consumed. This will be replaced by consumption of oxygen and performance dependence on partial pressure of oxygen, when VTB allows mixed material stream connections. This will also allow for thermal balance of material streams.

## Mathematical Description of Model

For each cell of a fuel cell stack,

$$E_{\text{cell}} = E_o - b \cdot \log(I) - r \cdot I - m \cdot e^{n \cdot I}$$

$E_o$  is the standard potential of reaction for  $\text{H}_2\text{-O}_2$  reaction.  $b$  and  $r$  are functions of temperature. And,  $m$  and  $n$  are functions of pressure. Assuming that each cell has equivalent potential, the current for the complete stack can be found using iterative methods. Thus the overall equation for the electrical terminals is:

$$V = N_{cell} \cdot \left[ E_o - (b_0 \cdot t^2 + b_1 \cdot t + b_2) \cdot \text{Log} \left( \frac{I}{A_{cell}} \right) - (r_0 \cdot t^2 + r_1 \cdot t + r_2) \cdot \left( \frac{I}{A_{cell}} \right) - (m_0 \cdot p^2 + m_1 \cdot p + m_2) \cdot e^{(n_0 \cdot p^2 + n_1 \cdot p + n_2)} \right]$$

Where I is the stack current, V is the stack voltage, t is the stack temperature, and p is the fuel/air pressure. All other variables are defined as model parameters above.

The mass flow is simply proportional to current and number of cells.

$$\dot{M} = N_{cell} \cdot K \cdot I$$

The proportionality constant K is in units of Kg/Coulomb for air, and Moles/Coulomb for hydrogen, and is fixed internally.

The total power contribution to the system from the reaction is:

$$\dot{Q} = q \cdot \Delta H = N_{cells} \cdot \left( \frac{\Delta H}{n \cdot F} \right) \cdot I = N_{cells} \cdot U_o \cdot I$$

Where  $U_o$  is the higher heating value of the reaction. The difference between this and the electrical power release is the thermal power that must be expelled. Thus, the thermal power expelled from the fuel cell stack is:

$$\dot{Q} = N_{cells} \cdot U_o \cdot I - V \cdot I$$

Where I is the stack current, V the stack voltage, and the other variables are defined above in the model parameters.

## Example of Model Use

The following Figures show a test schematic that can be used to evaluate parameter settings, and sample results.



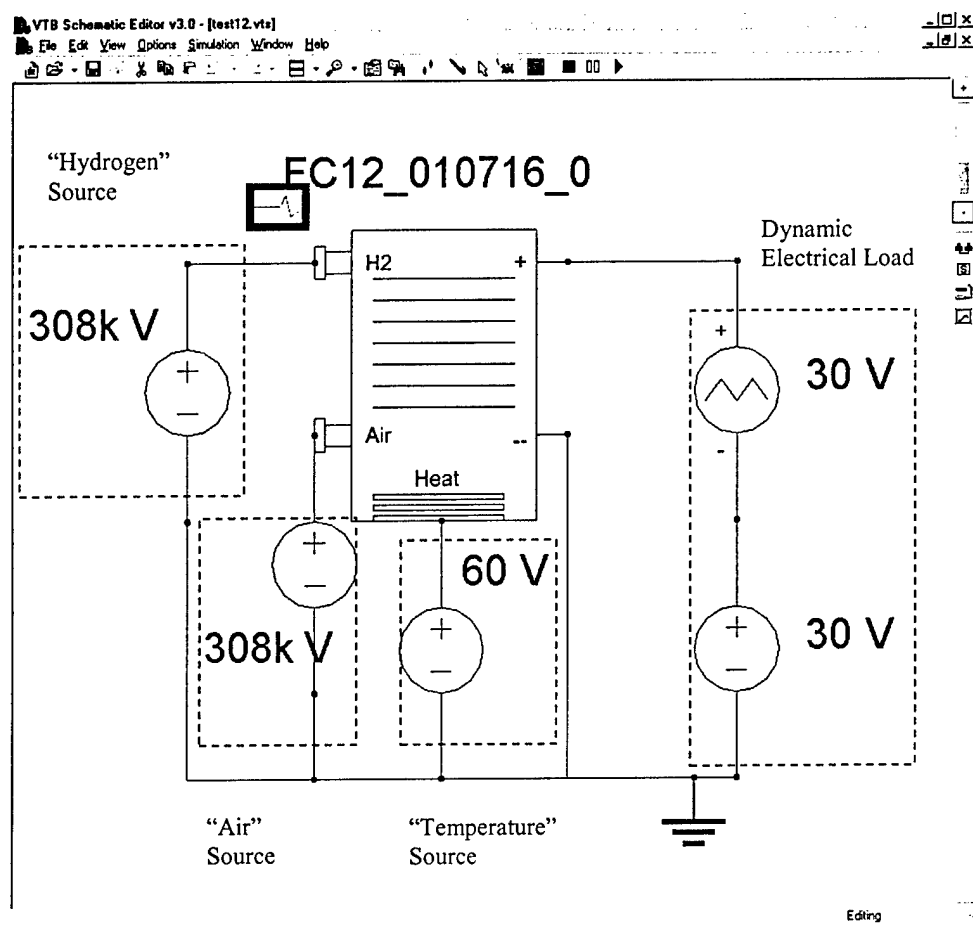


Figure 1 Test Schematic for Fuel\_Cell\_12.15\_010716

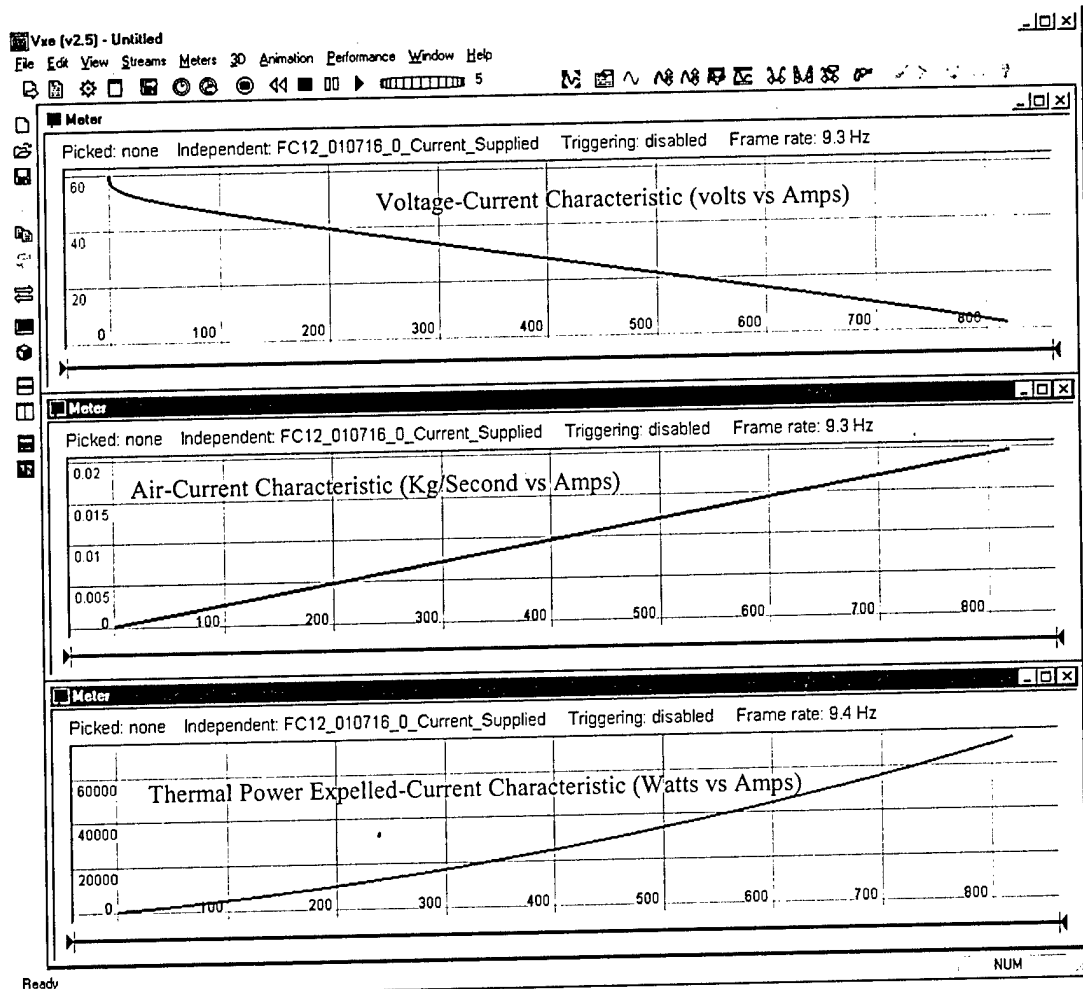


Figure 2 Test Schematic Results

## Model Validation

The model was compared with experimental data. An exact match is difficult to achieve, and will change with water management, construction materials, and construction methods. Therefore, the model only approximates actual performance characteristics of the desired fuel cell.

## References

## Metal Hydride Bed VTB Model

Author: Zhenhua Jiang

Date: 03/18/2002

Model name: HydrideBed

DLL name: HydrideBed\_020318.vtm

Version number: 1.0

### Pictorial Representation of Model

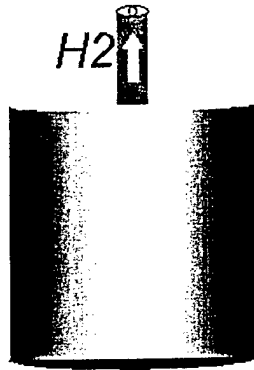


*Fig.1 Pictorial representation of constant flow source model*

### Brief Description of Model

This model represents the dynamics of the discharge of hydrogen from a cylindrical metal hydride bed. This model takes into account the heat exchange of metal hydride bed with the external heating/cooling system (Not included in the current version).

### Model Validity Range and Limitations

This model is valid to be used in a system level simulation. It can be connected in series with a gas pressure regulator downstream to provide hydrogen at a relatively constant pressure, for example, to the fuel cell. This model can be used for actual process design and hypothetical process feasibility, respectively. It can also be used to judge complexity of a particular hydrogen discharge process by comparing with experimental data.

### List of Terminals with Connectivity Information

Terminal Designation	Description
H2	Hydrogen mass flow terminal

## List of Model Parameters

Parameter Name	Description	Default Value	Units
Initial Pressure	Initial Pressure	1500000.0	Pa
Initial Temperature	Initial Temperature	298.0	K
Initial H2 concentration	Initial H2 concentration	1.059	Mol/mol
Radius	Radius of hydride bed	0.1	m
Length	Length of hydride bed	0.25	m
Porosity	Hydride bed porosity	0.4	-
Heat capacity of metal hydride	Heat capacity of metal hydride	10000.0	J/(mol.K)

## List of Output Variables

Parameter Name	Description	Units
Pressure	Pressure across the source	Pascal
Molar flow	Molar flow rate out of the terminal	Mol/second
Temperature	Temperature inside the hydride bed	K
H2 Concentration	H2 Concentration	Mol/mol

## Assumptions in Model Derivation

Ignored are various mass and heat transfer resistances in both the axial and radial directions and internal heat exchange with a circulating fluid. In this model, isothermal local equilibrium conditions prevail and the isotherm relationship is represented by a composite Langmuir model.

## Mathematical Description of Model

The set of equations below represent a simplified dynamic model of the discharge of hydrogen from a metal hydride bed [1-5].

$$\frac{1}{RT} \frac{\partial P}{\partial t} - \frac{P}{RT^2} \cdot \frac{\partial T}{\partial t} + \frac{\epsilon}{A \cdot L} + \frac{1-\epsilon}{\epsilon} \cdot \frac{\rho_s}{2M_{MH}} \cdot \frac{\partial q}{\partial t} = 0 \quad (1)$$

$$\left( \frac{P}{RT} C_{p_{H_2}} + \frac{1-\epsilon}{\epsilon} \rho_s C_{p_s} \right) \frac{\partial T}{\partial t} + \frac{\partial P}{\partial t} + \frac{1-\epsilon}{\epsilon} \frac{\rho_s}{2M} \Delta H \frac{\partial q}{\partial t} = 0 \quad (2)$$

$$\frac{\partial q}{\partial t} = k_q \cdot (q^* - q) \quad (3)$$

where both  $k_q$  and  $q^*$  are functions of  $P$  and  $T$  which are given by

$$k_q = 60 \times \frac{D_{H_2, MH0} e^{-\frac{E_D}{RT}}}{D_p^2} \quad (4)$$

$$q^* = \begin{cases} \frac{q_s \cdot (1 + b_{10} e^{-\frac{\Delta H_1}{RT}} \cdot P_s) \cdot \frac{P}{P_s}}{1 + b_{10} e^{-\frac{\Delta H_1}{RT}} \cdot P} & P \leq P_s \\ q_s + \frac{(q_{\max} - q_s) \cdot b_{20} e^{-\frac{\Delta H_2}{RT}} \cdot (P - P_s)}{1 + (P - P_s) \cdot b_{20} e^{-\frac{\Delta H_2}{RT}}} & P > P_s \end{cases} \quad (5)$$

$$P_s = e^{\frac{D_o + \Delta H_s}{RT}} \quad (6)$$

and the initial conditions are as follows:  $T = T_0$ ,  $P = P_0$ ,  $q = q_0 = q^*_0$ , for  $t = 0$ . Note that the explanation of the variables used here is given in Appendix 1.

## Model Validation

This is a simplified model that comes from a set of complex equations describing the dynamics of the hydrogen discharge from hydride bed. The model will be validated with the experimental data.

## Model Verification

The test bench consists of a constant flow source and hydride bed. The flow rate of the source is 1.0 mol/second. All the parameters are selected as the default values. The schematic diagram of the simulation system is shown in Fig.2.

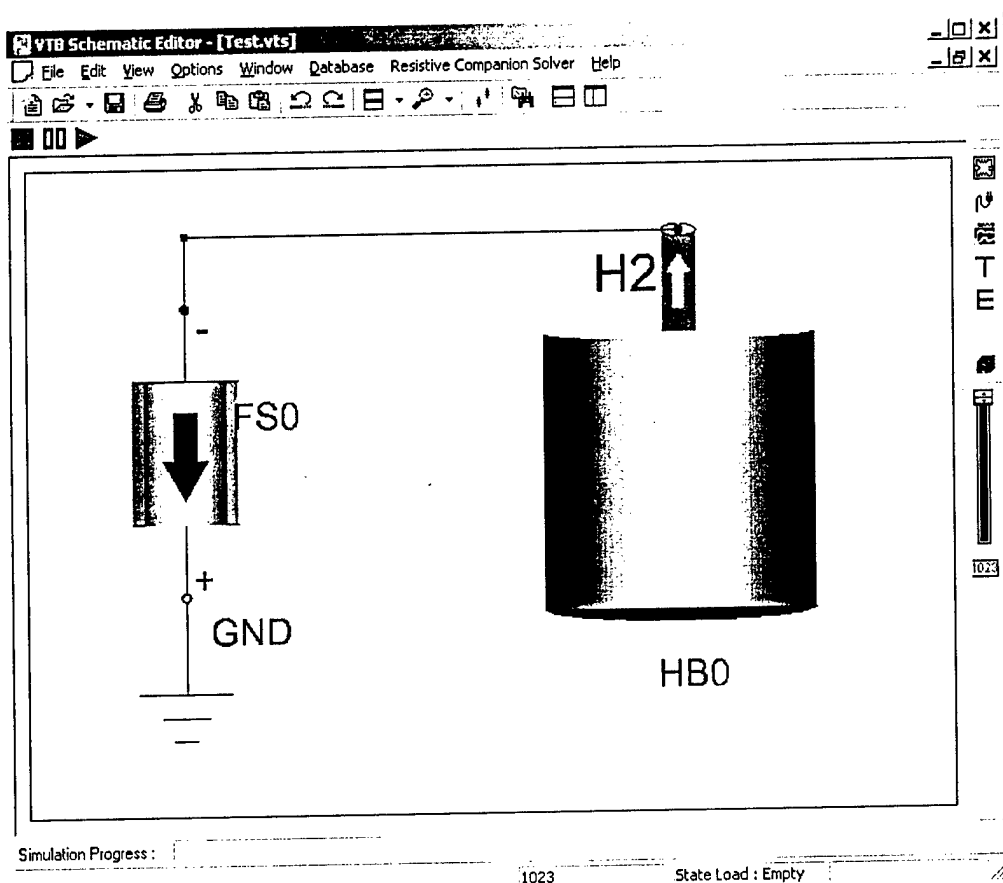


*Fig 2. Schematic diagram of the test system*

Fig 3 shows sample data from this system, including the pressure, temperature and molar flow rate of the hydride bed, H<sub>2</sub> concentration inside the hydride bed. From Fig 3, it is shown that the pressure declines rapidly initially from 15.0 atms and then decreases slowly after the pressure drops below 5.0 atms. It can also be seen that the temperature and H<sub>2</sub> concentration decrease linearly with the time when the molar flow is constant.

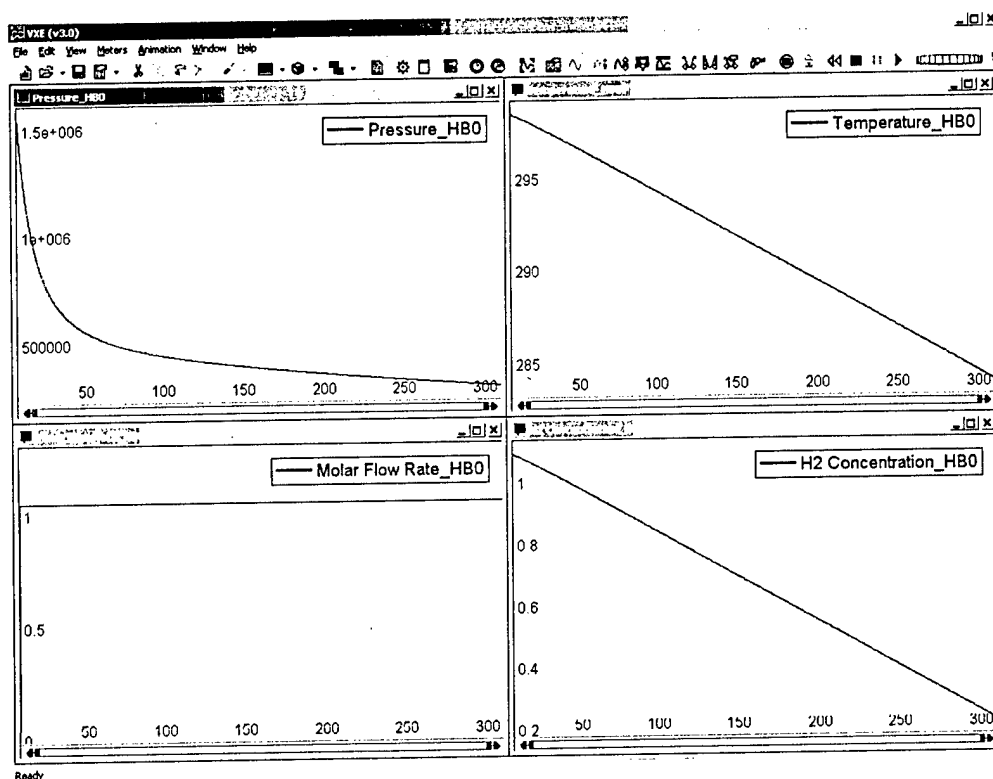


Fig 3. Simulation results of the test system

## Example of Model Use

See Model Verification Section.

## Reference

1. M. Ram Gopal, and S. Srinivasa Murthy, "Studies on Heat and Mass Transfer in Metal Hydride Beds", *International Journal of Hydrogen Energy*, Vol. 20, No. 11, pp.911-917, 1995.
2. Abdelmajid, Jemni, Sassi Ben Nasrallah, and Jilani Lamloumi, "Experimental and Theoretical Study of a Metal-Hydrogen Reactor", *International Journal of Hydrogen Energy*, Vol. 24, No. 7, pp631-644, 1999.
3. Soo-Geun Lee, Han-Ho Lee, Ki-Young Lee, and Jai-Young Lee, "Dynamic Reaction Characteristics of the Tubular Hydride Bed with Large Mass", *Journal of Alloy and Compounds*, Vol. 234, No. 1, pp.84-92, 1996.
4. Zhixiong Guo, Hyung Jin Sung, "Technical Note: Conjugate Heat and Mass Transfer in Metal Hydride Beds in the Hydriding Process", *International Journal of Heat and Mass Transfer*, Vol. 42, No. 2, pp379-382, 1999.
5. Malek Lamari, Asdin Aoufi, and Pierre Malbrunot, "Thermal Effects in Dynamic Storage of Hydrogen by Adsorption", *Environmental and Energy Engineering*, Vol. 46, No. 3, pp. 632-646, March 2000.

## Appendix 1. Variables used in the equations

$A$	Hydride bed cross sectional area, $m^2$
$b_{j(j=1,2)}$	Henry's law constant defined in Eq.( ), $Pa^{-1}$
$b_{j,0(j=1,2)}$	Temperature independent coefficient of the Henry's law constant, $Pa^{-1}$
$Cp_{H_2}$	Heat capacity of $H_2$ , $J/(Kg \cdot K)$
$Cp_s$	Heat capacity of the metal hydride, $J/(Kg \cdot K)$
$D_p$	Diameter of metal hydride particles, $m$
$E_D$	Armenians activation energy of the diffusion coefficient, $J/mol$
$k_q$	Mass transfer coefficient, $s^{-1}$
$L$	Hydride bed length, $m$
$M_{H_2}$	Molecular weight of $H_2$ , $kg/mol$
$M_{MH}$	Average molecular weight of metal hydride, $kg/mol$
$\dot{M}$	$H_2$ molar flow, $mol/s$
$P$	Pressure inside the hydride bed, <i>Pascal</i>
$P_0$	Pressure inside the hydride bed at the initial state, <i>Pascal</i>
$P_s$	Equilibrium pressure of $H_2$ in metal hydride at the envelop, <i>Pascal</i>
$q$	Concentration of hydrogen on the metal hydride bed, <i>mol <math>H_2</math>/mol metal hydride</i>
$q^*$	Equilibrium concentration of hydrogen on the metal hydride bed, <i>mol <math>H_2</math>/mol metal hydride</i>
$q_{max}$	Maximum equilibrium concentration of hydrogen on the metal hydride bed, <i>mol <math>H_2</math>/mol metal hydride</i>
$q_0^*$	Equilibrium concentration of hydrogen on the metal hydride bed at the initial state, <i>mol <math>H_2</math>/mol metal hydride</i>
$q_s$	Saturation concentration of hydrogen on the metal hydride bed at the low concentraion phase, <i>mol <math>H_2</math>/mol metal hydride</i>
$R$	Ideal gas constant ( $8.314 J/mol \cdot K$ )
$T$	Temperature inside the hydride bed, $K$
$T_0$	Temperature inside the hydride bed at the initial state, $K$
$\Delta H$	Isosteric heat of adsorption of the hydrogen in the metal hydride, $J/mol$
$\varepsilon$	Hydride bed porosity, dimensionless
$\rho_s$	Density of the metal hydride, $kg/m^3$



## 1 VanePump11 VTB Model

Author: Wei Jiang

Date: 06/10/02

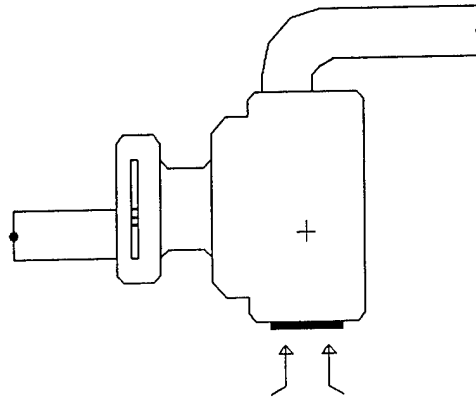
Model name: VanePump1

DLL name: VanePump1\_020610.dll

Version number:

Report errors or changes to: [jiangw@engr.sc.edu](mailto:jiangw@engr.sc.edu)

## Pictorial Representation



## Description

This model represents a rotary vane pump.

## Validity Range and Limitations

1. The vane pump model is only valid for small (Mass flow Rate is around  $6.0\text{E-}05$  kg/s) one-way vane pump.
2. The equations (1)(2) for pressure and pump efficiency are derived from experimental data for a specific pump (G12/04-E, see reference1). So this model is only valid for the Pumps similar to G12/04-E type.
3. For better performance, Rotational speed of shaft should be (2806 730) rad/s

## Terminals and Connectivity Information

This model has the following terminals.

Variable Name	Description	Type of variable	Units
Mass Flow Rate( $\dot{M}$ )	Mass Flow Rate of fluid	Through Variable	$\text{kg/s}$
Outlet Pressure ( $p$ )	Outlet Pressure of the pump	Across Variable	Pa
Torque( $\tau$ )	Input torque	Through Variable	$\text{N} \cdot \text{m}$
Rotational speed ( $\omega$ )	The rotational speed of shaft	Across Variable	$\text{radians/s}$

## Parameters and Output Variables

This is a complete list of user accessible parameters. SI units are used throughout.

Parameter Name	Description	Default Value	Units
Density( $\rho$ )	Density of the gas	1.205	$\text{kg/m}^3$

Gas constant ( $C_p$ )	Gas specific heat	1.005	$\text{kJ/kg K}$
Gas constant ( $k$ )	Gas specific heat ratio	1.4	No Units
Pressure atmosphere ( $p_0$ )	Pressure atmosphere	101000	$\text{pa}$
Temperature atmosphere ( $T_0$ )	Temperature atmosphere	25	$^{\circ}\text{C}$

The following variables are computed within the model and are user accessible.

Name	Description	Units
Torque	The torque applied to the Pump	$\text{N}\cdot\text{m}$
Rotational Speed	Rotational Speed of Pump	$\text{rad/s}$
Mass Flow Rate	Mass Flow Rate of fluid	$\text{kg/s}$
Pressure difference	Pressure difference of Pump	$\text{pa}$
Efficiency	The Efficiency of the Pump	No Units

## Assumptions in Model Derivation

1. The process in the vane pump is adiabatic.
2. Air is considered ideal gas.
3. Pressure difference is the function of mass flow rate and rotational speed.
4. Efficiency is the function of mass flow rate.

## Mathematical Description

For a vane pump the following equations encapsulate the useful pump characteristics:

$$\Delta p = a \cdot \dot{M}^2 + b \cdot \dot{M} + c \cdot \omega \quad (1)$$

$$\eta = d \cdot \dot{M}^2 + e \cdot \dot{M} + f \quad (2)$$

From the following data [1] we can obtain constant  $a, b, c$  and  $d, e, f$  when  $\omega$  is 471.23 rad/s.

Pressure (mbar)	0.0	68.9	103.4
Efficiency (NU)	0.02 %	9.5 %	14.07 %
Mass flow (kg/s)	10.27 E-05	6.032 E-05	3.95 E-05

We can get

$$a = -4.5782\text{E}+11$$

$$b = -9.8635\text{E}+07$$

$$c = 31.746$$

$$d = -7.5025\text{E}+06$$

$$e = -1.16\text{E}+03$$

$$f = 1.983\text{E}-01$$

From energy conversion law and ideal gas performance, we can get following equations

$$\tau \cdot \omega = \frac{\dot{M} \cdot c_p \cdot (T_2 - T_1)}{\eta}, \quad T_2 = T_0 \cdot \left( \frac{p_2}{p_0} \right)^{\frac{k-1}{k}} \quad (3)$$

$$\Delta p = p_2 - p_0 \text{-----Pressure difference}$$

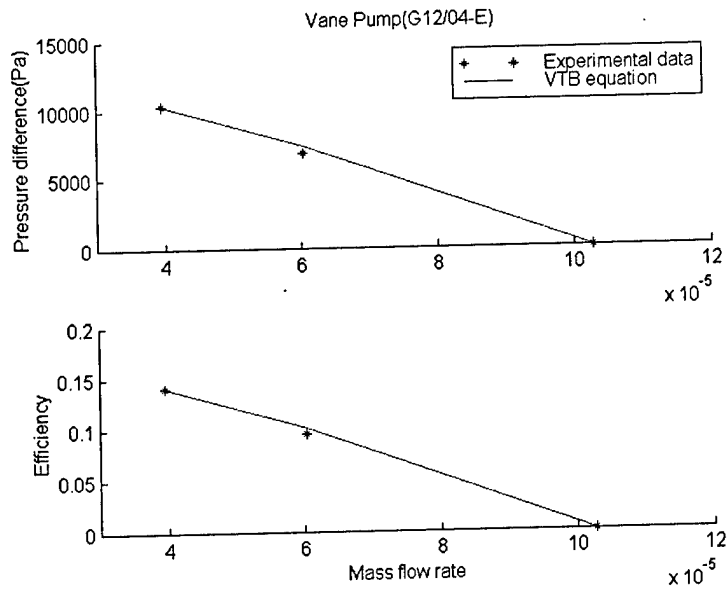
$$p_2 \text{-----Outlet pressure}$$

$$p_0 \text{-----Pressure atmosphere}$$

$$\dot{M} \text{-----Mass flow rate}$$

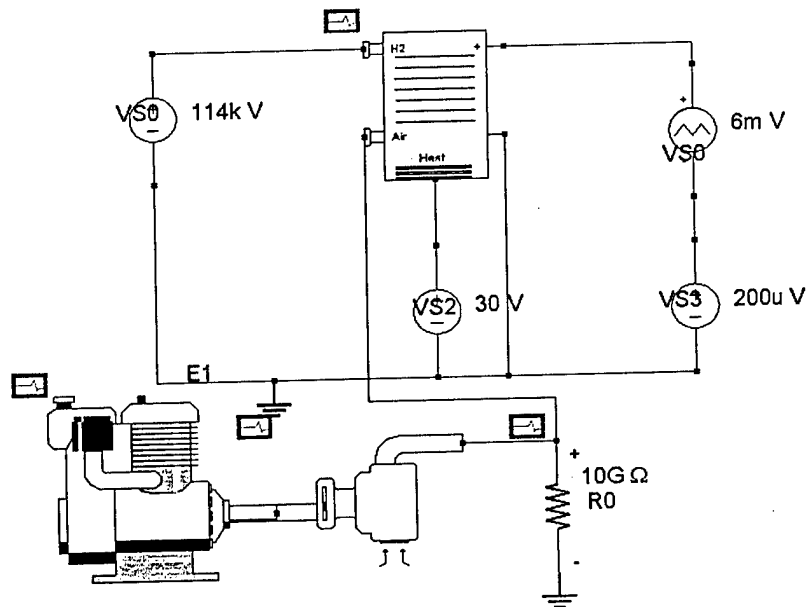
$\omega$	-----Rotational speed
$\eta$	-----Vane pump efficiency
$T_2$	-----Outlet temperature
$T_0$	-----Temperature atmosphere
$\tau$	-----Torque

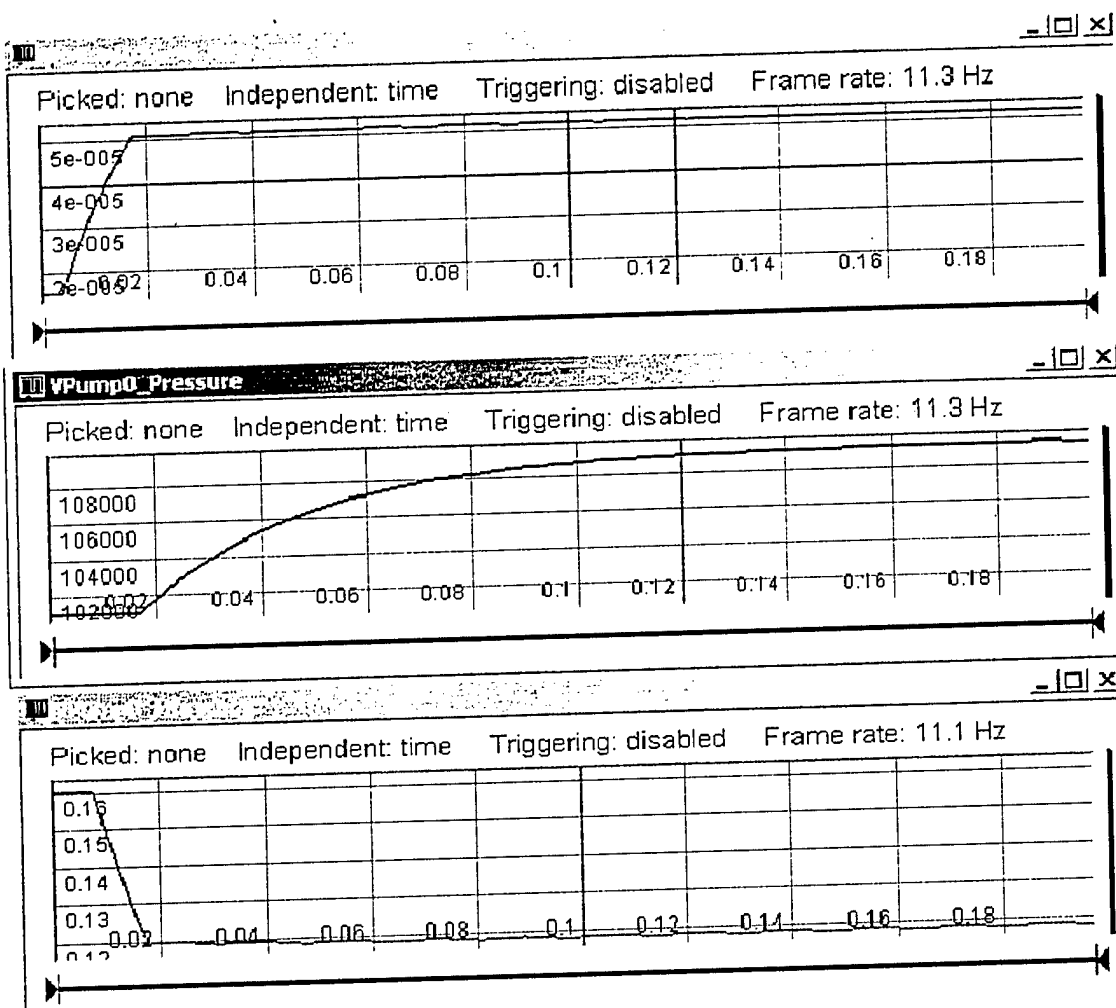
The following graphic is to compare experimental data with results from equations (1) (2).



## Example of Model Use

This example is to test the characteristics of air vane pump.





## Model Validation

In order to verify this Pump model, we compare VTB output results with Equations (1) (2) just as follows when  $\omega$  is 471 rad/s.

		4.6018E-05	5.4601E-05	6.7051E-05	8.6642E-05
Mass flow rate (kg/s)					
Output pressure(pa)	VTB	110444	109202	107281	103970
	Equa.	110450	109210	107290	103980
Efficiency	VTB	0.129	0.113	0.087	0.041
	Equa.	0.1290	0.1126	0.0868	0.0415

## References

1. iG04 SERIES performance data from THOMAS compressors & pumps Co.:  
<http://www.thomaspumps.com>
2. \\erv-vtb\VTB2002\_New\_Models\Zip\RotationalSpeedSource.zip

**APPENDIX 4 – PUBLICATIONS (COPIES ATTACHED)**

1. A. T. Haug, J.W. Weidner, R.E. White, and W. Huang **“Development of a Novel CO Tolerant Anode,”** *J. Electrochem. Soc.*, **149** (7) A862-A867 (2002).
2. A. T. Haug, J.W. Weidner, R.E. White, W. Huang, Steven Shi, Timothy Stoner, and Narender Rana, **“Using Sputter Deposition to Increase CO Tolerance in a PEM Fuel Cell,”** *J. Electrochem. Soc.*, **149** (7) A868-A872 (2002).
3. D. Tianping, J.W. Weidner, and R.E. White, **“Extension of Newman’s Method to Electrochemical Reaction-Diffusion in a Fuel-Cell Catalyst Layer,”** *J. Power Sources*, 107 (1), 24-33, 2002.
4. A. T. Haug, R.E. White, J.W. Weidner, W. Huang, Steven Shi, Timothy Stoner, and Narender Rana, **“Increasing PEM Fuel Cell Catalyst Effectiveness Through Sputter Deposition,”** *J. Electrochem. Soc.*, **149**, A280-A287 (2002).



## Development of a Novel CO Tolerant Proton Exchange Membrane Fuel Cell Anode

Andrew T. Haug,<sup>a,\*</sup> Ralph E. White,<sup>a,\*\*</sup> John W. Weidner,<sup>a,\*\*\*,z</sup>  
and Wayne Huang<sup>b</sup>

<sup>a</sup>Center for Electrochemical Engineering, Department of Chemical Engineering, University of South Carolina, Columbia, South Carolina 29208, USA

<sup>b</sup>Plug Power, Incorporated, Latham, New York 12110, USA

<sup>c</sup>Energy and Environment Applications Center, Institute for Materials, School of Nanosciences and Engineering, State University of New York at Albany, Albany, New York 12203, USA

Typically Pt is alloyed with metals such as Ru, Sn, or Mo to provide a more CO-tolerant, high-performance proton exchange membrane fuel cell (PEMFC) anode. In this work, a layer of carbon-supported Ru is placed between the Pt catalyst and the anode flow field to form a filter. When oxygen is added to the fuel stream, it was predicted that the slow H<sub>2</sub> kinetics of Ru in this filter would become an advantage compared to Pt and Pt:Ru alloy anodes, allowing a greater percentage of O<sub>2</sub> to oxidize adsorbed CO to CO<sub>2</sub>. With an anode feed of H<sub>2</sub>, 2% O<sub>2</sub>, and up to 100 ppm CO, the Pt + Ru filter anode performed better at 70°C than the Pt:Ru alloy. The oxygen in the anode feed stream was found to form a hydroxyl species within the filter. The reaction of these hydroxyl groups with adsorbed CO was the primary means of CO oxidation within the filter. Because of the resulting proton formation, the Ru filter must be placed in front of and adjacent to the Pt anode and must contain Nafion in order to provide the ionic pathways for proton conduction, and hence achieve the maximum benefit of the filter.  
© 2002 The Electrochemical Society. [DOI: 10.1149/1.1479726] All rights reserved.

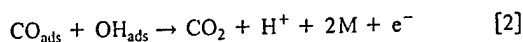
Manuscript submitted July 11, 2001; revised manuscript received January 11, 2002. Available electronically May 15, 2002.

Proton exchange membrane fuel cells (PEMFCs) are gaining popularity due to their benefits such as environmental friendliness and increased fuel efficiency. Because of the difficulties inherent to storing hydrogen, liquid fuels such as propane, natural gas, and gasoline are used to produce reformat gas. Dry reformat is typically composed of 35-45% hydrogen, 15-25% carbon dioxide, 50-10,000 ppm carbon monoxide, and a balance of nitrogen. It has been shown extensively that CO poisons the platinum catalyst used in PEMFC systems.<sup>1-3</sup> Carbon monoxide chemically adsorbs onto available Pt catalyst sites as shown in Eq. 1

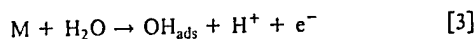


At concentrations as low as 10 ppm, CO lowers power output of the PEMFC-containing Pt electrodes by 50%.<sup>4,5</sup> The addition of a preferential oxidation (PROX) unit to the fuel processing system can reduce CO concentrations in the reformat gas stream to approximately 50 ppm. Attempts to find catalysts both tolerant to CO and equivalent in performance to Pt have led to the alloying of Pt with Ru, Mo, W, Co, Ir, Ni, and Sn.<sup>5-10</sup> Used by themselves as anode catalysts, these metals do not provide the high rate of hydrogen oxidation necessary to achieve the current densities that make PEMFCs competitive in the marketplace.<sup>7,11,12</sup> The most commonly used alloy is Pt:Ru. The Pt:Ru alloys combine the high catalyst activity of Pt with the increased CO tolerance of Ru.<sup>11-13</sup>

The oxidation of CO<sub>ads</sub> from the platinum catalyst surface in the anode shown in Eq. 2 has been found to follow Langmuir-Hinshelwood kinetics<sup>11,12</sup>



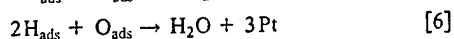
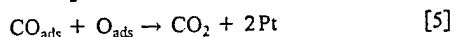
where M represents Pt or Ru. The reactions by which OH<sub>ads</sub> is formed on Pt and Ru are shown in Eq. 3<sup>14,15</sup>



The formation of OH<sub>ads</sub>, shown in Eq. 3, is the rate-determining step of this reaction and occurs on platinum at potentials of 0.7 V/RHE and above.<sup>12,14,15</sup> Ruthenium has the ability to form OH<sub>ads</sub>

from water at significantly lower potentials than Pt, 0.35 V for 50 atom % Ru, and 0.2 V for 90 atom % Ru.<sup>11,12,15</sup> This allows the catalytic desorption of CO as CO<sub>2</sub> to commence at lower potentials. There is a linear relationship between the onset of CO oxidation and Ru composition (i.e., the shift in potential is linear with respect to atomic fraction of Ru in the alloy). However, the benefit of alloying Pt with Ru has only been shown to provide near equivalent performance to pure H<sub>2</sub> on Pt for CO concentrations up to 100 ppm in the feed stream for low-temperature fuel cell PEMFC operation.<sup>2,6</sup>

The injection of oxygen into the fuel stream has also been shown to increase catalyst tolerance to CO.<sup>13,16</sup> This "air bleeding" provides a greater concentration of active oxygen on the catalyst that will then react with CO to form CO<sub>2</sub>. The following reactions are assumed to occur at the Pt catalyst surface (in addition to Eq. 1)



The goal of the addition of an air bleed to the anode feed is to promote the reaction shown in Eq. 5, the oxidation of CO<sub>ads</sub> to CO<sub>2</sub>. Note the difference between Eq. 2 and 5. The reaction of CO<sub>ads</sub> with OH<sub>ads</sub> on Pt requires an overpotential, and hence ionic contact to the cathode region (in the form of the Nafion electrolyte), whereas the reaction shown in Eq. 5 does not. One of the problems of adding O<sub>2</sub> to the gas inlet stream is that the reaction shown in Eq. 6 occurs at a much higher rate than the reaction shown in Eq. 5. Only about one of 400 O<sub>2</sub> molecules oxidizes CO<sub>ads</sub> to CO<sub>2</sub>.<sup>13</sup> This, and the fact that the mixture becomes combustible for concentrations of oxygen in hydrogen above 4 vol %, limits the amount of oxygen in the feed stream and limits the effectiveness of the air bleeding technique.

The first objective of this study was to determine if depositing a layer of carbon-supported Ru on top of a typical carbon-supported Pt anode (see Fig. 1) increases the effectiveness of the air-bleeding technique in preventing CO poisoning. By first coming in contact with Ru instead of Pt, it was speculated that a larger percentage of the O<sub>2</sub> in the H<sub>2</sub>/CO/O<sub>2</sub> feed will react with CO<sub>ads</sub> than in either a Pt or a Pt:Ru alloy electrode. The selectivity of Eq. 5 and 6 would then shift toward the oxidation of CO<sub>ads</sub>. Studies have shown that the rate of hydrogen oxidation on pure Ru at 62°C (roughly the operating temperature used in this experiment) was two orders of magnitude lower than that of Pt measured under similar

\* Electrochemical Society Student Member.

\*\* Electrochemical Society Fellow.

\*\*\* Electrochemical Society Active Member.

<sup>z</sup> E-mail: weidner@engr.sc.edu

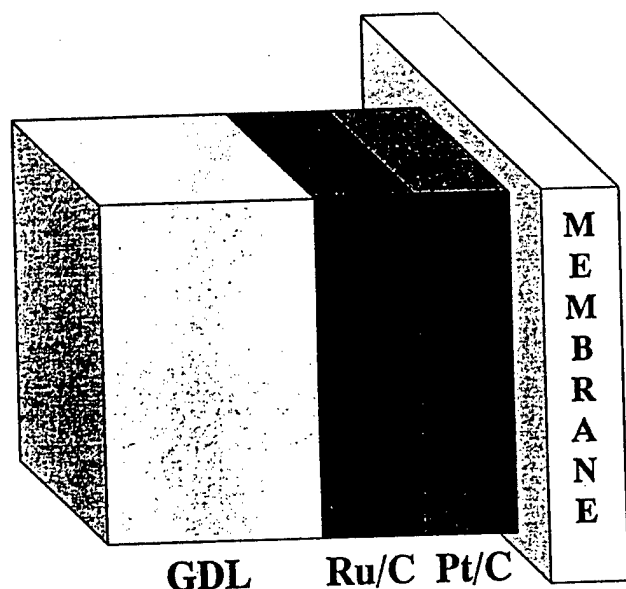


Figure 1. Diagram of the Ru-filtered anode. The feed gases pass through the GDL and come in contact with the Ru filter before reaching the Pt anode. The Ru filter acts as a chemical barrier on which  $O_2$  oxidizes the CO present in the feed stream to  $CO_2$ , preventing a loss in the Pt anode performance due to CO poisoning.

conditions.<sup>12</sup> CO has been shown to have similar adsorption strengths onto Ru as Pt.<sup>12,17-19</sup> Thus, the slow  $H_2$  kinetics of pure Ru would become an advantage, allowing a greater percentage of  $O_2$  to oxidize  $CO_{ads}$  to  $CO_2$  rather than reacting with adsorbed hydrogen to form water. Pt catalyst is then placed after Ru to oxidize  $H_2$  and maintain the high PEMFC performance.

The second objective was to characterize the mechanism of CO oxidation occurring within the Ru filter by varying the Nafion content (10 or 35 wt %) within it and its placement along the anode. The Ru filter can be placed between the gas diffusion layer (GDL) and Pt anode as shown in Fig. 1, or between the flow channels and the GDL. By varying the placement of the Ru filter, the role of Nafion electrolyte in CO oxidation could be determined.

### Experimental

**Development of Pt and Pt:Ru catalyst MEAs.**—The method described in Patent no. 5,211,984 provides an outline for NCI and membrane electrode assembly (MEA) manufacture in this project.<sup>20</sup> The Pt and Pt:Ru (1:1 atomic ratio) catalysts were bonded to the Nafion 112 proton exchange membrane (PEM) in several steps. These steps included the formulation of the catalyst inks, application of the inks to decals, and transference of the dried catalyst ink from the decal to the membrane. Inks were prepared for Pt and Pt:Ru by adding the E-TEK catalyst to a solution of 5 wt % Nafion (DuPont).

The components of the ink were added to an appropriate size bottle (evacuated with helium to avoid sparking) and then stirred for a minimum of 8 h to ensure uniformity of the ink. Three-ply Teflon decals were weighed prior to applying the application of the ink. The ink was drawn across the surface of the Teflon decals using a Meyer rod. The loadings of  $0.40 \text{ mg Pt/cm}^2$  (anode),  $0.61 \text{ mg Pt:Ru/cm}^2$ , and  $0.50 \text{ mg Pt/cm}^2$  (cathode) were achieved. The coated decals were then dried in an oven at  $105^\circ\text{C}$  and ambient pressure for 10 min to remove any remaining alcohols from the ink.

To form an MEA with an active area of  $50 \text{ cm}^2$ , decals coated with an anode and cathode were placed on either side of a Nafion 112 membrane (proton form). The assembly was then hot-pressed

Table I. Types of MEUs tested.

MEU name	Description
Pt (baseline)	0.4 mg Pt/cm <sup>2</sup> anode 0.5 mg Pt/cm <sup>2</sup> cathode Uncatalyzed Zoltek GDLs on anode and cathode
Pt:Ru	0.61 mg Pt:Ru/cm <sup>2</sup> anode 0.5 mg Pt/cm <sup>2</sup> cathode Uncatalyzed Zoltek GDLs on anode and cathode The atomic ratio of Pt to Ru in the Pt:Ru alloy is 1:1, resulting in an anode Pt loading of $0.4 \text{ mg/cm}^2$ .
Pt + Ru (Ru filter)	0.4 mg Pt/cm <sup>2</sup> anode 0.5 mg Pt/cm <sup>2</sup> cathode 0.21 mg Ru/cm <sup>2</sup> coated Zoltek GDL on the anode Uncatalyzed Zoltek GDL on the cathode side

for 2 min at  $205^\circ\text{C}$ . The assembly was cooled to room temperature before the decals were carefully peeled from the assembly, leaving an MEA.

**Development of the Ru filter.**—Ru filters on both the catalyst and flow channel sides of the GDL were studied. Ru inks containing 35 and 10% Nafion solids by weight, respectively, were prepared in a similar method to Pt and Pt:Ru catalyst inks. The ruthenium ink was applied to the microlayer side of an uncatalyzed Zoltek GDL with a cross-sectional area of  $50 \text{ cm}^2$ . A Meyer rod was used to achieve a target loading of  $0.21 \text{ mg Ru/cm}^2$ . After the Ru/C catalyst was applied, the GDLs were dried at  $105^\circ\text{C}$  and ambient pressure for 10 min. Ru filters placed on the flow channel side of the GDL were prepared in a similar manner and with identical loadings.

**Cell assembly and testing.**—The three types of  $50 \text{ cm}^2$  membrane-electrode units (MEUs) prepared and tested are shown in Table I.

The MEUs were placed in a  $50 \text{ cm}^2$  cell. The cell was assembled and incubated for 4–8 h at ambient pressure, cell temperature of  $70^\circ\text{C}$ , an anode feed of hydrogen, a cathode feed of air, and a stoichiometric ratio (actual flow/stoichiometric flow required for a  $1.0 \text{ A/cm}^2$  current) of 1.5 at the anode and 2.0 at the cathode. Single-cell performance curves were obtained under the conditions set in Table II.

An alternate test station was used to conduct trials using CO concentrations greater than 50 ppm ( $H_2$ ,  $H_2$  + 50 ppm CO,  $H_2$  + 100 ppm CO, and  $H_2$  + 200 ppm CO). The data attained on this station were consistent and reproducible, however, problems arising from excess water entering the test cell on these trials limit comparisons of this data to a qualitative nature.

### Results and Discussion

**Performance of the Ru filter.**—Figures 2 and 3 show the performance of a Pt:Ru and Pt + Ru filter anode under five different anode feeds: (i) hydrogen, (ii) reformat; (iii) reformat + 2%  $O_2$ , (iv) reformat + 1%  $O_2$ , and (v) reformat + 0.5%  $O_2$ . In the case of Pt:Ru, as the amount of oxygen in the feed is reduced, the performance decreases in a continuous fashion. For a Pt + Ru anode, there is very little difference in performance between reformat + 2%  $O_2$  and reformat + 1%  $O_2$ , but as the concentration of the oxygen in the reformat is reduced to 0.5%, there is a sudden drop in performance such that the performance curve resembles that of pure reformat. For conditions of 1–2%  $O_2$  (by volume of  $H_2$ ) addition to the reformat feed stream, the Pt + Ru filter performed better than the Pt:Ru alloy anode.

Figure 4 compares the cell performance of Pt, Pt:Ru, and Pt + Ru filter anodes under conditions of reformat + 1.0%  $O_2$  bleed. Under these conditions, the Ru filter outperforms a Pt:Ru

Table II. Fuel-cell test conditions.

Pressure	1 atm (anode and cathode)
Cell temperature	70°C
Stoichiometric ratio (at 1 A/cm <sup>2</sup> )	1.5 Anode (hydrogen) 2.0 Cathode (air)
Feedstreams	Anode: hydrogen, reformat, reformat + air bleed, H <sub>2</sub> + CO + air bleed Cathode: air
Dry reformat composition	40% H <sub>2</sub> 20% CO <sub>2</sub> 50 ppm CO balance N <sub>2</sub>
Humidification	Complete humidification of anode and cathode gas streams for all trials.
Air bleed	0.5, 1.0, 2.0% O <sub>2</sub> (in the form of an air bleed relative to the volumetric flow of hydrogen in slm).
CO amounts	50 ppm in reformat 50, 100, 200 ppm in H <sub>2</sub>

alloy anode of an identical loading by the greatest margin. At 0.6 V, the current density produced from the cell containing the Pt + Ru filter is almost double that of an identical cell using the Pt:Ru alloy. The Pt:Ru shows performance improvement over the plain Pt anode only at voltages below 0.5 V.

Conversely in Fig. 5, the cell performance of the Pt:Ru alloy for reformat + 0.5% O<sub>2</sub> shows the greatest tolerance to CO of the three anodes. At 0.6 V, the Pt:Ru cell provides 50% more current than the Pt + Ru filter. Both Ru-containing anodes do perform better than the pure Pt anode, but there is little benefit gained from using the Pt + Ru filter instead of a pure Pt anode. Similarly, in Fig. 6, with no air bleed in the reformat stream, the Ru filter shows performance resembling that of a pure Pt anode, while the Pt:Ru alloy anode exhibits some CO tolerance. In all cases these results were reproducible over several trials using different MEAs of identical loadings.

Thus, without sufficient oxygen in the anode feed to oxidize CO to CO<sub>2</sub>, the CO penetrates the Ru filter and poisons the Pt region of the anode. A representation of this is shown in Fig. 7 where the

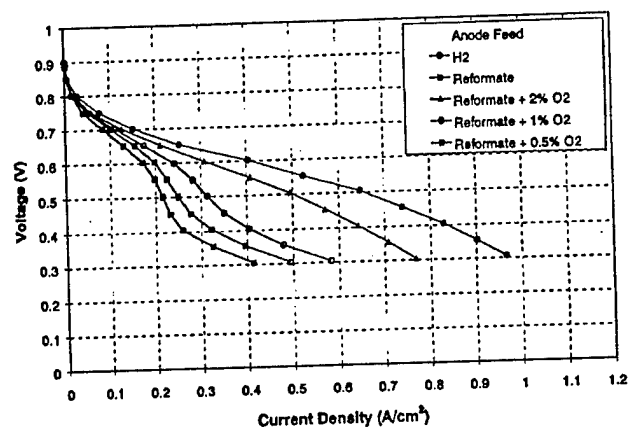


Figure 2. Single-cell performance comparison of Pt:Ru for various anode feeds.  $P = 1$  atm,  $T = 70^\circ\text{C}$ .

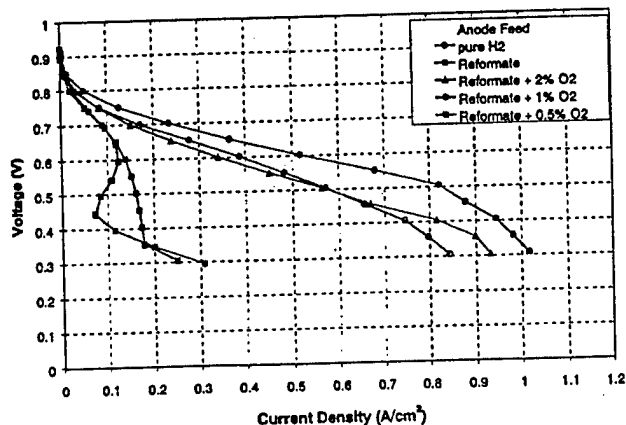


Figure 3. Single-cell performance comparison of the Pt + Ru filter for various anode feeds.  $P = 1$  atm,  $T = 70^\circ\text{C}$ .

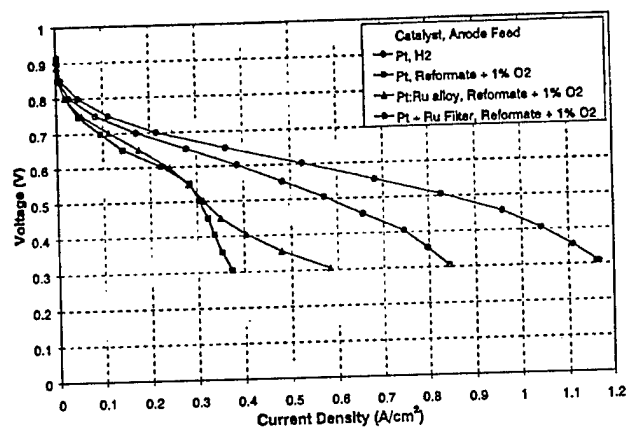


Figure 4. Single-cell performance comparison of Pt, Pt:Ru, and Pt + Ru filter for an anode feed of reformat + 1% O<sub>2</sub> bleed.  $P = 1$  atm,  $T = 70^\circ\text{C}$ .

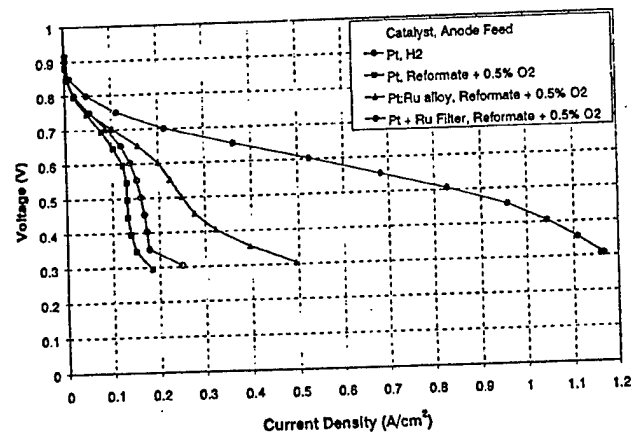


Figure 5. Single-cell performance comparison of Pt, Pt:Ru, and Pt + Ru filter for an anode feed of reformat + 0.5% O<sub>2</sub> bleed.  $P = 1$  atm,  $T = 70^\circ\text{C}$ .

shading indicates the relative concentration of CO in the anode. As CO is oxidized, the concentration of CO decreases as it passes through the filter region. Figure 7a is indicative of adding 1-2% O<sub>2</sub> to the reformat stream. All CO is oxidized from the feed stream



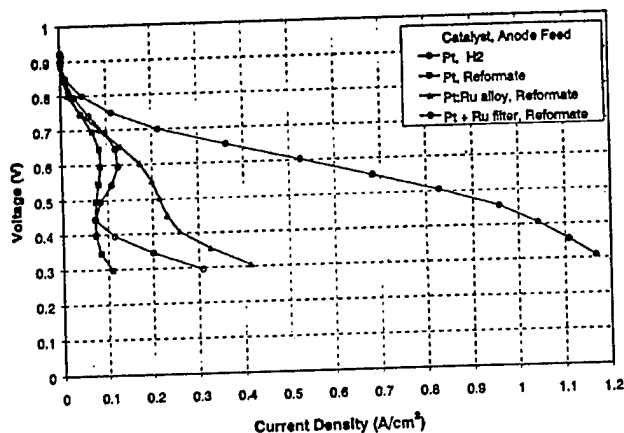


Figure 6. Single-cell performance comparison of Pt, Pt:Ru, and Pt + Ru filter for an anode feed of reformate.  $P = 1$  atm,  $T = 70^\circ\text{C}$ .

before it reaches the Pt portion of the electrode and as a result, the cell operates with minimal performance losses. Figure 7b illustrates that when the Ru filter fails to oxidize CO before it diffuses through the filter region, the remaining CO then encounters the pure Pt electrode where it poisons the Pt through the reaction shown in Eq. 1.

A decrease of the  $\text{O}_2$  concentration in the anode feed (Fig. 3) or an increase in the CO concentration in the anode feed stream results in the eventual failure of the Pt + Ru filter anode. Figure 8 shows the performance of the Ru filter anode when using an anode feed of hydrogen, 2%  $\text{O}_2$ , and various levels of CO. When 50 ppm CO is present, there is almost no reduction in performance ( $0.43\text{--}0.42$  A/cm<sup>2</sup> at 0.6 V). This is inconsistent with the same amount of CO contained in a reformate stream (Fig. 3) and can be attributed to the dilution of hydrogen in the reformate stream. (Completely humidified at  $70^\circ\text{C}$ , reformate + 2%  $\text{O}_2$  in the form of an air bleed contains 28%  $\text{H}_2$  by volume compared to a 70 vol %  $\text{H}_2$  for an  $\text{H}_2$  + 2%  $\text{O}_2$  feed.) Because hydrogen must diffuse through the Ru filter in order to react on the Pt electrode, additional diffusional resistance accounts for the remaining performance losses compared to the performance of a baseline MEA with an anode feed of pure hydrogen. As the CO level increases to 100 ppm, the current density decreases from  $0.42$  to  $0.38$  A/cm<sup>2</sup> at 0.6 V, indicating that the limit of the Ru filter may have been reached. At 200 ppm CO, the drop in performance is much larger ( $0.38\text{--}0.23$  A/cm<sup>2</sup> at 0.6 V). In this case, not all the CO is oxidized in the Ru filter region, resulting in the poisoning of the Pt portion of the electrode. This trend is qualitatively similar to the reduction of the air bleed as shown in Fig. 3.

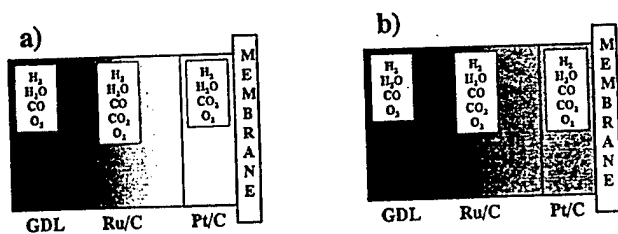


Figure 7. A schematic representation of the species present in the various regions of the Pt + Ru filter anode. The shading indicates the relative concentration of the CO in each region (the lighter the shade, the lower the concentration). In (a) all CO is oxidized within the filter region and the Pt catalyst receives CO-free gas. In (b) the concentration of CO in the inlet gas is too great to be completely oxidized within the filter and poisons the anode catalyst.

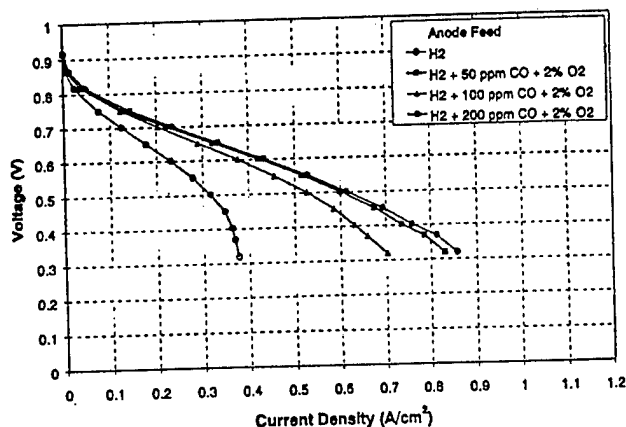


Figure 8. Single-cell performance comparison of the Pt + Ru filter for an anode feed consisting of hydrogen + 2%  $\text{O}_2$  + various CO concentrations.  $P = 1$  atm,  $T = 70^\circ\text{C}$ .

**Mechanism of the Ru filter.**—Equations 2 and 5 present two different methods for CO oxidation. In the mechanism shown in Eq. 2, the oxidation of CO generates  $\text{H}^+$ , whereas the CO oxidation described in Eq. 5 produces no ions. Thus, by removing the electrolyte that allows  $\text{H}^+$  to diffuse away from the reaction site, CO oxidation through the mechanism in Eq. 2 can be effectively prevented. This enables the CO oxidation through Eq. 5 to be isolated and analyzed.

The isolation of the Ru filter was achieved by applying it to the flowfield side of the electrolyte, thus separating it from the Pt electrode by the GDL. The Toray GDL contained no Nafion electrolyte and was sufficiently thick ( $175\text{ }\mu\text{m}$ ) to provide adequate separation from the Pt electrode. To further characterize these two mechanisms, Ru filters containing 10 wt % Nafion were tested on both the membrane and flowfield sides of the GDL.

Figure 9 shows the effect of varying the Nafion content within the Ru filter and the effect of the placement of the Ru filter for an anode feed of reformate + 2%  $\text{O}_2$ . Of the four types tested, the Ru filter placed on the membrane side of the GDL and containing 35 wt % Nafion showed the greatest performance. Both Ru filter types

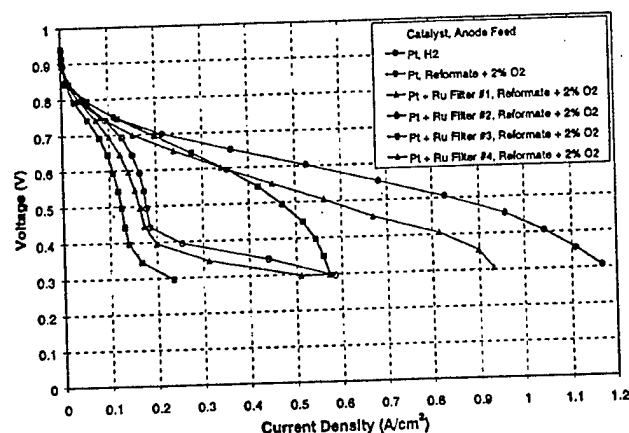
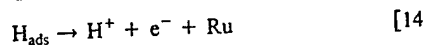
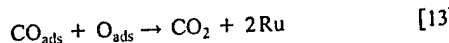
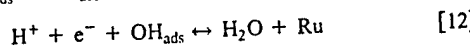
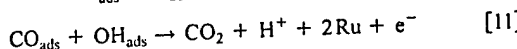
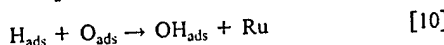
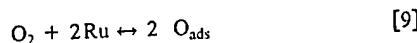


Figure 9. Single-cell performance comparison of the Pt + Ru filter for an anode feed of reformate + 2%  $\text{O}_2$ .  $P = 1$  atm,  $T = 70^\circ\text{C}$ . The filter configurations are defined as follows: filter no. 1 ( $\blacktriangle$ ) contains 35 wt % Nafion and is placed on the membrane side of the GDL; filter no. 2 ( $\circ$ ) contains 35 wt % Nafion and is placed on the flowfield side of the GDL; filter no. 3 ( $\square$ ) contains 10 wt % Nafion and is placed on the membrane side of the GDL; filter no. 4 ( $\triangle$ ) contains 10 wt % Nafion and is placed on the flowfield side of the GDL.

placed on the flowfield side of the GDL provide almost no benefit over the pure Pt anode, providing 0.14 and 0.16 A/cm<sup>2</sup> at 0.6 V compared to 0.34 A/cm<sup>2</sup>. The Ru filter on the membrane side of the GDL and containing 10 wt % Nafion performed similar to the 35 wt % filter for 0.6 V and above, but the lack of electrolyte present most likely induced H<sup>+</sup> diffusion limitations at a lower current density.

Thus, it is believed that the following mechanism is occurring in the ruthenium filter for a fully humidified fuel stream containing oxygen, hydrogen, and carbon monoxide<sup>21-33</sup>



Reactions 7-9 represent the adsorption of species onto the Ru catalyst. Reaction 10 represents an intermediate reaction on Ru resulting in the formation of OH<sub>ads</sub>. Like on Pt, oxygen dissociatively adsorbs on Ru to form O<sub>ads</sub>.<sup>25,29,32</sup> Reactions 11-14 represent competing desorption reactions on the Ru catalyst. Equation 13 is well documented as following Langmuir-Hinshelwood kinetics on Pt and Ru.<sup>34,35</sup> Of the desorption reactions, Eq. 11 and 13 are desired as they result in the oxidation of CO<sub>ads</sub>. The above-described mechanism is not a comprehensive list of all reactions occurring within the anode region. It focuses on those reactions that lead to CO oxidation. For example, evidence has been found that H<sub>2</sub>O<sub>2</sub> is formed as an intermediate during oxygen reduction at overpotentials as low as 0.5 V.<sup>36</sup> However, H<sub>2</sub>O<sub>2</sub> breaks back down to oxygen-containing compounds at or even before reaching the catalyst surface.<sup>2,5,13</sup>

The rationale for the placement of the filter on the flowfield side of the GDL is that if the oxidation of CO<sub>ads</sub> were to proceed via Eq. 11, a three-phase interface (anode gas, Nafion, and Pt/C) is not needed in the catalyst mixture because there are no ions or electrons to be transported away from the reaction site. Because some Nafion is necessary in the Ru filter to act as a binder, the Ru filter was merely placed on the flowfield side of the GDL. There is no Nafion electrolyte in the GDL to allow proton transport and the GDL is sufficiently thick (~5 mil). Without the Nafion electrolyte as a conduit and because of the long distance that the protons must travel, the formation of CO<sub>2</sub> through Eq. 11 does not occur to any significant extent and the reaction shown in Eq. 13 is isolated. Thus, the amount of CO<sub>ads</sub> oxidized through the reaction shown in Eq. 13 is also insufficient to provide the levels CO tolerance shown in both Fig. 3 and 8. This is consistent with literature, where it is also shown that Ru is one of the least active metals for this method of CO oxidation at the oxygen partial pressures used in these experiments.<sup>25,29</sup>

Further evidence of the role of Nafion content in the membrane is shown for the cases in Fig. 9. Significant CO oxidation only occurs when the Ru filter is placed adjacent to the Pt anode. This is evidence that protons are formed as product of CO oxidation. The Nafion electrolyte is the necessary conduit for the protons to move away from the reaction site and when this conduit is present, cell performance increases when all other parameters are unchanged. The increased performance under conditions of increased Nafion content shown in Fig. 9 is further proof that CO<sub>ads</sub> oxidation is occurring by the mechanism that involves the formation of protons which is described in Reaction 11. Thus, Reaction 13 does occur to a small extent as evidenced by the slight increase in performance

when the filter is placed on the flowfield side of the GDL, but the rate of Reaction 11 is far greater than Reaction 13 when the filter is ionically connected to the MEA.

The hydroxyl group in Reaction 11 can be formed either from oxygen through Reactions 9 and 10 or from water through Reaction 12. In fact, both are occurring within an Ru filter when it is adjacent to the Pt anode. The mechanism primarily responsible for the CO tolerance of the Pt:Ru alloy is comprised of Reactions 11 and 12. Figure 6 shows that in the absence of an air bleed, there is only a small performance increase relative to a pure Pt anode. Thus, the formation of OH<sub>ads</sub> through the reverse of Reaction 12 is not the primary source of the hydroxyl species needed for Eq. 11. It is clear that the Pt:Ru alloy performs better under reformat conditions. Gasteiger<sup>11,12,14,30</sup> performed extensive research on this mechanism and found that while OH<sub>ads</sub> is indeed formed at lower potentials on Ru than Pt, the hydroxyl group also forms a stronger bond on pure Ru than a 1:1 atomic ratio Pt:Ru alloy, resulting in higher CO oxidation potentials on pure Ru than on the Pt:Ru alloy. It can be speculated that the rate of formation of OH<sub>ads</sub> in the Ru filter is equivalent to that in the Pt:Ru alloy.<sup>30</sup> However, it is clear from Fig. 6 that without the presence of oxygen in the anode feed that only a fraction of the CO is oxidized in the Ru filter and that the remaining CO poisons the Pt anode.

Thus, the primary method by which CO tolerance is achieved by the Ru filter is by the formation of OH<sub>ads</sub> from oxygen in the air bleed. The explanation of near complete oxidation of CO at concentrations up to 100 ppm is the result of Reactions 9-11. That near CO-free performance is achieved with the addition of 2% O<sub>2</sub> to the anode feed while the filter provides almost no benefit under reformat conditions is evidence that Reactions 9-11 are the primary means of CO oxidation within the filter region.

The key is that O<sub>ads</sub> forms OH<sub>ads</sub> before reacting with a second proton to form water. This is where the benefit of the Ru filter lies. The oxidation of H<sub>ads</sub> occurs within the filter according to Reaction 14 forming H<sup>+</sup>. Because the kinetics of hydrogen adsorption on Ru is several orders of magnitude slower than on Pt, there is a lower concentration of H<sub>ads</sub> in the filter region and more of an opportunity for CO<sub>ads</sub> to react with OH<sub>ads</sub>, resulting in the formation of CO<sub>2</sub>. The bulk of the hydrogen oxidation occurs in the Pt region. However, protons must be present within the Ru filter for Reaction 10 to occur, and because these protons will also shift Reaction 12 toward the formation of H<sub>2</sub>O, there is a limit to the benefit of the Ru filter.

## Conclusions

For an anode feed stream consisting of reformat (containing 50 ppm CO) and 1-2% oxygen, the Pt + Ru filter electrode shows increased CO tolerance compared to a Pt:Ru alloy containing similar amounts of Pt and Ru. For CO concentrations up to 100 ppm and 2 vol % O<sub>2</sub>, the Pt + Ru filter anode also shows superior performance. It is likely that the oxidation of the CO within the Ru filter is primarily due to oxygen reacting to form OH<sub>ads</sub>, which then electrochemically reacts with CO<sub>ads</sub> to form CO<sub>2</sub> and protons.

However, with insufficient oxygen (<1 vol %) or too much CO (>100 ppm), not all CO is oxidized in the Ru filter. Remaining CO reaches and then poisons the Pt region of the Pt + Ru filter anode. As a result, cell performance under those conditions is worse than the Pt:Ru alloy anode.

Because benefits of the Ru filter occur at high levels air bleed (2% O<sub>2</sub>) and the Pt:Ru alloy provides CO tolerance even without air bleed, it is suggested that the anode configuration that would provide optimal CO tolerance would consist of an Ru filter placed in front of and adjacent to a Pt:Ru alloy.

## Acknowledgments

The authors acknowledge the financial support from the National Institute of Standards and Technology under cooperative agreement no. 70NANB8H4039.

The University of South Carolina assisted in meeting the publication costs of this article.

# References

1. H. P. Dhar, L. G. Christner, A. K. Kush, and H. C. Maru, *J. Electrochem. Soc.*, **133**, 1574 (1986).
2. H. F. Oetjen, V. M. Schmidt, U. Stimming, and F. Trila, *J. Electrochem. Soc.*, **143**, 3838 (1996).
3. H. P. Dhar, L. G. Christner, and A. K. Kush, *J. Electrochem. Soc.*, **134**, 3021 (1987).
4. B. N. Grgur, N. M. Markovic, and P. N. Ross, *J. Electrochem. Soc.*, **146**, 1613 (1999).
5. R. J. Bellows, E. P. Marucchi-Soos, and D. T. Buckley, *Ind. Eng. Chem. Res.*, **35**, 1235 (1996).
6. M. Iwase and S. Kawatsu, in *Proton-Conducting Membrane Fuel Cells*, A. R. Landgrebe, S. Gottesfeld, and G. Halpert, Editors, PV 95-23, pp. 12-23, The Electrochemical Society Proceedings Series, Pennington, NJ (1995).
7. M. Watanabe, H. Igarashi, and T. Fujino, *Electroanal. Chem.*, **67**, 1194 (1999).
8. B. N. Grgur, N. M. Markovic, and P. N. Ross, Jr., in *Proton Conducting Membrane Fuel Cells*, S. Gottesfeld, T. F. Fuller, and G. Halpert, Editors, PV 98-27, p. 176, The Electrochemical Society Proceedings Series, Pennington, NJ (1998).
9. A. B. Anderson, E. Grantscharova, and P. Schiller, *J. Electrochem. Soc.*, **142**, 1880 (1995).
10. M. Gotz and H. Wendt, *Fuel Cell Seminar Abstracts*, Palm Springs, CA, p. 616, Nov 16-19, 1998.
11. H. A. Gasteiger, N. M. Markovic, and P. N. Ross, Jr., *J. Phys. Chem.*, **99**, 8290 (1995).
12. H. A. Gasteiger, N. M. Markovic, and P. N. Ross, Jr., *J. Phys. Chem.*, **99**, 16757 (1995).
13. R. J. Bellows, E. Marucchi-Soos, and R. P. Reynolds, *Electrochem. Solid-State Lett.*, **1**, 69 (1998).
14. K. Wang, H. A. Gasteiger, N. M. Markovic, and P. N. Ross, Jr., *Electrochim. Acta*, **41**, 2587 (1996).
15. M. T. M. Koper, J. J. Lukkien, A. P. J. Jansen, and R. A. van Santen, *J. Phys. Chem.*, **103**, 5522 (1999).
16. V. M. Schmidt, H.-F. Oetjen, and J. Divisek, *J. Electrochem. Soc.*, **144**, L237 (1997).
17. C. T. Campbell, G. Ertl, H. Kuipers, and J. Segner, *J. Chem. Phys.*, **73**, 5862 (1980).
18. T. Madey, A. Engelhardt, and D. Menzel, *Surf. Sci.*, **48**, 304 (1975).
19. S. J. Lee, S. Mukerjee, E. A. Ticianelli, and J. McBreen, *Electrochim. Acta*, **44**, 3283 (1999).
20. M. S. Wilson, U.S. Pat. 5,211,984 (1993).
21. S. H. Oh and R. M. Sinkevitch, *J. Catal.*, **142**, 254 (1993).
22. N. M. Markovic, T. J. Schmidt, B. N. Grgur, H. A. Gasteiger, R. J. Behm, and P. N. Ross, *J. Phys. Chem.*, **103**, 8568 (1999).
23. N. M. Markovic, B. N. Grgur, C. A. Lucas, and P. N. Ross, *J. Phys. Chem. B*, **103**, 487 (1999).
24. K. Bleakley and P. Hu, *J. Am. Chem. Soc.*, **121**, 7644 (1999).
25. C. Zhang, P. Hu, and A. Alavi, *J. Am. Chem. Soc.*, **121**, 7931 (1999).
26. E. Yeager, *J. Mol. Catal.*, **38**, 5 (1986).
27. E. Yeager, *Electrochim. Acta*, **29**, 1527 (1984).
28. A. Alavi, P. J. Hu, T. Deutsch, P. L. Silvestrelli, and J. Hutter, *Phys. Rev. Lett.*, **80**, 3650 (1998).
29. H.-I. Lee, G. Praline, and J. M. White, *Surf. Sci.*, **91**, 581 (1980).
30. H. A. Gasteiger, N. Markovic, P. N. Ross, and E. J. Cairns, *J. Phys. Chem.*, **98**, 617 (1994).
31. P. Ferreira-Aparicio, A. Guerrero-Ruiz, and I. Rodriguez-Ramos, *Appl. Catal. A*, **170**, 177 (1998).
32. P. Ferreira-Aparicio, I. Rodriguez-Ramos, J. A. Anderson, and A. Guerrero-Ruiz, *Appl. Catal. A*, **202**, 183 (2000).
33. P. Freni, G. Calogero, and S. Cavallaro, *J. Power Sources*, **87**, 28 (2000).
34. P. J. Berlowitz, C. H. F. Peden, and D. W. Goodman, *J. Phys. Chem.*, **92**, 5213 (1998).
35. R. Imbihl, M. P. Cox, and G. Ertl, *J. Chem. Phys.*, **83**, 1578 (1985).
36. N. M. Markovic, T. J. Schmidt, V. Stamenkovic, and P. N. Ross, *Fuel Cells*, **1**, 105 (2001).



## Using Sputter Deposition to Increase CO Tolerance in a Proton-Exchange Membrane Fuel Cell

Andrew T. Haug,<sup>a,\*</sup> Ralph E. White,<sup>a,\*\*\*,z</sup> John W. Weidner,<sup>a,\*\*\*</sup> Wayne Huang,<sup>b</sup> Steven Shi,<sup>b,\*\*\*</sup> Narendra Rana,<sup>c</sup> Stephan Grunow,<sup>c</sup> Timothy C. Stoner,<sup>c</sup> and Alain E. Kaloyeros<sup>c</sup>

<sup>a</sup>Center for Electrochemical Engineering, Department of Chemical Engineering, University of South Carolina, Columbia, South Carolina 29208, USA

<sup>b</sup>Plug Power, Incorporated, Latham, New York 12110, USA

<sup>c</sup>Energy and Environment Applications Center, Institute for Materials, and School of Nanosciences and Engineering, State University of New York at Albany, Albany, New York 12203, USA

Placing a layer of Ru atop a Pt anode increases the carbon monoxide tolerance of proton-exchange membrane fuel cells when oxygen is added to the fuel stream. Sputter-deposited Ru filter anodes composed of a single Ru layer and three Ru layers separated by Nafion-carbon ink, respectively, were compared to Pt, Pt:Ru alloy, and an ink-based Ru filter anodes. The amount of Pt in each anode was 0.15 mg/cm<sup>2</sup> and the amount of Ru in each Ru-containing anode was 0.080 mg/cm<sup>2</sup>. For an anode feed consisting of hydrogen, 200 ppm CO, and 2% O<sub>2</sub> (in the form of an air bleed), all Ru filter anodes outperformed the Pt:Ru alloy. The performance of the Pt + single-layer sputtered Ru filter was double that of the Pt:Ru alloy (0.205 vs. 0.103 A/cm<sup>2</sup> at 0.6 V). The performance was also significantly greater than that of the ink-based Ru filter (0.149 A/cm<sup>2</sup> at 0.6 V). Within the filter region of the anode, it is likely that the decreased hydrogen kinetics of the Ru (compared to Pt) allow for more of the OH<sub>ads</sub> formed from oxygen in the fuel stream to oxidize adsorbed CO to CO<sub>2</sub>.

© 2002 The Electrochemical Society. [DOI: 10.1149/1.1479727] All rights reserved.

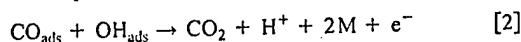
Manuscript submitted August 15, 2001; revised manuscript received January 10, 2002. Available electronically May 15, 2002.

Proton-exchange membrane-based fuel cells (PEMFCs) are gaining popularity due to their high operating efficiency and environmental friendliness. Because of the difficulties inherent to storing hydrogen, hydrocarbon fuels such as propane, natural gas, and gasoline are used to produce reformat gas. Dry reformat is typically composed of 40-75% hydrogen, 15-25% carbon dioxide, 10-10,000 ppm carbon monoxide, and a balance of nitrogen, depending on the fuel processing system used.<sup>1,2</sup> It has been shown extensively that CO poisons the platinum catalyst used in PEMFC systems.<sup>3-7</sup> Carbon monoxide chemically adsorbs onto available Pt catalyst sites as shown in

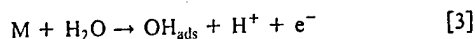


As little as 10 ppm CO in the fuel stream can lower the power output of the PEMFC by 50%.<sup>6,7</sup> For the reforming process to be effective in the fuel cell system, this problem must be solved. Attempts to find catalysts both tolerant to CO and equivalent in performance to Pt have led to the alloying of Pt with Ru, Mo, W, Co, Os, Ir, Ni, and Sn.<sup>7-11</sup> Used by themselves as catalysts, these metals do not provide the high hydrogen activity necessary to achieve the current densities that make PEMFCs competitive in the marketplace.<sup>9,12,13</sup> The most commonly used alloy is Pt:Ru. The Pt:Ru alloy combines the high catalyst activity of pure Pt with the increased CO tolerance of pure Ru catalyst.<sup>12-14</sup>

The oxidation of CO<sub>ads</sub> from the Pt:Ru catalyst surface in the anode shown in Eq. 2 follows Langmuir-Hinshelwood kinetics<sup>12,13</sup>



where M represents Pt or Ru. The reactions by which OH<sub>ads</sub> is formed on Pt and Ru are shown in Eq. 3<sup>15,16</sup>

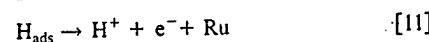
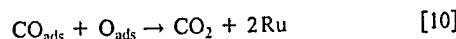
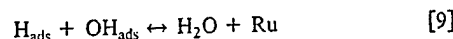
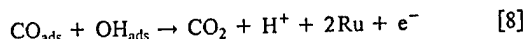
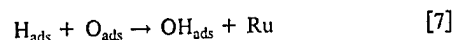


The formation of OH<sub>ads</sub>, shown in Eq. 3 is the rate-determining step of this reaction and occurs on platinum at potentials of 0.7 V vs.

the reversible hydrogen electrode (RHE) and above.<sup>13,15,16</sup> Ruthenium has the ability to form OH<sub>ads</sub> from water at significantly lower potentials than Pt, 0.35 V for 50 atom % Ru and 0.2 V for 90 atom % Ru,<sup>12,13,16</sup> allowing for a certain amount of CO tolerance. At low temperatures (70-85°C), the Pt:Ru (1:1 atomic ratio) alloy catalyst provides nearly equivalent performance to pure H<sub>2</sub> on Pt for CO concentrations up to 100 ppm in the feedstream.<sup>8,12</sup>

The injection of oxygen into the fuel stream increases catalyst tolerance to CO.<sup>14,17</sup> However, even the addition of high levels of oxygen to the feedstream (2-4% by volume of hydrogen) provides approximately 100 ppm CO tolerance. Roughly one out of every 400 O<sub>2</sub> molecules oxidizes an adsorbed CO molecule, with the balance reacting with hydrogen.<sup>14</sup> The placement of a layer of Ru catalyst before the Pt electrode to act as a filter has been shown to increase the effectiveness of oxygen addition over conventional Pt:Ru alloy catalysts.<sup>18</sup> This method also eliminates the process of alloying the Pt and Ru metals, and by using a filter, the Pt loading in the anode is free to be varied.

It is believed that the following mechanism is occurring in the Ru filter for a fully humidified fuel stream containing oxygen, hydrogen, and carbon monoxide<sup>14,18-33</sup>



Reactions 4, 5, and 6 represent the adsorption of species onto the Ru catalyst. Reaction 7 represents an intermediate reaction on Ru resulting in the formation of OH<sub>ads</sub>. Reactions 8-11 represent competing desorption reactions on the Ru catalyst. Equation 10 is well documented as following Langmuir-Hinshelwood kinetics on Pt and Ru.<sup>34,35</sup> Of the desorption reactions, Reactions 8 and 10 are desired

\* Electrochemical Society Student Member.

\*\* Electrochemical Society Fellow.

\*\*\* Electrochemical Society Active Member.

<sup>z</sup> E-mail: white@enr.sc.edu

as they result in the oxidation of  $\text{CO}_{\text{ads}}$ . Earlier work<sup>18</sup> showed that the reaction shown in Eq. 8 is the primary means by which  $\text{CO}_{\text{ads}}$  is oxidized within the filter, resulting in the formation of  $\text{H}^+$ . Thus, like the Pt region following the filter, a three-phase interface of catalyst (Ru here), carbon and Nafion are required for the filter to operate. The above mechanism is not a comprehensive list of all reactions occurring within the anode region. The mechanism focuses on those reactions that lead to CO oxidation. For example, evidence has been found that  $\text{H}_2\text{O}_2$  is formed as an intermediate during oxygen reduction at overpotentials as low as 0.5 V.<sup>19</sup> However,  $\text{H}_2\text{O}_2$  breaks down to oxygen-containing compounds at or even before reaching the catalyst surface.<sup>4,7,17</sup>

The goal of this work is to increase the effectiveness of the Ru filter by applying it through sputter deposition as opposed to conventional catalyst ink-based application methods. Sputter deposition is widely used for integrated circuit manufacturing and has been investigated for us in fuel cells for more than a decade.<sup>36-39</sup> Hirano *et al.*<sup>40</sup> sputter deposited platinum on uncatalyzed gas-diffusion layers (GDLs) resulting in cell performances at loadings of 0.10 mg Pt/cm<sup>2</sup> equivalent to those of standard methods at loadings of 0.40 mg Pt/cm<sup>2</sup>. Witham *et al.*<sup>41</sup> achieved direct methanol fuel cell (DMFC) anode catalyst activities one to two orders of magnitude higher than those of conventional ink-based catalysts, suggesting that DMFC anodes may be manufactured containing less than one-tenth the amounts presently used (2.5-4 mg Pt/cm<sup>2</sup>) without loss in performance. Holleck *et al.*<sup>42</sup> have sputtered catalyst mixtures at the front surface of the anode electrode. These mixtures included Pt:Ru:X where X represents Ni, Pd, Co, Rh, Ir, Mn, Cr, W, Nb, and Zr. For low levels of CO (10 ppm), specific Pt:W and Pt:Ru:W alloys performed better than Pt:Ru.

In this work, the Ru filter is sputter-deposited as a single layer and as a series of three layers (separated by Nafion-carbon ink) and compared to a conventional ink-based filter. By manufacturing membrane-electrode assemblies (MEAs) composed of multiple sputter-deposited Pt layers, Cha and Lee<sup>43</sup> were able to increase the Pt catalyst activity significantly over conventional ink-based MEAs by increasing the amount of Pt in contact with Nafion and carbon. This process was further improved upon by reducing the amount of Nafion-carbon ink (NCI) separating the Pt layers, resulting in thinner, more effective electrodes.<sup>44</sup> For the same loading of catalyst, sputter-depositing catalyst between layers of NCI increases the active area of the catalyst vs. a single sputter-deposited layer.<sup>43,44</sup> For Pt catalyst, this results in greater performance of the fuel cell electrodes.<sup>43,44</sup> It is predicted that for the Ru filter, this process will create more sites upon which CO can be oxidized, resulting in a more CO-tolerant PEMFC MEA.

### Experimental

**Development of ink-based MEAs.**—The method described in U.S. Patent 5,211,984 provides an outline for the catalyst ink preparation and MEA fabrication performed in this project.<sup>45</sup> The following catalyst inks were prepared: (i) Nafion + carbon only (Nafion-carbon Ink or NCI), (ii) Nafion + 20% Pt on carbon, (iii) Nafion + 20% Pt:Ru on carbon, and (iv) Nafion + 20% Ru on carbon.

The inks were prepared for Pt, Pt:Ru, Ru by adding the E-TEK catalyst (20% catalyst on XC-72 Carbon) to a solution of 5 wt % Nafion (DuPont). For NCI, XC-72 Carbon was added to a solution of 5 wt % Nafion.

Decals (Teflon, 10 cm<sup>2</sup>, three-ply) were weighed prior to application of catalyst ink. The ink was drawn across the surface of the decals using a Meyer rod. The coated decals were dried in an oven at 105°C under ambient pressure for 10 min.

Target loadings were 0.15 mg Pt/cm<sup>2</sup> (anode), 0.230 mg Pt:Ru/cm<sup>2</sup> (anode), and 0.15 mg Pt/cm<sup>2</sup> (cathode). Target loadings of 0.230 mg Pt:Ru/cm<sup>2</sup> and of 0.080 mg Ru/cm<sup>2</sup> for the Ru filter were chosen so that a 1:1 atomic ratio of Pt:Ru is maintained, while Pt catalyst is maintained at a loading of 0.15 mg/cm<sup>2</sup>.

Table I. Types of ink-based MEUs tested.

MEU name	Description
Pt	0.15 mg Pt/cm <sup>2</sup> anode 0.15 mg Pt/cm <sup>2</sup> cathode Uncatalyzed Toray GDLs on anode and cathode
Pt:Ru	0.23 mg Pt:Ru/cm <sup>2</sup> anode 0.15 mg Pt/cm <sup>2</sup> cathode Uncatalyzed Toray GDLs on anode and cathode
Pt + Ru (Ru filter)	0.15 mg Pt/cm <sup>2</sup> anode 0.15 mg Pt/cm <sup>2</sup> cathode 0.080 mg Ru/cm <sup>2</sup> coated Toray GDL on the anode Uncatalyzed Toray GDL on the cathode side

To form a MEA with ink-coated decals, appropriate decals were placed on either side of the PEM (Nafion 117, protonated form). This assembly was hot-pressed to ensure bonding. It was then cooled to room temperature, before the decals were carefully peeled from the assembly.

To form a membrane-electrode unit (MEU, equivalent to a GDL + MEA + GDL) with ink-coated GDLs, appropriate GDLs were placed on either side of a PEM (Nafion 117, protonated form, soaked in deionized water for 1 h). This assembly was hot-pressed to ensure a well-bonded MEU. The types of ink-based MEUs made are shown in Table I.

**Development of sputter-deposition-based MEAs.**—Plasma modifications and sputter-deposition augmentations/additions were both completed using an Anatech Hummer 10.2 sputter-coating tool. A modified sample stage was used to support Nafion 117 substrates up to 6 × 6 cm while masking 1.5 cm about the membrane's perimeter.

It has been shown previously that alternating current (ac) plasma should be used for all plasma modifications, as Nafion 117 and MEAs from Nafion 117 suffer no ill effects from this treatment.<sup>44</sup> An aluminum target was used for ac plasma modifications, while the Ru (Kurt J. Lesker) target and carbon evaporation system (Anatech) were used for sputter augmentations/additions.

All MEAs subject to sputter deposition were first ac plasma cleaned for 5 min at 5 mA and 1.2 kV to remove residual buildup from the target as well as roughen the substrate surface. All treatments were completed at ~62 mTorr. A separate vacuum chamber was used to evacuate each substrate to ~45 mTorr, before it was placed in the sputter-coating tool to minimize contaminant outgassing in the deposition chamber. A potential of 1.8 kV and a current of 8 mA were maintained to control the deposition rate for Ru. A  $\text{SiO}_2$  sample was sputter-deposited *in situ* with each MEA. The resultant metal/ $\text{SiO}_2$  stack was subjected to cross-sectional view scanning electron microscopy (SEM) imaging to verify the thickness of the sputter-deposited film and top-view SEM imaging to determine surface characteristics of the film.

Multilayered Ru filters were manufactured by a method similar to that described by Cha and Lee.<sup>43</sup> On the MEA anode, a layer of NCI was sprayed on the surface of the sputter-deposited Ru layer. The MEA was then dried at 80°C under vacuum for 10 min. Additional layers of sputter-deposited Ru and NCI were added until the desired Ru loading and number of Ru layers were attained.

MEAs containing sputter-deposited catalyst layers were manufactured into MEUs through similar methods as the ink-based MEAs.

**Cell assembly and testing.**—The MEUs were placed in a 10 cm<sup>2</sup> cell assembly and incubated for 4 to 8 h at ambient pressure, cell temperature of 70°C, stoichiometric ratio ([actual flow]/[stoichiometric flow] required for a 1.0 A/cm<sup>2</sup> current) of 1.5 at the anode and 2.0 at the cathode. Fuel cell performance curves were obtained under the conditions given in Table II.

Table II. Fuel cell test conditions.

Pressure	1 atm
Cell temperature	70°C
Stoichiometric ratio (at 1 A/cm <sup>2</sup> )	1.5 hydrogen 2.0 air
Feedstreams	Anode: hydrogen, H <sub>2</sub> + CO, H <sub>2</sub> + CO + air bleed Cathode: air
Humidification	Complete humidification of anode and cathode gas streams for all trials
Air bleed	2.0% O <sub>2</sub> (in the form of an air bleed relative to the volumetric flow of hydrogen in slm)
CO amounts	50, 200 ppm

### Results

**Determination of sputter-deposition rates and catalyst loading.**—The sputter-deposition rates for Ru were determined with loadings calculated from cross-sectional and top-view SEM images of sputter-deposited Ru films on SiO<sub>2</sub> substrates. The top-view SEM images in Fig. 1 were analyzed to determine the surface coverage of the sputter-deposited film (Pt ~ 65%, Ru ~ 56%). Ru did not form a continuous film on the SiO<sub>2</sub> substrate, but rather agglomerated. This is consistent with literature.<sup>46</sup> The surface coverages were used in conjunction with the bulk density of Ru (12.2 g/mL) and the film thicknesses from the cross-sectional SEM images to calculate the subsequent Ru loadings. The Ru sputter-deposition rate was constant with time at 3.3  $\mu\text{g Ru/cm}^2/\text{min}$ .

The cross-sectional view in Fig. 1 shows that the thickness of 30 and 45 min sputter-deposited Ru is roughly two and three times the thickness of a 15 min deposition of Ru, respectively. Semiquantitative analyses via energy dispersive X-ray spectroscopy (EDXS) and Rutherford backscattering spectrometry (RBS) confirm these Pt and Ru deposition rates.

**CO testing.**—The three types of Pt + Ru filter anodes prepared are shown in Fig. 2. They were made to the following specifications: filter 1: 0.08 mg/cm<sup>2</sup> ink-based 20% Ru/C, filter 2: NCI + 25 min (0.08 mg/cm<sup>2</sup>) of sputter-deposited Ru, and filter 3: NCI + 3  $\times$  (8.33 min of sputter-deposited Ru + NCI). The total Ru loading was 0.08 mg/cm<sup>2</sup>.

Filter 1 is an ink-based Ru filter, while filter 2 and 3 are comprised of one and three layers of a sputter-deposited Ru, respec-

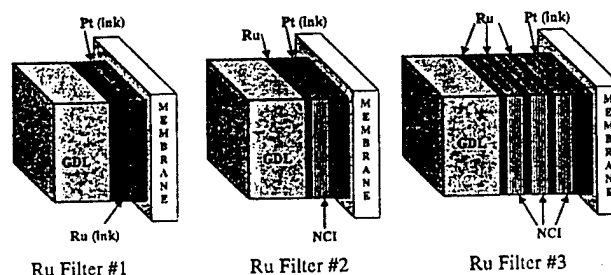


Figure 2. Diagram of the Ru filtered anode. The filter is a layer of Ru catalyst placed between the Pt catalyst and the gas-diffusion layer for oxidizing CO present within the anode. Filter 1 is the standard Ru filter prepared from a catalyst ink. Filter 2 is a single sputter-deposited layer of Ru separated from the Pt electrode by a layer of NCI. Filter 3 is a three-layer sputter-deposited Ru filter separated from the Pt electrode by a layer of NCI. All filters have a loading of 0.08 mg Ru/cm<sup>2</sup> and were placed atop a Pt electrode with a loading of 0.15 mg Pt/cm<sup>2</sup>.

tively. As shown in Fig. 2, NCI is used to separate the layers of sputter-deposited Ru layered between Nafion-carbon ink (NCI).

Figure 3 compares various Ru filters to the Pt:Ru alloy and the baseline MEA at 70°C for an anode feed of hydrogen + 50 ppm CO. All MEAs prepared with Pt, Pt:Ru alloy, and Pt + Ru filters 1-3 exhibited a dramatic loss of performance when 50 ppm CO was added to the hydrogen feedstream. In all cases, fuel cell performance dropped to less than 40% of the baseline MEA running on pure hydrogen fuel. It is clear that the filters do not completely oxidize the CO in the feedstream to CO<sub>2</sub>. The remaining CO passes through the filter and poisons the Pt portion of the anode, resulting in performance resembling that of a typical Pt anode as evidenced in Fig. 3. The Pt:Ru alloy demonstrates CO tolerance over a Pt anode consistent with literature, more than doubling the current density of any other anode configuration at 0.6 V.

When 2% O<sub>2</sub> (in the form of an air bleed) is added to the anode feed, all Ru-containing anodes show significant performance improvement over the Pt baseline as shown in Fig. 4. For the 25 min Ru (0.08 mg Ru/cm<sup>2</sup>) sputter-deposited filter, there is almost no performance loss except at lower voltages. The Pt:Ru alloy and standard Ru filter show almost identical performance, roughly 20% less than the baseline (0.227 vs. 0.275 A/cm<sup>2</sup> at 0.6 V). The performance of the Ru filter cannot be explained by the formation of a Pt:Ru alloy as there is no interface between Pt and Ru. A layer of NCI separates the sputter-deposited Ru from the Pt electrode for the sputter-deposited Ru filters. The multilayered filter performed the

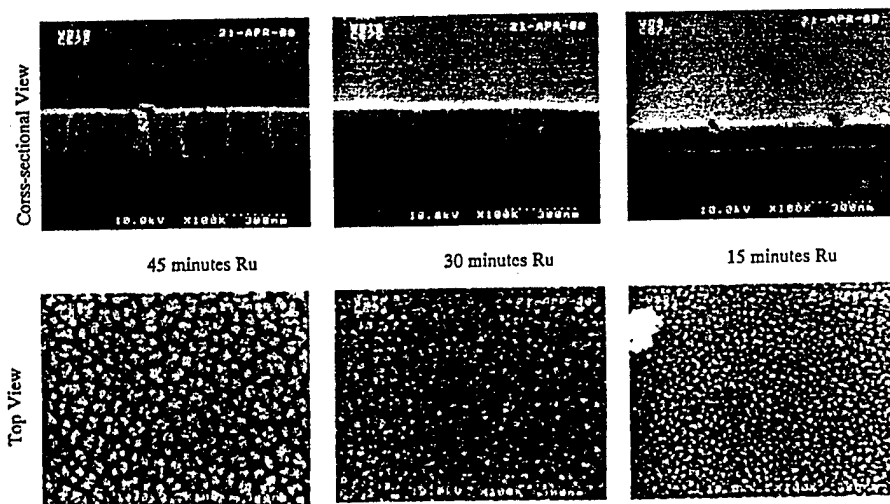


Figure 1. Top and cross-sectional SEM images of sputter-deposited Ru on Si/SiO<sub>2</sub> substrates.

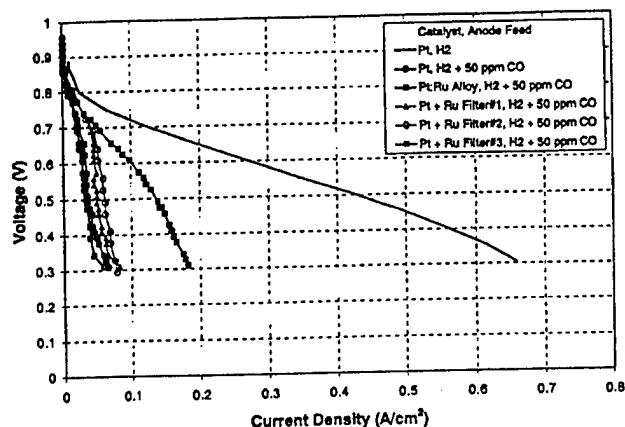


Figure 3. Performance comparison of MEUs with sputter-deposited Ru filter under  $\text{H}_2 + 50 \text{ ppm CO}$  conditions.  $P = 1 \text{ atm}$ ,  $T = 70^\circ\text{C}$ . The filter configurations are defined as follows: filter 1 ( $\blacktriangle$ ) is the standard Ru filter prepared from an ink; filter 2 ( $\circ$ ) is a single 25 min sputter-deposited layer of Ru separated from the Pt electrode by a layer of NCI; filter 3 ( $\times$ ) is a three-layer sputter-deposited Ru filter (8.33 min per layer, see Fig. 2 for design) separated from the Pt electrode by a layer of NCI.

worst of the Ru-containing anodes. This is likely due to the increased diffusional resistances caused by the thickness of the Ru filter.

As the amount of CO is increased from 50 to 200 ppm, the benefit of the Ru filters is seen more clearly. Figure 5 shows that all three Ru filter types outperform the Pt:Ru alloy. For the anode consisting of Pt + Ru filter 2, the performance is double that of the Pt:Ru alloy (0.205 vs. 0.103  $\text{A/cm}^2$  at 0.6 V). The MEA containing filter 2 loses only 20% of its performance (0.255 vs. 0.205  $\text{A/cm}^2$  at 0.6 V) as the CO concentration is increased from 50 to 200 ppm CO, and loses only 25% vs. the hydrogen baseline. There have been other reports of 200 ppm CO tolerance with an air bleed, but the conditions involved higher temperatures and higher loadings.<sup>14</sup> The MEA containing filter 2 significantly outperformed ink-based filter 1 by more than 35% (0.205 vs. 0.149  $\text{A/cm}^2$  at 0.6 V). These results also constitute a significant improvement over the previous work done on the Ru filter.<sup>18</sup> Under conditions identical to those shown in Table II, the Ru filter of 0.21  $\text{mg/cm}^2$  developed in Ref. 18 showed an equivalent loss in performance to filter 2 of this work when only 100 ppm CO was added to the anode feed containing 2%  $\text{O}_2$  in the form

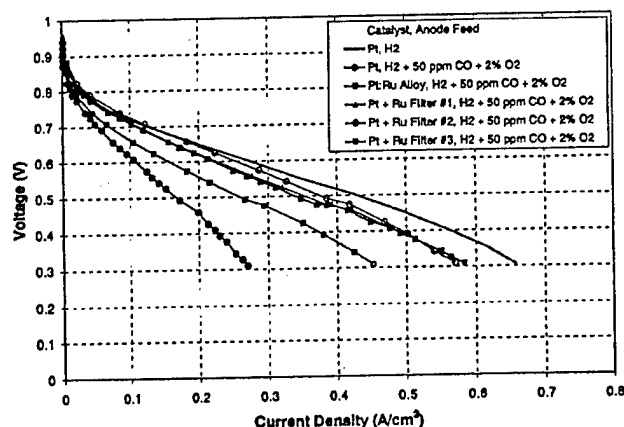


Figure 4. Performance comparison of MEUs with sputter-deposited Ru filter for an anode feed of hydrogen + 50 ppm CO + 2%  $\text{O}_2$ .  $P = 1 \text{ atm}$ ,  $T = 70^\circ\text{C}$ . The filter configurations are defined in Fig. 3.

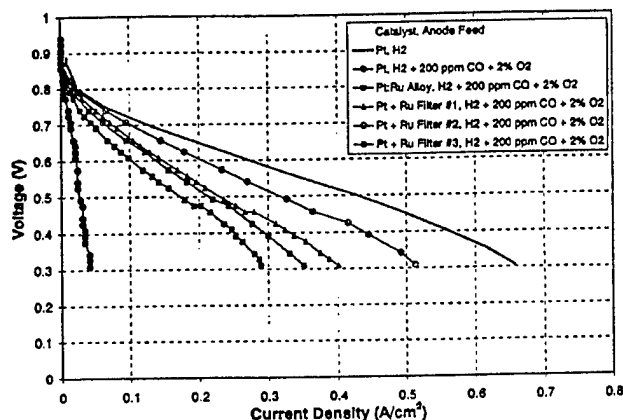


Figure 5. Performance comparison of MEUs with sputter-deposited Ru filter for an anode feed of hydrogen + 200 ppm CO + 2%  $\text{O}_2$ .  $P = 1 \text{ atm}$ ,  $T = 70^\circ\text{C}$ . The filter configurations are defined in Fig. 3.

of an air bleed. The Ru filter in Ref. 18 showed a 50% loss in performance when the CO concentration was doubled to 200 ppm.

Of the three Ru-filtered MEAs tested, filter 3 performed the worst at 200 ppm CO, but suffered only a 12% loss compared to its performance at 50 ppm CO (0.138 vs. 0.157  $\text{A/cm}^2$  at 0.6 V). That there is so little drop-off from this three-layer filter configuration suggests that the lower performance compared to the single-layer sputter-deposited filter 2 is due to diffusional resistances caused by the increased thickness of this filter. The layers of NCI are very thick relative to each Ru deposition ( $\sim 40 \text{ nm}$  for each sputter-deposited Ru layer compared to  $\sim 12 \text{ }\mu\text{m}$  for each NCI layer),<sup>44</sup> accounting for more than 99.5% of the Ru filter layer thickness. The increased thickness of this three-layer filter requires hydrogen to travel further to reach the Pt vs. a single-layer filter, and vs. the baseline MEA giving rise to greater diffusional resistances. By reducing the amount of NCI used in each sputter-deposited layer (by diluting the NCI), a thinner, more effective multilayered Ru filter may be developed.

The addition of a layer of NCI between the Pt electrode and the sputter-deposited Ru filter is evidence that the CO oxidation is not the result of a layer of Pt:Ru alloy being formed at the interface of the filter and the Pt electrode. Thus, it can be hypothesized that the CO oxidation is occurring very fast in relation to the diffusion of the gases through the filter region. Nearly all the CO is oxidized within a region  $\sim 100$  to  $120 \text{ nm}$  thick (see Fig. 1). Therefore, it is assumed that a filter of identical loading (0.08  $\text{mg Ru/cm}^2$ ) would perform similarly in front of a Pt electrode of any loading.

It is assumed that all oxygen reacts almost immediately within the filter region and that the hydroxyl groups produced then react with CO to produce  $\text{CO}_2$ . Even with 200 ppm CO tolerance, only one out 200  $\text{O}_2$  molecules is being used to oxidize CO. Further research into catalysts with lower activity than Ru with respect to hydrogen may provide even further CO oxidation by further shifting the selectivity of the oxygen reactions toward the oxidation of CO to  $\text{CO}_2$ .

### Conclusions

The sputter-deposited Ru filters developed here, containing less than 40% the amount of Ru (0.080 vs. 0.21  $\text{mg/cm}^2$ ) of the previous work,<sup>18</sup> achieved twice the CO tolerance (200 ppm CO vs. 100 ppm CO) under similar operating conditions ( $\text{H}_2 + 2\% \text{ O}_2$  anode feed, a cathode feed of air,  $70^\circ\text{C}$  operating temperature).

For an anode feedstream consisting of hydrogen, 200 ppm CO, and 2% oxygen, all MEAs containing Pt + Ru filter anodes showed increased CO tolerance compared to a Pt:Ru alloy containing similar amounts of Pt and Ru (0.150 and 0.080  $\text{mg/cm}^2$ , respectively). The

MEA containing a single sputter-deposited Ru filter exhibited greater CO tolerance than that of the MEA containing the ink-based Ru filter (0.205 vs. 0.149 A/cm<sup>2</sup> at 0.6 V).

Attaining 200 ppm CO tolerance by using 2% oxygen is equivalent to one out of 200 O<sub>2</sub> molecules being used to oxidize CO<sub>ads</sub> molecule, while the rest likely react with H<sup>+</sup> to form water. Catalysts with characteristics similar to Ru but with lower hydrogen activity would likely allow for a higher percentage of oxygen in the feed-stream to react with adsorbed CO, resulting in a more effective filter.

While the three-layered sputter-deposited Ru filter (filter 3) performed the worst of the three filters, its drop in performance (12%) as the CO in the anode feed was increased from 50 to 200 ppm (balance H<sub>2</sub> + an air bleed containing 2% O<sub>2</sub>) was the smallest of all the anodes tested. NCI accounts for 99.7% of the multilayered Ru filter thickness. Further research can be done to optimize this three-phase interface area of the Ru filter and eliminate the unused portion of the electrode, resulting in thinner, more effective filters. However, to generate a filter with a high number of Ru layers is neither the most economical (due to the time required to generate such a multilayered MEA) nor most effective approach. The generation of a continuous three-phase interface is the ultimate goal of this method and this is what should be pursued using the method of sputter deposition. Simultaneously sputter-depositing Ru and spray depositing NCI could produce a continuous three-phase interface region. This would result in an extremely thin (~1 μm) filter that may provide high Ru activity with minimal diffusional resistances. And by applying this Ru/C/Nafion filter in a single application to the PEM, the process is less time-consuming and thus more economical.

Because benefits of the Ru filter occur at high level air bleed (2% O<sub>2</sub>) and the Pt:Ru alloy provides CO tolerance even without air bleed, it is suggested that the anode configuration that would provide optimal CO tolerance would consist of a sputter-deposited Ru filter placed in front of and adjacent to a Pt:Ru alloy.

#### Acknowledgments

The authors acknowledge financial support from the National Institute of Standards and Technology under cooperative agreement no. 70NANB8H4039.

The University of South Carolina assisted in meeting the publication costs of this article.

#### References

1. M. A. Inbody, N. E. Vanderborgh, J. C. Hedstrom, and J. I. Tafeye, *Fuel Cell Seminar*, p. 624 (1996).
2. Y.-L. Cheng, L.-D. Chen, and J. P. Seaba, *Fuel Cell Power for Transportation*, SAE SP-1425, 55 (1999).
3. H. P. Dhar, L. G. Christner, A. K. Kush, and H. C. Maru, *J. Electrochem. Soc.*, **133**, 1574 (1986).
4. H. F. Oetjen, V. M. Schmidt, U. Stimming, and F. Trila, *J. Electrochem. Soc.*, **143**, 3838 (1996).
5. H. P. Dhar, L. G. Christner, and A. K. Kush, *J. Electrochem. Soc.*, **134**, 3021 (1987).
6. B. N. Grgur, N. M. Markovic, and P. N. Ross, *J. Electrochem. Soc.*, **146**, 1613 (1999).
7. R. J. Bellows, E. P. Marucci-Soos, and D. T. Buckley, *Ind. Chem. Eng. Rev.*, **35**, 1235 (1996).
8. M. Iwase and S. Kawatsu, in *Proton-Conducting Membrane Fuel Cells I*, S. Gottesfeld, G. Halpert, and A. Landgrebe, Editors, PV 95-23, p. 12, The Electrochemical Society Proceedings Series, Pennington, NJ (1995).
9. M. Watanabe, H. Igarashi, and T. Fujino, *J. Electroanal. Chem.*, **67**, 1194 (1999).
10. B. N. Grgur, N. M. Markovic, and P. N. Ross, Jr., in *Proton-Conducting Membrane Fuel Cells II*, S. Gottesfeld and T. F. Fuller, Editors, PV 98-27 p. 176, The Electrochemical Society Proceedings Series, Pennington, NJ (1999).
11. A. B. Anderson, E. Grantscharova, and P. Schiller, *J. Electrochem. Soc.*, **142**, 1880 (1995).
12. H. A. Gasteiger, N. M. Markovic, and P. N. Ross, Jr., *J. Phys. Chem.*, **99**, 8290 (1995).
13. H. A. Gasteiger, N. M. Markovic, P. N. Ross, Jr., *J. Phys. Chem.*, **99**, 16757 (1995).
14. R. J. Bellows, E. Marucci-Soos, and R. P. Reynolds, *Electrochem. Solid-State Lett.*, **1**, 69 (1998).
15. K. Wang, H. A. Gasteiger, N. M. Markovic, and P. N. Ross, Jr., *Electrochim. Acta*, **41**, 2587 (1996).
16. M. T. M. Koper, J. J. Lukkien, A. P. J. Jansen, and R. A. van Santen, *J. Phys. Chem.*, **103**, 5522 (1999).
17. V. M. Schmidt, H.-F. Oetjen, and J. Divisek, *J. Electrochem. Soc.*, **144**, L237 (1997).
18. A. Haug, R. E. White, J. W. Weidner, W. Huang, *J. Electrochem. Soc.*, **149**, A862 (2002).
19. N. M. Markovic, T. J. Schmidt, V. Stamenkovic, and P. N. Ross, *Fuel Cells*, **1**, 105 (2001).
20. N. M. Markovic, B. N. Grgur, C. A. Lucas, and P. N. Ross, *J. Phys. Chem. B*, **103**, 487 (1999).
21. K. Bleakley and P. Hu, *J. Am. Chem. Soc.*, **121**, 7644 (1999).
22. C. Zhang, P. Hu, and A. Alavi, *J. Am. Chem. Soc.*, **121**, 7931 (1999).
23. S. H. Oh and R. M. Sinkevitch, *J. Catal.*, **142**, 254 (1993).
24. N. M. Markovic, T. J. Schmidt, B. N. Grgur, H. A. Gasteiger, R. J. Behm, and P. N. Ross, *J. Phys. Chem.*, **103**, 8568 (1999).
25. E. Yeager, *J. Mol. Catal.*, **38**, 5 (1986).
26. E. Yeager, *Electrochim. Acta*, **29**, 1527 (1984).
27. A. Alavi, P. J. Hu, T. Deutsch, P. L. Silvestrelli, and J. Hutter, *Phys. Rev. Lett.*, **80**, 3650 (1998).
28. H.-I. Lee, G. Praline, and J. M. White, *Surf. Sci.*, **91**, 581 (1980).
29. H. A. Gasteiger, N. Markovic, P. N. Ross, and E. J. Cairns, *J. Phys. Chem.*, **98**, 617 (1994).
30. S. Wasmsus and A. Küver, *J. Electroanal. Chem.*, **461**, 14 (1999).
31. P. Ferreira-Aparicio, A. Guerrero-Ruiz, and I. Rodriguez-Ramos, *Appl. Catal., A*, **170**, 177 (1998).
32. P. Ferreira-Aparicio, I. Rodriguez-Ramos, J. A. Anderson, and A. Guerrero-Ruiz, *Appl. Catal., A*, **202**, 183 (2000).
33. P. Freni, G. Calogero, and S. Cavallaro, *J. Power Sources*, **87**, 28 (2000).
34. P. J. Berlowitz, C. H. F. Peden, and D. W. Goodman, *J. Phys. Chem.*, **92**, 5213 (1998).
35. R. Imbuhl, M. P. Cox, and G. Ertl, *J. Chem. Phys.*, **83**, 1578 (1985).
36. E. A. Ticianelli, C. R. Derouin, and S. Srinivasan, *J. Electroanal. Chem.*, **251**, 275 (1988).
37. S. Srinivasan, D. J. Manko, J. Koch, M. A. Enayattullah, and A. J. Appleby, *J. Power Sources*, **29**, 367 (1990).
38. E. A. Ticianelli, C. R. Derouin, A. Redondo, and S. Srinivasan, *J. Electrochem. Soc.*, **135**, 2209 (1988).
39. S. Mukerjee, S. Srinivasan, and A. J. Appleby, *Electrochim. Acta*, **38**, 1661 (1993).
40. S. Hirano, J. Kim, and S. Srinivasan, *Electrochim. Acta*, **42**, 1587 (1997).
41. C. K. Witham, W. Chun, T. I. Valdez, and S. R. Narayanan, *Electrochem. Solid-State Lett.*, **3**, 497 (2000).
42. G. L. Holleck, D. M. Pasquariello, and S. L. Clauson, in *Proton-Conducting Fuel Cells II*, S. Gottesfeld and T. F. Fuller, Editors, PV 98-27, p. 150, The Electrochemical Society Proceedings Series, Pennington, NJ (1999).
43. S. Y. Cha and W. M. Lee, *J. Electrochem. Soc.*, **146**, 4055 (1999).
44. A. T. Haug, R. E. White, J. W. Weidner, W. Huang, S. Shi, T. Stoner, and N. Rana, *J. Electrochem. Soc.*, **149**, A280 (2002).
45. M. S. Wilson, U.S. Pat. 5,211,984 (1993).
46. J. A. Poirier and G. E. Stoner, *J. Electrochem. Soc.*, **141**, 425 (1994).



# Extension of Newman's method to electrochemical reaction–diffusion in a fuel cell catalyst layer

Tianping Duan, John W. Weidner\*, Ralph E. White

*Department of Chemical Engineering, Center for Electrochemical Engineering, University of South Carolina, Columbia, SC 29208, USA*

Received 4 September 2001; accepted 9 October 2001

## Abstract

A numerical technique is developed for solving coupled electrochemical reaction–diffusion equations. Through analyzing the nonlinearity of the problem, a trial and error iterating procedure is constructed. The coefficient matrix is arranged as a tridiagonal form with elements of block matrix and is decomposed to *LU* form. A compact forward and backward substitution algorithm based on the shift of inverting block matrix by Gauss–Jordan full pivoting is developed. A large number of node points is required to converge the calculation. Computation experiences show that the iteration converges very quickly. The effects of inner diffusion on the electrochemical reaction are analyzed by numerical solutions. © 2002 Published by Elsevier Science B.V.

**Keywords:** Electrochemical reaction–diffusion; Non-linear analysis; Numerical algorithm; Convergence; Thiele modulus

## 1. Introduction

Industrial chemical reactions are usually accompanied with mass and energy transfer, either homogeneously or heterogeneously. Mathematical modeling for these processes is based on material and energy balance. One can generate a set of differential equations known as the reaction–diffusion problem. Owing to the strong nonlinearity of the reaction rate, mainly from the effect of temperature, reaction–diffusion equations are paid more attention in analyzing and designing chemical and catalytic reactors and are the major role in analyzing the nonlinear dynamic behaviors in reactor engineering. The same phenomena exist in electrochemical processes, with the add complexity of a varying potential field, and considerable research has been reviewed for electrochemical reactions occurring in the porous electrode [1].

Newman discussed the numerical solution of boundary-value problems consisting coupled ordinary differential equations which one can often met in chemical engineering science, and developed a unique technique to solve coupled, linear differential equations [2–4]. In his procedure, a large, sparse matrix was collapsed to a tridiagonal matrix with elements of block matrixes, which make it easy to be inversed in solving the algebraic equations transformed from

the original differential equations. Accordingly, the subroutine in his numerical method is called Newman's Band(*j*). White discussed Newman's method, and promoted this technique for wide application [5–7]. However, for solving reaction–diffusion equations—the nonlinear two-point boundary value problem, respective trial and error algorithms are needed. Shooting methods, such as Runge–Kutta integration scheme, is a marching technique that must be backwards processed from end point to beginning point to avoid inherent instability. This method is commonly used, but it depends on a proper choice of the initial value at the ending point. Linearizing the nonlinear kinetics term that convert the nonlinear differential equations into a linear one is called the linearization trial-and-error technique, but it does not guarantee that all steady state solutions can be determined. Compared with these two methods, transforming the nonlinear differential equations into nonlinear algebraic equations that are then solved by the Newton method did not receive the appropriate attention because the calculating time and storage is greater.

In this paper, we extend Newman's matrix method to solve coupled electrochemical reaction–diffusion equations—a coupled high nonlinear two-point boundary value problem that is encountered in modeling of a fuel cell catalyst layer. Based on Taylor expansion, a trial and error iteration algorithm is developed for solving the nonlinear algebraic equations transformed from the electrochemical reaction–diffusion equations. Owing to the adoption of

\* Corresponding author. Tel.: +1-803-777-3207; fax: +1-803-777-8265.  
E-mail address: weidner@engr.sc.edu (J.W. Weidner).

**Nomenclature**

$a$	specific interfacial area ( $\text{cm}^{-1}$ )
$c_0$	dimensionless form of $C_{H^+}$ ( $c_0 = C_{H^+}/C_{H_2}^0$ )
$c_1$	dimensionless form of $C_{H_2}$ ( $c_1 = C_{H_2}/C_{H_2}^0$ )
$c_2$	dimensionless electric potential in the solid matrix phase ( $c_2 = nf\phi_1$ )
$c_3$	dimensionless electric potential in the pore ionic phase ( $c_3 = nf\phi_2$ )
$C_{H^+}$	effective concentration of proton per unit volume of solution ( $\text{mol cm}^{-3}$ )
$C_{H_2}$	effective concentration of hydrogen per unit volume of solution ( $\text{mol cm}^{-3}$ )
$C_{H_2}^0$	initial effective concentration of hydrogen ( $\text{mol cm}^{-3}$ )
$D_{H_2}$	effective diffusion coefficient of hydrogen in pore phase ( $\text{cm}^2 \text{s}^{-1}$ )
$E^0$	formal potential (V)
$f$	constant ( $f = F/RT$ ( $\text{V}^{-1}$ ))
$F$	Faraday's constant ( $96485 \text{ C eq.}^{-1}$ )
$i$	total current density leaving the matrix phase ( $\text{A cm}^{-2}$ )
$i_1$	superficial electronic current density in the matrix ( $\text{A cm}^{-2}$ )
$i_2$	superficial ionic current density in pore phase ( $\text{A cm}^{-2}$ )
$I_{\text{cell}}$	current density of fuel cell, defined as positive ( $\text{A cm}^{-2}$ )
$k^0$	heterogeneous rate constant for hydrogen oxidation ( $\text{cm s}^{-1}$ )
$k_1$	dimensionless parameter ( $k_1 = nFI_{\text{cell}}/\sigma$ )
$k_2$	dimensionless parameter ( $k_2 = nFI_{\text{cell}}/\kappa$ )
$l$	thickness of anode catalyst layer (cm)
$n=2$	number of electrons transferred in electrode reaction ( $=2$ )
$N_{H_2}$	superficial flux density of hydrogen ( $\text{mol cm}^{-2} \text{s}^{-1}$ )
$R$	universal gas constant ( $8.314 \text{ J mol}^{-1} \text{K}^{-1}$ )
$R_{H_2}$	electrode reaction rate of hydrogen, defined as positive ( $\text{mol cm}^{-3} \text{s}^{-1}$ )
$T$	absolute temperature (K)
$U$	dimensionless formal potential ( $U = nfE^0$ )
$x$	dimensionless form of distance through porous electrode ( $x = X/l$ )
$X$	distance through porous electrode (cm)
<b>Greek symbols</b>	
$\alpha$	transfer coefficient
$\phi_1$	electric potential in the solid matrix phase (V)
$\phi_2$	electric potential in the pore ionic phase (V)
$\Phi$	Thiele modulus ( $\Phi^2 = al^2k^0/D_{H_2}$ )
$\Phi_1$	dimensionless parameter ( $\Phi_1^2 = an^2fFk^0l^2C_{H_2}^0/\sigma$ )
$\Phi_2$	dimensionless parameter ( $\Phi_2^2 = an^2fFk^0l^2C_{H_2}^0/\kappa$ )
$\kappa$	effective conductivity of the pore ionic (proton) phase ( $\Omega^{-1} \text{cm}^{-1}$ )
$\sigma$	effective conductivity of the solid matrix ( $\Omega^{-1} \text{cm}^{-1}$ )

Newman's unique method, in each iteration loop a compact forward substitution can be processed. In each forward or backward substitution, we use Gauss–Jordan full pivoting technique to guarantee the numerical stability. The whole computing is very fast, even though we set 2000 node points to make the substitution effectively. For a general case of an electrochemical reaction–diffusion process in a fuel cell catalyst layer, just two iteration loops can converge the solution. Using this method to study the effect of Thiele modulus on the electrochemical reaction–diffusion process, some intrinsic phenomena due to the nonlinear behavior of the system is found by numerical solution that is beneficial to analyze and scale-up a fuel cell system.

**2. Model equation**

We consider for the isothermal hydrogen oxidation reaction occurring in a porous catalyst layer of a fuel cell anode.



A schematic representation of it is shown in Fig. 1. The catalyst layer is viewed as a continuum of two phases, each phase either a pure ionic or electronic conductor. The ionic phase is considered a cationic selective polymer, such as Nafion. Therefore, the proton concentration throughout the catalyst layer is fixed. This uniform electrolyte concentration means the superficial current density in the pore ionic phase is due only to ion migration. This is represented mathematically as

$$i_2 = -\kappa \frac{d\phi_2}{dX} \quad (2)$$

The rate at which ionic current enters the pore solution,  $di_2/dX$ , is proportional to the reaction rate on a volumetric basis that is expressed by Butler–Volmer expression (defining anodic current as positive) [8]

$$\frac{di_2}{dX} = nFR_{H_2} = anFk^0 [C_{H_2} e^{(1-\alpha)nf(\phi_1 - \phi_2 - E^0)} - C_{H^+} e^{-\alpha nf(\phi_1 - \phi_2 - E^0)}] \quad (3)$$

The movement of electrons in the solid matrix phase of the porous electrode is governed by Ohm's law

$$i_1 = -\sigma \frac{d\phi_1}{dX} \quad (4)$$

The consequence of electroneutrality is that the divergence of the total current density is zero.

$$\frac{di}{dX} = \frac{di_1}{dX} + \frac{di_2}{dX} = 0 \quad (5)$$

The flux of dissolved hydrogen in the porous anode is determined by diffusion

$$N_{H_2} = -D_{H_2} \frac{dC_{H_2}}{dX} \quad (6)$$

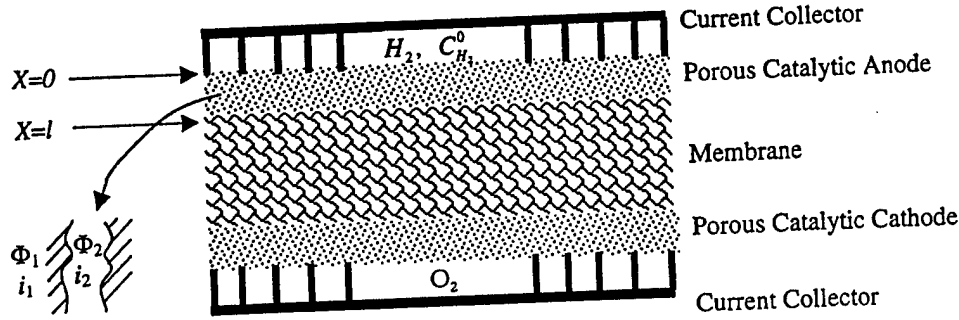


Fig. 1. Hydrogen oxidation in a fuel cell anode.

Material balance for this reaction–diffusion process can be modeled according to equation of continuity at steady state [9]

$$-\frac{dN_{H_2}}{dX} = R_{H_2} \quad (7)$$

Substituting Eq. (3), (6) into Eq. (7) yields

$$D_{H_2} \frac{d^2 C_{H_2}}{dX^2} = ak^0 [C_{H_2} e^{(1-\alpha)nf(\phi_1 - \phi_2 - E^0)} - C_{H^+} e^{-\alpha nf(\phi_1 - \phi_2 - E^0)}] \quad (8)$$

Differentiating Eqs. (2) and (4) and substituting Eq. (3) into the resulting equation gives

$$\sigma \frac{d^2 \phi_1}{dX^2} = nFak^0 [C_{H_2} e^{(1-\alpha)nf(\phi_1 - \phi_2 - E^0)} - C_{H^+} e^{-\alpha nf(\phi_1 - \phi_2 - E^0)}] \quad (9)$$

$$\kappa \frac{d^2 \phi_2}{dX^2} = -nFak^0 [C_{H_2} e^{(1-\alpha)nf(\phi_1 - \phi_2 - E^0)} - C_{H^+} e^{-\alpha nf(\phi_1 - \phi_2 - E^0)}] \quad (10)$$

Boundary conditions:

1. @  $X = 0$ ,

$$C_{H_2} = C_{H_2}^0 \quad (11)$$

$$\frac{d\phi_1}{dX} = -\frac{I_{cell}}{\sigma} \quad (12)$$

$$\phi_2 = 0 \quad (13)$$

2. @  $X = l$ ,

$$\frac{dC_{H_2}}{dX} = 0 \quad (14)$$

$$\frac{d\phi_1}{dX} = 0 \quad (15)$$

$$\frac{d\phi_2}{dX} = -\frac{I_{cell}}{\kappa} \quad (16)$$

Setting the following dimensionless variables and parameters

$$c_0 = \frac{C_{H^+}}{C_{H_2}^0}, \quad c_1 = \frac{C_{H_2}}{C_{H_2}^0}, \quad c_2 = nf\phi_1, \quad c_3 = nf\phi_2,$$

$$x = \frac{X}{l}, \quad \Phi^2 = a \frac{k^0 l^2}{D_{H_2}} \text{ (Thiele modulus)}, \quad U = nfE^0,$$

$$\Phi_1^2 = \frac{an^2 f F k^0 l^2 C_{H_2}^0}{\sigma}, \quad \Phi_2^2 = \frac{an^2 f F k^0 l^2 C_{H_2}^0}{\kappa},$$

$$k_1 = \frac{nf l}{\sigma} I_{cell}, \quad k_2 = \frac{nf l}{\kappa} I_{cell}$$

Then Eqs. (8), (10) and (11) are reduced to the dimensionless form

$$\frac{d^2 c_1}{dx^2} = \Phi^2 [c_1 e^{(1-\alpha)(c_2 - c_3 - U)} - c_0 e^{-\alpha(c_2 - c_3 - U)}] \quad (17)$$

$$\frac{d^2 c_2}{dx^2} = \Phi_1^2 [c_1 e^{(1-\alpha)(c_2 - c_3 - U)} - c_0 e^{-\alpha(c_2 - c_3 - U)}] \quad (18)$$

$$\frac{d^2 c_3}{dx^2} = -\Phi_2^2 [c_1 e^{(1-\alpha)(c_2 - c_3 - U)} - c_0 e^{-\alpha(c_2 - c_3 - U)}] \quad (19)$$

Boundary conditions:

1. @  $x = 0$ ,

$$c_1 = 1 \quad (20)$$

$$\frac{dc_2}{dx} = -k_1 \quad (21)$$

$$c_3 = 0 \quad (22)$$

2. @  $x = 1$ ,

$$\frac{dc_1}{dx} = 0 \quad (23)$$

$$\frac{dc_2}{dx} = 0 \quad (24)$$

$$\frac{dc_3}{dx} = -k_2 \quad (25)$$

Although the above model Eqs. (17)–(25) are for an isothermal system, due to the unique nonlinear characteristics of the electrochemical reaction term that is similar to the effect of temperature on a chemical reaction rate, the numerical solving method for these electrochemical reaction–diffusion equations can be transformed to study non-isothermal problems.

### 3. Numerical solution

For solving the model Eqs. (17)–(25), they are cast into sets of nonlinear algebraic equations approximated by finite difference. Then an iterative algorithm is constructed based on the Taylor expansion. However, if one adds the Eqs. (17)–(19) together to try to eliminate the nonlinear term, the computation is not stable. Analyzing the computing process on a microcomputer with eight word bits for a double precision real showed that the block matrixes were ill-conditioned. The condition numbers are too large to inverse the coefficient block matrixes correctly due to the error accumulation even for the second node point.

Therefore, at each node point except the boundary points, the second-order derivatives can be approximated by three point central difference accurate to  $O(h^2)$ . For example, Eq. (17) is approximated as

$$c_1(j-1) - 2c_1(j) + c_1(j+1) - h^2 \Phi^2 (c_1(j) e^{(1-\alpha)[c_2(j)-c_3(j)-U]} - c_0 e^{-\alpha[c_2(j)-c_3(j)-U]}) = 0 \quad (26)$$

If there are enough node points, we can suppose that the difference equation at node point  $j$ , such as Eq. (26), depends

only on the variables at three points. If the left-hand term is expressed as  $F_{1,j}$ , then the Taylor series expands it to accuracy  $O(h^2)$  as

$$\begin{aligned} F_{1,j}(c_1(j-1), c_1(j), c_1(j+1), c_2(j), c_3(j)) \\ = c_1^0(j-1) - 2c_1^0(j) + c_1^0(j+1) \\ - h^2 \Phi^2 [c_1^0(j) e^{(1-\alpha)[c_2^0(j)-c_3^0(j)-U]} - c_0 e^{-\alpha[c_2^0(j)-c_3^0(j)-U]}] \\ + [c_1(j-1) - c_1^0(j-1)] \frac{\partial F_{1,j}}{\partial c_{1,j-1}} \bigg|_0 + [c_1(j) - c_1^0(j)] \frac{\partial F_{1,j}}{\partial c_{1,j}} \bigg|_0 \\ + [c_1(j+1) - c_1^0(j+1)] \frac{\partial F_{1,j}}{\partial c_{1,j+1}} \bigg|_0 + [c_2(j) - c_2^0(j)] \frac{\partial F_{1,j}}{\partial c_{2,j}} \bigg|_0 \\ + [c_3(j) - c_3^0(j)] \frac{\partial F_{1,j}}{\partial c_{3,j}} \bigg|_0 = 0 \end{aligned} \quad (27)$$

Substituting corresponding partial derivatives and introducing

$$\begin{aligned} r_0 &= e^{(1-\alpha)[c_2^0(j)-c_3^0(j)-U]}, \\ r_{j0} &= c_1^0(j) e^{(1-\alpha)[c_2^0(j)-c_3^0(j)-U]} - c_0 e^{-\alpha[c_2^0(j)-c_3^0(j)-U]}, \\ r_{c_0} &= (1-\alpha)c_1^0(j) e^{(1-\alpha)[c_2^0(j)-c_3^0(j)-U]} + \alpha c_0 e^{-\alpha[c_2^0(j)-c_3^0(j)-U]} \end{aligned} \quad (28)$$

it can be simplified as a more compact matrix form.

$$\begin{aligned} [1 \ 0 \ 0] \begin{pmatrix} c_{1,j-1} \\ c_{2,j-1} \\ c_{3,j-1} \end{pmatrix} + [-(2+h^2 \Phi^2 r_0) \ -h^2 \Phi^2 r_{c_0} \ h^2 \Phi^2 r_{c_0}] \begin{pmatrix} c_{1,j} \\ c_{2,j} \\ c_{3,j} \end{pmatrix} + [1 \ 0 \ 0] \begin{pmatrix} c_{1,j+1} \\ c_{2,j+1} \\ c_{3,j+1} \end{pmatrix} \\ = [-h^2 \Phi^2 r_0 \ -h^2 \Phi^2 r_{c_0} \ h^2 \Phi^2 r_{c_0}] \begin{pmatrix} c_{1,j}^0 \\ c_{2,j}^0 \\ c_{3,j}^0 \end{pmatrix} + h^2 \Phi^2 r_{j0}, \quad 0 < j < N \end{aligned} \quad (29)$$

In the same way, model Eqs. (18) and (19) can be approximated as Eqs. (30) and (31), respectively,

$$\begin{aligned} [0 \ 1 \ 0] \begin{pmatrix} c_{1,j-1} \\ c_{2,j-1} \\ c_{3,j-1} \end{pmatrix} + [-h^2 \Phi_1^2 r_0 \ -(2+h^2 \Phi_1^2 r_{c_0}) \ h^2 \Phi_1^2 r_{c_0}] \begin{pmatrix} c_{1,j} \\ c_{2,j} \\ c_{3,j} \end{pmatrix} + [0 \ 1 \ 0] \begin{pmatrix} c_{1,j+1} \\ c_{2,j+1} \\ c_{3,j+1} \end{pmatrix} \\ = [-h^2 \Phi_1^2 r_0 \ -h^2 \Phi_1^2 r_{c_0} \ h^2 \Phi_1^2 r_{c_0}] \begin{pmatrix} c_{1,j}^0 \\ c_{2,j}^0 \\ c_{3,j}^0 \end{pmatrix} + h^2 \Phi_1^2 r_{j0}, \quad 0 < j < N \end{aligned} \quad (30)$$

$$\begin{aligned} [0 \ 0 \ 1] \begin{pmatrix} c_{1,j-1} \\ c_{2,j-1} \\ c_{3,j-1} \end{pmatrix} + [h^2 \Phi_2^2 r_0 \ h^2 \Phi_2^2 r_{c_0} \ -(2+h^2 \Phi_2^2 r_{c_0})] \begin{pmatrix} c_{1,j} \\ c_{2,j} \\ c_{3,j} \end{pmatrix} + [0 \ 0 \ 1] \begin{pmatrix} c_{1,j+1} \\ c_{2,j+1} \\ c_{3,j+1} \end{pmatrix} \\ = [h^2 \Phi_2^2 r_0 \ h^2 \Phi_2^2 r_{c_0} \ -h^2 \Phi_2^2 r_{c_0}] \begin{pmatrix} c_{1,j}^0 \\ c_{2,j}^0 \\ c_{3,j}^0 \end{pmatrix} - h^2 \Phi_2^2 r_{j0}, \quad 0 < j < N, \end{aligned} \quad (31)$$

Letting

$$C(j) = (c_{1,j} \ c_{2,j} \ c_{3,j})^T, \quad 0 \leq j \leq N \quad (32)$$

then Eqs. (29)–(31) become

$$A(j)C(j-1) + B(j)C(j) + D(j)C(j+1) = G(j), \quad 0 < j < N, \quad (33)$$

in which

$$\begin{aligned} A(j) &= \begin{pmatrix} 1 & 0 & 0 \\ 0 & 1 & 0 \\ 0 & 0 & 1 \end{pmatrix}, \\ B(j) &= \begin{pmatrix} -(2+h^2\Phi^2r_0) & -h^2\Phi^2r_{c0} & h^2\Phi^2r_{c0} \\ -h^2\Phi_1^2r_0 & -(2+h^2\Phi_1^2r_{c0}) & h^2\Phi_1^2r_{c0} \\ h^2\Phi_2^2r_0 & h^2\Phi_2^2r_{c0} & -(2+h^2\Phi_2^2r_{c0}) \end{pmatrix}, \\ D(j) &= \begin{pmatrix} 1 & 0 & 0 \\ 0 & 1 & 0 \\ 0 & 0 & 1 \end{pmatrix}, \\ G(j) &= \begin{pmatrix} -h^2\Phi^2r_0 & -h^2\Phi^2r_{c0} & h^2\Phi^2r_{c0} \\ -h^2\Phi_1^2r_0 & -h^2\Phi_1^2r_{c0} & h^2\Phi_1^2r_{c0} \\ h^2\Phi_2^2r_0 & h^2\Phi_2^2r_{c0} & -h^2\Phi_2^2r_{c0} \end{pmatrix} \begin{pmatrix} c_{1,j}^0 \\ c_{2,j}^0 \\ c_{3,j}^0 \end{pmatrix} \\ &\quad + \begin{pmatrix} h^2\Phi^2r_{j0} \\ h^2\Phi_1^2r_{j0} \\ -h^2\Phi_2^2r_{j0} \end{pmatrix} \end{aligned} \quad (34)$$

Two-point boundary conditions are approximated by three point forward or backward difference accurate to  $O(h^2)$  and are also expressed as a compact matrix form

$$B(0)C(0) + D(0)C(1) + XC(2) = G(0), \quad j = 0 \quad (35)$$

and

$$YC(N-2) + A(N)C(N-1) + B(N)C(N) = G(N), \quad j = N \quad (36)$$

where

$$\begin{aligned} B(0) &= \begin{pmatrix} 1 & 0 & 0 \\ 0 & 3 & 0 \\ 0 & 0 & 1 \end{pmatrix}, \quad D(0) = \begin{pmatrix} 0 & 0 & 0 \\ 0 & -4 & 0 \\ 0 & 0 & 0 \end{pmatrix}, \\ X &= \begin{pmatrix} 0 & 0 & 0 \\ 0 & 1 & 0 \\ 0 & 0 & 0 \end{pmatrix}, \quad G(0) = \begin{pmatrix} 1 \\ 2hk_1 \\ 0 \end{pmatrix} \quad (37) \\ Y &= \begin{pmatrix} 1 & 0 & 0 \\ 0 & 1 & 0 \\ 0 & 0 & 1 \end{pmatrix}, \quad A(N) = \begin{pmatrix} -4 & 0 & 0 \\ 0 & -4 & 0 \\ 0 & 0 & -4 \end{pmatrix}, \\ B(N) &= \begin{pmatrix} 3 & 0 & 0 \\ 0 & 3 & 0 \\ 0 & 0 & 3 \end{pmatrix}, \quad G(N) = \begin{pmatrix} 0 \\ 0 \\ -2hk_2 \end{pmatrix} \quad (38) \end{aligned}$$

Eqs. (33), (35) and (36) can be rewritten as a matrix form

$$\begin{bmatrix} B(0) & D(0) & X \\ A(1) & B(1) & D(1) \\ & \vdots & \vdots \\ & & A(j) & B(j) & D(j) \\ & & \vdots & \vdots & \vdots \\ & & & A(N-1) & B(N-1) & D(N-1) \\ & & & Y & A(N) & B(N) \end{bmatrix} \begin{bmatrix} C(0) \\ C(1) \\ \vdots \\ C(j) \\ \vdots \\ C(N-1) \\ C(N) \end{bmatrix} = \begin{bmatrix} G(0) \\ G(1) \\ \vdots \\ G(j) \\ \vdots \\ G(N-1) \\ G(N) \end{bmatrix} \quad (39)$$

The block matrixes  $B(j)$  and vectors  $G(j)$  at node points  $0 < j < N$  are not determined due to the variables at expanded points (with superscript 0) being unknown. As a result, the tridiagonal matrix algebraic Eq. (39) cannot be solved directly. But if these unknown values at expanded points are guessed as trial values, then Eq. (39) can be solved. For a tridiagonal matrix algebraic equation, a compact forward and backward substitution algorithm can solve it quickly. This algorithm, at first, decomposes the tridiagonal matrix into a  $LU$  form. Then in the forward substituting, an intermediate vector will be acquired, and in the backward substituting, the variable vector can be obtained. In all the process of  $LU$  decomposition and forward and backward substitution, the Gauss–Jordan full pivoting algorithm is needed to inverse the block matrixes. Then the block matrix in the lower and upper matrix, the intermediate vector, and, at last, the variable vector can be solved. These solved variables are based on guessed values, they are not the real solution for the problem. They are set as new guessed values in the block matrixes  $B(j)$  and  $G(j)$  and reproduce the whole procedure. The iteration will not stop until the setting accuracy is reached, which makes the solutions satisfy the whole difference equations at each node point.

The procedure is illustrated as follows. When the values for determining the  $B(j)$  and  $G(j)$  are guessed, then the coefficient matrix in Eq. (39) can be decomposed

$$\begin{bmatrix} B(0) & D(0) & X \\ A(1) & B(1) & D(1) \\ & \vdots & \vdots \\ & & A(j) & B(j) & D(j) \\ & & \vdots & \vdots & \vdots \\ & & & A(N-1) & B(N-1) & D(N-1) \\ & & & Y & A(N) & B(N) \end{bmatrix}$$

$$= \underbrace{\begin{bmatrix} \bar{B}(0) & & & & \\ \bar{A}(1) & \bar{B}(1) & & & \\ & \vdots & \vdots & & \\ & & \bar{A}(j) & \bar{B}(j) & \\ & & & \vdots & \vdots \\ & & & & \bar{A}(N-1) & \bar{B}(N-1) \\ & & & & \bar{Y}(N) & \bar{A}(N) & \bar{B}(N) \end{bmatrix}}_L \quad (40)$$

$$\underbrace{\begin{bmatrix} I & \bar{D}(0) & \bar{X} & & \\ & I & \bar{D}(1) & & \\ & & \vdots & \vdots & \\ & & & I & \bar{D}(j) \\ & & & & \vdots & \vdots \\ & & & & & I & \bar{D}(N-1) \\ & & & & & & I \end{bmatrix}}_U$$

Through the shift of matrixes, the block matrix in the  $L$  and  $U$  matrixes can be solved. For  $j = 0, 1$ , we have

$$\bar{B}(0) = B(0), \quad \bar{X} = \bar{B}^{-1}(0)X, \quad \bar{D}(0) = \bar{B}^{-1}(0)D(0) \quad (41)$$

$$\bar{A}(1) = A(1), \quad \bar{B}(1) = B(1) - A(1)\bar{D}(1), \quad (42)$$

$$\bar{D}(1) = \bar{B}^{-1}(1)D(1) - \bar{B}^{-1}(1)A(1)\bar{X}$$

As the same way, for other node points at  $j = 2, \dots, N-1$ ,

$$\bar{A}(j) = A(j), \quad \bar{B}(j) = B(j) - \bar{A}(j)\bar{D}(j-1), \quad (43)$$

$$\bar{D}(j) = \bar{B}^{-1}(j)D(j)$$

can be solved. At the last node point  $j = N$ , we obtain

$$\bar{Y}(N) = Y, \quad \bar{A}(N) = A(N) - \bar{Y}(N)\bar{D}(N-2), \quad (44)$$

$$\bar{B}(N) = B(N) - \bar{A}(N)\bar{D}(N-1)$$

Then Eq. (41) can be solved through the solution of two sets of matrix algebraic equations.

$$\underbrace{\begin{bmatrix} \bar{B}(0) & & & & \\ \bar{A}(1) & \bar{B}(1) & & & \\ & \vdots & \vdots & & \\ & & \bar{A}(j) & \bar{B}(j) & \\ & & & \vdots & \vdots \\ & & & & \bar{A}(N-1) & \bar{B}(N-1) \\ & & & & \bar{Y}(N) & \bar{A}(N) & \bar{B}(N) \end{bmatrix}}_L$$

$$\underbrace{\begin{bmatrix} W(0) \\ W(1) \\ \vdots \\ W(j) \\ \vdots \\ W(N-1) \\ W(N) \end{bmatrix}}_W = \underbrace{\begin{bmatrix} G(0) \\ G(1) \\ \vdots \\ G(j) \\ \vdots \\ G(N-1) \\ G(N) \end{bmatrix}}_G \quad (45)$$

and

$$\underbrace{\begin{bmatrix} I & \bar{D}(0) & \bar{X} & & \\ & I & \bar{D}(1) & & \\ & & \vdots & \vdots & \\ & & & I & \bar{D}(j) \\ & & & & \vdots & \vdots \\ & & & & & I & \bar{D}(N-1) \\ & & & & & & I \end{bmatrix}}_U$$

$$\times \underbrace{\begin{bmatrix} C(0) \\ C(1) \\ \vdots \\ C(j) \\ \vdots \\ C(N-1) \\ C(N) \end{bmatrix}}_C = \underbrace{\begin{bmatrix} W(0) \\ W(1) \\ \vdots \\ W(j) \\ \vdots \\ W(N-1) \\ W(N) \end{bmatrix}}_W \quad (46)$$

The intermediate vector  $W(j)$ ,  $j = 0, \dots, N$  in Eq. (45) can be determined by forward substituting

$$W(0) = \bar{B}^{-1}(0)G(0) \quad (47)$$

$$W(1) = \bar{B}^{-1}(1)G(1) - \bar{B}^{-1}(1)\bar{A}(1)W(0) \quad (48)$$

$$W(j) = \bar{B}^{-1}(j)G(j) - \bar{B}^{-1}(j)\bar{A}(j)W(j-1) \quad (49)$$

$$W(N) = \bar{B}^{-1}(N)G(N) - \bar{B}^{-1}(N)\bar{Y}(N)W(N-2) - \bar{B}^{-1}(N)\bar{A}(N)W(N-1) \quad (50)$$

With backward substituting, the solution vector  $C(j)$ ,  $j = 0, N$  are solved.

$$C(N) = W(N) \quad (51)$$

$$C(N-1) = W(N-1) - \bar{D}(N-1)C(N) \quad (52)$$

$$C(j) = W(j) - \bar{D}(j)C(j+1) \quad (53)$$

$$C(0) = W(0) - \bar{D}(0)C(1) - \bar{X}C(2) \quad (54)$$

The solved  $C(j)$  are as new guessed values to determine the block matrixes  $B(j)$  and  $G(j)$ ,  $j = 1, \dots, N - 1$  and to continually carry out the iteration, until the approximated solutions are obtained.

## 4. Results and discussion

### 4.1. Convergence

To test the solving technique, we chose a set of physical-chemical parameters shown in Table 1 that are common used for hydrogen oxidation in a fuel cell anode, then the following dimensionless model parameters are obtained

$$c_0 = 0.5714, \quad \alpha = 0.5, \quad U = 0, \\ \Phi^2 = 0.1406, \quad \Phi_1^2 = \Phi_2^2 = 0.8277$$

Different currents density ( $0.2\text{--}1.6 \text{ A cm}^{-2}$ ) at two-point boundary that make  $k_1$  and  $k_2$  change between  $0.2191\text{--}1.7526$  were adopted. A Fortran 95 code was developed to do the numerical solution on a micro computer (Dell, Dimension 4100, Pentium III, 260 MB memory). After the number of node points was determined and a set of proper initial values were guessed for each variables at all the node points, the iterating process was carried out. It converged very quickly in just two loops. The numerical results are illustrated as Figs. 2–5.

It was found that a large number of node points, for example,  $>1000$ , is required to converge the iteration. We set it as 2000. Setting too many node points is the need for our assumption in the Taylor expansion that the nonlinear difference equation at node point  $j$ , depends only on variables at the three points. The iteration precision was chosen as  $10^{-4}$ . The zero in the right-hand side of the sets of nonlinear algebraic equations in the form of Eq. (26) is approximated by this value. If all the absolute values of computation for the terms in the left-hand side are not  $>10^{-4}$ , then the iteration processes stop. For the case of 2000 node points, correspondingly, there are 6000 algebraic

Table 1  
Common physical-chemical parameters in modeling the hydrogen oxidation in a fuel cell anode

Parameter	Value
$a \text{ (cm}^{-1}\text{)}$	250
$C_{H^+} \text{ (mol cm}^{-3}\text{)}$	$0.4 \times 10^{-4}$
$C_{H_2}^0 \text{ (mol cm}^{-3}\text{)}$	$0.7 \times 10^{-4}$ ; $0.38 \times 10^{-4}$ for $\Phi = 0.15$
$D_{H_2} \text{ (cm}^2 \text{ s}^{-1}\text{)}$	$2 \times 10^{-4}$
$I_{\text{cell}} \text{ (A cm}^{-2}\text{)}$	$0.2\text{--}1.6$
$k^0 \text{ (cm s}^{-1}\text{)}$	0.45
$l \text{ (cm)}$	$5 \times 10^{-4}$
$T \text{ (K)}$	353.15
$U$	0
$\alpha$	0.5
$\kappa \text{ (}\Omega^{-1} \text{ cm}^{-1}\text{)}$	$0.3 \times 10^{-1}$
$\sigma \text{ (}\Omega^{-1} \text{ cm}^{-1}\text{)}$	$0.3 \times 10^{-1}$

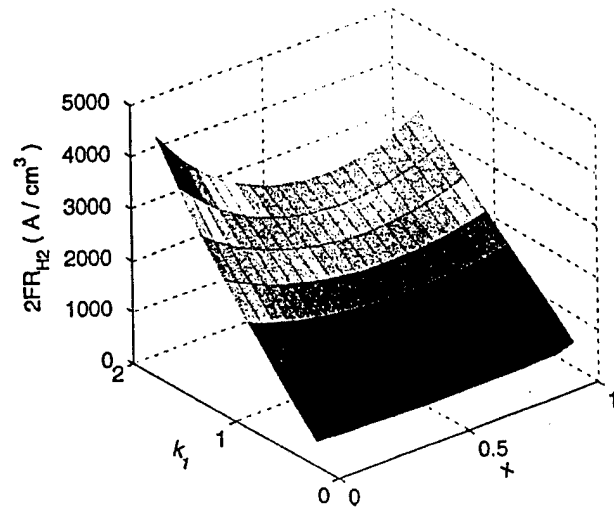


Fig. 2. Distribution of electrochemical reaction rate of hydrogen along  $x$  at different  $k_1$  (current).

equations like Eq. (26) except those at the two-point boundary. Like all trial and error iteration algorithm, different initial estimations yield different results, in order to make the solution meet the physical meanings in the system, following current criteria are introduced in our computing to determine the initial trial solution and check the results

$$i_1 = -\sigma \frac{d\Phi_1}{dx} \Big|_{x=0} = I_{\text{cell}} \quad (55)$$

$$i_1 = -\sigma \frac{d\Phi_1}{dx} \Big|_{x=l} = 0 \quad (56)$$

$$i_2 = -\kappa \frac{d\Phi_2}{dx} \Big|_{x=l} = I_{\text{cell}} \quad (57)$$

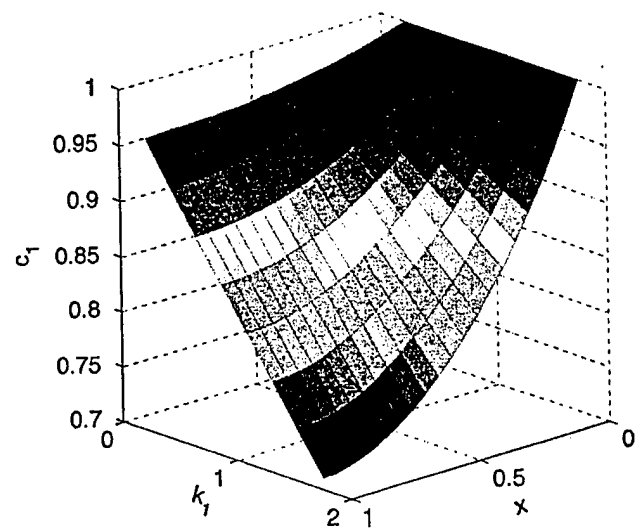


Fig. 3. Distribution of dimensionless hydrogen concentration  $c_1$  along  $x$  at different  $k_1$  (current).

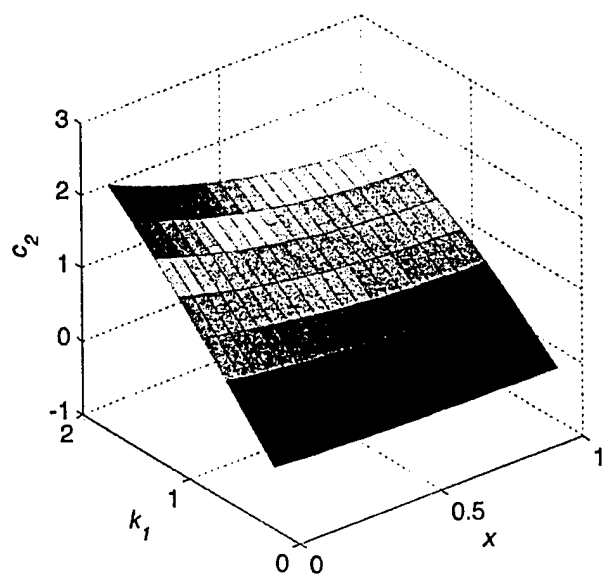


Fig. 4. Distribution of dimensionless potential in matrix along  $x$  at different  $k_1$  (current).

$$i_2 = -\kappa \frac{d\Phi_2}{dx} \Big|_{x=0} = 0 \quad (58)$$

$$I_{\text{cell}} = \int_0^l \frac{di_2}{dx} dx \quad (59)$$

For Eqs. (55)–(58), the five point formula of numerical differential are adopted to calculate the potential gradient. For Eq. (59), complex Simpson's method is used to calculate the integration along the catalyst layer. All the calculations in these five equations are based on the data obtained from the numerical solution of the model equations.

#### 4.2. Characteristics of electrochemical reaction–diffusion

The characteristics of reaction–diffusion problems are usually analyzed by the Thiele modulus  $\Phi$  [10]. We changed the model parameters that is shown in Table 2 to get different Thiele modulus  $\Phi$  in a range of 0.008–10, and corresponding electrochemical Thiele modulus  $\Phi_1$  and  $\Phi_2$  in a range of 0.01–8.06 and 0.02–10.95, respectively. The numerical solutions converge to the results very fast too, two loops of iteration for all case. The results are showed in Figs. 6–9.

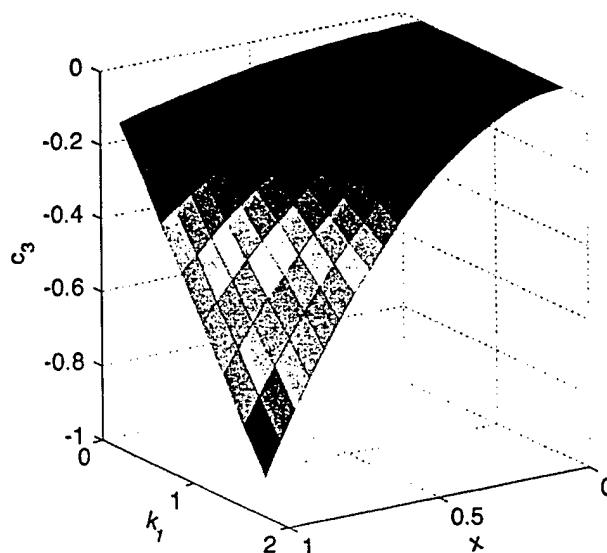


Fig. 5. Distribution of dimensionless potential in pore solution  $c_3$  along  $x$  at different  $k_1$  (current).

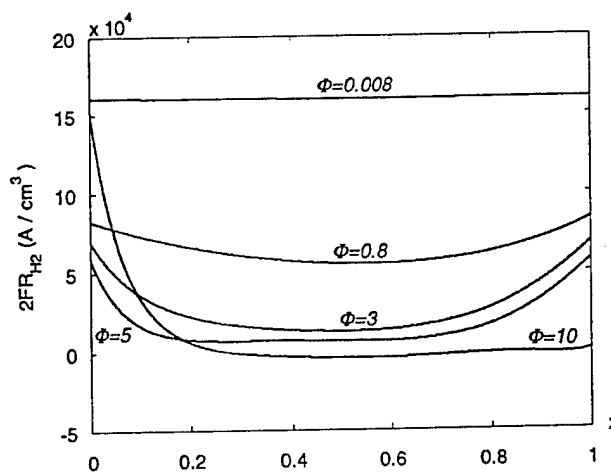


Fig. 6. Dependence of reaction rate on Thiele modulus, the parameters corresponding to these values of  $\Phi$  are shown in Table 2.

When the Thiele modulus is low, such as  $\Phi = 0.008$ , the resistance of diffusion can be neglected, the distributions of reaction rate and hydrogen concentration are nearly uniform. When the Thiele modulus becomes larger, the diffusion

Table 2

Parameters for studying the dependence of hydrogen electro-oxidation reaction–diffusion on Thiele modulus in Figs. 6–9<sup>a</sup>

$\Phi$	$\Phi_1$	$\Phi_2$	$D_{H_2}$ (cm <sup>2</sup> s <sup>-1</sup> )	$k^0$ (cm s <sup>-1</sup> )	$l$ (cm)	$\sigma$ (Ω <sup>-1</sup> cm <sup>-1</sup> )	$\kappa$ (Ω <sup>-1</sup> cm <sup>-1</sup> )
0.008	0.012	0.018	$2.0 \times 10^{-4}$	0.45	$0.1 \times 10^{-4}$	$0.6 \times 10^{-1}$	$0.3 \times 10^{-1}$
0.8	0.41	1.85	$0.1 \times 10^{-4}$	$0.4 \times 10^2$	$0.25 \times 10^{-4}$	$0.3 \times 10^{-1}$	$0.15 \times 10^{-2}$
3	1.41	4.71	$0.08 \times 10^{-4}$	$0.8 \times 10^2$	$0.6 \times 10^{-4}$	$0.3 \times 10^{-1}$	$0.268 \times 10^{-2}$
5	1.73	6.42	$0.08 \times 10^{-4}$	$0.8 \times 10^2$	$1.0 \times 10^{-4}$	$0.55 \times 10^{-1}$	$0.40 \times 10^{-2}$
10	8.06	10.95	$0.08 \times 10^{-4}$	$0.8 \times 10^2$	$2.0 \times 10^{-4}$	$0.1 \times 10^{-1}$	$0.55 \times 10^{-2}$

<sup>a</sup> Non-changing parameters:  $C_{H^+} = 0.4 \times 10^{-4}$  mol cm<sup>-3</sup>;  $C_{H_2} = 0.65 \times 10^{-4}$  mol cm<sup>-3</sup>;  $I_{\text{cell}} = 1.6$  A cm<sup>-2</sup>;  $T = 353.15$  K;  $U = 0$ ;  $a = 0.5$ .



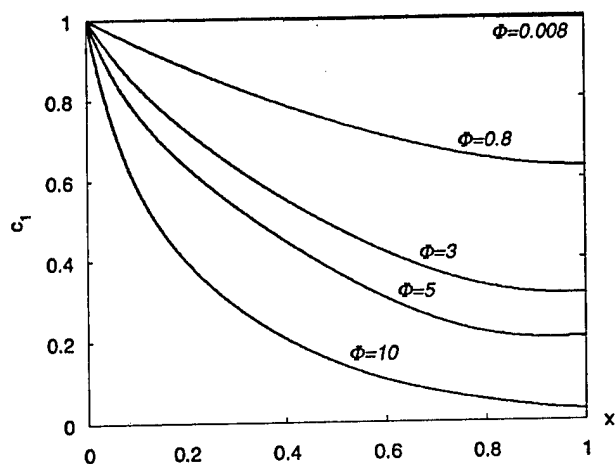


Fig. 7. Dependence of dimensionless hydrogen concentration on Thiele modulus, the parameters corresponding to these values of  $\Phi$  are shown in Table 2.

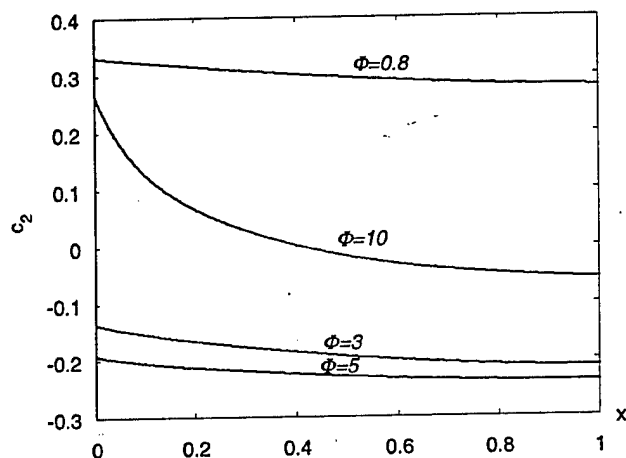


Fig. 8. Dependence of dimensionless potential in matrix on Thiele modulus, the parameters corresponding to these values of  $\Phi$  are shown in Table 2.

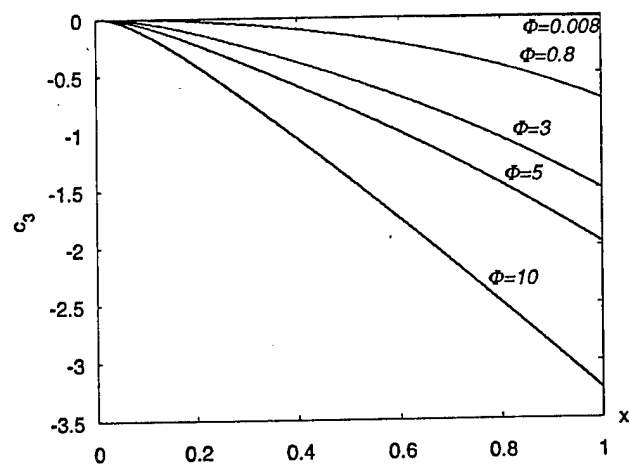


Fig. 9. Dependence of dimensionless potential in solution on Thiele modulus, the parameters to these values of  $\Phi$  are shown in Table 2.

resistance increases, as a result, the reaction is not uniform along the catalyst layer, the larger the Thiele modulus is, the more non-uniform the reaction rate is. When the Thiele modulus is equal to 10, the reaction rate and hydrogen concentration decreases rapidly in the region near the surface of porous catalyst layer. It should be pointed out that in high Thiele modulus region, the rate of mass transfer by diffusion cannot meet the rate of electrochemical reaction, the process will lose its stability and become a dissipative system. As the same case in the stability issues in chemical reaction engineering, our numerical computing also found sensitive dependence of the solution results on some parameters when the Thiele modulus is high. It has been reported by a large amount of literature that in open chemical reaction system, especially coupled nonlinear chemical reaction and diffusion occur simultaneously, many complex phenomena will take place, such as multiple steady states, unstable states and self-generated sustained oscillations. Our present work just makes a beginning in this field, further attention should be paid to it because the electrochemical oxidation reaction rate of hydrogen is very fast under the catalysis of platinum catalyst. When a fuel cell stack is needed to scale up, it is necessary to know the dissipative behavior.

## 5. Conclusion

A numerical solution method is developed for coupled electrochemical reaction–diffusion equations. Even though the convergence of this technique depends mainly on the large number of node points, computation experiences on a microcomputer with double precision real only eight word bites shows that the procedure converges very fast. After the Taylor series is expanded and the corresponding iterating procedure is constructed, the computation process is stable. Arranging the elements in the coefficient matrix to block matrix form, the whole coefficient matrix is easily decomposed to lower and upper matrix, and the compact forward and backward substitution algorithm based on the shift of block matrixes with Gauss–Jordan full pivoting method can perform the numerical calculation quickly. Local convergence depends on the first trial solution, current criteria are required to make the solution converge to the correct results. It is suggested by the model solutions that dissipative behaviors in a electrochemical reaction–diffusion system might occur when the Thiele modulus is high.

## Acknowledgements

This work was sponsored by the US Army Communications and Electronics Command under contact number (NRO-00-C-0134). The first author also got financial support from the China Scholarship Council (CSC, no. 99851035) and youth fund of Sichuan University.

## References

- [1] J. Newman, W. Tiedemann, *AIChE J.* 21 (1) (1975) 25.
- [2] J. Newman, *Ind. Eng. Chem. Fundam.* 7 (1968) 514.
- [3] J. Newman, *Electrochem. Chem.* 6 (1973) 187.
- [4] J. Newman, *Electrochemical Systems*, Appendix C, Prentice-Hall, Englewood Cliff, NJ, 1992, p. 539.
- [5] R.E. White, *Ind. Eng. Chem. Fundam.* 17 (4) (1978) 367.
- [6] D. Fan, R.E. White, *Comput. Chem. Eng.* 15 (11) (1991a) 797.
- [7] D. Fan, R.E. White, *J. Electrochem. Soc.* 138 (6) (1991) 1688.
- [8] A.J. Bard, L.R. Faulkner, *Electrochemical Methods*, Wiley, New York, 1980, p. 96.
- [9] R.B. Bird, W.E. Stewart, E.N. Lightfoot, *Transport Phenomena*, Wiley, New York, 1960, p. 559.
- [10] R. Aris, *The Mathematical Theory of Diffusion and Reaction in Permeable Catalysts*, Vol. I, Clarendon Press, Oxford, 1975, p. 40.



## Increasing Proton Exchange Membrane Fuel Cell Catalyst Effectiveness Through Sputter Deposition

Andrew T. Haug,<sup>a,\*</sup> Ralph E. White,<sup>a,\*\*\*</sup> John W. Weidner,<sup>a,\*\*\*\*,z</sup> Wayne Huang,<sup>b</sup> Steven Shi,<sup>b,\*\*\*</sup> Timothy Stoner,<sup>c</sup> and Narendra Rana<sup>c</sup>

<sup>a</sup>Center for Electrochemical Engineering, Department of Chemical Engineering, University of South Carolina, Columbia, South Carolina 29208, USA

<sup>b</sup>Plug Power, Incorporated, Latham, New York 12110, USA

<sup>c</sup>New York State Fuel Cell Institute, Center for Advanced Thin Film Technology, Albany, New York 12203, USA

Sputter deposition has been investigated as a tool for manufacturing proton-exchange membrane fuel cell (PEMFC) electrodes with improved performance and catalyst utilization vs. ink-based electrodes. Sputter-depositing a single layer of Pt on the gas diffusion layer provided better performance (0.28 A/cm<sup>2</sup> at 0.6 V) than sputtering the Pt directly onto a Nafion membrane (0.065 A/cm<sup>2</sup> at 0.6 V) and equaled the performance of the baseline for an equivalent Pt loading. Sputter-depositing alternating layers of Pt and Nafion-carbon ink (NCI) onto the membrane did not increase the performance over the baseline as measured in amperes per centimeter squared due to the excessive thickness of the NCI (the NCI accounted for 99.9% of the electrode thickness). However, three and six layer Pt/NCI membrane electrode assemblies (MEAs) resulted in Pt activities double that of the 905 A/g at 0.6 V achieved by the ink-based baseline. Decreasing the thickness of each NCI layer increased the performance of the six-layered Pt/NCI MEA from 0.132 to 0.170 A/cm<sup>2</sup> at 0.6 V, providing an activity of 2650 A/g at 0.6 V. It is likely that by further decreasing the ratio of NCI to Pt in these electrodes, Pt activity, and PEMFC electrode performance can be increased.  
© 2002 The Electrochemical Society. [DOI: 10.1149/1.1446082] All rights reserved.

Manuscript submitted July 11, 2001; revised manuscript received October 5, 2001. Available electronically January 29, 2002.

Proton exchange membrane fuel cells (PEMFCs) are gaining popularity due to their high operating efficiency and environmental friendliness. One of the barriers to commercialization is the prohibitive cost of this technology.<sup>1</sup> In a recent solicitation, the U.S. Department of Energy set long-term goals for PEMFC performance in a 50 kW stack that included operation with cathode loadings of 0.05 mg/cm<sup>2</sup> or less of precious metals.<sup>2</sup>

Typical methods of manufacturing membrane-electrode assemblies (MEAs) for PEMFCs involve painting, spraying, or printing of catalyst inks that contain a matrix of electrolyte and carbon-supported catalyst.<sup>3-6</sup> It is this three-phase interface of catalyst, carbon, and electrolyte (typically Nafion<sup>®</sup>) that allows effective gas and water diffusion and proton transport and electron transport to and from the catalyst sites. Refinements of this process have involved optimizing the ratios of Pt, C, and Nafion present in this three-phase interface.<sup>3,5</sup> There are limitations on the catalyst activity imposed by the particle size of Pt on activated carbon.

As alternatives, electrodeposition and sputter deposition have been used to manufacture MEAs of low catalyst loadings.<sup>3,7-14</sup> Both pulse and direct current (dc) electrodeposition have been used to localize a thin layer of Pt near the surface of the MEA,<sup>7,8</sup> resulting in the development of electrodes on the order of 0.05 mg Pt/cm<sup>2</sup>.<sup>8</sup> Sputter deposition is widely used for integrated circuit manufacturing and has been investigated for the preparation of more effective fuel cell electrodes for more than a decade. Srinivasan *et al.*<sup>3,9-11</sup> applied a 50 nm Pt-sputtered film to the front surface of a catalyzed gas diffusion layer (GDL) to reduce the loading tenfold (4 mg/cm<sup>2</sup> to 0.4 mg Pt/cm<sup>2</sup>) without reduction in performance. Hirano *et al.*<sup>12</sup> sputter deposited platinum on uncatalyzed GDLs resulting in cell performances at loadings of 0.10 mg Pt/cm<sup>2</sup> equivalent to those of standard methods at loadings of 0.40 mg Pt/cm<sup>2</sup>. Sputter deposition has been used to reduce the amount of anode catalyst required for direct methanol fuel cell (DMFC) anodes as well. Witham *et al.*<sup>13</sup> achieved DMFC anode catalyst activities one to two orders of magnitude higher than those of conventional ink-based catalysts, sug-

gesting that DMFC anodes could be manufactured containing less than one-tenth the amounts presently used (2.5-4 mg Pt/cm<sup>2</sup>) without loss in performance.

Cha and Lee<sup>14</sup> alternated sputtering microthin (5 nm) Pt layers and painting layers of Nafion and carbon ink directly onto the membrane. By reducing the amount of Pt on each layer, they were able to achieve cell performances at extremely low loadings (~0.043 mg/cm<sup>2</sup>) that were nearly equivalent to that of higher loadings (~0.5 mg/cm<sup>2</sup>) under similar conditions. Very efficient usage of Pt is demonstrated in this method.

The goal of this work was to examine the sputter-deposition technique as a means to improve performance and/or reduce the catalyst loading of proton exchange membrane (PEM) fuel cells. First Pt was sputtered on the different substrates that comprise individual fuel cells. These were built into MEAs and compared to MEAs made through ink-based methods and ink-based MEAs augmented through sputter deposition. Based on these results, GDLs and membranes were then subjected to the layered technique first developed by Cha and Lee<sup>14</sup> with the goal of reducing the amount of Pt catalyst used and increasing fuel cell performance. Based upon the findings, improvements were made on Cha and Lee's technique allowing for the manufacture of thinner, more effective electrodes for MEAs.

### Experimental

**Catalyst inks.**—The method for the catalyst ink preparation and MEA fabrication performed in this project have been described elsewhere.<sup>4</sup> The following catalyst inks were prepared: (i) Nafion + carbon only (Nafion-carbon ink or NCI) and (ii) Nafion + 20% Pt on carbon.

The inks were prepared for Pt by adding the E-TEK catalyst (20% catalyst on XC-72 carbon) to a solution of 5 wt % Nafion (DuPont). In the case of NCI, XC-72 carbon was added to a solution of 5 wt % Nafion.

**Ink-based MEAs.**—Decals (Teflon, 10 cm<sup>2</sup>, three ply) were weighed prior to application of the catalyst ink. The ink was drawn across the surface of the decals using a Meyer rod. Anode and cathode target loadings for the baseline ink-based MEA were both 0.15 mg Pt/cm<sup>2</sup> for a combined MEA loading of 0.30 mg Pt/cm<sup>2</sup>. A low Pt loading was chosen as the baseline because low catalyst loading is a goal for commercializing PEMFCs.<sup>2</sup> The coated decals were dried in an oven at 105°C under ambient pressure for 10 min.

\* Electrochemical Society Student Member.

\*\* Electrochemical Society Fellow.

\*\*\* Electrochemical Society Active Member.

<sup>z</sup> E-mail: weidner@engr.sc.edu

To form a MEA with ink-coated decals, appropriate decals were placed on either side of the PEM (Nafion 117, protonated form). This assembly was hot-pressed to ensure bonding. It was then cooled to room temperature, before the decals were carefully peeled from the assembly. An uncatalyzed gas diffusion layer (Toray) was placed on either side of the MEA to complete the membrane-electrode unit (MEU).

**Plasma treatment and Pt sputter deposition.**—Nafion 117 membranes, uncatalyzed GDLs (Toray) and MEAs were chosen as substrates for sputter deposition. Plasma modifications and sputter-deposition augmentations/additions were both completed using an Anatech Hummer 10.2 sputter-coating tool. A modified sample stage was used to support PEM, MEA, and GDL substrates of sizes up to  $6 \times 6$  cm while masking 1.5 cm about the membrane's perimeter. An aluminum target was used for ac and dc plasma modifications, while the Pt (Anatech) targets as well as a carbon evaporation system (Anatech) were used for sputter-deposition augmentations/additions.

All PEMs, MEAs, and GDLs subject to sputter-deposition were first ac plasma cleaned for a period of 5 min at 5 mA and 1.2 kV to remove residual buildup from the target as well as roughen the substrate surface. All treatments were completed at a pressure of  $\sim 62$  mTorr. A separate vacuum chamber was used to evacuate each substrate to a pressure of  $\sim 45$  mTorr, before it was placed in the sputter-coating tool to minimize contaminant out-gassing in the deposition chamber.<sup>15</sup>

Since all plasma and sputter-deposition treatments must be performed under vacuum, the stability of Nafion 117 under vacuum was evaluated. Each PEM material was slowly evacuated to a pressure below 1 mTorr. Nafion 117 remained very pliable following evacuation. Mass measurement of Nafion before and after seven different evacuation and processing sequences indicated that the membrane loses approximately 2.3% of its total mass as a result of dehydration during evacuation. In each case however, Nafion quickly ( $\sim 30$  min) rehydrates upon exposure to ambient air. The exposed membranes were then built into MEAs and subjected to performance testing. They performed analogously to nonevacuated membranes, indicating that Nafion was a viable candidate for plasma and sputter-deposition treatments. The performance of a vacuum-treated MEA also showed no adverse effects when tested.

A potential of 1.8 kV and a current of 8 mA was maintained to control the deposition rate for Pt. A  $\text{SiO}_2$  sample was sputter-deposited *in situ* with each PEM, MEA, or GDL. The resultant metal/ $\text{SiO}_2$  stack was subjected to cross-sectional view SEM imaging to verify the sputter-deposited film thickness and top-view SEM imaging to determine surface characteristics of the film.

Multilayered MEAs were prepared by first spraying the anode and cathode sides of PEM with NCI. The MEA was then subject to a vacuum of 30 mTorr before the appropriate catalyst was sputter deposited. This sequence was repeated until the desired number of layers was achieved. Multilayered GDLs were prepared by an identical process except that only one side of the GDL was treated.

MEAs containing sputter-deposited catalyst layers were built into MEUs through methods similar to that of the baseline. In the case of multilayered GDLs, appropriate GDLs were placed on either side of a blank Nafion 117 membrane and hot-pressed to ensure a well-bonded MEU.

**Cell assembly and testing.**—The MEUs were placed in a  $10 \text{ cm}^2$  cell assembly and incubated for 4 to 8 h at ambient pressure, cell temperature of  $70^\circ\text{C}$ , stoichiometric ratio ([actual flow]/[stoichiometric flow] required for a  $1.0 \text{ A/cm}^2$  current) of 1.5 at the anode and 2.0 at the cathode. Fuel cell performance curves were obtained under the conditions set out in Table I.

## Results

**AC and dc plasma roughening.**—The AFM images in Fig. 1 show the effects of an ac plasma treatment on Nafion. Both ac

Table I. Fuel cell test conditions.

Pressure	1 atm
Cell temperature	$70^\circ\text{C}$
Stoichiometric ratio (at $1 \text{ A/cm}^2$ )	1.5 Hydrogen 2.0 Air
Feedstreams	Anode: hydrogen Cathode: air
Humidification	Complete humidification of anode and cathode gas streams for all trials.

plasma and dc plasma substantially roughen the surface of the PEM. Analogous roughening by ac plasma or dc plasma did not significantly increase the surface of MEAs or GDLs, since the surfaces of these samples are much rougher in their original state. The SEM images in Fig. 2 document the influence of ac and dc plasma modification of MEAs. The high and medium magnification SEM images both suggest ac and dc plasma minimally alter the surface of the MEA. However, the low magnification SEM images indicate that dc plasma treatments create cracks in the surface layer of the MEAs. Therefore, ac plasma treatments were used throughout the remainder of this program. It was hoped that roughening the surface of the PEM or MEA would enhance fuel cell performance by increasing the number of active catalytic sites. However, performance of MEUs made from roughened PEMs and MEAs showed no improvement over a baseline MEU.

**Determination of sputter-deposition rates and catalyst loading.**—The top view SEM images in Fig. 3 were analyzed to determine the surface coverage of the sputter-deposited film (Pt

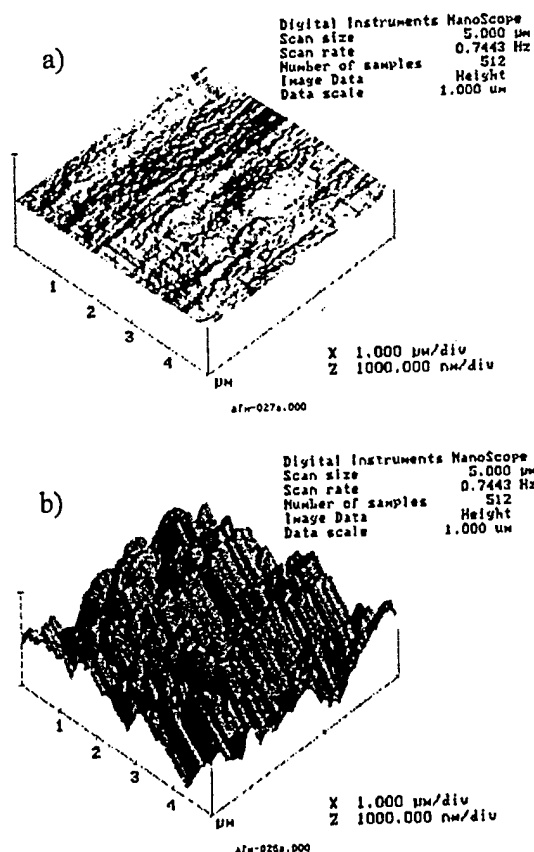


Figure 1. AFM images: (a) as-received Nafion 117, (b) ac plasma roughened Nafion 117 (potential, 1350 V; current, 11 mA; duration, 10 min). Scale:  $1.0 \mu\text{m}$  division.

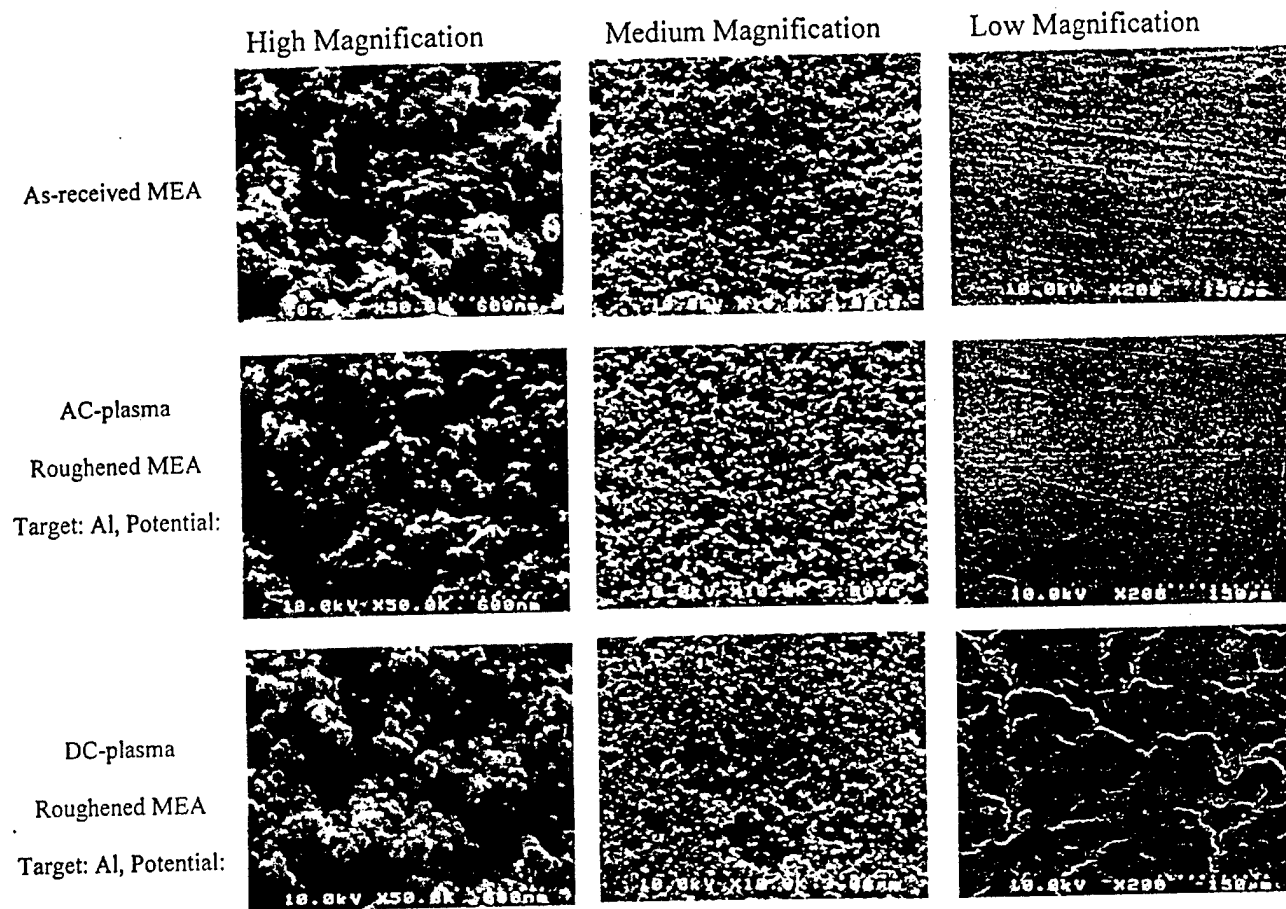


Figure 2. SEM images of plasma roughening of MEAs at high (50,000 times), medium (10,000 times), and low (200 times) magnification. The plasma modification had negligible effect on the roughness of the MEA, however, dc roughening tended to crack the surface of the MEA.

~ 65%). Pt did not form continuous films on the  $\text{SiO}_2$  substrate, but rather agglomerated. This is consistent with the literature.<sup>16</sup> The surface coverage was used in conjunction with the bulk density ( $\text{Pt} = 21.4 \text{ g/mL}$ ) and the film thicknesses from the cross-sectional SEM images to calculate the subsequent Pt loadings. Based on this method, the Pt sputter-deposition rate was found to be  $5.6 \mu\text{g Pt/cm}^2/\text{min}$ . Pt loading analyses of all sputtered PEMs, GDLs, and MEAs from Adirondack Environmental Services on yielded Pt loadings that were generally consistent with the deposition rate determined from cross-sectional and top view SEM images.

This sputter deposition rate ( $\mu\text{g/cm}^2/\text{min}$ ) for Pt was found to be constant with respect to time for durations of 5 min or more. The cross-sectional view in Fig. 3 shows that the thickness of 30 and 45 min sputter-deposited Pt is roughly two and three times the thickness of a 15 min deposition of Pt, respectively. Semiquantitative analyses via energy dispersive X-ray spectroscopy (EDXS) and Rutherford backscattering spectrometry (RBS) confirm these Pt deposition rates. These methods in combination with the analysis provided by Adirondack Environmental Services were also used to determine loadings of individual MEUs composed of Pt sputter-deposited layers of less than 5 min duration.

**Sputter-deposition augmentation and addition.**—The sputter deposition treatments performed for this experiment are listed in Table II.

Pt was sputter-deposited on GDLs, PEMs, and MEAs. Figure 4 compares the cell performance of MEUs made from GDLs upon which 15, 30, 45, and 90 min of Pt was sputter deposited as a single layer. In all cases, the equivalent amounts of Pt were added to the

anode and cathode. The MEU comprised of 30 min of sputter-deposited Pt is closest to the baseline MEU in loading ( $0.168$  and  $0.150 \text{ mg Pt/cm}^2$ , respectively). Under conditions of hydrogen/air (anode/cathode) feed at  $70^\circ\text{C}$  and  $1 \text{ atm}$ ,  $15 \text{ min Pt}$  ( $0.084 \text{ mg/cm}^2$ ) deposited on the anode and cathode GDL,  $0.147 \text{ A/cm}^2$  was observed at  $0.6 \text{ V}$  compared to  $0.276 \text{ A/cm}^2$  for the baseline. Doubling the sputter-deposition time to 30 min resulted in a cell performance comparable to the baseline MEA. Figure 4 shows that further amounts of sputter-deposited Pt showed no appreciable increase in cell performance.

The goal of the sputter depositing an additional layer of Pt on the surface of the anode and cathode of the baseline MEA is to increase the performance of the electrodes (primarily the cathode). Oxygen kinetics (at high potentials) and oxygen diffusion (low potentials) are two factors that limit the performance of the fuel cell. It was hoped that the application of this additional Pt layer would increase the rate of the oxygen reduction (by having more available sites) and that by having a layer of Pt on the surface of the MEA, that there would be less diffusional resistances as oxygen would not have to diffuse far to get to a reaction site. Figure 5 compares the cell performance of a baseline MEA to those onto which Pt has been sputter deposited. Under conditions of hydrogen/air feed at  $70^\circ\text{C}$  and  $1 \text{ atm}$ ,  $15 \text{ min}$  of Pt ( $0.84 \text{ mg/cm}^2$ ) deposited on the anode and cathode of a baseline MEA provides an increase in performance at high voltages (from  $0.025$  to  $0.072 \text{ mg/cm}^2$  at  $0.8 \text{ V}$ ). However, the added sputter-deposited layer of Pt clearly reduced the limit at which the gases (oxygen, hydrogen, water vapor) could diffuse through the electrodes. This effect resulted in a reduction in performance of 52%

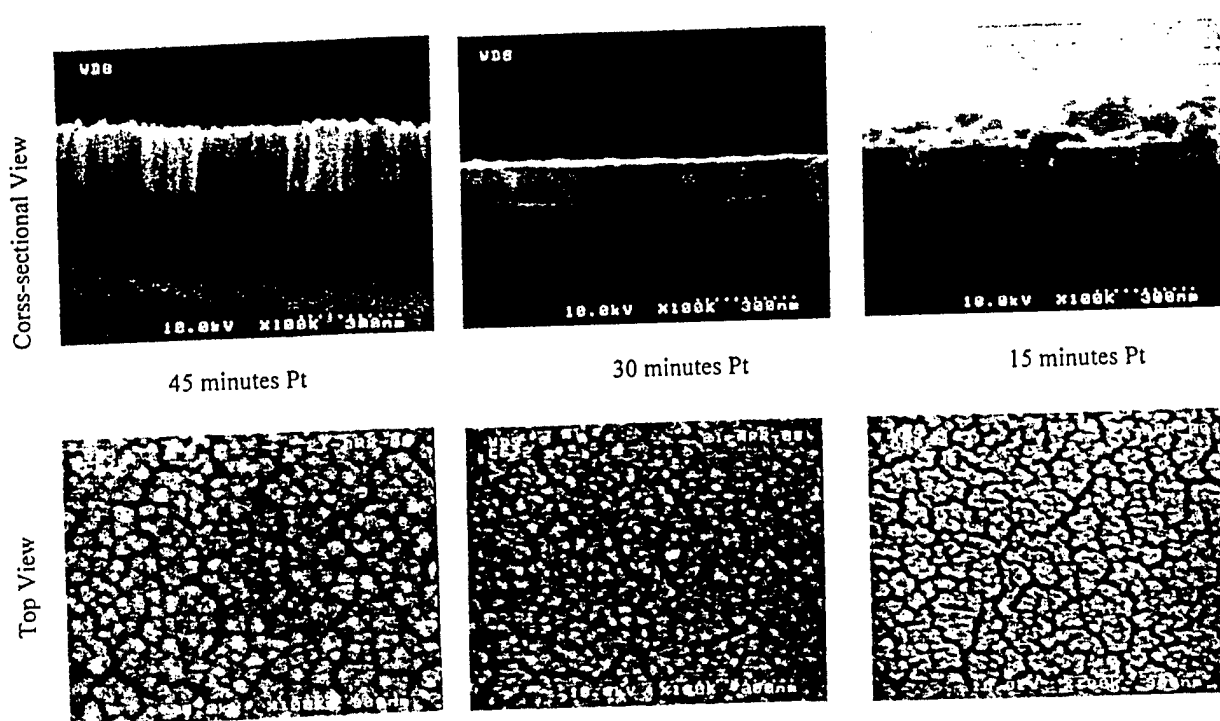


Figure 3. Top and cross-sectional SEM images (100,000 times) of sputter-deposited Pt on Si/SiO<sub>2</sub> substrates. Scale: 300 nm (such that the thickness of the 45 min deposition is 200 nm).

Table II. Sputter-deposition treatments. All Pt depositions were performed identically on the anode and cathode. In the case of a sputter-deposition on a GDL substrate, identical depositions were performed on two GDLs that would then form the anode and cathode.

Substrate	Addition
MEA (baseline)	15 min sputter-deposited Pt
MEA (baseline)	30 min sputter-deposited Pt
Nafion 117	15 min sputter-deposited Pt
Nafion 117	30 min sputter-deposited Pt
Nafion 117	15 min sputter-deposited Pt + NCI
Nafion 117	30 min sputter-deposited Pt + NCI
GDL	15 min sputter-deposited Pt
GDL	30 min sputter-deposited Pt
GDL	45 min sputter-deposited Pt
GDL	60 min sputter-deposited Pt
GDL	90 min sputter-deposited Pt
GDL	NCI + (5 min sputter-deposited Pt + NCI) × 3
Nafion 117	NCI + (15 min sputter-deposited Pt + NCI) × 3
Nafion 117	NCI + (5 min sputter-deposited Pt + NCI) × 3
Nafion 117	NCI + (2.5 min sputter-deposited Pt + NCI) × 3
Nafion 117	NCI + (1.0 min sputter-deposited Pt + NCI) × 3
Nafion 117	NCI + (0.5 min sputter-deposited Pt + NCI) × 3
Nafion 117	NCI + (0.5 min sputter-deposited Pt + NCI) × 6
Nafion 117	NCI + (0.5 min sputter-deposited Pt + diluted NCI) × 6

at 0.4 V (from 0.56 A/cm<sup>2</sup> to 0.27 cm<sup>2</sup>) for the case where a 15 min (0.084 mg/cm<sup>2</sup>) Pt layer is added to the anode and cathode. Gas diffusion is all but stopped in the case where 30 min of Pt is deposited on top of the baseline MEA, and the result is negligible cell performance. This lack of performance is accompanied by an increase in cell resistance from 25 to 200 mΩ as shown in Table III. It is likely that the resistance is ionic in nature, as the coating of the

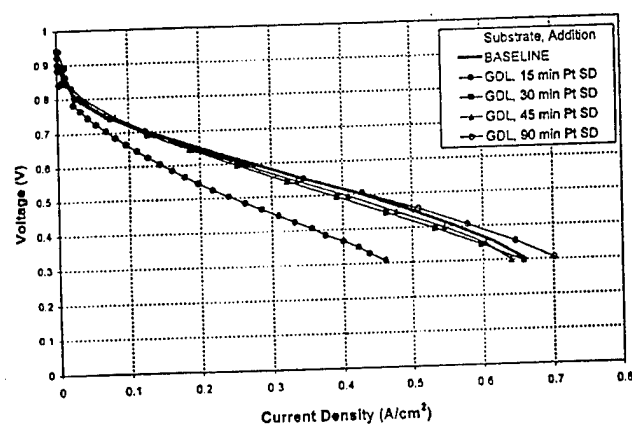


Figure 4. Performance comparison for MEUs prepared from GDLs with various sputter-deposited Pt loadings.  $P = 1$  atm,  $T = 70^\circ\text{C}$ .

surface of the MEA fills the pores necessary for the transport of water through to the membrane resulting in a reduction in proton conductivity.

The sputter deposition of Pt onto a Nafion 117 substrate yielded an MEU that showed very poor performance as shown in Fig. 6. Under conditions of hydrogen/air (anode/cathode) feed at 70°C and 1 atm, 15 and 30 min of sputter-deposited Pt deposited on the anode and cathode side of Nafion 117 resulted in current densities of 0.044 and 0.065 A/cm<sup>2</sup> at 0.6 V, respectively. The resistance of the cell at open-circuit voltage was very high compared to the baseline (250 vs. 25 mΩ). In contrast to the sputter-deposition augmented MEAs, it is believed that the high resistance is the result of poor electrical conduction between the catalytic Pt sites and the cathode. As shown in Fig. 3, Pt is not deposited as a continuous film, but an agglomeration

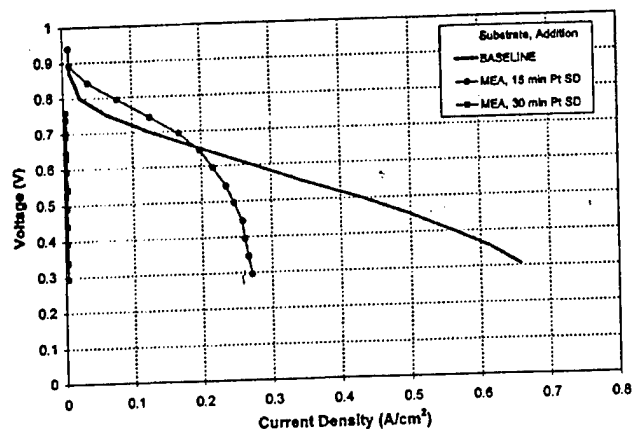


Figure 5. Performance comparison of baseline MEAs onto which various amounts of Pt has been sputter deposited.  $P = 1$  atm,  $T = 70^\circ\text{C}$ .

Table III. Cell resistance of various MEUs at open-circuit voltage. Resistances were measured by a micrometer set at 1 kHz ac voltage.

Substrate	Addition	Resistance $\epsilon$ (m $\Omega$ )
Baseline	—	25
Baseline	15 min Pt SD	27
Baseline	30 min Pt SD	200
Nafion membrane	15 min Pt SD	250
Nafion membrane	15 min SD + NCI	40
Nafion membrane	30 min Pt SD	83
Nafion membrane	30 min Pt SD + NCI	54
Nafion membrane	NCI + 3 $\times$ (5 min Pt SD + NCI)	27
GDL	15 min Pt SD	21
GDL	30 min Pt SD	23
Baseline	Ru filter (ink-based)	31

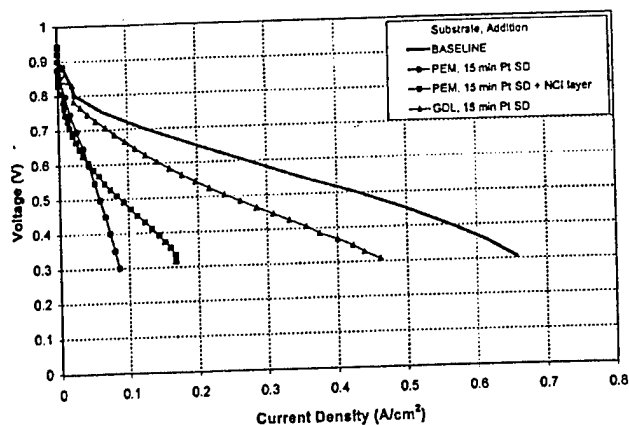


Figure 6. Performance comparison of MEUs prepared from PEMs and GDLs with one or several layers of sputter-deposited Pt.  $P = 1$  atm,  $T = 70^\circ\text{C}$ .

of Pt islands with a columnar microstructure. The addition of a layer of NCI (50% Nafion solids by weight) over the layer of sputter-deposited Pt decreases cell resistance and increases performance. Islands of sputter-deposited Pt are connected by the carbon in the NCI, activating the sites by providing a pathway for electrons to flow to and from the sites. In the case of a 15 min Pt deposited on

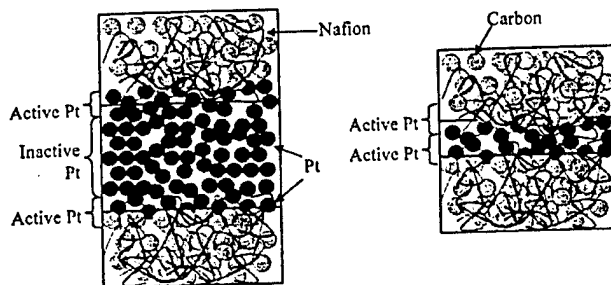


Figure 7. Representation of a single layer of a high (left) and low (right) amount of sputter-deposited Pt between layers of Nafion-carbon ink (NCI).

Nafion. Table III shows the drop in resistance from 250 to 40 m $\Omega$  with the addition of the NCI layer, while Fig. 6 shows that there is some improvement in cell performance at lower voltages (0.137 vs. 0.074 A/cm $^2$  at 0.4 V). The Pt islands not in contact with the GDL provide no conduit for the electrons and are thus deactivated.

For an equal amount of sputter-deposited Pt, performance of the resultant MEU was better when applied to the GDL as opposed to the MEA or PEM. The sputter deposition of Pt directly on the membrane showed far less performance (0.044 vs. 0.138 A/cm $^2$  at 0.6 V) than when deposited on the GDL. The rough surface of the GDL allows for the generation of a greater Pt active area. Also the high porosity of the GDL allows gas diffusion to and from the electrodes even after Pt deposition. It is hypothesized that the deposition of a single Pt layer creates regions of active and inactive Pt as shown in the schematic in Fig. 7. Pt is only active as a catalyst when it is in contact with the electrolyte and a conductive support. Pt not in contact with Nafion is inactive because proton transport is not possible. The inherent roughness of the GDL increases this area of active Pt compared to the relative smoothness of the MEA and bare membrane. Even on the GDL the deposition of Pt beyond a given amount (30 min or 0.168 mg/cm $^2$ ) provides no added performance, because the added Pt serves only to increase the layer of inactive Pt described in Fig. 7.

A multilayer electrode technique<sup>14</sup> was used to increase the regions of active Pt area by increasing the number of layers of sputter-deposited Pt. MEAs were prepared from PEMs with multiple layers of sputter-deposited Pt and spray-deposited NCI as shown in Fig. 8. The anode and cathode were built in an identical manner. Figure 9 compares the performance of cells for which the anode and cathode is composed of three sputter-deposited Pt layers dispersed between NCI. Individual Pt layer thicknesses of 15, 5, 2.5, 1.0, and 0.5 min resulted in electrode loadings of 0.2089, 0.07, 0.0795, 0.0407, and 0.027 mg Pt/cm $^2$ , respectively. As the thickness of each layer and resultant Pt loading decreases, the cell performance remains constant. This verifies the theory that the fraction of inactive Pt shown

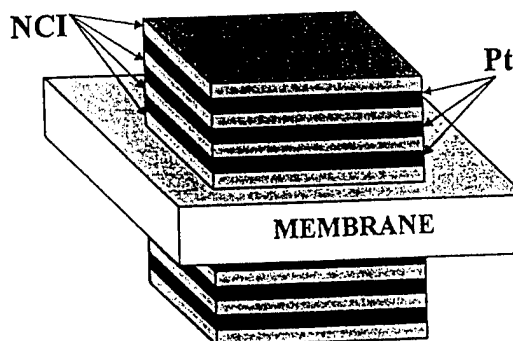


Figure 8. Representation of a three layer Pt-NCI MEA.

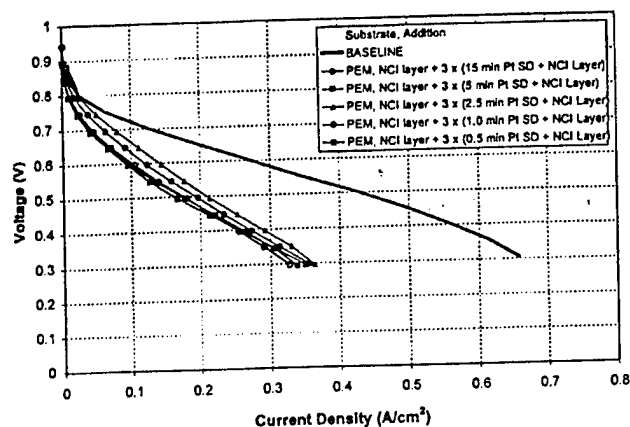


Figure 9. Performance comparison between the baseline and three-layer MEAs using various Pt loadings.  $P = 1$  atm,  $T = 70^\circ\text{C}$ . Individual Pt layer thicknesses of 15, 5, 2.5, 1.0, and 0.5 min resulted in electrode loadings of 0.2089, 0.07, 0.0795, 0.0407, 0.027 mg Pt/cm<sup>2</sup>, respectively.

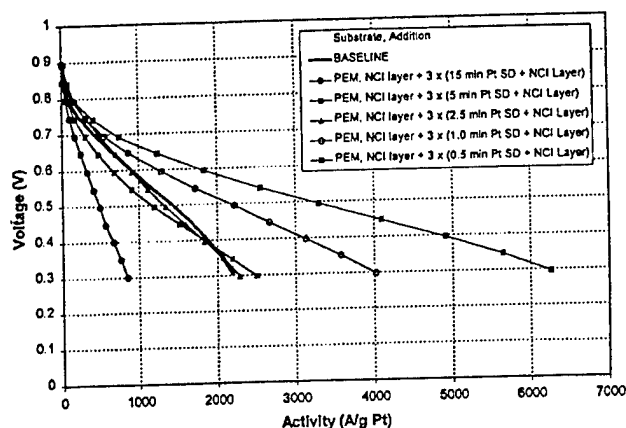


Figure 10. Comparison Pt Activity between the baseline and various three-layer anode and cathode MEAs.  $P = 1$  atm,  $T = 70^\circ\text{C}$ .

in Fig. 7 is eliminated as the thickness of each Pt layer is reduced. The amount of active Pt in the three-layer electrode did not change with the thickness of each sputter-deposited layer. Furthermore, all three-layer MEAs outperformed the single Pt layer MEA (0.091–0.140 vs. 0.044 A/cm<sup>2</sup> at 0.6 V), suggesting that using multiple layers increased the active Pt area available for reaction.

Figure 10 shows that fuel cell activity continuously increases as the amount of sputter-deposited Pt in each of the multiple layers is reduced. At 0.6 V, the activity of the 0.5 min Pt/layer MEU is 1835 A/g Pt vs. 905 A/g Pt for the baseline MEA and 670 A/g Pt for the 15 min Pt on the GDL. Even higher activity should be attainable, since a sputter-deposited Pt layer only a few monolayers thick could provide an equivalent number of active catalytic sites (a 0.5 min sputter-deposited layer of Pt is roughly equivalent to six monolayers).

Multilayer treatments were of no benefit when applied to the GDLs as shown in Fig. 11. This is consistent with the high degree of roughness and porosity of the GDL. A high surface area allows successful distribution of sputter-deposited Pt throughout the GDL. As a result, the performance of the single 15 min sputter-deposited layer of Pt on the GDL is greater than an equivalent amount of Pt deposited directly on the membrane in three layers (0.147 vs. 0.091 A/cm<sup>2</sup> at 0.6 V).

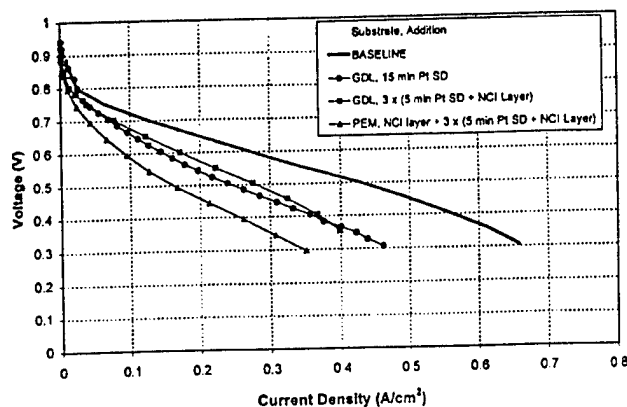


Figure 11. Performance comparison of layered PEM and GDL electrodes.  $P = 1$  atm,  $T = 70^\circ\text{C}$ .

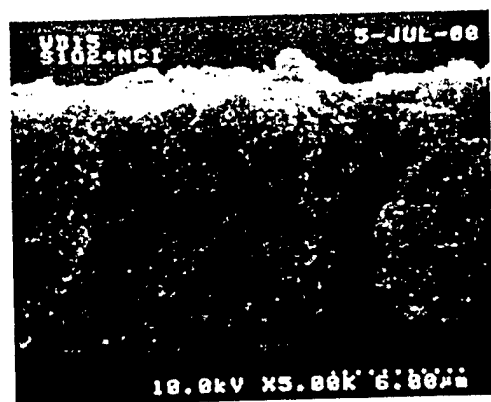
To determine the effect of layering on the performance of the MEA when the layers are applied to the membrane, three different layered catalyst structures were fabricated: (1) an anode and cathode consisting of NCI + (1 min of sputter-deposited Pt + NCI)  $\times$  3; (2) an anode and cathode consisting of NCI + (0.5 min of sputter-deposited Pt + NCI)  $\times$  6; and (3) an anode and cathode consisting of NCI + (0.5 min of sputter-deposited Pt + NCI diluted 1:5 with isopropanol)  $\times$  6.

MEA 2 contains the same amount of Pt as MEA 1, but MEA 2 contains twice the amount of Pt-NCI interfaces as a result of doubling the number of Pt layers from three to six. Comparing the performances of the single-layer 15 min sputtered MEA shown in Fig. 6 and the three-layer sputtered MEAs shown in Fig. 9, the active area and hence cell performance is a function of the number of sputtered layers and not the amount of Pt. Therefore, MEA 2 has roughly double the active area of MEA 1. MEA 3 contains the same number of Pt layers as 2, but the NCI used in 3 is diluted in order to reduce the thickness of the NCI region between each Pt layer. Figure 12a shows a cross-sectional view SEM image of a spray-deposited NCI layer on an SiO<sub>2</sub> substrate. The spray deposited NCI layer is  $\sim 12$   $\mu\text{m}$  thick. Therefore for MEA 2, the anode and cathode stacks are roughly  $\sim 70$   $\mu\text{m}$  thick (the thickness of the Pt is negligible). This is much thicker than the anode and cathode of the baseline MEU, which are typically 5–10  $\mu\text{m}$  thick. Like the layers of sputter-deposited Pt, it is not necessary for the NCI layers to be so thick. Based on the fact that a layer of 15 min of sputter-deposited layer is 75 nm thick (see Fig. 3), that the 0.5 min sputter-deposited layer of Pt is a fraction of the thickness of the 15 min layer, and that the NCI layer is roughly 12  $\mu\text{m}$  thick, it can be concluded that the NCI comprises at least 99.9% of the thickness of the multilayer electrodes.

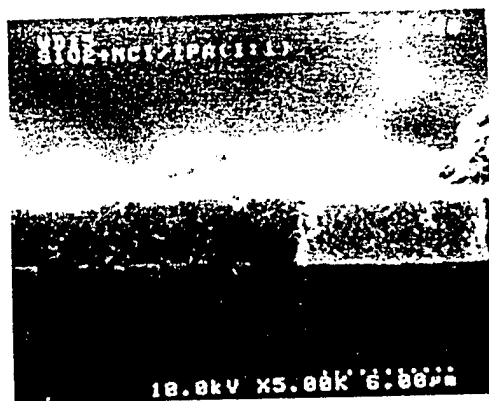
To reduce the thickness of the NCI layers and thus reduce these resistance losses, the NCI was diluted with isopropanol. The thickness of a spray-deposited layer of NCI diluted 1:1 by volume with isopropanol, shown in Fig. 12b, is roughly  $\sim 4$   $\mu\text{m}$  thick, compared to the 12  $\mu\text{m}$  thickness of the pure NCI. To achieve a multilayered electrode of less than 10  $\mu\text{m}$  (MEA 3), a dilution of 1:5 NCI to isopropanol was used.

Figure 13 shows that as the number of electrode layers is increased from three (MEA 1) to six (MEA 2), the cell performance increases (0.105 to 0.132 A/cm<sup>2</sup> at 0.6 V). However, there is not a doubling of performance that accompanies the doubling of the active area. The increased diffusional, ionic, and electronic resistances caused by the increased thickness of the electrodes of MEA 2 vs. MEA 1 are likely causes for the limited performance increase seen in Fig. 13. Versus the three-layer electrode, gases, protons, and electrons must travel further in the six-layer electrode to get to and from all available Pt sites.





a) Pure NCI



b) Diluted NCI

Figure 12. Cross-sectional view SEM images of coating produced by (a) pure NCI, (b) diluted NCI (1:1 by volume with isopropanol).

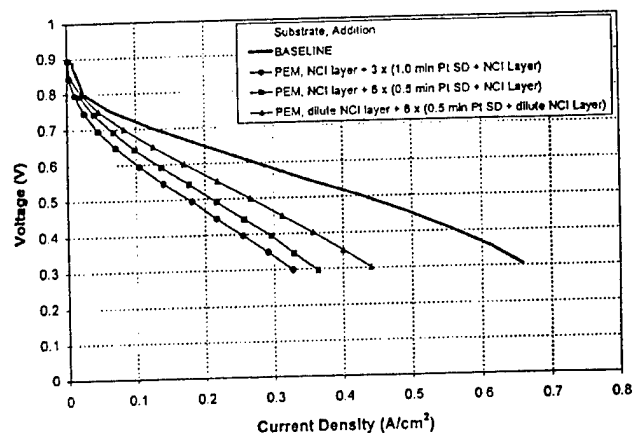


Figure 13. Performance comparison of MEAs comprised of three and six layers (anode and cathode) using pure NCI.  $P = 1$  atm,  $T = 70^\circ\text{C}$ .

As shown in Fig. 13, MEA 3 outperforms MEA 2 0.170 to 0.132  $\text{A}/\text{cm}^2$  at 0.6 V. This value is closer to double that of MEA 1, containing three-layer electrodes. This further emphasizes the fact that as the thickness of the NCI decreases, performance increases. The performance of MEA 3 is also greater than the MEU containing 15 min of Pt was sputtered onto the anode and cathode GDL, but

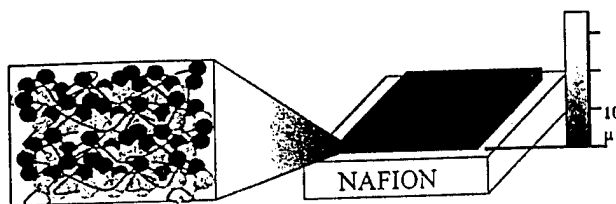


Figure 14. Representation of a continuous three-phase interface (Nafion, carbon, catalyst) prepared by applying Nafion, carbon, and Pt simultaneously.

less than the MEU containing 30 min of Pt on the anode and cathode GDL and less than the performance of the baseline MEA. The loading for each electrode for the MEA 3 was found to be  $\sim 0.0324$  mg  $\text{Pt}/\text{cm}^2$  anode/cathode ( $0.0648$  mg  $\text{Pt}/\text{cm}^2$  in the entire MEA) resulting in an activity of 2650  $\text{A}/\text{g}$  Pt at 0.6 V, the highest value of all MEAs tested and three times greater than the baseline (905  $\text{A}/\text{g}$ ).

### Conclusions

1. Of the three substrates studied (membrane, GDL, and MEA), sputter-depositing Pt on the GDL showed the best performance, equalling that of the baseline MEA for an equivalent amount of Pt. However, sputter-depositing multiple layers of Pt on the GDL showed no improvement in performance over an equivalent amount of Pt sputtered as a single layer.

2. MEAs built from multilayered sputter-deposited Pt and spray-deposited NCI demonstrated improved performance over single-layer, sputter-deposited MEAs of equivalent or greater Pt loadings. By reducing the amount of Pt and NCI in each layer, a level of Pt activity higher than that of the baseline has been achieved. This level of activity is maintained as the number of layers increase from three to six, provided the NCI layers are sufficiently thin. The preparation of MEAs with extremely high activity suggests future study. This is hypothesized to be the result of increasing the three phases of Pt, Nafion, and carbon necessary for an active catalyst.

3. The optimal performance achieved from the MEA containing six-layer Pt + dilute NCI anode and cathode was  $0.17$   $\text{A}/\text{cm}^2$  at 0.6 V. This is less than the performance achieved by Cha and Lee (roughly  $0.32$   $\text{A}/\text{cm}^2$  at 0.6 V). However, all fuel cells in this experiment were fed  $\text{H}_2/\text{air}$  at 1 atm and  $70^\circ\text{C}$ , compared to an  $\text{H}_2/\text{O}_2$  feed at 1 atm and  $60^\circ\text{C}$  used by Cha and Lee.<sup>14</sup>

4. Catalyst activities of greater than 2650  $\text{A}/\text{g}$  were achieved at 0.6 V and 5500  $\text{A}/\text{g}$  at 0.4 V from the MEA containing six-layer Pt + dilute NCI anode and cathode.

5. Further research can be done to optimize this three-phase interface area and eliminate the unused portion of the electrode. Even diluting the NCI between each sputter-deposited layer 5:1 with isopropanol results in a catalyst electrode in which NCI accounts for 99% of the width. However, to generate an electrode with even more than six Pt + NCI layers is neither the most economical (due to the time required to generate such a multilayered MEA) nor most effective approach. The generation of a continuous three-phase interface is the ultimate goal of this method, and this is what should be pursued using the method of sputter deposition. Simultaneously sputter-depositing Pt and spray-depositing NCI could produce a continuous three-phase interface region such as that shown in Fig. 14. This would result in an extremely thin ( $\sim 1$  micrometer) electrode that is conceptually almost identical to the ink-based catalyst electrode used in the baseline. The only difference is that the particle size of the sputter-deposited Pt would be much smaller, resulting in greater Pt surface area, higher Pt activity, higher Pt utilization, and hence a superior performing electrode compared to a conventional electrode prepared from colloidal catalyst inks. Also by applying this Pt/CI/Nafion electrode in a single application to the proton-exchange membrane, the process is less time consuming and, thus, more economical.

### Acknowledgments

The authors acknowledge the financial support from the National Institute of Standards and Technology under cooperative agreement no. 70NANB8H4039.

University of South Carolina assisted in meeting the publication costs of this article.

### References

1. Arthur D. Little Inc., *Cost Analysis of Fuel Cell Systems for Transportation: Baseline System Cost Estimate*, Final Report to Department of Energy (2000).
2. Solicitation for Financial Assistance Applications (SFAA) no. DE-RP04-01AL67057 Research and Development and Analysis for Energy Efficient Technologies in Transportation and Buildings Applications, Nov 21, 2000.
3. E. A. Ticianelli, C. R. Derouin, and S. Srinivasan, *J. Electroanal. Chem.*, **251**, 275 (1988).
4. M. S. Wilson. U.S. Pat. 5,211,984 (1993).
5. V. A. Paganin, E. A. Ticianelli, and E. R. Gonzalez, in *Proton Conducting Fuel Cells I*, S. Gottesfeld, G. Halpert, and A. Landgrebe, Editors, PV 95-23, p. 102, The Electrochemical Society Proceedings Series, Pennington, NJ (1995).
6. C. K. Witham, W. Chun, T. I. Valdez, and S. R. Narayanan, *Electrochem. Solid-State Lett.*, **3**, 497 (2000).
7. E. J. Taylor, E. B. Anderson, and N. R. K. Vilambi, *J. Electrochem. Soc.*, **139**, L45 (1992).
8. K. H. Choi, H. S. Kim, and T. H. Lee, *J. Power Sources*, **75**, 230 (1998).
9. S. Srinivasan, D. J. Manko, J. Koch, M. A. Enayetullah, and A. J. Appleby, *J. Power Sources*, **29**, 367 (1990).
10. E. A. Ticianelli, C. R. Derouin, A. Redondo, and S. Srinivasan, *J. Electrochem. Soc.*, **135**, 2209 (1988).
11. S. Mukerjee, S. Srinivasan, and A. J. Appleby, *Electrochim. Acta*, **38**, 1661 (1993).
12. S. Hirano, J. Kim, and S. Srinivasan, *Electrochim. Acta*, **42**, 1587 (1997).
13. C. K. Witham, W. Chun, T. I. Valdez, and S. R. Narayanan, *Electrochem. Solid-State Lett.*, **3**, 497 (2000).
14. S. Y. Cha and W. M. Lee, *J. Electrochem. Soc.*, **146**, 4055 (1999).
15. J. A. Thornton, *Deposition Technologies for Films and Coatings*, p. 170, Noyes Publications, Park Ridge, NJ (1982).
16. J. A. Poirier and G. E. Stoner, *J. Electrochem. Soc.*, **141**, 425 (1994).